Numéro d'ordre : DU 2037 PCCF T 1005

UNIVERSITE BLAISE PASCAL

(U.F.R. Recherche Scientifique et Technique)

ECOLE DOCTORALE DES SCIENCES FONDAMENTALES N° 648

THESE

présentée pour obtenir le grade de

DOCTEUR D'UNIVERSITE

Spécialité : Physique Corpusculaire

par

Eric FUCHEY

Diplômé d'un Master Recherche Physique

Électroproduction de pions neutres dans le Hall A au Jefferson Laboratory

soutenue publiquement le 22 juin 2010, devant la commission d'examen :

Président :	Mme.	B.	ERAZMUS	
Examinateurs :				
	M.	E.	VOUTIER	Rapporteur
	M.	Ch.	HYDE	Directeur de thèse
	M.	A.	BALDIT	Examinateur
	M.	P.	GUICHON	Examinateur
	M.	B.	MICHEL	Examinateur
Non present lors de la soutenance :	M.	Ch.	WEISS	Rapporteur

Acknowledgments

First of all, I would like to thank all the jury members which accepted to spend time examining this work. This jury, lead by Barbara Erazmus, included Charles Hyde, Eric Voutier, Alain Baldit, Pierre Guichon and Bernard Michel.

For his kind welcome inside the Laboratoire de Physique Corpusculaire, which hosted me during most of these three years, I would like to thank (again) Alain Baldit. As well, for allowing me to the École Doctorale des Sciences Fondamentales of Clermont Ferrand, I wish to thank its director, Pierre Henrard. For all the time I had to spend at Jefferson Lab, I am also grateful to Kees de Jager for his welcome, and more generally to all the staff for the administrative support needed.

I am grateful to Eric Voutier and Christian Weiss for reporting on this work. All discussions I could have with them, and all remarks they could do, either about this manuscript or about the article written on this work, were very helpful, constructive and enlighting. I still have the occasion to discuss with them from times to times, and the discussions I can have with them about the work I currently do are very enriching. As if they were not kind enough, they also accepted to write letters of recommandation to help me to find another job after my thesis. For those reasons, I would like to thank them warmly.

I owe the achievement of this thesis to really few people. Among these people, impossible not to mention Charles Hyde. Charles was my advisor for this thesis, and I have to tell that he did his job remarkably well. He was always available when I needed him, and I've learned a lot about the job of physicist, including physics of course, but also about "the art to expose your work to other physicists", which is always useful. He also made judicious choices about the work he allocated me for, and these choices with no doubt helped me to find another job after my thesis. Furthermore, and to be a little bit more materialist, it is also thanks to him that we had reliable funding (not just me, but all the Clermont-Ferrand Hall A DVCS team) to live on JLab site with no financial trouble for the period of the new experiment installation and data taking. Since a significant part of my thesis has been written and corrected on JLab site (and since I had enough worries with that...), this is not something to be completely neglected from my point of view (even if it is somehow secondary).

Two other people significantly contributed to the progress of my thesis, Pierre Bertin and Helène Fonvieille. Both were very experienced physicists, and agreed to spend lots of time sharing a part of their enourmous knowledge with me.

Pierre was particularly available and helpful, in spite of his official retirement, and was actually almost a second advisor to me. The work I expose in this thesis used to

be his analysis that I redid, completely independently from him if we except of course the precious advices he gave me about this work in particular, and physics in general. Moreover, all kinds of discussions with him were enriching, not only from the work point of view but from the personnal point of view, since his knowledge does not seems to have limits, and not only in physics (I remember for instance when he brought me with him for a walk on the coast, and knew about all kinds of birds that could be met there).

Helène may not have spend as much time as Pierre with me (I have to say that it is mainly because I used to ask her about something less often than Charles or Pierre), but was completely available whenever I had something to ask her. I remember that her advices about oral presentations were particularly valuables at the beginning, and helped me to avoid me some catastrophic failures at conferences, workshops, and meetings..

In addition to Charles Hyde, Pierre Bertin and Hèlene Fonvieille, I also have to mention Alexandre Camsonne, Carlos Muñoz-Camacho, and Malek Mazouz. All three where students on this experiment. No need to mention then how priceless was the information they could give me on every technical detail about the experiment and the analysis. In the manner of Charles, Pierre and Helène, they also used to give me good advices about oral communication (Carlos mostly, but Malek's remarks were very pertinent and helpful for my defence). They accepted to spend time sharing their knowledge with me, and I am grateful to them because of this, even if bad news sometimes came from them. I would cite for instance the time I've learned that I made an error of normalization of about 40 % less than three weeks before the defence. On the other hand (and also because it was not my fault...) they still helped me at the best they could do. This is why I'd like to thank wholeheartedly all three of them, with additional thanks to Alexandre which also introduced me to life in Newport News.

Finally, even though their "influence" were smaller than all the people cited above, I would like to thank warmly all other DVCS Hall A collaborators, physicists and technicians, form Clermont-Ferrand and elsewhere. On the physicists side I may cite Julie Roche (from Ohio University), which also used to advise me, from times to times only, but always pertinently, and Hisham Albataineh. On the technicians side (which are all from Clermont-Ferrand), I would cite Magali Magne, Michel Brossard, and Michel Crouau from the electronic team of Clermont Ferrand, and Guy Savinel and François Daudon from the mechanical engineering team of Clermont Ferrand.

I could not write any acknowledgements without saying a word on the so-called "les pipolos", which includes some of my fellow students during my masters and my thesis. This "team" includes Florian Itard, which was the only fellow which followed me in the USA, Loïc Manceau, Aurelien Blanc, Luc Peilleron, François Médard, Céline Planche and Frédéric Tridon. All these people were really important to me, as they were my friends and as I spent my life with them aside this thesis. Some of them had to bear me when I was not friendly because things were wrong (mostly Loïc, Florian and Aurelien). To these, I owe, in addition to my acknowledgments, sincere apologizes (though I already made them oraly, but twice better than never in this case).

Also, to be complete, I want to thank all fellows met in the USA, at JLab and elsewhere, wherever they come from, such as Johnathan Dumas, Yohan Perrin, Vivien Lainé, Lionel Quettier, François-Xavier Girod, Medhi Meziane, and also Megan Friend, Abdurahim Rakhmann, Mark Dalton, John Leacock, Diane Schott, and I might forget some.

Finally, I would like to thank wholeheartedly my parents and my sisters for their sometimes invisible but always unfailing support, specifically during these three years, and more generally from my birth till now. Last but not least, I would also like to give my sincere acknowledgements to all the people who supported me from the beginnings of my schooling, thus allowing me to go through it from preschool to the very highest level of university graduation represented by this thesis. Besides my parents, these people include Mrs Reboa, Mrs Duport, Mrs Chabrat, Mrs Moreno, as well as Mr Legrand, Mrs Lherme, and Mr Fayet. I could not even have get through secondary school without the help of all those people, so thank them here seems to be the least thing I could do.

Résumé en Français

L'intérêt de la physique subatomique est de réveler la structure sous-jacente de la matière dont nous sommes fait et qui nous environne, à des echelles qui sont en deça de l'echelle atomique. À ces echelles, notre niveau de connaissances actuelles est le suivant :

- Les atomes sont fait de noyaux, entourés d'un nuage d'électrons. Les interactions entre noyaux et électrons sont decrites, à toute les echelles d'énergie enviseageables, des très basses aux très hautes énergies, par l'électro-dynamique quantique (Quantum Electro Dynamics ou QED), qui est une theorie complètement comprise.

- Ces noyaux sont constitués de nucléons (protons et neutrons). Les interactions entre nucléons au sein du noyau sont assez bien comprises dans le cadre de theories approximées (ou effectives) impliquant l'échange de mésons.

- Les nucléons (ainsi que les mésons) sont constitués de quarks. Les interactions entre quarks sont décrites par la chromo-dynamique quantique (Quantum Chromo Dynamics ou QCD), dont certains aspects restent à éclaircir.

La QCD est une théorie de gauge non-abelienne, ce qui signifie que les messagers de l'interaction, les gluons, peuvent interagir avec eux mêmes. Étant donné que les gluons n'ont pas de masse, la qualité non-abelienne de la QCD entraine des propriétés particulières. Considérons deux quarks qui s'éloignent l'un de l'autre. L'amplitude de l'interaction entre ces deux quarks augmente, jusqu'à l'infini quand les distances considérées sont infinies. Un quark ne peut jamais etre observé complètement libre, il est par conséquent toujours confiné dans un hadron (méson ou nucléon). C'est ce que l'on appelle le confinement des quarks. Considérons maintenant deux quarks qui s'approchent l'un de l'autre. Dans ce cas, l'amplitude de l'interaction entre eux diminue, jusqu'à s'annuler complètement pour deux quarks infiniment proches. C'est ce que l'on appelle la liberté asymptotique.

À cause de ces propriétés, la structure du nucléon qui est gouvernée par la QCD n'est pas encore complètement comprise. Un certain nombres de techniques existent pour etudier la structure du hadron dans le contexte de la QCD. À haute énergie, la structure du nucléon peut etre étudiée par le biais de la QCD perturbative, qui exploite la propriété de liberté asymptotique, de grandes énergies équivalent à de petites distances. À basse énergie, la structure des hadrons peut être étudiée grâce à la QCD sur réseau. Cette technique utilise aussi la propriété de liberté asymptotique, en remplaçant le continuum d'espace temps par un espace temps discret, de maille finie. Malgré tout, la meilleure manière d'acceder à la structure du hadron reste l'expérience. Le type d'expérience le plus courant est la diffusion électron-nucléon, et ceci pour deux raisons. La première est que l'on prefère étudier la diffusion lepton-nucléon, a cause de l'élémentarité du lepton, qui prévient de toute ambiguïté lors de l'étude de la reaction de diffusion. Ensuite,

parmi les leptons, les électrons sont les plus aisés à obtenir et à manipuler sous forme de faisceau. Un grand nombre d'installations ont été dédiées a l'étude de reactions électron-nucléon, comme par exemple l'accélérateur SLAC (Stanford Linear Accelerator Center, à Stanford, Californie, USA), le collisionneur électron-proton DESY (Deutsches Elektronen Synchrotron, à Hambourg, Allemagne), ou, plus recemment, l'accélérateur CEBAF (Continuous Electron Beam Accelerator Facility, à Newport News, Virginie, USA).

Actuellement, et par la grâce des nombreuses expériences qui ont été dédiées a la structure du nucléon, celle-ci est relativement bien comprise, que ce soit en termes de distribution spatiale des composants du nucléon (les facteurs de forme, obtenus par diffusion élastique électron-proton), ou en termes de distribution d'impulsion des composants du nucléon (les fonctions de distribution de partons, obtenues par diffusion électron-proton profondément inélastique). Malheureusement, ces informations ne permettent pas une description complete du nucléon. La somme des spins de l'ensemble des partons (quarks et gluons) au sein du nucléon ne represente qu'une fraction du spin total du nucléon. C'est ce que l'on appelle la "crise du spin" ou "spin crisis".

La solution à ce problème reside vraisemblablement dans le manque de connaisance du moment orbital des partons au sein du nucléon, qui est susceptible d'apporter la contribution manquant au spin total du nucléon. La connaissance du moment orbital des partons revient à une représentation tridimensionnelle de la structure du nucleon.

La dernière décennie a connu une grande evolution dans l'étude de la structure du hadron, par le biais de l'étude des processus exclusifs qui permettent l'accès a la structure tridimensionnelle des hadrons. Les processus exclusifs englobent la diffusion compton profondement inélastique (Deeply Virtual Compton Scattering ou DVCS)

$$\gamma^* p \to \gamma p \tag{1}$$

et la production exclusive de méson

$$\gamma^* p \to m p \tag{2}$$

Ce document est dédié à l'étude du second processus, et plus particulièrement à la production exclusive de pions neutres

$$\gamma^* p \to \pi^0 p \tag{3}$$

dans le regime profondément inélastique, ou la virtualité du photon virtuel, Q^2 est superieure a 1 GeV^2 et l'énergie dans le centre de masse proton-photon virtuel, W est superieure à 2 GeV.

Nous présentons des mesures de sections efficaces différentielles pour l'électroproduction exclusive de la réaction $ep \to ep\pi^0$ par l'absorption de photons virtuels. Un diagramme de ce processus, incluant les définitions des variables cinématiques, est présenté Figure 1. Ces resultats vont être présentés pour quatre cinématiques. Deux de ces cinématiques sont caractérisées par la même valeur moyenne de $x_{Bj} = 0.36$ à deux Q^2 différents, 1.9 GeV^2 et 2.3 GeV^2 (nommées respectivement Kin2 et Kin3). Cela permet d'étudier la dépendance en Q^2 de la section efficace. Les deux autres cinématiques sont caractérisées par la même valeur moyenne de $Q^2 = 2.1$ GeV^2 à deux x_{Bj} différents, 0.33 et 0.40 (nommées respectivement KinX3 et KinX2). Cela permet d'étudier la dépendance en x_{Bj}.

Les sections efficaces et leurs dépendances vont être comparées aux différents modèles disponibles pour decrire l'électroproduction exclusive de π^0, de la théorie effective de

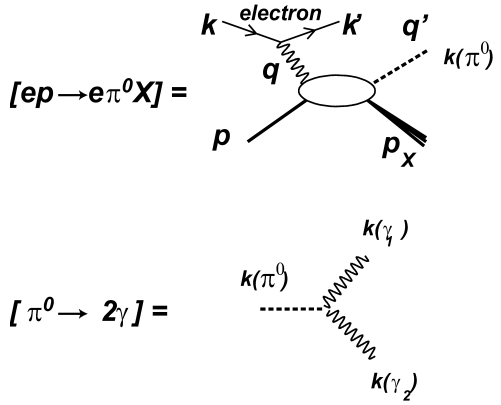

Figure 1: Diagramme de la réaction d'électroproduction de π^0 (en haut), et du mode de décroissance dominant de ce dernier (en bas). Les invariants cinématiques sont définis comme suit: $Q^2 = -(k-k')^2$, $x_{Bj} = Q^2/(2p\cdot q)$, $t = (q-q')^2$, $W^2 = s = M_p + Q^2(1/x_{Bj} - 1)$, et $t_{min} = \frac{(Q^2-m_\pi^2)^2}{4s} - (|q^{CM}| - |q'^{CM}|)^2$, avec $|q^{CM}|$ et $|q'^{CM}|$ les normes de $\vec{q}$, $\vec{q'}$ dans le referentiel de centre de masse de l'état initial $\gamma * p$.

Regge au formalisme des distributions de partons généralisées (Generalized Parton Distributions, ou GPDs).

La photoproduction vers l'avant à énergie asymptotiquement grande peut être décrite par la théorie de Regge, qui exploite les propriétés analytiques de l'amplitude de diffusion dans la limite $t/s \to 0$. De précédentes analyses ont appliqué la phénoménologie de Regge à la photo- et électro-productions exclusive dans le domaine cinématique présenté ici. Des calculs récents avec des modèles inspirés de la phénomenologie de Regge existe pour nos cinématiques. Ces modèles incluent les échanges de mésons ρ, ω, et b dans la voie t, ainsi que que la rediffusion de $\pi^\pm$. Parmi ces modèles, on retiendra particulièrement le modèle d'échange de mésons dans la voie t de J. M. Laget. Une breve description de ce modèle est disponible dans la publication des travaux de R. De Masi sur la mesure d'assymetrie d'hélicité de faisceau dans le domaine exclusif. Des résultats d'expérience du Hall C étudiant la dépendance en Q^2 de la section efficace d'électroproduction exclusive de pions chargés, avec une séparation transverse longitudinale. Ce modèle a récemment été amélioré par l'inclusion de la production de ρ chargés avec rediffusion sur le nucléon.

Dans la limite de Bjorken, à $Q^2 \to \infty$ et $t/Q^2 \ll 1$ à x_{Bj} fixé, l'amplitude de diffusion se limite aux premier ordre (ou "leading twist") des GPD, convolué avec l'amplitude de distribution du pion. Les GPD sont les elements de matrices bilinéaires des operateurs de quarks et de gluons considérés sur le cône de lumière, et qui unifient les facteurs de formes électrofaibles et les fonctions de distributions de partons longitudinales. Des prédictions de section efficace longitudinale σ_L existent dans le cadre du modèle des GPDs. Dans la convention la plus courante (utilisée par M. Vanderhaeghen, P. Guichon et M. Guidal), la prediction de dépendance en Q^2 est $\sigma_L \sim 1/Q^6$ pour la section efficace longitudinale et $\sigma_T \sim 1/Q^8$ pour la section efficace transverse. Ceci implique la dominance de σ_L par rapport à σ_T à grand Q^2. C'est pour tester cette dépendance en Q^2 que nous avons effectué des mesures de section efficace à deux Q^2 différents pour une même valeur de x_{Bj}.

Une interpretation de données d'électroproduction exclusive grâce à des mécanismes semi-inclusifs existent également pour expliquer la section efficace transverse d'électroproduction exclusive de pions chargés.

Quleques détails de l'experience vont être donnés, et je m'attarderais un peu sur la calibration du calorimètre. Le formalisme d'électroproduction de pions que nous avons utilisé (de D. Drechsel et L. Tiator) sera explicité, et j'insisterais sur l'expression des tenseurs hadroniques. J'expliquerais la méthode d'extraction des sections efficaces, et j'aborderais les corrections à effectuer sur ces sections efficaces, ainsi que l'évaluation des erreurs systématiques. Finalement, je présenterais les resultats et les comparerais aux différents modèles disponibles.

Conditions expérimentales

Les données présentées ont été acquises grâce à l'instrumentation de l'expérience DVCS du Hall A. Nous analysons les événements en triple coincidence $\mathrm{H}(e, e'\gamma\gamma)X$. Un faisceau d'électrons de 5.75 GeV était envoyé sur une cible d'hydrogène liquide longue de 15 cm, pour une luminosité typique de 10^{37} $\mathrm{cm}^{-2}\mathrm{s}^{-1}$. Les électrons diffusés étaient détectés dans un spectromètre de haute résolution (High Resolution Spectrometer ou HRS); et les photons par un calorimètre élctromagnétique comptant 132 éléments de fluorure de plomb PbF_2, chacun de ces éléments mesurant 3×3 $\mathrm{cm}^2 \times 20X_0$. Les résolutions, excellentes, permettent de définir, avec une grande précision :

- le photon virtuel, avec les cinématiques centrées à $x_{Bj} = 0.36$ et deux valeurs de $Q^2 = 1.9$ et 2.3 GeV^2.
- la direction des photons réels, grâce à la résolution sur le vertex du HRS combiné à la résolution en position du calorimètre.

Le seuil de validation du calorimètre pour le système de déclenchement de l'acquisition de données est de 1 GeV environ pour chaque photon. Afin d'assurer que l'événement est bien exclusif, il convient d'apporter une information sur le proton de recul qui n'est pas mesuré. Celle ci est donnée par la masse manquante carrée reconstruite $M_X^2 = (k - k' + p - q_1 - q_2)^2$. De même, il est nécessaire, pour assurer que les deux photons soient bien issus d'une désintegration de π^0, de reconstruire la masse invariante des deux photons $m_{\gamma\gamma} = \sqrt{(q_1 + q_2)^2}$. Ces deux quantités etant corrélées par la résolution du calorimètre, nous avons la possibilité d'améliorer sensiblement la distribution en masse manquante par un ajsutement empirique :

$$M_X^2|_{\mathrm{Corr}} = M_X^2|_{\mathrm{Raw}} + C \times (m_{\gamma\gamma} - m_{\pi^0}) \tag{4}$$

avec $C = 13$ GeV.

L'analyse repose sur deux qualités spécifiques à l'expérience :

- grâce à la résolution du spectromètre et du calorimètre, on peut utiliser une simple coupure sur la masse manquante carrée pour assurer l'exclusivité;
- pour les événements exclusifs, la reconstruction de la norme du quadrimoment de transfert au proton, t, et son minimum, t_{min}, reposent sur la position du photon reconstruit, dont la résolution est meilleure que celle de l'énergie. Toutes les données sont présentées en fonction de $t_{min} - t$, qui est directement relié à l'angle de production du pion par rapport au photon virtuel dans le centre de masse proton-photon virtuel θ_π^{CM}: $t_{min} - t = 2q^{CM}q'^{CM}(1 - \cos\theta_\pi^{CM})$.

Calibration

Nous avons effectué des calibrations élastiques (grâce à la réaction $\mathrm{H}(e, e'_{\in Calo}\, p_{\in HRS})$) au début, au milieu et à la fin de l'expérience. Le calorimètre était reculé à une position de 5.5 m de la cible, dans le but d'optimiser la couverture angulaire de l'électron dans le calorimètre avec le proton dans l'acceptance du spectromètre. Après cette calibration la résolution en énergie du calorimètre est de 2.4 %, et la résolution en position est de 2 mm. Les données élastiques ont aussi fourni un test d'efficacité des détecteurs et de l'électronique associée grâce à l'analyse de la section efficace élastique, en accord avec la paramétrisation récente des facteurs de forme de Kelly à 1.1 % près.

Pendant l'expérience, la lumière produite par effet Čerenkov dans les cristaux de PbF_2 a été atténuée par jusqu'à 20 % pour certains blocs. De plus, l'amplitude de cette diminution de lumière produite est très corrélée avec la position des blocs dans le calorimètre. Ceci est attribué à l'endommagement des blocs dû aux radiations. Nous avons donc ajusté la calibration de chaque bloc, en faisant l'hypothèse d'une dose linéairement proportionnelle à l'atténuation de la lumière. Outre les dommages dûs aux radiations, chaque cristal recevait une accumulation d'électrons de basse énergie, qui résulte en une dégradation de la résolution en énergie et un décalage de la calibration en fonction de la distance à la ligne de faisceau. Cet effet est pris en compte grâce aux opérations suivantes :

- Pour chaque bloc la position de la masse manquante reconstruite est centrée sur celle du proton, par la calibration en énergie des données expérimentales.
- Pour la simulation GEANT de l'expérience, la résolution en masse manquante pour chaque bloc a été choisie meilleure que la résolution observée pour les données. Pour chaque bloc, une dégradation de la résolution en énergie a été effectuée simultanément avec la calibration, dans le but d'égaliser les resolutions respectives de la simulation et des données em même temps que l'on centre la position du pic de masse manquante sur la masse du proton.

Cette calibration effectuée grâce à la masse manquante permet de reconstruire la distribution de la masse invariante des deux photons en accord à mieux que 2 MeV avec la masse physique du π^0, et la résolution sur cette distribution est en dessous de 10 MeV.

Extraction des sections efficaces

Pour extraire la section efficace différentielle, il est avantageux d'incorporer toutes les dépendances cinématiques du formalisme de section efficace différentielle dans la simulation experimentale. Dans ce but, nous exprimons la section efficace differentielle en termes de fonction de structure telles que décrites dans l'article de Drechsel et Tiator.

Nous définissons les espaces de phase différentiels, $d^3\Phi_e = dQ^2 dx_{Bj} d\phi_e$ et $d^5\Phi = d^3\Phi_e d[t_{min} - t] d\phi_\pi$, et également l'énergie equivalente d'un photon réel dans le centre de masse $k_\gamma^{CM} = (W^2 - M^2)/2W$. Ces quantités sont définies dans les conventions de Drechsel et Tiator :

- l'axe $\hat{z}$ défini le long du photon virtuel.
- $\hat{y} = (\hat{k}_i \wedge \hat{k}_f)/\sin\theta_e$ orthogonal au plan leptonique.
- $\hat{x} = (\hat{y} \wedge \hat{z})$

Au premier ordre en α, la constante de structure fine, la section efficace différentielle pour un électron d'hélicité h est :

$$\frac{d\sigma(h)}{d^5\Phi} = \Gamma \frac{d^2\sigma_v(h)}{dtd\phi_\pi} \tag{5}$$

avec $k_\gamma = (W^2 - M^2)/2M$. La section efficace d'absorption de photons virtuels est décomposée comme :

$$\begin{aligned}\frac{d^2\sigma_v(h)}{dtd\phi_\pi} = \frac{1}{2\pi}\Bigg\{ &\frac{d\sigma_T}{dt} + \epsilon_L \frac{d\sigma_L}{dt} + \sqrt{2\epsilon_L(1+\epsilon)}\frac{d\sigma_{TL}}{dt}\cos\phi_\pi + \epsilon\frac{d\sigma_{TT}}{dt}\cos 2\phi_\pi \\ &+ \sqrt{2\epsilon_L(1-\epsilon)}\frac{d\sigma_{TL'}}{dt}\sin\phi_\pi\Bigg\}\end{aligned} \tag{6}$$

avec $\epsilon = 1/[1+2(q^2/Q^2)\tan^2\theta_e/2]$ le degré de polarisation linéaire et $\epsilon_L/\epsilon = 4M^2x_{Bj}^2/Q^2$. On definit les tenseurs hadroniques usuels $W^{\mu\nu}$ comme :

$$\begin{aligned}\frac{d^2\sigma_v(h)}{dtd\phi_\pi} = \frac{1}{q^{CM}k_\gamma^{CM}}\Bigg\{ &\frac{W_{xx}+W_{yy}}{2} + \epsilon_L W_{zz} - \sqrt{2\epsilon_L(1+\epsilon)}\Re eW_{xz} \\ &+ \epsilon\frac{W_{xx}-W_{yy}}{2} - \sqrt{2\epsilon_L(1-\epsilon)}\Im mW_{yz}\Bigg\}.\end{aligned} \tag{7}$$

Les termes d'interférence $\Re eW_{xz}$, $\Im mW_{yz}$ possèdent une dépendance en $\sin\theta_\pi^{CM}$, et le terme d'interférence $(W_{xx}-W_{yy})/2$ possède quant à lui une dépendance en $\sin^2\theta_\pi^{CM}$.

Pour cette raison, nous définissons les fonctions de structure réduites r_Λ, qui enlèvent cette dépendance d'espace de phase :

$$\begin{aligned}\frac{W_{xx}+W_{yy}}{2} &= r_T; \\ W_{zz} &= r_L; \\ \frac{W_{xx}-W_{yy}}{2} &= r_{TT}\sin^2\theta_\pi^{CM}\cos 2\phi_\pi; \\ \begin{pmatrix}\Re eW_{xz}\\ \Im mW_{yz}\end{pmatrix} &= \sin\theta_\pi^{CM}\begin{pmatrix}\cos\phi_\pi r_{TL}\\ \sin\phi_\pi r_{TL'}\end{pmatrix}.\end{aligned} \tag{8}$$

Étant donné que nos cinématiques couvrent une large plage de valeurs de x_{Bj} ainsi que de Q^2, il nous faut également inclure les dépendances en Q^2 et en W du tenseur hadronique $(W_{xx}+W_{yy})/2 + \epsilon_L W_{zz} = r_T + \epsilon_L r_L$. Comme nous ignorons *a priori* ces dépendances, nous devons effectuer une extraction préliminaire de la section efficace aux deux points cinématiques à x_{Bj} fixé (respectivement Q^2 fixé) pour obtenir une estimation de la dépendance en Q^2 (respectivement en W) du tenseur hadronique. Ces dépendances peuvent ensuite être introduites explicitement dans le formalisme pour effectuer une nouvelle extraction "définitive". La section efficace totale, ainsi que les dépendances en Q^2 et en W du tenseur hadronique peuvent changer de quelques pourcents de la première à la seconde extraction. Néanmoins, La variation de la section efficace totale doit être négligeable entre l'extraction "définitive" et une troisième extraction qui incluraient les nouvelles dépendences en Q^2 et en W du tenseur hadronique dans le formalisme. Ainsi, l'integration sur une large plage en Q^2 et en x_{Bj} d'une quantité dépendante de Q^2 et W affecte la section efficace par moins de 0.3 %.

On divise l'acceptance en 24 bins égaux en $\phi_\pi \in [0, 2\pi]$ et huit bins en $t_{min} - t \in [0, 0.3]\,\mathrm{GeV}^2$, que ce soit pour les composantes de la section efficace indépendantes et dépendantes de l'helicité. Le taux de comptage experimental N_d dans ces bins j_d avec le taux de comptage obtenu avec une simulation complete de l'expérience, incluant l'acceptance et la réponse des détecteurs, N_s, qui depend des valeurs de r_Λ moyennées sur ces bins. Les valeurs des fonctions de structure réduites r_Λ sont celles qui minimisent

$$\chi^2 = \sum_{j_d} \left(\frac{N_d - N_s(r_\Lambda)}{\sigma_d} \right)^2 , \tag{9}$$

avec σ_d l'erreur expériementale de chaque bin.

Les résultats vont être présentés suivant la décomposition habituelle disponible dans la litterature donnée dans l'équation (6).

Corrections radiatives

On compte trois types d'effets radiatifs :

- les effets radiatifs externes, qui ont lieu dans un champ électromagnetique différent de celui dans lequel a lieu l'interaction principale;
- les effets radiatifs internes réels, qui ont lieu dans le champ électromagnetique de l'interaction principale, mais se propagent à l'infini;
- les effets radiatifs internes virtuels, qui ont lieu dans le champ électromagnetique de l'interaction principale et sont réabsorbés dans le même champ.

Les effets radiatifs externes sur l'électron incident ainsi que les effets radiatifs internes réels sont traités dans l'approximation du radiateur équivalent. La pré-radiation est modelée en générant une perte d'énergie ΔE_{in} événement par événement, suivant la distribution ($b \simeq 4/3$)

$$I_{in}(E_0, \Delta E_{in}, t_{in}) = \frac{b t_{in} + \delta_S/2}{\Delta E_{in}} \left[\frac{\Delta E_{in}}{E_0} \right]^{b t_{in} + \delta_S/2} , \tag{10}$$

avec

$$\delta_S = \frac{2\alpha}{\pi} \left[\ln \frac{Q^2}{m_e} - 1 \right] \tag{11}$$

et t_{in} l'épaisseur de cible (en longueurs de radiation) traversée par l'électron avant la diffusion. Le terme de Schwinger δ_S modèle la pré-radiation interne. L'énergie diffusée au vertex est $E'_v = E_0 - \Delta E_{in} - Q^2/(2M_p x_{Bj})$. La post-radiation interne est modelée par une distribution similaire de la perte d'énergie après diffusion ΔE_{out}

$$I_{out} = \frac{\delta_S/2}{\Delta E_{out}} \left[\frac{\Delta E_{out}}{E'_v} \right]^{\delta_S/2} . \tag{12}$$

La post-radiation externe est modelée avec la simulation GEANT3 décrite dans les sections précedentes. Les radiations internes virtuelles sont prises en compte par un coefficient multiplicatif de correction de la section efficace, calculée pour nos cinématiques par Marc Vanderhaeghen *et al.*.

Erreurs systématiques

Deux types de canaux hadroniques inclusifs sont en concurrence avec la reaction H$(e, e'\pi^0)p$: les canaux de production de plusieurs pions H$(e, e'\pi^0)N\pi, N\pi\pi, ...$, à un seuil en masse manquante $M_X^2 = (M_p + m_\pi)^2 = 1.15$ GeV^2, et le canal H$(e, e'\pi^0)p\gamma$. Le premier type inclut la production résonante (N^*) et non résonante de $N\pi$ dans l'état final et la production diffractive de ρ^+ donnant $\pi^+\pi^0$. Le canal H$(e, e'\pi^0)p\gamma$ vient de la production diffractive $ep \to ep\omega$, avec la désintegration du ω en $\pi^0\gamma$ avec un rapport de branchement de 8.5 %. Dans notre acceptance, le seuil de production de l'état final $(e, e'\pi^0)$ a partir de l'électroproduction exclusive de ω est de 1.0 GeV^2, un peu en dessous du seuil de production de plusieurs pions. Néanmoins, grâce à des mesures d'électroproduction de ω dans nos cinématiques, on estime la contamination de ce canal pour des masses manquantes inferieures à 1.15 GeV^2 à moins de 1 % pour l'ensemble des bins en $t_{min} - t$.

Les erreurs systématiques dans la méthode d'extraction sont dues aux coupures en masse manquante et au seuil du calorimètre E_{Thr}. La stabilité des résultats selon ces coupures sont verifiées en variant ces deux coupures l'une après l'autre. L'estimateur suivant :

$$R = \sum_{Bin=0}^{6} (r_T + \epsilon_L r_L) \tag{13}$$

doit être stable avec la variation de chaque coupure, aux erreurs expérimentales près, au moins sur un certain intervalle, dit de stabilité. La coupure optimale est prise au milieu de l'intervalle ou cette stabilité est observée effectivement. Si la stabilité de R n'est pas verifiée sur l'intervalle de stabilité *aux erreurs expérimentales près*, l'erreur systematique est donnée par la deviation de R par rapport à sa valeur moyenne sur la totalité de l'intervalle. Les fonctions de structure réduites r_Λ sont extraites aux valeurs optimales de ces coupures.

Les sources instrumentales d'erreurs systematique sont disponibles, avec les erreurs systématiques dues à l'analyse, dans le tableau 1. Toutes ces sources d'erreurs systématiques étant indépendantes entre elles, elles ont été ajoutées quadratiquement.

Résultats

La section efficace totale d'électroproduction exclusive de π^0, ainsi que les différentes composantes dépendantes de ϕ_π ont été extraites pour Kin2, Kin3, KinX2 et KinX3. La statistique disponible permet d'obtenir une précision statistique pour la section efficace totale de 3 % pour $x_{Bj} = 0.36$ (Kin2, Kin3) et de 5 % pour $Q^2 = 2.1$ GeV^2 (KinX2, KinX3). Cette différence est due au fait que la totalité de la statistique est utilisée pour $x_{Bj} = 0.36$, tandis que moins de la moitié de cette statistique est utilisée pour $Q^2 = 2.1$ GeV^2.

Les figures 2 **(a)** et 3 **(a)** montrent $\sigma_T + \epsilon_L\sigma_L$ en fonction de $t_{min} - t$, respectivement pour $x_{Bj} = 0.36$ et $Q^2 = 2.1$ GeV^2. Ces sections efficaces ne montrent pas de dépendances très marquées en fonction de $t_{min} - t$.

Les figures 2 **(b)** et 3 **(b)** montrent quant à elles les rapports des deux sections efficacesdifferentielles en $t_{min} - t$ à $x_{Bj} = 0.36$ et des deux sections efficaces differentielles en $t_{min} - t$ à $Q^2 = 2.1$ GeV^2 respectivement, indiquant respectivement les dépendances en Q^2 et en W de la section efficace, qui se comporte comme $1/Q^{4.5}$ et $1/W^{3.5}$.

	Kin3 KinX3	Kin2 KinX2
Coupure d'exclusivité	1.0 %	3.0 %
Acceptance du HRS	2.2 %	
Corrections radiatives	1.5 %	
Seuil du calorimètre	1.0 %	
Longueur de cible	0.5 %	
Integration du tenseur hadronique	0.3 %	
Corrections multi-traces	0.1 %	
Corrections 3-clusters	0.1 %	
Luminosité	0.1 %	
Temps mort	0.1 %	
dentification des particules	0.1 %	
Erreur quadratique totale	3.1 %	4.2 %
Polarization du faisceau	2.0 %	
Erreur quadratique totale	3.7 %	4.6 %

Table 1: Erreurs systématiques expérimentales. La première ligne "Erreur quadratique totale" donne l'erreur systématique pour les sections efficaces indépendantes de l'hélicité. La seconde ligne "Erreur quadratique totale" donne l'erreur systématique pour la section efficace dépendant de l'hélicité.

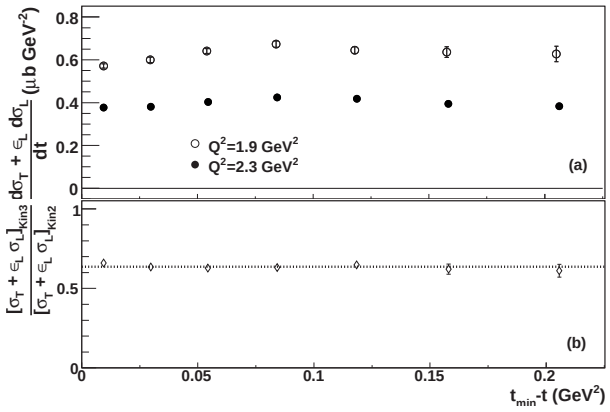

Figure 2: **(a)** Composante $\sigma_T + \epsilon_L\sigma_L$ de la section efficace $\mathrm{H}(e,e'\pi^0)p$, en fonction de $t_{min} - t$ pour $x_{Bj} = 0.36$. les barres d'erreurs representent les erreurs statistiques uniquement. **(b)**: Rapport $\sigma_T + \epsilon_L\sigma_L$ pour les deux cinématiques en fonction de $t_{min} - t$. L'ajustement de ce rapport (ligne pointillée) donne la dépendance en Q^2 de la section efficace.

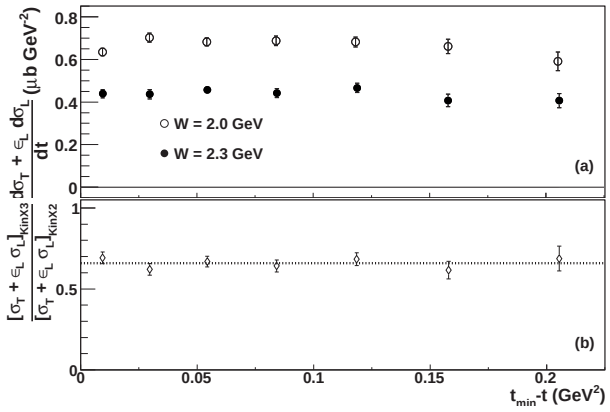

Figure 3: **(a)** Composante $\sigma_T + \epsilon_L\sigma_L$ de la section efficace $\mathrm{H}(e,e'\pi^0)p$, en fonction de $t_{min} - t$ pour $Q^2 = 2.1$ GeV^2. les barres d'erreurs representent les erreurs statistiques uniquement. **(b)**: Rapport $\sigma_T + \epsilon_L\sigma_L$ pour les deux cinématiques en fonction de $t_{min} - t$. L'ajustement de ce rapport (ligne pointillée) donne la dépendance en W de la section efficace.

La section efficace totale $\sigma_T + \epsilon_L\sigma_L$, ainsi que la composante dépendante de l'hélicité $\sigma_{TL'}$ sont décrites, pour $x_{Bj} = 0.36$ de façon satisfaisante par le modèle d'échange de mésons dans la voie t de J.M. Laget. En revanche, les deux autres composantes montrent un net désaccord, que ce soit en amplitude pour σ_{TT}, voire en signe pour σ_{TL}, et ce pour ces mêmes cinématiques.

La section efficace totale $\sigma_T+\epsilon_L\sigma_L$ se comporte donc comme $1/Q^{4.5}$, qu'il faut comparer au comportement asymptotique $\sigma_T + \epsilon_L\sigma_L \sim 1/Q^8$. De plus, dans l'hypothèse du régime perturbatif, où $\sigma_L \gg \sigma_T$, on obtiendrait $\sigma_L \sim 1/Q^3$, ce qui est très loin du comportement asymptotique à très haute énergie prédit par le formalisme des GPDs. Les données que nous avons extraites nous conduisent à deux conclusions vis-à-vis des modèles disponibles :

- le modèle de J.M. Laget est capable de décrire correctement les composantes $\sigma_T + \epsilon_L\sigma_L$ et $\sigma_{TL'}$, mais échouent a décrire σ_{TL} et σ_{TT};
- la dépendance en Q^2 de la section efficace (Fig. 2) démontre que nous sommes éloignés de la prédiction à l'ordre dominant en QCD perturbative de $d\sigma_L/dt$, qui se comporte comme $1/Q^6$. En revanche, cette dépendance est similaire à la dépendance en Q^2 de la section efficace transverse d'électroproduction de pion chargés publiée par le Hall C.

De plus, le π^0 n'ayant ni charge ni spin, un couplage direct entre le photon virtuel et un pion neutre est très supprimé, ce qui enlève la contribution du pôle du pion à la section efficace longitudinale. Cela suggère que la section efficace transverse σ_T est vraisemblablement dominante devant σ_L. D'autre part, la section efficace transverse d'électroproduction de π^+ a déjà été décrite par un mécanisme de fragmentation de quark habituellement utilisé pour décrire les processus semi-inclusifs.

T. Horn *et al.* ont mesuré la section efficace d'électroproduction exclusive de π^+ à $Q^2 = 1.60$ et 2.45 GeV^2, avec une séparation transverse-longitudinale. Le modèle de J.M. Laget reproduit bien la composante σ_L, mais la composante σ_T n'est pas bien reproduite par ce même modèle. Kaskulov, Gallmeister et Mosel ont effectué des calculs utilisant PYTHIA-JETSET basé sur le modèle de Lund appliqués à la section efficace transverse d'électroproduction de π^+ aux cinématiques du Hall C. Ces calculs sont en excellent accord avec les données de section efficace transverse de $ep \to en\pi^+$ du Hall C.

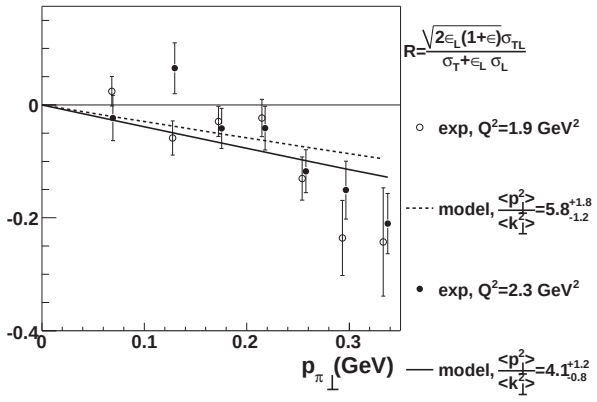

Figure 4: Rapport $\sqrt{2\epsilon_L(1+\epsilon)}\sigma_{TL}/(\sigma_T+\epsilon_L\sigma_L)$ pour $x_{Bj}=0.36$, en fonction de l'impulsion transverse du pion $p_{\pi\perp}$. L'ajustement du modèle à cette quantité est representée par la courbe pointillée pour $Q^2=1.9$ GeV^2 et par la courbe pleine pour $Q^2=2.3$ GeV^2.

Cela donne une forte indication que la section efficace transverse de production exclusive de π^+ à $Q^2>1$ GeV^2 au delà de la région de resonance peut être décrite de par un processus partonique. Cela suggere également que les données π^0 presentées ici peuvent être décrites de façon similaire par un processus de diffusion incoherente du photon virtuel sur la structure partonique du nucléon.

Pour ces raisons, nous considerons nos données dans le contexte de la diffusion profondément inelastique semi-inclusive ("Semi-Inclusive Deep Inelastic Scaterring", ou SIDIS). Nous avons tenté d'ajuster à nos données un formalisme de SIDIS écrit par M. Anselmino *et al.*. Ce formalisme fournit l'expression, valable à $\mathcal{O}(k_\perp/\sqrt{Q^2})$, de la section efficace de production semi-inclusive de n'importe quel hadron ainsi que la contribution dépendante de $\cos\phi_\pi$ de cette section efficace ("effet de Cahn"). L'idée de cette analogie est d'ajuster le rapport entre cette contribution en $\cos\phi_\pi$ (identifiée à σ_{TL}) et le terme constant (identifié à $\sigma_T+\epsilon_L\sigma_L$), avec comme paramètre d'ajustement $\langle p_\perp^2\rangle/\langle k_\perp^2\rangle$:

$$\frac{\sqrt{2\epsilon_L(1+\epsilon)}\sigma_{TL}}{\sigma_T+\epsilon_L\sigma_L}=\frac{4(2-y)\sqrt{1-y}z_\pi p_{\pi\perp}}{\left(\frac{\langle p_\perp^2\rangle}{\langle k_\perp^2\rangle}+z_\pi^2\right)\sqrt{Q^2}(1+(1-y)^2)} \tag{14}$$

Le résultat de cet ajustement est montré figure 4. Nos données exclusives (où la multiplicité de particules produites est 1) sont reproduites par ce modèles si $\langle p_\perp^2\rangle/\langle k_\perp^2\rangle\sim 5.0$, tandis que pour les données inclusives (où la multiplicité est grande), on obtient plutôt $\langle p_\perp^2\rangle/\langle k_\perp^2\rangle\sim 0.8$.

Conclusions

La première experience DVCS/π^0 du Hall A à Jefferson Lab fournit des résultats de section efficace d'éléctroproduction de π^0 avec une haute précision statistique, en dépit d'un énorme bruit experimental environnant dû à une forte luminosité (10^{37} cm^{-2}s^{-1}) et à un appareillage expérimental proche du faisceau d'électrons incident. Ceci est attribuable au spectromètre de haute résolution combiné à notre calorimètre, qui permettent une excellente resolution sur la masse manquante des événements en triple coïncidence $\mathrm{H}(e,e'\gamma\gamma)X$ ainsi que sur la masse invariante des deux photons, facilitant la sélection des événements $ep\to ep\pi^0$ parmi les événements bruts. La statistique que nous avons enregistrée permet

d'obtenir une incertitude statistique sur la section efficace de 3 % pour $x_{Bj} = 0.36$ et de 5 % pour $Q^2 = 2.1$ GeV^2. L'instrumentation très précise qui a été utilisée donne une erreur systematique totale d'environ 3 à 5 % sur la section efficace totale. Ces données ne sont pour autant pas simples à interpreter. Récapitulons, parmi les modèles disponibles, ce que donne leur comparaisons respectives avec les données :

- nous sommes loin du régime de Bjorken, et le comportement en Q^2 données n'obéit pas à la prédiction au premier ordre de la QCD perturbative. Cependant, rien n'interdit que σ_L uniquement obéisse à cette prédiction, mais sans séparation transverse/longitudinale, rien ne permet de l'affirmer;

- le modèle d'échange de mésons dans la voie t de J.M. Laget est capable de reproduire la section efficace totale $\sigma_T + \epsilon_L \sigma_L$ ainsi que la section efficace dépendante de l'hélicité $\sigma_{TL'}$, mais reste à parfaire pour les composantes restantes;

- la tentative d'interprétation de nos données exclusives avec un formalisme semi-inclusif donne une description du rapport $\sigma_{TL}/(\sigma_T + \epsilon_L \sigma_L)$.

Une meilleure comprehension de ces données passe par la séparation des deux composantes σ_T et σ_L. Pour cela, il est nécessaire d'effectuer une séparation de Rosenbluth.

C'est pourquoi une nouvelle expérience DVCS/π^0 pour le Hall A a été mise au point. Cette expérience a beaucoup de points en commun avec la précendente, et quelques differences. Résumons en quelques points ce qui restera et ce qui changera de l'ancienne expérience à la nouvelle.

- La couverture cinématique étudiée sera similaire, bien qu'un peu plus réduite en Q^2 (1.5 à 2.0 GeV^2 en Q^2 à x_{Bj} équivalent), la faute a une énergie de faisceau disponible plus faible. Cependant, nous prendrons des données à plusieurs énergies pour chaque cinématique, afin de permettre la séparation de Rosenbluth.

- Le calorimètre a été agrandi, passant de $12 \times 11 = 132$ blocs à $16 \times 13 = 208$ blocs de PbF_2, essentiellement pour améliorer l'acceptance des événements $H(e, e'\pi^0)X$. De plus, un blindage a été concu afin de proteger le calorimètre contre le bruit de fond de particules de basse énergie.

- Le système de déclenchement a été modifié pour enregistrer, en plus des événements DVCS et π^0, des événements de bruit de fond afin d'améliorer la connaissance de ce dernier. Le seuil de déclenchement du calorimètre a en outre été abaissé afin d'augmenter la statistique d'événements π^0.

Toutes ces modifications devraient permettre d'obtenir des sections efficaces DVCS et π^0, dans un domaine cinématique similaire avec une séparation transverse/longitudinale. La précision statistique sur ces nouvelles mesures devraient être du même niveau de precision que les anciennes mesures. En outre, l'incertitude systematique devrait être inferieure à celles des anciennes mesures. Ces nouvelles données, mises en relation avec les données presentées dans ce document, devraient en ameliorer sensiblement la comprehension, et peut être même être utilisables pour l'étude des GPDs.

Contents

Introduction

The interest of subatomic physics is to reveal the underlying structure of the matter we and our environment are made out of, at the level which is below the atomic structure. At this level, here is what we understand:

- the atoms are built out of a nucleus, with electrons orbiting around it. The interaction between the electrons and the nucleus are described, at every energy scale from low to very high energy, by Quantum Electro-Dynamics (QED), which is a well understood theory;
- this nucleus is constituted of nucleons (protons and neutrons). The interaction between nucleons in the nucleus (or at least at reasonable energy scales) are rather well understood within approximate theories implying exchange of mesons;
- the nucleon is constituted of quarks. The interaction between these quarks are described by Quantum Chromo-Dynamics (QCD), which remains to be fully studied.

The QCD theory is a non-abelian gauge theory, which means the carriers of the interactions, the gluons, can couple to themselves. Since gluons have no mass, the non-abelian property of QCD leads to a particular behavior. On the one hand, considering two quarks getting further to each other, the amplitude of the interaction between them grows to infinity with infinite distances. This implies a quark cannot be observed completely free, it is always confined into a hadron (nucleon or meson). This is what we call the quark confinement. On the other hand, considering two quarks getting closer to each other, the amplitude of the interaction between them decreases to vanish at infinitely close distances. This is what we call the asymptotic freedom [Wilczek(1974)].

Because of this, the nucleon structure, which is governed by QCD still remains to be understood. Several techniques, such as lattice QCD, are available to study QCD and the structure of hadrons, but the best and most reliable information for the nucleon structure is the experiment. Among the large variety of experiments which could be imagined to study the nucleon structure electron-nucleon reaction is prefered by many experimentalists for these reasons:

- lepton-hadron reactions are prefered because of the elementarity of the lepton.
- among all leptons, the electron has always been easier to get and to handle in beams.

Several facilities (including the Continuous Electron Beam Accelerator Facility (CEBAF) at Jefferson Lab) have been dedicated to electron-nucleon reaction studies, allowing plenty of experiments to study the nucleon structure.

Nowadays, and thanks to the numerous experiments which allowed to study it, the structure of the nucleon is actually rather well understood, either in terms of form factors (spatial distributions of the nucleon components) or in terms of parton distribution functions (momentum distribution of the nucleon constituents). Unfortunately, these informations do not allow a complete description of the nucleon. For instance, the sum of the spins of all quarks and gluons which are in the nucleon are only a fraction of the total nucleon spin (spin crisis). The rest of the spin may come from quark and gluon orbital momenta contributions.

The solution to the spin crisis requires new informations on the nucleon which may be provided by a three-dimensional description of the proton [1, 2]. Fortunately, in the late 90s, new quantities for the study of the nucleon structure appeared. These quantities, called the Generalized Parton Distributions (GPDs) contains the structural information of the Parton Distribution Functions (PDFs) correlated with the spatial information of the Form Factors (FF). They are accessible through exclusive processes such as Deeply Virtual Compton Scattering (DVCS),

$$\gamma^* p \to \gamma p, \tag{15}$$

or Deeply Virtual Meson Production (DVMP).

In the present document, we are interested in deeply virtual π^0 production,

$$\gamma^* p \to \gamma \pi^0, \tag{16}$$

and more particularly in the π^0 electroproduction experiment performed at Jefferson Lab, Hall A. This experiment was complementary to the Jefferson Lab Hall A DVCS experiment and was recorded with the same apparatus. We measured exclusive π^0 electroproduction cross sections in the deep inelastic regime ($Q^2 > 1$ GeV^2, $W > 2$ GeV), for several Q^2 at x_{Bj} fixed, to extract a Q^2 dependence.

In the first chapter are reviewed the different models that are available to describe π^0 production. The second chapter is dedicated to the description of the experimental setup. The calibration of the electromagnetic calorimeter which is specific to our experiment is available in chapter three. The analysis methods we used to extract the cross section are detailed in the fourth chapter. In the fifth chapter, the results are finally provided and confronted with some of the models reviewed in chapter one. Finally, I will conclude on π^0 experiment and results, and give an outlook on further experiments.

Chapter 1

Phenomenology of pion electroproduction

To probe the structure of the hadrons, we collide the hadrons with other particles we use as probes. These particles can be other hadrons, leptons or photons. It is more convenient however to use structureless probes such as leptons or photons. The electron is the most widely used, because the electron-nucleon interaction is governed by quantum electro-dynamics, which is perfectly known. Moreover, the electron is the easiest lepton to handle in beams.

Among the large number of electron-nucleon scattering experiments, a large part are dedicated to elastic scattering, which allows to access the nucleon form factors. In the non-relativistic approximation, the nucleon form factors are Fourier transforms of the charge and current distributions in the proton [3]. Another broad part of these experiments have been devoted to deep inelastic scattering (DIS), to study the PDFs. The PDFs are the probability for a parton to carry a momentum fraction x of the total proton momentum p in the so-called Infinite Momentum Frame (IMF). The IMF is defined as the frame where the momentum of the proton is infinite.

On the side of these two kind of experiments, other kinds of experiments, such as meson electroproduction, were studied. The pion is the lightest of the broad family of hadrons. Moreover, it has the simplest content in terms of constituent quarks, and it has no spin. Thanks to this, the pion electroproduction always had a particular place among all electron-nucleon scattering processes [4].

This chapter is dedicated to the description of the different models available for pion electroproduction. In the first section of this chapter, we write the formalism of pion electroproduction cross section. We emphasize on the expression of the hadronic tensors. The second section is dedicated to pion electroproduction related to hadron form factors. The Regge phenomenology is treated in the third section. We present the principle of Regge phenomenology and we focus on the most recent developments of Regge-inspired models. In the fourth section, we give some generalities on the GPDs, and its supposed role in pion electroproduction. Finally, the fifth section is devoted to the description of the formalism of Semi-Inclusive Deep Inelastic Scattering (SIDIS).

1.1 Formalism of pion electroproduction

We present the general expression of pion electroproduction. Particularly, we give the general decomposition of this cross section in terms of angular dependences. The expressions

of the hadronic tensors are also provided.

1.1.1 Kinematic variables

We show a Feynman diagram of the pion electroproduction on Fig. 1.1. This figure

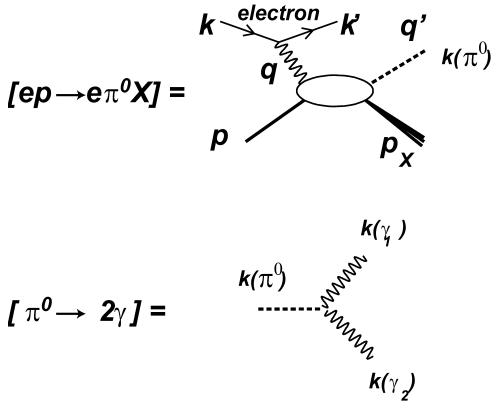

Figure 1.1: Diagram of the forward π^0 electroproduction reaction (above), and of the dominant π^0 decay mode (below). Notations attached to the propagators have to be understood as quadrimomenta, and write, for any quadrimomentum v: $v = (v^0, \mathbf{v} \equiv \vec{v})$

defines the following kinematic quantities:

- $Q^2 = (k - k')^2$ is the virtuality of the virtual photon carrying the interaction;
- $W^2 \equiv s = (p + q)^2 = M^2 + 2p \cdot q - Q^2$ is the invariant mass of the total hadronic system; this quantity is also the square of the total energy available in the center of mass frame;
- θ_e is the polar angle of the scattered electron with respect to the incident electron;
- $t = (q - q')^2$ is the momentum transfer to the nucleon;
- the minimal value of t for each event, defined by the electron kinematics, is $t_{min} = \frac{(Q^2 - m_\pi^2)^2}{4s} - (|q^{CM}| - |q'^{CM}|)^2$;
- the DIS variable $x_{Bj} = Q^2/(2p \cdot q)$ is the momentum fraction carried by the interacting parton in DIS limit.

We also define, within the following conventions of Drechsel and Tiator [5]:

- $\hat{z}$ axis along the virtual photon;
- $\hat{y} = (\hat{k}_i \wedge \hat{k}_f)/\sin\theta_e$ orthogonal to the leptonic plane;
- $\hat{x} = \hat{y} \wedge \hat{z}$;

the angular variables of pion production. θ_π is the polar angle of the produced pion with respect to the virtual photon direction. We also define θ_π^{CM} which is the same variable considered in the virtual-photon proton center of mass frame. ϕ_π is the azimuthal angle of the pion relative to the leptonic plane *i.e.* the scattered electron.

1.1.2 Cross sections

The general expression of the 5-fold unpolarized pion electroproduction cross sections is, in the conventions of Drechsel and Tiator [5], and in the One-Photon-Exchange-Approximation (OPEA):

$$\frac{d^5\sigma}{d\cos(\theta_e)d\phi_e dk' d\cos(\theta_\pi)d\phi_\pi} = \Gamma\frac{d\sigma_v}{d\Omega_\pi} \tag{1.1}$$

In this expression, most of the electron kinematic dependence is contained in Γ, the virtual photon flux, defined as:

$$\Gamma = \frac{\alpha}{2\pi^2}\frac{k'}{k}\frac{k_\gamma}{Q^2}\frac{1}{1-\epsilon} \tag{1.2}$$

where $k_\gamma = (W^2 - M^2)/(2M)$ is the energy a real photon might have to give the same W^2, and

$$\epsilon = \left(1 + 2\frac{\mathbf{q}^2}{Q^2}\tan^2\frac{\theta_e}{2}\right)^{-1} \tag{1.3}$$

is the degree of linear polarization of virtual photons. Note that ϵ is also the degree of longitudinal polarization.

The remaining term in Eq. (1.1) is the reduced cross section, which contains the cross section components

$$\left.\frac{d\sigma_v}{d\Omega_\pi}\right|_{unpol} = \frac{d\sigma_T}{d\Omega_\pi} + \epsilon_L\frac{d\sigma_L}{d\Omega_\pi} + \sqrt{2\epsilon_L(1+\epsilon)}\frac{d\sigma_{TL}}{d\Omega_\pi}\cos\phi_\pi + \epsilon\frac{d\sigma_{TT}}{d\Omega_\pi}\cos 2\phi_\pi \tag{1.4}$$

where $\epsilon_L = \epsilon\nu^2/Q^2$. The σ_T and the σ_L are respectively the transverse and longitudinal cross section, corresponding to target response to respectively transverse and longitudinal polarization of the virtual photon. The σ_{TL} is the interference between the longitudinal and transverse responses. It contains a leading dependence in $\sin\theta_\pi^{CM}$. The σ_{TT} is the interference between the target responses of the two possible transverse polarizations of the virtual photon. It contains a leading dependence in $\sin^2\theta_\pi^{CM}$. The superscript CM correspond to the variable evaluated in the $\gamma^* - p$ center-of-mass frame.

The expression of the polarized cross section differs from the unpolarized cross section by the expression of the reduced cross section, which becomes ($h = \pm 1$ the electron helicity):

$$\left.\frac{d\sigma_v}{d\Omega_\pi}\right|_{pol} = \left.\frac{d\sigma_v}{d\Omega_\pi}\right|_{unpol} + h\sqrt{2\epsilon_L(1-\epsilon)}\frac{d\sigma_{TL'}}{d\Omega_\pi d\phi_\pi}\sin\phi_\pi \tag{1.5}$$

where $\sigma_{TL'}$ correspond to the helicity-odd transverse-longitudinal interference. It contains a dependence in $\sin\theta_\pi^{CM}$.

1.1.3 Hadronic tensors

To get information on the nucleon structure, it is generally more convenient to use hadronic tensors instead of separated cross sections. In [5], D. Drechsel and L. Tiator write the π electroproduction cross section in terms of hadronic tensors. To this end, they express the electroproduction cross section first in terms of leptonic and hadronic

currents, using the conventions of Bjorken and Drell [6]:

$$\begin{aligned} d\sigma = & \frac{k^0}{|\mathbf{k}|}\frac{m_e}{k^0}\frac{M}{p^0}\frac{m_e}{k'^0}\frac{d^3k'}{(2\pi)^3}\frac{1}{q'^0}\frac{d^3q'}{(2\pi)^3}\frac{M_X}{p_X^0}\frac{d^3p_X}{(2\pi)^3}(2\pi^4)\delta^4(p+q-q'-p_X) \\ & \times \left| \langle p', q' \,|J^\mu|\, p\rangle \frac{1}{Q^2} \langle k' \,|j_\mu|\, k\rangle \right|^2 \end{aligned} \tag{1.6}$$

where J^μ is the hadronic current and j_μ is the leptonic current. In this expression the contribution of the weak interaction have been neglected.

In this formalism, we define the hadronic tensor:

$$W_{\mu\nu} = \left(\frac{M}{4\pi W}\right)^2 \langle \chi_i \,|J_\mu|\, \chi_f\rangle \langle \chi_f \,|J_\nu|\, \chi_i\rangle \tag{1.7}$$

where $|\chi_{i,f}\rangle$ are the Pauli spinors of the nucleon in the initial and final state.

The reduced cross section, in terms of these hadronic tensors, becomes, in the polarized case:

$$\begin{aligned} \frac{d\sigma_v}{d\Omega_\pi^{CM}} = & \frac{q'^{CM}}{k_\gamma^{CM}} \left[\frac{W_{xx}+W_{yy}}{2} + \epsilon_L W_{zz} - \sqrt{2\epsilon_L(1+\epsilon)}\Re\mathrm{e}W_{xz} + \epsilon\frac{W_{xx}-W_{yy}}{2} \right. \\ & \left. - h\sqrt{2\epsilon_L(1-\epsilon)}\Im\mathrm{m}W_{yz} \right] \end{aligned} \tag{1.8}$$

where $k_\gamma^{CM} = k_\gamma \times M/W$ is the energy a real photon might have to give the same W^2 evaluated in the CM frame and q'^{CM} is the norm of $\mathbf{q}'$ evaluated in the CM frame.

The cross sections and the hadronic tensors are only the observable quantities encapsulating the underlying physics. Pion cross section measurements allow to parameterize several models of the nucleon content.

1.2 Pion electroproduction and hadron form factors

In this section, we discuss pion electroproduction within the form factor framework. This part concerns more precisely charged pion electroproduction at low $-t$. We give generalities on hadron form factors, and we give the description of $ep \to en\pi^+$ in terms of hadron form factors. See [7] for a more complete review.

1.2.1 Hadron form factors

As said in the introduction of this chapter, the form factor of the hadron is related with the charge distribution in this hadron. It is actually the two dimensional Fourier transform of the charge distribution $\rho(\mathbf{b})$ with respect to the impact parameter b [8], meaning it gives the scattering amplitude of an electromagnetic probe on the hadron (see Fig. 1.2) as a function of the probe momentum $|\mathbf{q}|$:

$$F^h(|\mathbf{q}|) = \int \rho(\mathbf{b}) e^{-\mathbf{q}\cdot\mathbf{b}} d^3b \tag{1.9}$$

The form factor is normalized as $F(0) = 1$. For spin 1/2 baryons such as the proton and the neutron, there are two electromagnetic form factors, denoted F_1 and F_2. For the pion which is a spinless quark-antiquark bound state, there is only one form factor F_π.

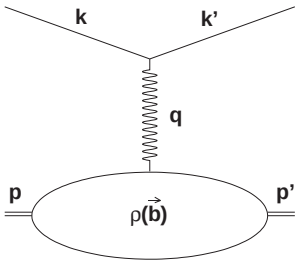

Figure 1.2: Charge distribution inside the hadron probed by a virtual photon.

The elastic cross on a given unpolarized hadron is a bilinear combination of the hadron form factors [9]. For the proton for instance, we have:

$$\left.\frac{d\sigma^{ep\to ep}}{d\Omega}\right|_{lab} = \sigma_{Mott}\left[\left((F_1^p)^2 + (\kappa^p)^2\tau(F_2^p)^2\right)\cos^2\frac{\theta}{2} + \left(2\tau(F_1^p + \kappa F_2^p)^2\right)\sin^2\frac{\theta}{2}\right]; \quad (1.10)$$

with $\tau = Q^2/(4M_p^2)$, κ^p the proton anomalous magnetic moment and:

$$\sigma_{Mott}\left(\frac{\alpha^2}{4k^2\sin^4\frac{\theta}{2}}\right)\frac{k'}{k} \quad (1.11)$$

the electron scattering cross section on a structureless *i.e.* point-like particle of mass M (α is the fine structure constant).

However, if electron-proton elastic scattering experiments can be performed directly, electron-neutron scattering, and *a fortiori* electron-meson scattering can only be performed indirectly. Electron-neutron scattering can be implemented with nuclei, but then one needs to take into account of the nuclear effects. Direct electron-pion scattering data have been obtained by colliding pion beams on atomic electrons [10, 11], but this technique is limited to a very small Q^2 coverage.

This is why people have always found more convenient to use pion electroproduction to determine pion form factors. The next sub-section deals about methods to extract form factors from pion electroproduction.

1.2.2 Hadron form factors in pion electroproduction

Several charged pion electroproduction experiments were designed to extract pion form factor (for example [12, 13] for old experiments, and [14, 15] for a very recent experiment).

In the Born term model, the interaction $ep \to en\pi^+$ is modeled by a pion exchange. Actually, in this model, the virtual photon interacts with a charged pion from the pion cloud of the nucleon. The pion becomes real, and the nucleon isospin flips. Thanks to this, $ep \to en\pi^+$ contains information on the pion form factor, as well as the proton and the neutron form factors. According to [4], the transverse and longitudinal cross sections of the reaction $ep \to en\pi^+$ in the Born approximation (OPEA) is expressed as:

$$\begin{aligned}\left.\sigma_T^{ep\to ep\pi^+}\right|_{B.A} \propto \Bigg|&\frac{1}{2M+m_\pi}\left[F_1^p(Q^2) - \frac{m_\pi}{2M}F_2^p(Q^2)\right] \\ &-\frac{1}{2M^2+m_\pi M-Q^2}\left[(m_\pi+M)F_1^n(Q^2) - \frac{Q^2+m_\pi M}{2M}F_2^n(Q^2)\right]\Bigg|^2\end{aligned} \quad (1.12)$$

$$\sigma_L^{ep\to ep\pi^+}\Big|_{B.A} \propto \left| \frac{1}{2M+m_\pi}\left[\frac{m_\pi}{Q^2}F_1^p(Q^2) - \frac{1}{2M}F_2^p(Q^2)\right] \right.$$
$$- \frac{1}{2M^2+m_\pi M - Q^2}\left[(1+\frac{m_\pi M}{Q^2})F_1^n(Q^2) - \frac{m_\pi+M}{2M}F_2^n(Q^2)\right] \quad (1.13)$$
$$\left. + \frac{Q^2-m_\pi^2}{Q^2(2Mm_\pi^2+m_\pi^3-MQ^2)}F_\pi(Q^2)\right|$$

Thus, cross sections with transverse-longitudinal separation allow with a good nucleon form factor parameterization to extract the pion form factor. The authors of [4] even propose to get independent neutron form factor measurements compared to electron neutron scattering on nuclei.

This method, known as the Born term model method, knew a first improvement with the model of Gutbrod and Kramer [16]. In the Born term model, the nucleon form factors are considered to be the on-shell nucleon form factors, whereas at the nucleon-pion vertex, the nucleon is off-shell. Gutbrod and Kramer allow in their model the nucleon form factor to be different from the on-shell nucleon form factor. Brauel *et al.* [12] and Ackermann *et al.* [13] use this model to extract the pion from factor from separated longitudinal cross section at $Q^2 = 0.70$ GeV^2, $W = 2.19$ GeV, $|t| < 0.28$ GeV^2 and $Q^2 = 0.35$ GeV^2, $W = 2.10$ GeV, $|t| < 0.05$ GeV^2 respectively.

The Born term models are valid when the energy W involved in the reaction is not too large (typically at $W < 2$ GeV, [17, 18]). When this energy increases, other contributions from the ρ meson for instance contribute to the reaction. To take all these contributions into account, Vanderhaeghen, Guidal, and Laget [18] recently developed a model including the exchange of Regge trajectories instead of exchange of particles (see next section for details on Regge models).

Horn *et al.* [14, 15] used this model to extract the pion form factor from separated cross sections at $Q^2 = 1.60$ and 2.45 GeV^2 and $Q^2 = 2.15$ and 3.80 GeV^2. Huber *et al.* [7] used this method to extract the pion form factor from separated cross sections from $Q^2 = 0.6$ GeV^2 to $Q^2 = 2.45$ GeV^2, and to reanalyze Brauel data and Ackermann data. These very recent analysis found that in the scanned Q^2 range, the pion form factor is likely dominated by non-perturbative contributions (See Fig. 1.3).

Nowadays, the pion form factor extraction from charged pion electroproduction process relies on Regge phenomenology. Regge phenomenology is also able to describe neutral pion electroproduction processes. We treat Regge models in the next section.

1.3 Regge phenomenology

This section deals with the Regge phenomenology. We give the basic principles of Regge phenomenology and explicit formulae. Then we summarize the description of the old π^0 data with the Regge phenomenology.

1.3.1 Principle and formalism of Regge phenomenology

The interaction between two particles is usually modeled by the exchange of a virtual boson. Considering the example of $\gamma(^*)p \to \pi^+ n$, (Fig. 1.4), the amplitude of the

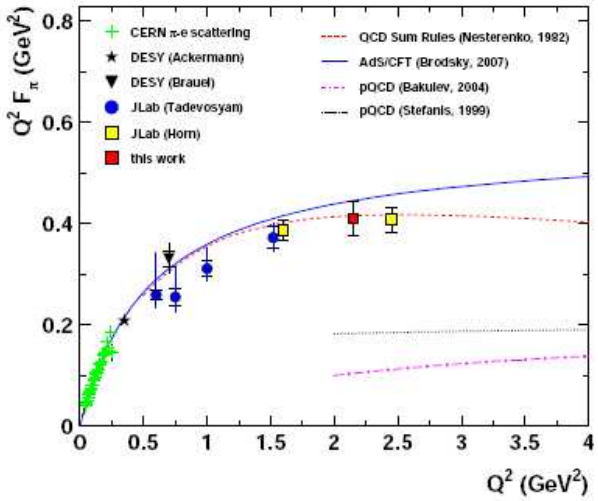

Figure 1.3: Figure extracted from [15]. Charged pion form factor measurements from [12, 13] (black markers), [10, 11] (green markers), and [14, 15] (yellow and red markers). These measurements are in reasonable agreement with non-pertubative models (blue and red curve), but are in complete disagreement with perturbative models (magenta and black curves).

reaction depends on the particle exchanged, depending on the energy available for the reaction. The diagram of Fig. 1.4 can be decomposed in three main Feynman sub-

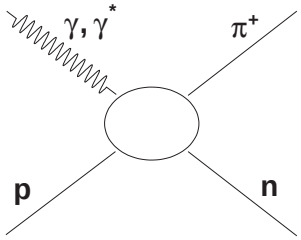

Figure 1.4: Diagram of the reaction $\gamma(^*)p \to \pi^+ n$.

diagrams (Fig. 1.5), representing the three Mandelstam variables channels (respectively the "annihilation" diagram for s-channel, the "forward scattering" diagram for t-channel, and the "backward scattering" for u-channel).

The Regge phenomenology is an approximate formalism in the sense that this parameterization uses a tree-level Lagrangian based on hadronic degrees of freedom, instead of quark and gluons. For instance, for the exchange of a π^+ in the t-channel, the current is [19]:

$$J^\mu_\pi(\gamma^{(*)}p \to \pi^+ n) = -i\sqrt{2}e\frac{f_{\pi NN}}{m_\pi}\bar{N}_f(q - p_\pi)^\mu \mathcal{P}^0 \not{q}\gamma^5 N_i. \tag{1.14}$$

where $\mathcal{P}^0$ is the propagator of the particle, and $f_{\pi NN}$ is the pion-nucleon coupling constant.

The idea of the Regge phenomenology is to model the interaction, in the t-channel, with an exchange of families of particles instead of particles themselves. Indeed, a given process involves more and more exchanged particles in the t-channel as the available energy in this channel grows. These families of particles are characterized by the same quantum numbers (except the spin which increases by two units for each new particle), and are called trajectories. The trajectory describes in an elegant way the t-dependence of a

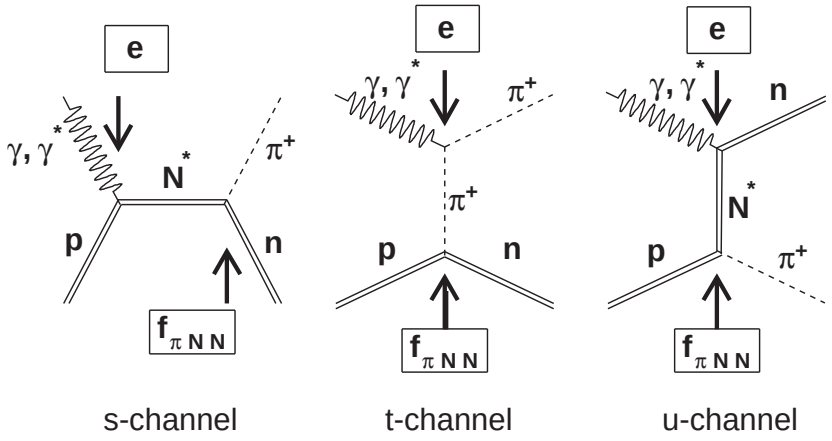

Figure 1.5: Diagrams of the reaction $\gamma(^*)p \to \pi^+ n$ in the s-channel (left), t-channel (middle), and u-channel (right).

process, since it aims to give a relevant relation between the value of the quadrimomentum transfer t and the amplitude of the process in the t-channel, depending on the number of particles involved. Notice that a given process possibly involves several trajectories.

The notion of trajectory corresponds analytically to replace, in equation (1.14) the propagator of a single boson (see Fig. 1.5 for our example) with the propagator of a trajectory (see [19, 20] for recent sources). The trajectory propagator for a scalar S, or a pseudoscalar PS such as the π^+ is:

$$\mathcal{P}_{\text{Regge}} = \left(\frac{s}{s_0}\right)^{\alpha_{S,PS}(t)} \frac{\pi\alpha'_{S,PS}(t)}{\sin(\pi\alpha_{S,PS}(t))} \frac{\mathcal{S}_{S,PS} + e^{-iS,PS\alpha_{S,PS}(t)}}{2} \frac{1}{1+\Gamma(\alpha_{S,PS}(t))}, \tag{1.15}$$

where s_0 is a reference mass scale, taken conventionally as 1 GeV^2 and $\mathcal{S}_{S,PS} = +1$ is the signature of the trajectory. The Regge trajectory $\alpha_{S,PS}(t)$ is the "exchanged" spin in the t channel, as a function of t which is the squared mass of the trajectory. It is empirically found to be approximately linear $\alpha_{S,PS}(t) = \alpha'_{S,PS} \times (t - m^2_{S,PS})$. Note the trajectory is materialized by a particle when the spin J is equal to $J = 2N + J_0$, N integer, and J_0 the spin of the first particle of the trajectory (0 for scalars, pseudoscalars, and 1 for vectors, pseudovectors).

For a vector meson V, such as the ρ and the ω, or a pseudovector meson PV such as the b_1, the propagator is:

$$\mathcal{P}_{\text{Regge}} = \left(\frac{s}{s_0}\right)^{\alpha_{V,PV}(t)-1} \frac{\pi\alpha'_{V,PV}(t)}{\sin(\pi\alpha_{V,PV}(t))} \frac{\mathcal{S}_{V,PV} + e^{-i\pi\alpha_{V,PV}(t)}}{2} \frac{1}{\Gamma(\alpha_{V,PV}(t))}, \tag{1.16}$$

where $S_{V,PV} = -1$, and $\alpha(t) = \alpha_0 + \alpha' \times t$, with α_0 the intercept of the trajectory. The intercept is by definition $\alpha(t = 0)$.

The propagator of a particle trajectory has the property to reduce to the Feynman propagator of the particle itself at the neighborhood of the particle pole (*i.e* when $t \to m^2$). Since the propagator expression comes in the scattering matrix element $\mathcal{M}(s,t)$, the t-dependent cross section is given by:

$$\frac{d\sigma}{dt} \propto \frac{1}{s^2} \times |\mathcal{M}(s,t)|^2 \Rightarrow \frac{d\sigma}{dt} \propto s^{2\alpha(t)-2}, \tag{1.17}$$

which gives the deep inelastic scattering cross section behavior with the optical theorem

$$\sigma^{DIS} \propto \frac{1}{s} \times \Im m\{\mathcal{M}(s, t=0)\} \Rightarrow \sigma^{DIS} \propto s^{\alpha_0 - 1}. \tag{1.18}$$

In other words, the intercept of a trajectory carries the energy dependence of the total cross section. In an interaction, which generally involves more than one trajectory, the energy dependence of the total cross section is given by the trajectory with the highest intercept.

At asymptotically high energies, the inclusive scattering is dominated by the exchange of the "Pomeron" trajectory. The Pomeron has been created as an effective object which carries the quantum number of the vacuum. Its intercept is $\alpha_0 = 1.08$. Some theoretical hypotheses state it would be actually instantiated as glue-balls, which are gluon-gluon bound states [21, 22].

To describe a considered channel, one should generally include several trajectories. For reasons of completeness, one should have to consider channels where a particle is produced and then rescattered in the nucleon field. In the most general case, the particle initially produced may be different from the particle produced in the final state. In the case the particle initially produced is the same as the particle in the final state, the particle exchanged for the rescattering is a pomeron. The trajectory corresponding to such a channel is called a "cut trajectory".

After this short description of the Regge phenomenology, let us review the achievements of Regge-based models for pion photoproduction, and recent developments for electroproduction data.

1.3.2 Old neutral pion results, and Regge interpretation

The Regge phenomenology used to give successful results, mostly for the description of photoproduction processes. In this summarized review, we focus on π^0 production.

For the study of neutral pion production, one used to consider the trajectories of the ω and the ρ added with the $b_1(1235)$ [23, 24, 25]. Notice there is no π^0 trajectory, since the π^0 does not carry any charge or spin, and then cannot couple to a photon, real or virtual. The charged pion trajectory does not contribute as well, since it does not even have any hadronic decay channel. The contribution of the ρ has been quickly minimized because of the very weak $\rho \to \pi^0\gamma$ branching ratio. Braunschweig *et al.* in [23, 24] fitted their photoproduction data at 4 and 5.8 GeV photon energy. Their fit includes Primakoff effect, which is the production of a neutral pion by the interaction of the real photon with a virtual photon from the target ($\gamma\gamma^* \to \pi^0$). They showed the invalidity of a fit including only the Primakoff effect and the ω and b_1 trajectories for $-t > 0.4$ GeV^2. However, they successfully fitted all their data with a model including an effective cut trajectory taking into account the Pomeron exchange in pion elastic rescattering (Fig. 1.6).

Anderson *et al.* also minimized the role played by the b_1 trajectory based on their measurements of photoproduction asymmetries with linearly polarized photons on an overall beam energy range running from 4 to 18 GeV [26, 27, 28]. The asymmetry $A_{\perp||}$ is given by:

$$A_{\perp||} = \frac{\sigma_\perp - \sigma_{||}}{\sigma_\perp + \sigma_{||}} \tag{1.19}$$

with $\sigma_\perp(\sigma_{||})$ the cross section with photons normally (parallelly) polarized with respect to the reaction plane. The natural parity trajectories (*i.e.* vectors $J^P = 1^-$ such as ω)

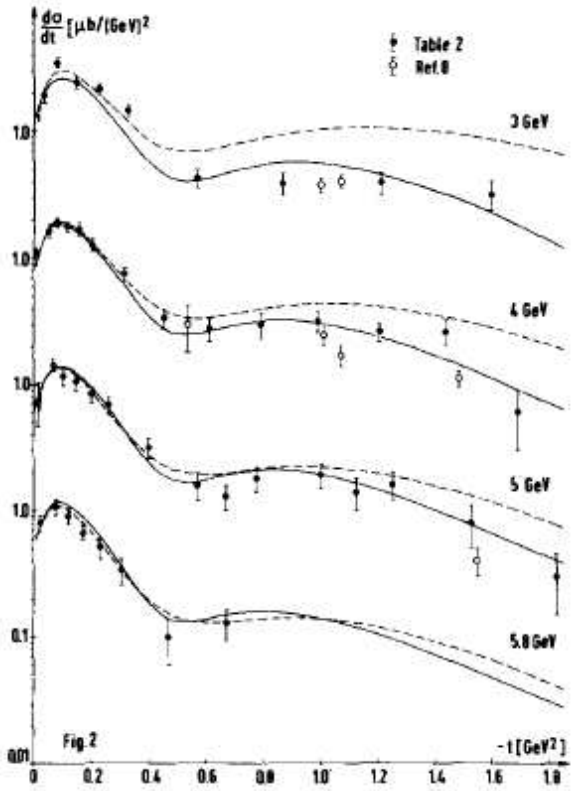

Figure 1.6: Figure extracted from [24] showing $d\sigma^{\gamma p \to \pi^0 p}/dt$. The dashed curves represent the fit including ω and b_1 trajectories. The solid curves represent the fit with the ω and the effective cut trajectories. The data show better agreement with the solid curves.

contribute to $\sigma_\perp$, whereas the unnatural parity trajectories (*i.e.* pseudovectors $J^P = 1^+$ such as b_1) contribute to ($\sigma_{||}$). Their measurements at beam energies of 4, 6 and 10 GeV give asymmetries between 0.8 and 1 at their kinematic coverage. This clearly indicates a dominance of the ω trajectory, and a negligible contribution to b_1.

All these previous data show a dip around $t = -0.5$ GeV^2. The trajectory of the ω has been pointed out to be responsible for the dip. However, the ω alone would have given a null cross section. The fact it is not zero is due to the contributions of other trajectories.

Goldstein and Owens [30] fitted π^0 photoproduction data with a global model based on SU(3) invariance, and vector meson dominance, including the ω and ρ trajectories, the b_1 and the h_1 trajectories. This model also takes into account an effective trajectory cut generated by elastic rescattering on the nucleon. This cut is parameterized by πN elastic scattering, instead of just being an effective trajectory cut as in [24]. Their fit to the model is in agreement with the individual conclusions of Braunschweig *et al.* and Anderson *et al.*.

Brasse *et al.* [31] and Berger *et al.* [32] measured π^0 electroproduction cross section at very low Q^2 (below 1 GeV^2) in order to make the connection with π^0 photoproduction. Brasse *et al.* measured cross sections at three values of Q^2: 0.22, 0.55, and 0.85 GeV^2. They observed a big gap between photoproduction cross section and the cross section at $Q^2 = 0.22$ GeV^2. After this huge gap, their behavior in Q^2 is surprisingly rather smooth (see Fig. 1.9). These measurements also point out the disappearance, even at the lowest Q^2, of the cross section dip at $t = 0.5$ GeV^2. This is due to the appearance of the longitu-

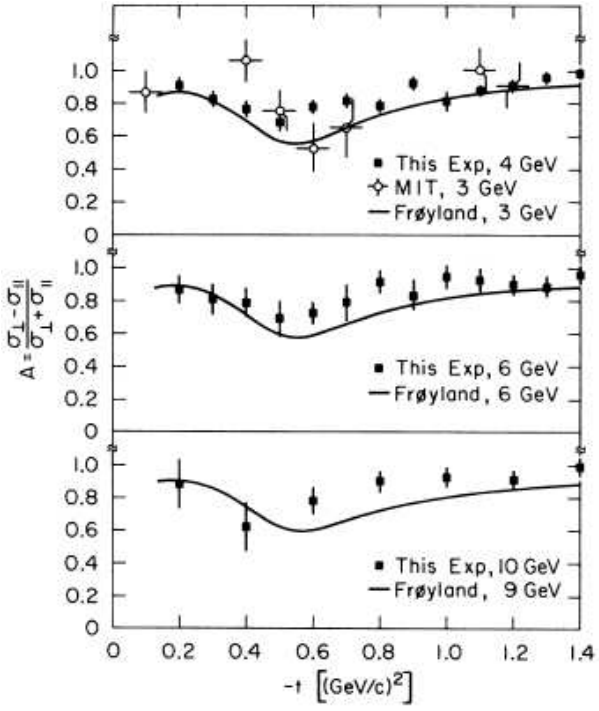

Figure 1.7: Figure extracted from [28] showing $A_{\perp||}$ versus $-t$. The curve is a prediction from Frøyland [29] including ω, ρ and respective cut trajectories.

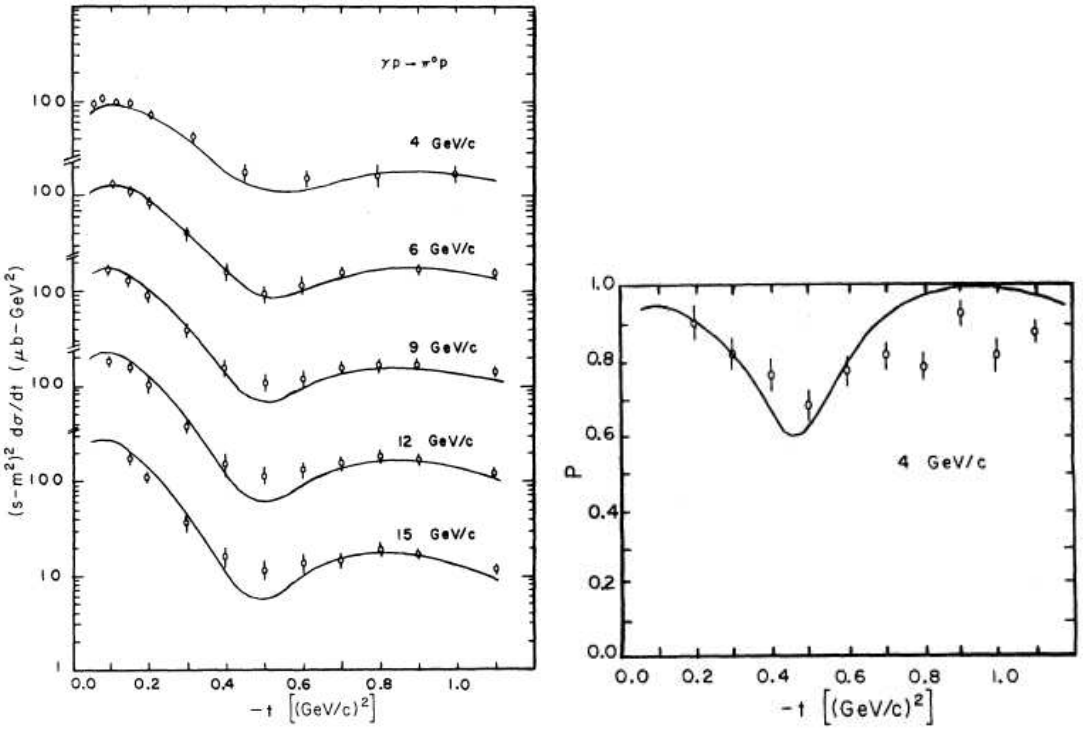

Figure 1.8: Figures extracted from [30]. Left panel shows $d\sigma_v^{\gamma p\to\gamma p\pi^0}/dtd\phi_\pi$ data. Right panel shows the asymmetry $A_{\perp||}$. The curves represent the fit of Goldstein and Owens.

dinal contribution and the growing contribution of $\sigma_{||}$. Although these contributions are small, they might be large enough to fill in the dip. Berger *et al.* also provide asymmetries measurements, at $Q^2 = 0.275$ GeV^2. These asymmetries are lower than photoproduction

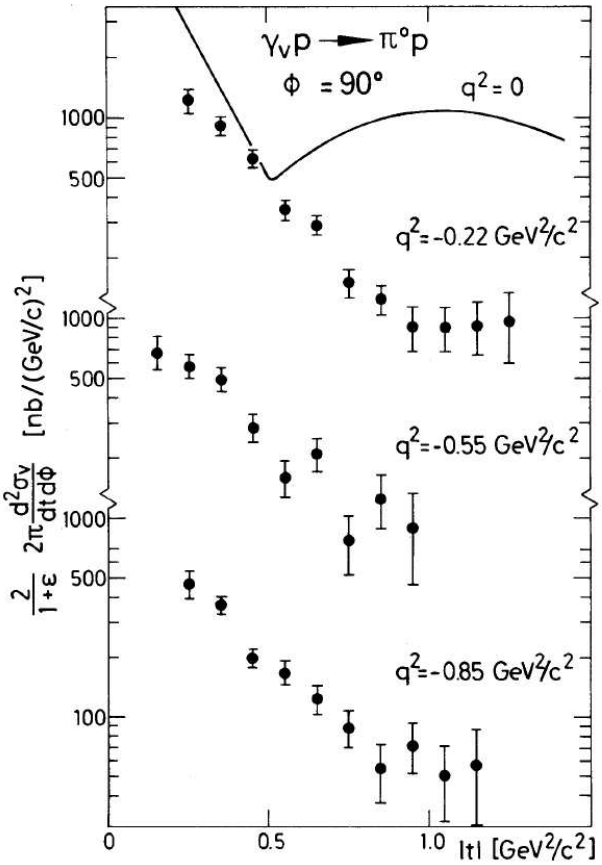

Figure 1.9: Figure extracted from [31] showing $d\sigma_v^{ep\to ep\pi^0}/dtd\phi_\pi$. The vertical scale has been offset for each kinematic for legibility reasons. The data points from one kinematic to another at the same $-t$ are actually rather close to each other. In contrast to this rather smooth Q^2 dependence, the cross section falls quickly from the photoproduction point to the lowest Q^2 electroproduction point, in exception with the accidental agreement in the dip region of the real photon data

asymmetries, giving further evidence of a growing contribution of $\sigma_{||}$.

After a golden age in the 1960s and the 1970s, and despite of all its successes, Regge phenomenology has been more and more abandoned. There are several reasons to that. First of all, it deals with hadronic degrees of freedom, so the link with QCD is not easy. Moreover, the advantage of Regge models, which used to be the relative simplicity and the relatively low numbers of needed parameters, is reduced as one tries to describe more and more accurately the data. Finally, more powerful tools, such as generalized parton distributions appeared in the late 1990s. This tool deals with partonic degrees of freedom (*i.e.* quarks and gluons) instead of hadronic degrees of freedom, what makes them integrated by construction in the QCD framework. Mostly, GPDs propose a new three-dimensional information on the nucleon. The following section is dedicated to the description of GPDs.

1.4 Generalized Parton Distributions

This section is dedicated to GPDs. GPDs are a new tool to explore the nucleon structure in terms of quarks and gluons. Particularly, they give a three-dimensional information

on the nucleon structure, allowing to get some information on the orbital momentum of the partons. We give a reminder about Deep Inelastic Scattering (DIS) and PDFs. We build the link between PDFs and GPDs *via* the optical theorem and Compton Scattering. We introduce the GPDs and we give their properties, particularly in the forward limit and their sum rules. We finally give a description of Deeply Virtual Meson Production (DVMP) within the GPD framework.

1.4.1 Deep inelastic scattering and parton distribution functions

Before to treat the GPDs, let us do a short reminder about parton distributions functions. PDFs are involved in DIS cross sections. DIS experiments focus on the electron scattering on the nucleon at high energy, without measuring the hadronic final state. A diagram of this process is shown in Fig. 1.10(a).

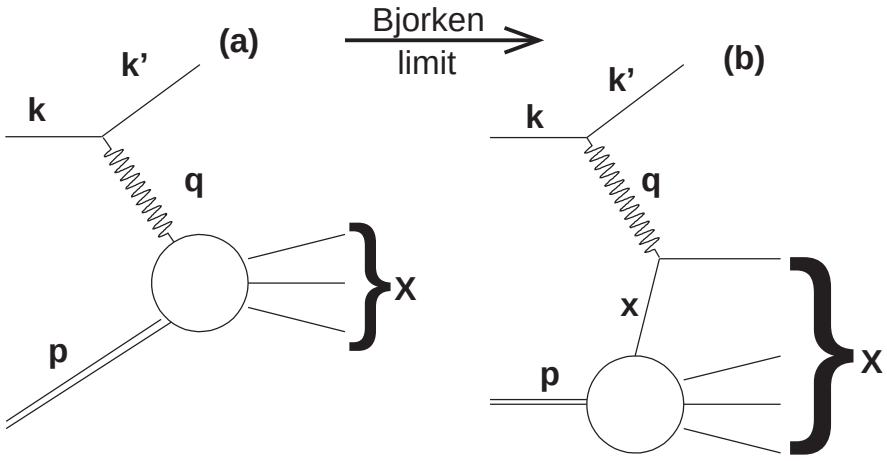

Figure 1.10: Feynman Diagram for Deep Inelastic Scattering $ep \to eX$: (a) most general Feynman diagram for inelastic scattering; (b) Feynman diagram for DIS in the Bjorken regime.

The Bjorken regime is defined by a large virtuality Q^2 of the virtual photon, a large energy ν of the virtual photon, and the Bjorken variable $x_{Bj} = Q^2/2p \cdot q$ fixed. In this Bjorken regime, the virtual photon selects in the proton a single quark, which momentum is xp in the Infinite Momentum Frame (IMF) of the nucleon. The perturbative dynamics of the reaction forces $x = x_{Bj}$. This mechanism is illustrated by Fig. 1.10(b).

This figure also illustrates the fact that this kind of process can be decomposed in a hard part and a soft part. The hard part is the interaction of the virtual photon with the asymptotically free quark, and can be computed in perturbative QCD (pQCD). The soft part is, in deep inelastic scattering, the sum of processes which transforms the nucleon into any final state accessible at the given W of the interaction. It cannot be computed by pQCD, and must be experimentally determined. The ability of such a process to be described by a soft and a hard part is called factorization.

Thus, the unpolarized DIS cross section can be written as a sum of elementary interactions between two point-like particles, the electron and the single quark:

$$\frac{d\sigma^{DIS}}{dk' d\Omega_e} = \sum_q \frac{d\sigma^{eq \to eq}}{dk' d\Omega_e} \times f_q(x). \tag{1.20}$$

where the $f_q(x)$ are the PDFs. The parton distribution function $f_q(x)$ corresponds to the probability for a parton q to carry the momentum fraction x of the proton. Similarly, the polarized DIS cross section will depend on $\Delta q_i(x)$ which is the helicity distribution function for the parton i.

The normalization of the PDFs is given by:

$$\sum_{i\in q,g} \int x f_i(x) dx = n_v \tag{1.21}$$

with $n_v = 0, 1, 2$ the number of valence partons of flavor i. In the case of deep inelastic scattering, the momentum fraction of the proton x is precisely the Bjorken variable x_{Bj}.

The unpolarized DIS cross section can also be written in the classic form, with hadronic tensors [9]:

$$\begin{aligned} \frac{d\sigma^{DIS}}{dk' d\Omega_e} &= \frac{\alpha^2}{4k^2 \sin\frac{\theta_e}{2}^4} \left[W_2(x_{Bj}, Q^2) \cos\frac{\theta_e}{2}^2 + 2W_1(x_{Bj}, Q^2) \sin\frac{\theta_e}{2}^2 \right] \\ &= \frac{\alpha^2}{4k^2 \sin\frac{\theta_e}{2}^4} \left[\frac{1}{\nu} F_2(x) \cos\frac{\theta_e}{2}^2 + 2\frac{1}{M} F_1(x) \sin\frac{\theta_e}{2}^2 \right], \end{aligned} \tag{1.22}$$

with the structure functions $F_1(x)$ and $F_2(x)$, given in the $Q^2 \to \infty$ limit by

$$F_2(x) = 2xF_1(x) = \sum_{i\in q,g} e_i^2 x f_i(x), \tag{1.23}$$

which encapsulate the soft processes.

1.4.2 From PDFs to GPDs, Optical theorem and handbag diagram

The link between parton distribution functions and generalized parton distributions is provided by the Compton scattering amplitude. Forward Compton process corresponds to the interaction of the virtual photon with a quark with a momentum fraction x of the nucleon. The quark becomes excited off its mass-shell and soon re-emits a virtual photon. This virtual photon is reabsorbed by the scattered lepton, and the quark is reabsorbed by the nucleon with the same momentum. The diagram of this process, known as the handbag diagram, is available on the right part of Fig. 1.11.

The optical theorem states that the DIS cross section at a given x is given by the imaginary part of the forward Compton amplitude (Fig. 1.11). Formally, if we write the DIS cross section into its most general form:

$$\sigma^{DIS} \propto \frac{\alpha^2}{q^4} L_{\mu\nu} W^{\mu\nu}, \tag{1.24}$$

with $L_{\mu\nu}$ the leptonic tensor and $W^{\mu\nu}$ the hadronic tensor, then the optical theorem states:

$$\begin{aligned} W^{\mu\nu} &= \frac{1}{4\pi} \int d^4 z e^{iq\cdot z} \sum_X \langle p \left| j^\mu(z) \right| X \rangle \langle X \left| j^\nu(0) \right| p \rangle \\ &= \frac{1}{2\pi} \Im m T^{\mu\nu} \end{aligned} \tag{1.25}$$

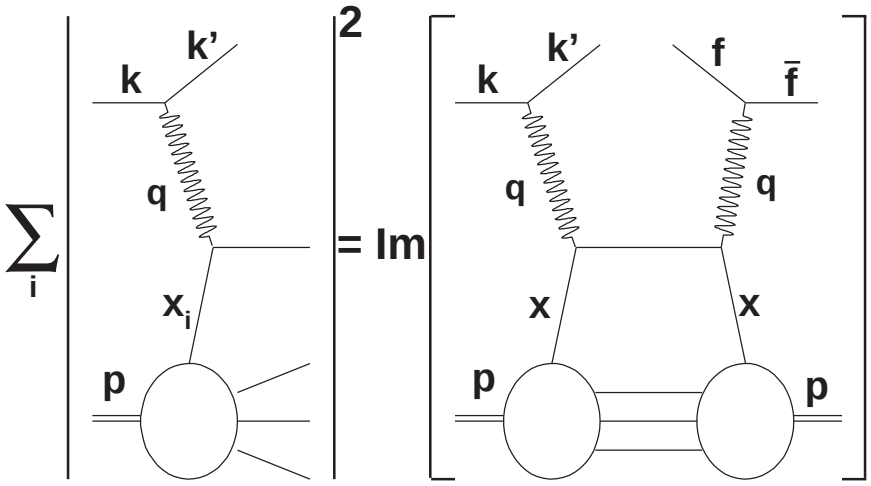

Figure 1.11: Diagram representation of the optical theorem. The right diagram is the so-called handbag diagram, and is the amplitude of forward Compton scattering.

with:

$$T^{\mu\nu} = i \int d^4z e^{iq\cdot z} \langle p\,|T\{j^\mu(z), j^\nu(0)\}|\,p\rangle. \tag{1.26}$$

Thanks to this theorem, we have access to the forward Compton scattering amplitude in terms of parton distribution functions. Forward Compton scattering is only a particular case at very small t of off forward Compton scattering. To be described however, this process may require more sophisticated objects that simple PDFs.

1.4.3 Generalized parton distributions (GPDs)

In analogy with forward Compton scattering which would allow to access parton distribution functions, off-forward Compton scattering could allow to access to the so-called off-forward parton distributions [1, 33, 2], now called Generalized Parton Distributions. The process is similar, but the momentum of the quark reabsorbed by the nucleon is different from the quark emitted by the nucleon (Fig. 1.12).

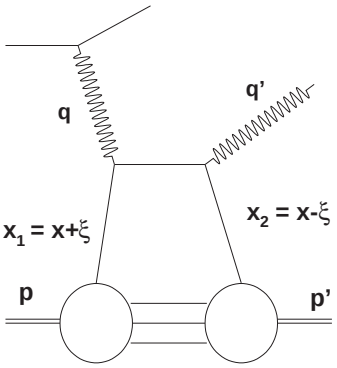

Figure 1.12: Off-forward Compton scattering diagram.

The amplitude of this process is expressed considering quadrimomenta of the involved particles in light cone coordinates, *i.e.* as a function of two light-like vectors (t, x, y, z). Let us use Ji conventions [2] for the light-like vectors of the coordinates: $p^\mu_{l.l.} = \Lambda(1, 0, 0, 1)$ and $n^\mu_{l.l.} = (1, 0, 0, -1)/(2\Lambda)$, with Λ fixed arbitrarily. The z-component is taken along the direction of the virtual photon. These two vectors verify $p^2_{l.l.} = 0 = n^2_{l.l.}$ and $p_{l.l.} \cdot n_{l.l.} = 1$. We define from Fig. 1.12 $\Delta^\mu = (p' - p)^\mu = (q - q')^\mu$ (with $\Delta^2 \equiv t$) and $P^\mu = (p + p')^\mu/2$, and we choose q^μ and P^μ collinear and in the z direction. Then we expand these vectors according to $p_{l.l.}, n_{l.l.}$, and when necessary, transverse components:

$$P^\mu = p^\mu_{l.l.} + \frac{\bar{M}^2}{2} n^\mu_{l.l.}, \tag{1.27}$$

$$q^\mu = -\xi p^\mu_{l.l.} + \frac{Q^2}{2\xi} n^\mu_{l.l.}, \tag{1.28}$$

$$\Delta^\mu = -\xi(p^\mu_{l.l.} + \frac{\bar{M}^2}{2} n^\mu_{l.l.}) + \Delta^\mu_\perp, \tag{1.29}$$

with $\bar{M}^2 = M^2 - \frac{\Delta^2}{4}$ and the skewedness variable ξ defined by:

$$\xi = \frac{Q^2}{2P \cdot q} \overset{\text{Bjorken limit}}{\longrightarrow} \frac{x_{Bj}}{2 - x_{Bj}}. \tag{1.30}$$

The Off-forward Compton Scattering amplitude has the form [2]:

$$\begin{aligned} T^{\mu\nu}(P, q, \Delta) &= i \int d^4 z e^{iq\cdot z} \langle p' | T\{j^\mu(z), j^\nu(0)\} | p \rangle \\ &= -\frac{1}{2}(p^\mu n^\nu + p^\nu n^\mu - g^{\mu\nu}) \int dx \left(\frac{1}{x - \xi + i\epsilon} + \frac{1}{x + \xi + i\epsilon} \right) \\ &\times \left[H(x, \xi, t) \bar{U}(p') \not{n} U(p) + E(x, \xi, t) \bar{U}(p') \frac{i\sigma^{\alpha\beta} n_\alpha \Delta_\beta}{2M} U(p) \right] \\ &- \frac{i}{2} \epsilon^{\mu\nu\alpha\beta} p_\alpha n_\beta \int dx \left(\frac{1}{x - \xi + i\epsilon} + \frac{1}{x + \xi + i\epsilon} \right) \\ &\times \left[\tilde{H}(x, \xi, t) \bar{U}(p') \not{n} \gamma_5 U(p) + \tilde{E}(x, \xi, t) \frac{\xi}{2M} \bar{U}(p') \gamma_5 U(p) \right] \end{aligned} \tag{1.31}$$

with $U(p)$ the proton spinor, $\not{n} = \gamma \cdot n$, and H, $\tilde{H}$, E, $\tilde{E}$, functions of Q^2, x, ξ and t the GPDs, which describe the amplitude for a parton picked in the proton with an momentum $x + \xi$ to return into it with a momentum $x - \xi$. It is important to note that in this case $x_{Bj} \neq x$.

H, E are the unpolarized GPDs *i.e.* parton helicity insensitive and $\tilde{H}$, $\tilde{E}$ are the polarized GPDs *i.e.* parton-helicity dependent relative to the proton spin direction. They provide correlated informations on the spatial distributions of partons in the proton, and on the momentum distribution of these partons in the proton [8]. There are actually four chiral-even GPDs for each type of parton q, g in the Bjorken limit.

The GPDs are theoretically constrained at some limits by the nucleon form factors, and by the parton distribution functions. These constraints have been introduced first by Ji in [2].

At $t = 0$ and $\xi = 0$ (forward limit), we recover the usual helicity independent and helicity dependent PDFs:

$$H^{g,q}(x, 0, 0) = f_{g,q}(x), \tag{1.32}$$

$$\tilde{H}^{g,q}(x, 0, 0) = \Delta q_{g,q}(x). \tag{1.33}$$

On the other hand, the GPDs obey to the following sum rules.

$$\int_{-1}^{1} dx H^{g,q}(x,\xi,t) = F_1^{g,q}(t), \tag{1.34}$$

$$\int_{-1}^{1} dx E^{g,q}(x,\xi,t) = F_2^{g,q}(t), \tag{1.35}$$

$$\int_{-1}^{1} dx \tilde{H}^{g,q}(x,\xi,t) = g_A^{g,q}(t), \tag{1.36}$$

$$\int_{-1}^{1} dx \tilde{E}^{g,q}(x,\xi,t) = g_P^{g,q}(t), \tag{1.37}$$

with $F_1(t)$, $F_2(t)$ the nucleon form factors as introduced in the second section of this chapter, and $g_A(t)$, $g_P(t)$ respectively the axial vector and pseudoscalar form factors (accessible with weakly interacting probes for example).

In addition to these constraints, Ji introduced an additional sum rule, now known as Ji sum rule, expressing the total angular momentum of a parton as a function of its corresponding GPDs:

$$\int_{-1}^{1} dx\, x \left[H^{q,g}(x,\xi,t) + E^{q,g}(x,\xi,t)\right] = A_{q,g}(t) + B_{q,g}(t) \tag{1.38}$$

with

$$A_{q,g}(0) + B_{q,g}(0) = 2J_{q,g}. \tag{1.39}$$

As we already know the spin contribution to the total angular momentum from DIS, the Ji sum rule is a way to access the parton orbital momentum contribution to the total nucleon spin.

1.4.4 GPDs in Deeply Virtual Meson Production (DVMP)

The GPDs are designed to describe all exclusive leptoproduction processes on the nucleon [34, 35]. Among these processes, the most studied is the Deeply Virtual Compton Scattering (DVCS), which is a particular case of off-forward Compton scattering with a real photon in the final state. The data we analyze in this document is the by-product of a DVCS experiment [36] and have been recorded with the same apparatus. Details on the DVCS cross sections in terms of GPDs are given in [34, 35, 37] for instance.

Our actual interest is the Deeply Virtual Meson Production (DVMP), which are described in great detail in [34, 35]. Factorization for DVMP has been proved with a longitudinally polarized virtual photon by Collins, Frankfurt and Strikman [38].

[34, 35] give the general structure of longitudinal cross sections for vector and pseudoscalar meson production in terms of GPDs. At leading order, vector meson production amplitudes only depend on unpolarized GPDs, whereas pseudoscalar meson production amplitudes only depend on polarized GPDs [38]. The quarks GPDs taking place in the amplitude depends on the meson quark content.

The longitudinal amplitude for π^0 electroproduction is given by [34]:

$$\begin{aligned}\mathcal{M}^L_{\pi^0} = -ie\frac{4}{9}\frac{1}{\sqrt{Q^2}}4\pi\alpha_S \left[\int_0^1 dz \frac{\Phi_{\pi^0}(z)}{z}\right] \frac{1}{2}\int_{-1}^{1} dx \left[\frac{1}{x-\xi+i\epsilon} + \frac{1}{x+\xi+i\epsilon}\right] \\ \times \left\{\tilde{H}^p_{\pi^0}(x,\xi,t)\bar{U}(p')\not{n}\gamma^5 U(p) + \tilde{E}^p_{\pi^0}(x,\xi,t)\bar{U}(p')\gamma^5 U(p)\frac{\xi}{2M}\right\},\end{aligned} \tag{1.40}$$

where:

$$\tilde{H}^p_{\pi^0}(x,\xi,t) = \frac{1}{\sqrt{2}}\left\{\frac{2}{3}\tilde{H}^{u/p} + \frac{1}{3}\tilde{H}^{d/p}\right\}, \tag{1.41}$$

$$\tilde{E}^p_{\pi^0}(x,\xi,t) = \frac{1}{\sqrt{2}}\left\{\frac{2}{3}\tilde{E}^{u/p} + \frac{1}{3}\tilde{E}^{d/p}\right\} \tag{1.42}$$

and $\Phi_{\pi^0}(z)$ is the Distribution Amplitude (DA) of the pion, experimentally parameterized by:

$$\Phi_{\pi^0}(z) = \sqrt{2} f_\pi 6 z(1-z), \tag{1.43}$$

with $f_\pi = 0.0924$ GeV and $z = (p\cdot q')/(p\cdot q)$. The longitudinal cross section then scales as $1/Q^6$ within the conventions used by [34, 35]. On the other hand, the transverse cross section scales as $1/Q^8$ in the Bjorken regime.

These GPDs need to be extracted from the experiments and parameterized. The deeply virtual π^0 production experiments allows to access the GPDs of quarks. In the Appendix 2 of this document, I describe a proposal for a deeply virtual $\phi(1020)$ production on the proton, which allows to access the GPDs of gluons. Several GPD *ansätze* (*i.e.* preliminary parameterizations) already exist to make predictions on DVCS and DVMP cross sections, such as in [34, 35], or to compute vector mesons cross sections such as Goloskokov and Kroll model [39, 40].

1.5 Semi-Inclusive Deep Inelastic Scattering

Even though we study an exclusive reaction, we study it in the DIS regime ($W^2 > 4$ GeV^2), so this reaction, as well as any other exclusive reaction in the DIS regime, can be seen as the limit of SIDIS, where the typical multiplicity of the measured particle is unity. Semi-Inclusive Deep Inelastic Scattering (SIDIS) describes electroproduction processes such as $ep \to ehX$ where only the produced hadron h and the scattered electron are measured (see Fig. 1.13(a)). They allow to extract quark transverse momentum dependent structure functions called Transverse Momentum Distributions (TMDs). We give a detailed description of semi inclusive process, as well as the achievements on SIDIS phenomenology for pion production. We introduce TMDs, particularly the Cahn effect and the Sivers function.

1.5.1 General description of semi-inclusive deep inelastic scattering processes

The phenomenology of SIDIS describes a process of leptoproduction of a hadron h on a nucleon. It differs from exclusive leptoproduction by the fact that any other particle can be produced in the interaction. A diagram of such a process is available on Fig. 1.13(a). The produced hadron has a quadrimomentum $q' = (q'^0, \mathbf{q}')$, and carries a fraction of the total energy

$$z = \frac{p\cdot q'}{p\cdot q} \overset{\text{lab.}}{=} \frac{q'^0}{\nu} \tag{1.44}$$

of the reaction. It is characterized by a transverse momentum $\mathbf{q}'_T$ relative to the virtual photon direction. At asymptotically high Q^2, ν, and $\mathbf{q}'_T \sim \sqrt{Q^2}$, the process factorizes. It even factorizes when the transverse momentum of the hadron $\mathbf{q}'_T$ is low relative to $\sqrt{Q^2}$ [41, 42]. This factorization is illustrated by Fig. 1.13(b).

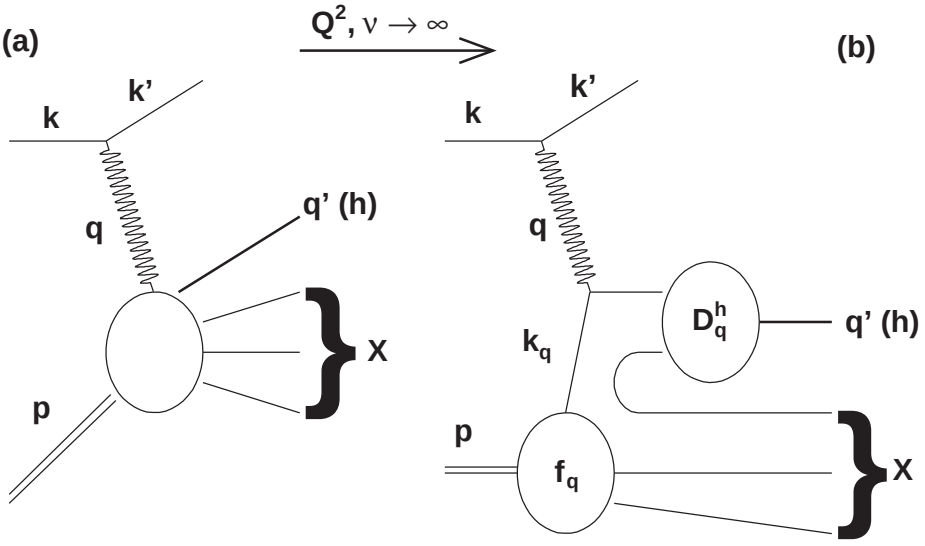

Figure 1.13: Feynman Diagram for Semi Inclusive Deep Inelastic Scattering $ep \to ehX$: (a) most general Feynman diagram for SIDIS; (b) Feynman diagram for SIDIS in the Bjorken regime. f_q is the structure function, and D_q^h is the fragmentation function *i.e.* the probabilities for each quark flavor q to hadronize into a hadron h.

Under the factorization hypothesis, the cross section has the form

$$\frac{d^5\sigma}{dx_{Bj}dQ^2dzd^2\mathbf{q}'_T} \propto \sum_q \frac{\alpha^2 e_q^2}{Q^4} f_q(x_{Bj}, k_{q\perp}) D_q^h(z, q'_\perp) \tag{1.45}$$

with

$$f_q(x_{Bj}, k_{q\perp}) = \frac{f_q(x_{Bj})}{\pi\langle k_{q\perp}^2\rangle} e^{-\frac{k_{q\perp}^2}{\langle k_{q\perp}^2\rangle}}, \tag{1.46}$$

and

$$D_q^h(z, q'_\perp) = \frac{D_q^h(z)}{\pi\langle q_\perp'^2\rangle} e^{-\frac{q_\perp'^2}{\langle q_\perp'^2\rangle}}. \tag{1.47}$$

This gives for Eq. 1.45

$$\frac{d^5\sigma}{dx_{Bj}dQ^2dzd^2\mathbf{q}'_T} \propto \sum_q \frac{\alpha^2 e_q^2}{Q^4} f_q(x_{Bj}) D_q^h(z) b e^{-b\mathbf{q}_T'^2} \tag{1.48}$$

where $f_q(x_{Bj})$ are the classical PDFs, $D_q^h(z)$ are the so-called fragmentation functions, which gives the probability for a struck quark of flavor q to yield the hadron h carrying the energy fraction z, and b is the slope parameter of the $\mathbf{q}_T'^2$ distribution, presumed to be exponential. Integrated on the transverse momentum of the hadron, the cross section can be written under the following convenient form:

$$\frac{d^3\sigma^{ep\to ehX}}{dx_{Bj}dQ^2dz} = \frac{d^2\sigma^{DIS}}{dx_{Bj}dQ^2} \times D_q^h(z), \tag{1.49}$$

which allows to write the fragmentation functions:

$$\begin{aligned} D_q^h(z) &= \frac{1}{\sigma^{DIS}(x_{Bj},Q^2)} \frac{d^3\sigma^{ep\to ehX}}{dx_{Bj}dQ^2dz} \\ &= \frac{1}{N^{DIS}} \frac{dN^h}{dz} \end{aligned} \tag{1.50}$$

where N^{DIS} is the predicted DIS counting rate, and dN^h is the number of counts of the hadron h carrying a fraction of the energy reaction comprised between z and $z+dz$.

Fragmentation functions are generally extracted from e^+e^- annihilation. Their parameterization frequently takes the form [43, 44]

$$D_q^h(z) \propto z^{\beta_1}(1-z)^{\beta_2}, \tag{1.51}$$

and they are normalized by

$$\int dz D_q^h(z) = \langle N_h \rangle, \tag{1.52}$$

with $\langle N_h \rangle$ the average multiplicity of the hadron h in inclusive process or in e^+e^- annihilation process.

1.5.2 Achievements for semi-inclusive pion production

Due to the theoretical ingredients it includes, SIDIS is a strong test for quark-parton model. Let us review in this sub-section experimental achievements and improvements of SIDIS. We focus on this review on semi-inclusive electroproduction of pions.

The work of McPharlin *et al.* [45], studying inclusive π^0 production in the kinematic range $1.8 < Q^2(\mathrm{GeV}^2) < 8.5$ and $0.06 < x_{Bj} < 0.25$, clearly gives credit to the quark model. On one the hand, their data confirms the factorization illustrated on Fig. 1.13 and in equations (1.49) and (1.50). On the other hand, their data exhibit a Q^2 and a x_{Bj} scaling of the fragmentations functions in their kinematics. Their data are summarized on Fig. 1.14 (extracted from [45]).

On contrast with these data, the work of Aubert *et al.*, which scanned very wide kinematics ($2.0 < Q^2(\mathrm{GeV}^2) < 100.0$ and $0.02 < x_{Bj} < 0.4$) for charged hadron production with muons [46] exhibits scaling and factorization violations. These results however do not put Quark Parton Model in question, since these violations of scaling and factorization were qualitatively compatible with higher order QCD calculations. This work is summarized on Fig. 1.15.

The left (resp. right) panel of Fig. 1.15 shows $(1/\sigma^{DIS})d\sigma^{\mu p\to\mu hX}/dz$ as a function of Q^2 (resp. x_{Bj}). The dashed curve is the leading order scaling quark-parton model, the solid curve is the quark-parton model with scaling violation given by next-to-leading order QCD calculations. Both figures show the leading order quark parton model is violated by higher order QCD contributions.

The same collaboration published neutral pion production at $Q^2 > 3.0$ GeV^2, and $50.0 < W^2(\mathrm{GeV}^2) < 350.0$ [47]. These data exhibits the role of transverse momentum contributions ($\mathbf{q}'_T$). Indeed, according to equation (1.48), SIDIS cross sections depend on the transverse momentum of the hadron. This dependence has several sources:

- soft and hard higher order QCD contributions;
- the intrinsic transverse momentum of partons $k_{q\perp}$;

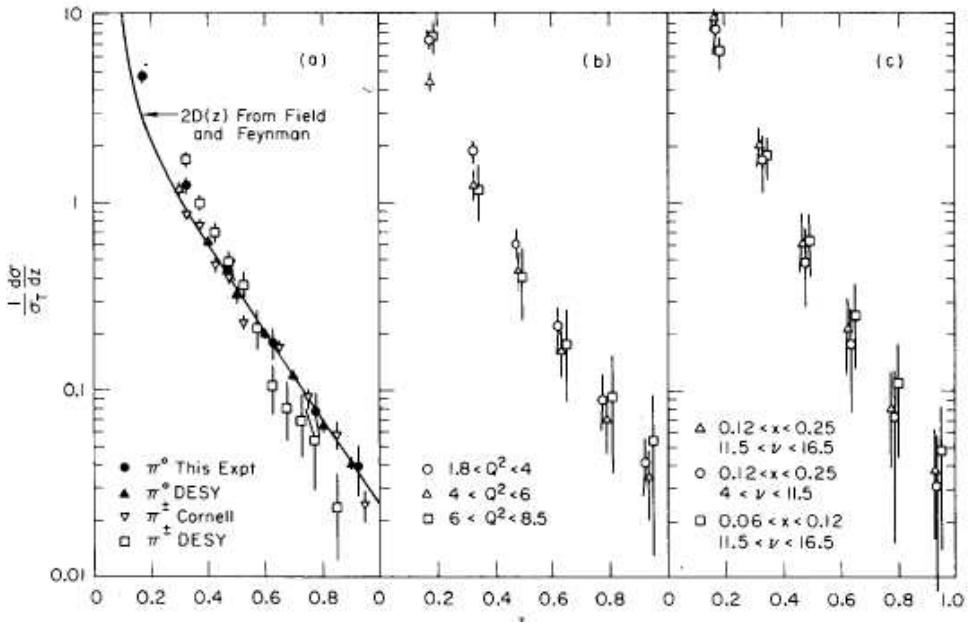

Figure 1.14: $(1/\sigma^{DIS})d\sigma^{ep\to eh\pi^0 X}/dz$ data from [45] as a function of z. Plot (a) demonstrates the factorization of the process, plots (b) and (c) exhibits the Q^2 and the x_{Bj} scalings respectively.

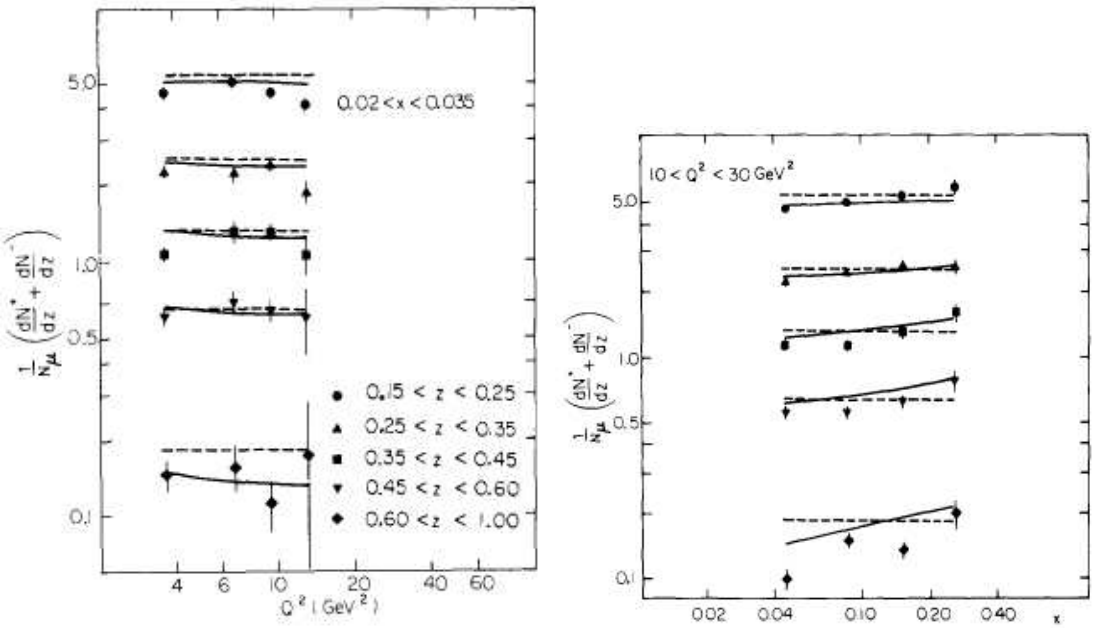

Figure 1.15: Part of the data from Aubert *et al.* published in [46]. On the left panel is plotted $(1/\sigma^{DIS})d\sigma^{\mu p\to\mu hX}/dz$ as a function of Q^2. On the right is plotted $(1/\sigma^{DIS})d\sigma^{\mu p\to\mu hX}/dz$ as a function of x_{Bj}. In both cases the curves are the predictions of the quark-parton model at leading order (dashed curves) and next-to-leading order (solid curves).

- a transverse momentum transfer occuring with the quark hadronization $q'_\perp$.

These two last quantities are generally modeled by gaussian distributions G_T writing $G_T(p_T) \propto \exp -p_T^2/\langle p_T^2\rangle$ for any transverse momentum distibution p_T implied in a SIDIS process. As well, the parameter b in equation (1.48) could be identified as $b = 1/\langle \mathbf{q}_T'^2\rangle$.

The work published in [47] emphasizes the need of intrinsic transverse momentum

of the partons. Fig. 1.16 shows $(1/\sigma^{DIS})d\sigma^{\mu p\to\mu\pi^0 X}/d\mathbf{q}'_T$ as a function of $\mathbf{q}'_T$, with its different contributions estimated with the Lund model [48]:

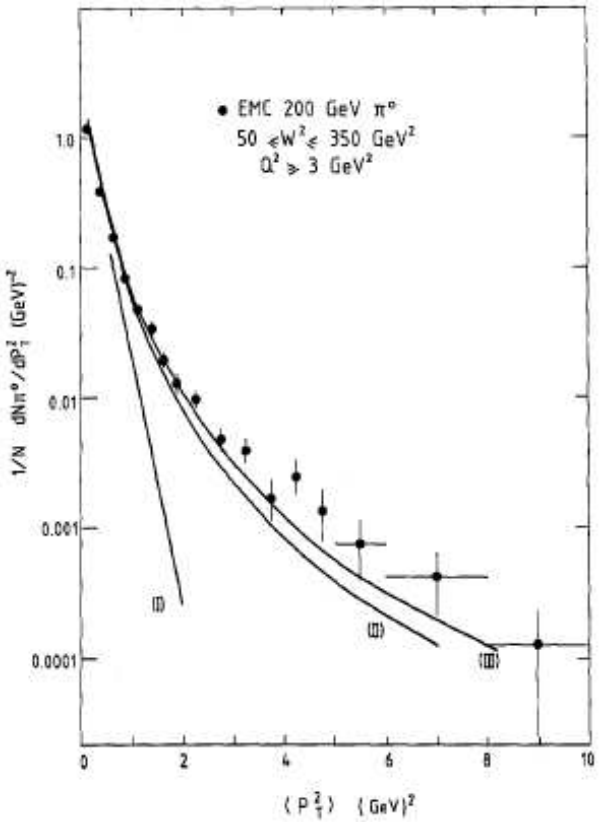

Figure 1.16: $(1/\sigma^{DIS})d\sigma^{\mu p\to\mu h\pi^0}/d\mathbf{q}'_T$ as a function of $\mathbf{q}'_T$ extracted from [47]. The solid curves represent the calculations of the Lund model model including different contributions to the global $\mathbf{q}'_T$ dependence (see text).

- (I) contribution of $q'_\perp$;
- (II) contribution of $q'_\perp$ plus QCD soft and hard processes;
- (III) contribution of $q'_\perp$ plus QCD soft and hard processes plus $k_{q\perp}$.

The slopes of the gaussian distributions of $k_{q\perp}$ and $q'_\perp$ were fixed, respectively, to $\langle k^2_{q\perp}\rangle = 0.19$ GeV^2 and $\langle q'^2_\perp\rangle = 0.31$ GeV^2. Thus, the non-Gaussian behaviour is given essentially by hard QCD contributions, but the intrinsic transverse momentum of the parton cannot be neglected for a good description of the data. According to the authors, (III) is equivalent to the contribution of $q'_\perp$ added only to hard QCD processes and $k_{q\perp}$, but with $\langle k^2_{q\perp}\rangle = 0.64$ GeV^2.

Assuming isospin invariance, the charged pion production cross section on the proton should be equal to the neutral pion production cross section on the proton, or, in other words, the study of $\ell p \to \ell\pi^0 X$ should be equivalent to $\ell p \to \ell\pi^\pm X$. Airapetian *et al.* [49] measured electroproduction of charged and neutral pions at $k = 27.5$ GeV, $1.0 < Q^2(\text{GeV}^2) < 7.5$, and $0.04 < x_{Bj} < 0.25$ in order to test isospin invariance. They compared their data to [45] and [46, 47] with the help of Q^2 evolution. They also compared the relative multiplicities in order to test isospin invariance.

Their data are in qualitative agreement with [45, 47]. Their conclusions concerning scaling and factorization violations are the same as [46]. The interesting result they point out is the violation of isospin invariance at $z > 0.7$, where charged pion multiplicities become significantly higher than neutral pion multiplicities (Fig. 1.17). This violation

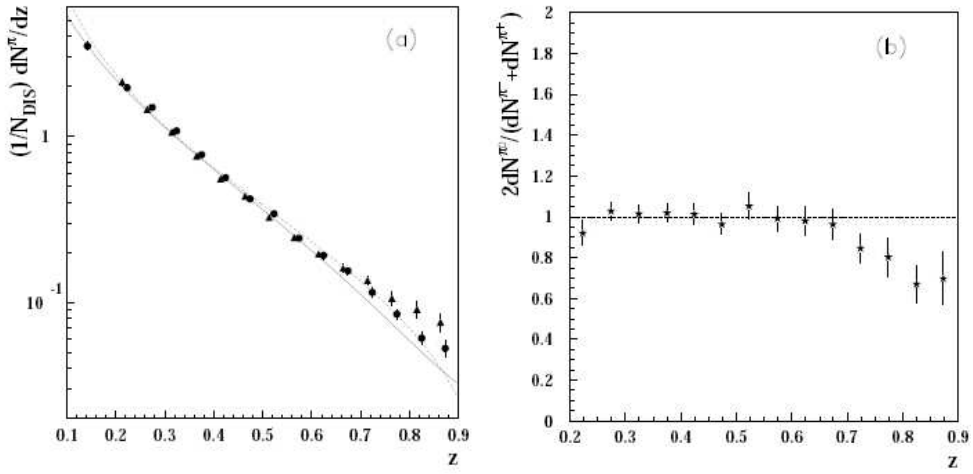

Figure 1.17: Data from Airapetian *et al.*, extracted from [49]. On the left are the multiplicities of charged (solid triangles) and neutral (solid circles) pions, as a function of z. The curves are different fragmentation models. Charged pions data starts to disagree with these models when $z > 0.7$ whereas neutral pion remains in rough agreement with these models as long as $z < 0.8$. The ratio $2dN^{\pi^0}/(dN^{\pi^+}+dN^{\pi^-})$ (right) appears to be in perfect agreement with 1 for $z < 0.7$, and decreases significantly beyond.

of isospin invariance at high z is similar to the scaling violation which is observed in the same kinematics.

To reproduce experimental data at high-z, Berger introduced a high-z scale-breaking term, which modifies the fragmentation functions in the following way [50]:

$$D_q^h(z,Q^2) = D_q^h(z) + \frac{2}{9}\frac{\langle k_{q\perp}^2 \rangle}{Q^2}. \tag{1.53}$$

At high z, the fragmentation function becomes very small (see equation (1.51)), and the scale-braking term dominates.

After this description of semi-inclusive processes, let us focus on the information this type of process could bring about proton structure. We will see in the next sub-section that SIDIS enables to access richer information on proton structure than simple DIS.

1.5.3 An introduction to transverse momentum distributions

This sub-section is devoted to the observables of the nucleon structure which can be accessed via SIDIS.

The previous subsection pointed out that only models with intrinsic transverse momenta of quarks could reproduce experimental results. Starting from this statement, SIDIS could then be described in the following way (we took the example of the SIDIS modelization by Anselmino *et al.* in [51]):

- the virtual photon strikes a quark with a transverse momentum $k_{q\perp}$; the probability of this interaction is given by $f_q(x, k_{q\perp})$;
- the struck quark hadronizes into the hadron h, and this hadronization occurs with a transfer of transverse momentum $q'_\perp$ relative to the direction of the struck quark after its interaction with the virtual photon; the probability of this hadronization is, assuming a quark of flavor q, $D_q^h(z, q'_\perp)$;
- the hadron h is finally measured with a transverse momentum $\mathbf{q}'_T$ relative to the direction of the virtual photon.

A scheme of this process is available on Fig. 1.18.

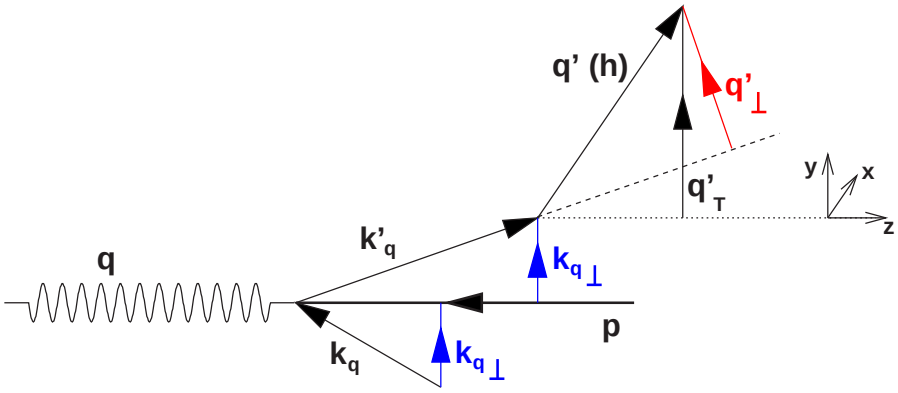

Figure 1.18: Schematic description of SIDIS, as modelized in [51]. Note the momentum transfer relevant of the hadronization occurs with respect to the direction of the struck quark.

The interesting information for the hadron is extracted from the primordial virtual photon-quark interaction. Indeed, the probability is not given by the classical parton distributions $f_q(x)$, but by a modified parton distribution, $f_q(x, k_{q\perp})$, which takes into account the transverse momentum of the quark. This quantity is precisely the Transverse Momentum Distribution (TMD) evoked above.

TMDs give access to a three-dimensionnal picture of the proton. They provide correlated informations on transverse and longitudinal momentum of the quark. TMDs could for instance give tomographic pictures of the nucleon [52].

There are several TMDs (eight at leading twist), which are accessible through processes with different polarization states of the quark and the nucleon [52]. We give in Table 1.1 all possible polarization states and the corresponding TMD which could be accessed. In the following, we only focus on TMDs which are accessible with unpolarized quarks, *i.e.* f_1 and $f_{1T}^\perp$, which are the most studied TMDs to date.

The unpolarized TMD f_1 gives the leading order of SIDIS process with both quark and nucleon unpolarized. The total unpolarized quark distribution $f_{q/p}(x, k_{q\perp})$ is given by the unpolarized TMD f_1:

$$f_{q/p}(x, k_{q\perp}) = f_1^q(x, k_{q\perp}). \tag{1.54}$$

Integrated on quark transverse momentum, f_1 yields the parton distribution

$$\int d^2 k_{q\perp} f_1^q(x, k_{q\perp}) = f_q(x). \tag{1.55}$$

pol. state		q			
		U	L	T	
N	U	f_1		$h_1^\perp$	
	L		g_1	$h_{1L}^\perp$	
	T	$f_{1T}^\perp$	g_{1T}	h_1	$h_{1T}^\perp$

Table 1.1: Twist-2 TMDs expressed referring to the quark q and nucleon N polarization states (columns, and rows, respectively; U: Unpolarized, L: Longitudinal, T: Transverse).

This is why the 5-fold differential SIDIS cross section (which is integrated on transverse momenta of partons) is written in terms of PDFs in equation (1.48). This doesn't mean however that the information on the initial parton is lost, it is integrated in the global q'_T dependence. The initial transverse momentum of the parton has even some supplementary consequences on the expression of the 5-fold differential SIDIS cross section. Indeed, such as in DIS (see equation (1.20)), SIDIS processes can be expressed as a sum of elementary electron-single quark interactions. This elementary interaction actually keeps the memory of the initial transverse momentum, and calculations (which are well detailed in [51]) naturally introduce a dependence in $\cos\phi_h$. This dependence in $\cos\phi_h$ is called Cahn Effect [53]. We finally get the following expression for the SIDIS cross section, which is valid at the order of $\mathcal{O}(k_{q\perp}/\sqrt{Q^2})$:

$$\begin{aligned}\frac{d^5\sigma^{ep\to ehX}}{dx_{Bj}dQ^2dzd^2\mathbf{q}'_T} = \sum_q \frac{2\pi\alpha^2 e_q^2}{Q^4} f_q(x_{Bj}) D_q^h(z) \Big[1+(1-y)^2 \\ - 4\frac{(2-y)\sqrt{1-y}\langle k_{q\perp}^2\rangle z\mathbf{q}'_T}{\langle q'^2_T\rangle\sqrt{Q^2}}\cos\phi_h\Big]\frac{1}{\pi\langle q'^2_T\rangle}e^{-\frac{q'^2_T}{\langle q'^2_T\rangle}}\end{aligned} \tag{1.56}$$

with $y = (p\cdot q)/(p\cdot k)$ and where $\langle \mathbf{q}'^2_T\rangle = \langle q'^2_\perp\rangle + z^2\langle k^2_{q\perp}\rangle$ gives the gaussian dependence of the cross section relative to the transverse momentum of the measured hadron.

The nucleon-polarized TMD $f_{1T}^\perp$, the so-called Sivers function is accessed through semi-inclusive deep inelastic scattering on a transversely polarized nucleon [54]. The total unpolarized quark distribution is given, for a polarized nucleon $p^\uparrow$:

$$f_{q/p^\uparrow}(x,k_{q\perp}) = f_1^q(x,k_{q\perp}) + \frac{1}{2}f_{1T}^{q\perp}(x,k_{q\perp})\mathbf{S}_T\cdot(\hat{p}\times\hat{k}_{q\perp}) \tag{1.57}$$

where, within [51] conventions, $\hat{p}$ is the direction of the proton (tri)momentum, $\hat{k}_{q\perp}$ is the direction of the quark in the transverse plane, and $\mathbf{S}_T$ is the proton transverse polarization vector. Note that $\mathbf{S}_T\cdot(\hat{p}\times\hat{k}_{q\perp})$ isolates the component of the parton function which is dependent on the component of the quark momentum perpendicular to the plane defined by the proton momentum and spin. It introduces the azimuthal dependence of the hadron, relative to the struck quark plane. Eq. (1.57) implies that to access the Sivers function, we need to measure:

$$f_{1T}^\perp(x,k_{q\perp})\mathbf{S}_T\cdot(\hat{p}\times\hat{k}_{q\perp}) = f_{q/p^\uparrow}(x,k_{q\perp}) - f_{q/p^\downarrow}(x,k_{q\perp}). \tag{1.58}$$

Thus the Sivers function can be accessible with SIDIS proton spin asymmetry, also called Target Spin Asymmetry (TSA). The TSA is given by:

$$A = \frac{d\sigma^\uparrow - d\sigma^\downarrow}{d\sigma^\uparrow + d\sigma^\downarrow} \tag{1.59}$$

with $d\sigma^{\uparrow}(^{\downarrow})$ the SIDIS cross section on a up (down) polarized proton. Note that in contrast with the unpolarized TMD f_1, the Sivers function vanishes when integrated over quark transverse momentum.

For more details on TMDs, one can refer to [41, 42], and [51, 52, 53, 54].

Chapter 2

Experimental Setup

The π^0 data we analyse in this work have been recorded with the Hall A DVCS apparatus [55] at Jefferson Laboratory. We recall that this experiment is an electron-proton scattering on a fixed target, with production of a single π^0 which decays in two photons. We have in the final state a scattered electron, a π^0 giving two photons, and a recoil proton, making a total of three particles. Thus we need at least a double arm experiment to get enough constraints in the final state. A very accurate measurement of two particles out of three will give the quadri-momentum of the missing particle within a good experimental precision. The choice which has been decided for this experiment is to measure very accurately the electron and the two photons *i.e.* the π^0, and to detect the recoil proton, even though this information has not been used in this analysis. This choice was motivated by the optimization of the missing mass squared resolution which requires to measure the most energetic particles.

The first section is dedicated to the description of the electron accelerator of Jefferson Lab, which supplies the electron beam. In the second section, we give some details on the beam line instrumentation, which allows to monitor this beam. The target system which provides the fixed proton target is described in the third section. The fourth and fifth sections deal respectively with the spectrometer, its detector package and the electromagnetic calorimeter. A few informations are given on the proton array. These two detectors are dedicated to measure respectively the scattered electron and the two photons issued from the π^0 decay. Finally, we give few details on the data acquisition and the triggering of this experiment in section six.

2.1 Continuous electron beam accelerator facility

In this section, we are interested in the electron accelerator facility available at Jefferson Lab, also called Thomas Jefferson National Accelerator Facility (TJNAF). TJNAF site is located in Newport News, Virginia (USA). Since its creation in 1984, Jefferson Lab has been devoted to the study of the nuclear matter at intermediate energies (up to 6 GeV), at the interface between nuclear and particle physics. It includes several facilities, such as the Continuous Electron Beam Accelerator Facility (CEBAF), which we are particularly interested in, the Free Electron Laser (FEL) facility, and the Computer Center (CC) dedicated to on-site data analysis and lattice QCD calculations.

CEBAF is a continuous wave accelerator, able to deliver a high-current electron beam to three experimental halls (Hall A, B, and C) simultaneously. We give some details about the setup and the specifications of this machine which make it an ideal tool to

study physics with high-precision. A more complete and detailed review of CEBAF is available in [56].

The basic arrangement of CEBAF is a pair of identical linacs positioned "head-to-tail", and connected together with half-circle shaped recirculation arcs. Each linac is composed of 20 cryomodules, and each cryomodule is composed of 8 radio-frequency cavities cooled by superfluid ^{4}He. Each recirculation arc is composed of several dipoles and quadrupoles. The schematic layout of CEBAF is available in Fig. 2.1. This pair of linacs is served

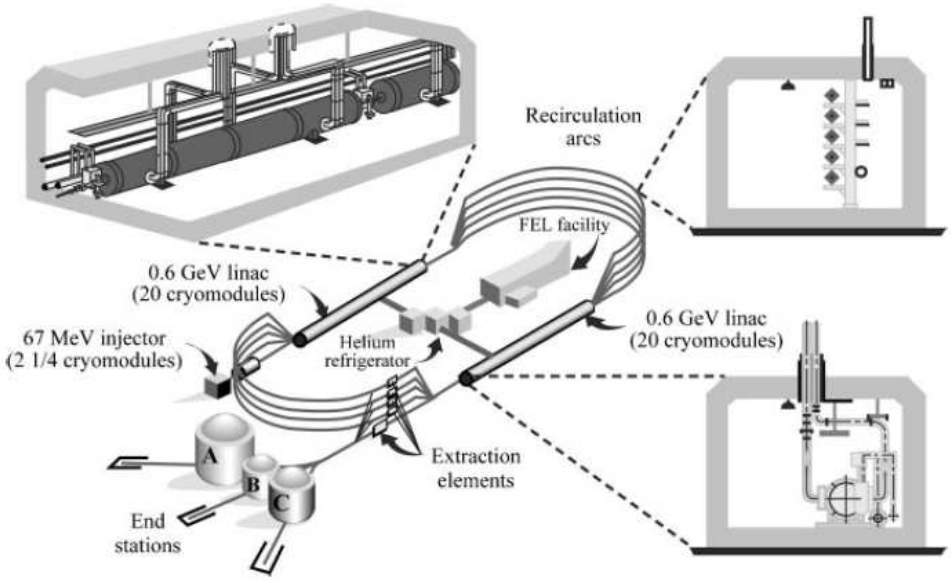

Figure 2.1: Schematic overview of CEBAF setup. A more detailed view of a cryomodule is available on the left top of this figure. Sectional views of the cryomodules (bottom right) and the recirculation arcs (top right) are also available.

by a 67 MeV/c injector. This primary beam is accelerated by the so-called north linac, recirculated by a first "north to south" arc, and re-accelerated by the so-called south linac, thus executing one pass. At the end of the south linac, the beam can either be distributed to the experimental halls (A, B, and C) or recirculated. Thanks to four "south to north" and five "north to south" recirculation arcs at total, the beam is able to execute up to five pass, reaching at most ten times the energy of what would provide a single linac. The maximal energy achieved so far is slightly above 6 GeV. The beam energy delived during our experiment was 5.7572 GeV.

Each hall receives its own beam, with the desired number of passes, independently of the beams received by the other halls. The superposition of the three individual beams to merge them into one is implemented at the injector level. The injector is made out of a photocathode gun which delivers photo-electrons from strained Ga-As illuminated with three polarized lasers (one per hall) working at 499 MHz each, for a total machine rate of 1497 MHz. These lasers create, at a 499 MHz rate, three interlaced bunches of electrons separated from each other by a 120° phase. These bunches have their owns properties (charge, ...) generally different from their immediate neighbours, but which is repeated every three bunches. Thus, and thanks to a system of adequately phased radio-frequency separators, the beam can be separated into three beams at the end of each pass, allowing to send the required energy and the required current for each hall. Hall A and C are

allowed to receive from 1 to 150 μA, whereas Hall B is allowed to receive from 1 to 200 nA. Our experiment ran at 2.5 μA.

CEBAF, besides its high duty, is also remarkable for the high beam polarizations it proposes. The beam polarization is generated by using a circularly polarized laser on the strained superlattice GaAs photocathode. The initial electron polarization is measured at the injector level with a 5 MeV Mott polarimeter. This polarization can then be oriented with a Wien filter. Thanks to this, the beam polarization can reach up to 85 %. For our experiment, the achieved polarization was about 75 %.

2.2 Hall A beamline instrumentation

Hall A is an experimental hall of TJNAF, dedicated to very high precision measurements. In order to minimize systematic errors on cross section measurements and more generally on any experimental observable, we need to have very precise information on the delivered beam including: position and direction, current, energy, and polarization. These informations are provided by the beamline instrumentation located on the beam path upstream the target. The layout of Hall A, with the relative location of the beam line instruments, is available on Fig. 2.2. We describe the standard beam monitoring, ensured by the Beam

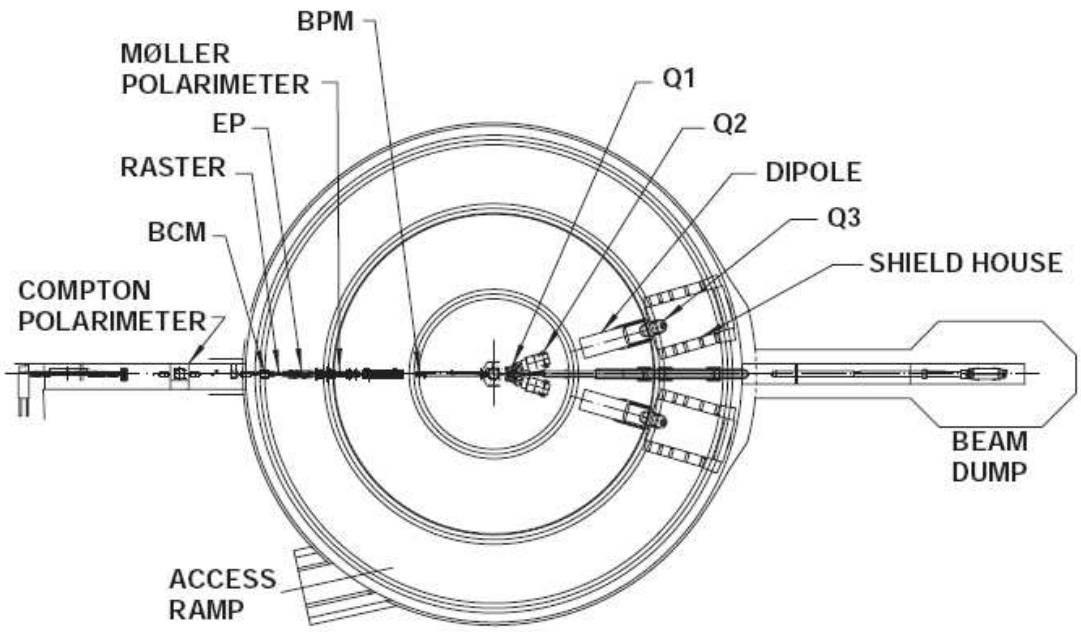

Figure 2.2: Schematic view from the top of Hall A with the layout of beamline instrumentation.

Current Monitor (BCM) and the Beam Position Monitors (BPMs). We give some details about the beam energy measurement, allowed by the ARC method on the one hand, and the "electron-Proton" (eP) device on the other hand. We finally focus on the polarimetry, which is also ensured by two independent polarimeters, the Compton polarimeter, and the Møller polarimeter. The beamline instrumentation is described within more details in [57].

2.2.1 Beam monitoring

We describe here the instruments providing information on the beam current and on the beam position and direction.

Beam Current Monitor

The measurement of the beam current is provided by the Beam Current Monitor (BCM). The BCM is composed of two radio-frequency cavities tuned to the same frequency as the beam (1497 MHz). The cavity is used in a passive mode in this case. The current passes through the cavity and excites the cavity modes, resulting in cavity responses *i.e.* voltage levels at the cavity outputs proportional to the current which passed through.

The BCM also includes a Unser monitor, which is a Parametric Current Transformer [58]. The Unser monitor can be calibrated by a wire passing through it where a known current is sent, making it able to provide an absolute reference. For unstability reasons however, this calibration cannot be performed continuously.

This apparatus, well enclosed in a temperature-stabilized magnetic shielding, provides a stable, low noise, non-invasive and absolute measurement of the beam current, at the $5 \cdot 10^{-3}$ accuracy level for currents as low as 1 μA.

Beam Position Monitors

The measurement of the position and the direction of the beam is ensured by two identical Beam Position Monitors (BPMs), which are located 7.524 m and 1.286 m upstream of the target. Each BPM is composed of four parallel antenna wires, parallel to the beam, and each in a plane at $\pm$ 45° to horizontal. Each pair of antennas provide a relative position information, thanks to the difference of current induced by the beam in each of the two antennas. With usual Hall A currents (from 1 μA), the measurement precision for the relative beam position is 100 μm.

To give absolute measurements of the beam position and direction, the BPMs need to be calibrated against complementary apparatus. These complementary devices are wire scanners called superharps, and located nearby the BPMs, and more precisely at 7.353 m and 1.122 m upstream of the target. They are surveyed absolutely with respect to the Hall A coordinates.

The full setup including BPMs and superharps provide absolute, non-invasive measurements with a typical accuracy of 140 μm for the beam position, and 30 μrad for the beam direction.

Note the beam position at the target can be changed by the raster, composed of two dipoles, in order to deviate the beam horizontally and vertically. Each dipole can change its polarity independently of the other, which makes the beam "scanning" the target. In this case, the beam is said to be rasterized.

2.2.2 Energy measurement

We focus in this subsection on the absolute beam energy measurement. There exist two independent methods to measure the beam energy. The so-called ARC method, which is a magnetic method, and the eP instrument, which was not used at the time of the experiment.

The ARC method is a magnetic method using the 34.3° deviation arc, which is necessary to bring the beam to Hall A, to measure precisely the beam energy [59, 60]. To drive smoothly the beam from the beam switch yard at the end of the south linac to the entrance of Hall A, there is a total of eight deviation dipoles, plus correction dipoles, quadrupoles and sextupoles, to make the deviation arc achromatic. The idea of the ARC method is to switch off the correction magnets, to have a dispersive arc which can be used as a spectrometer. The momentum (and the energy, assuming ultra-relativistic electrons) of the beam is thus given by

$$p_{\text{beam}}c = \frac{ec \int \vec{B} \times \vec{dl}}{\theta}, \tag{2.1}$$

with θ the actual bend angle of the beam and $\int \vec{B} \times \vec{dl}$ the field integral over the eight dipoles.

The measurement of the actual bend angle of the beam is provided by a set of wire scanners, such as the ones used for beam position measurement. The field integral over the eight dipoles is accessed by the measurement of the field integral of a ninth dipole, which is strictly identical to the eight magnets of the deviation arc.

The arc method thus provides an absolute beam energy measurement up to $5 \cdot 10^{-4}$ accuracy. Note there exists more accurate modes for the ARC energy measurement, but there are either invasive ($2 \cdot 10^{-4}$ accuracy) or relative ($1 \cdot 10^{-4}$ accuracy).

2.2.3 Polarization measurement

This subsection is dedicated to the polarimetry. Since a large part of the Hall A physics program uses polarized beams, very accurate polarization measurements are required. We give the main specifications and performances of the Møller and the Compton polarimeters. The first uses Møller scattering of the beam electrons on atomic electrons, whereas the second uses Compton scattering of the beam electrons on a photon beam.

Møller polarimeter

As its name denotes, the Møller polarimeter exploits Møller scattering of the polarized electrons of the beam on a magnetized target with polarized atomic electrons [61]. It includes, in addition to the target, a collimator composed of a steel plate, a spectrometer composed of three successive quadrupoles and a dipole at the end, followed by a lead glass calorimeter splitted in two arms which measure the scattered and recoil electrons in coincidence. A schematic view of the Møller polarimeter is available in Fig. 2.3.

The Møller scattering cross section depends of the polarization of the beam P^{beam} and of the target P^{target}:

$$\sigma^{\vec{e}\vec{e}\to ee} \propto \left[1 + \sum_{i=X,Y,Z} (A_{ii} P_i^{\text{beam}} P_i^{\text{target}})\right]; \tag{2.2}$$

with X, Y, Z the projections of the polarizations in the laboratory coordinates, and A_{ii} the analysing power in these directions, depending on the scattering angle in the $\vec{e}\vec{e}$ center-of mass frame $\theta_{\text{scat}}^{CM}$. The polarization is measured taking advantage of analysing power A_{ZZ}. The analysing power A_{ZZ} is maximal at $\theta_{\text{scat}}^{CM} = 90°$, and is equal to $A_{ZZ}^{\max} = 7/9$. The spectrometer selects a kinematic range $75° < \theta_{\text{scat}}^{CM} < 105°$, and an azimuthal angle ϕ_{scat}^{CM} range $-5° < \phi_{\text{scat}}^{CM} < +5°$.

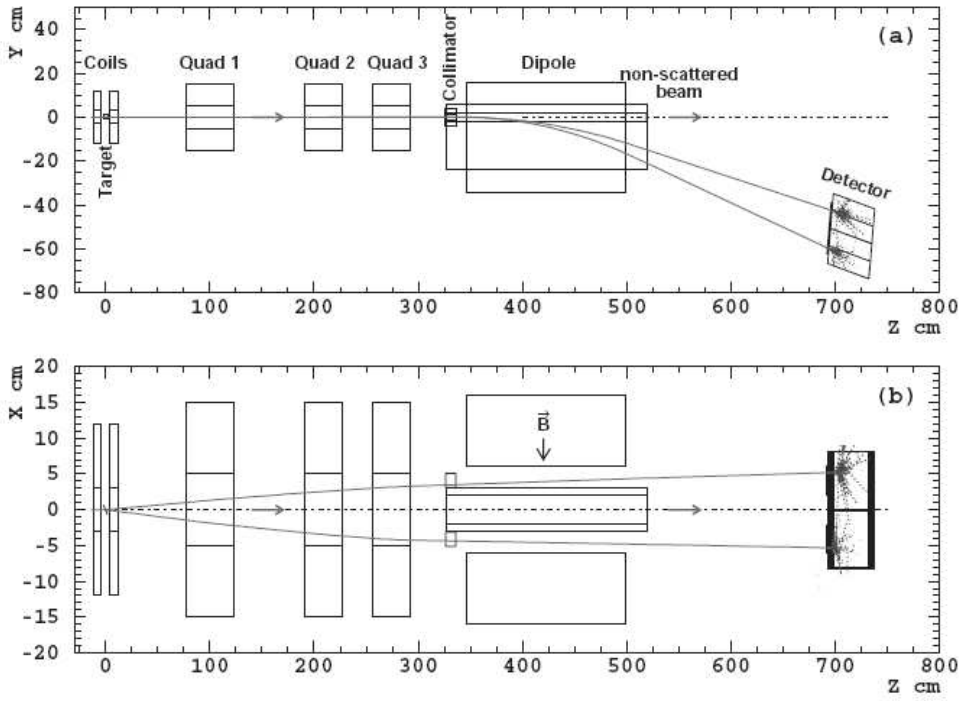

Figure 2.3: Schematic view of the Møller polarimeter, (a) shows a right side view, (b) a top view. The two displayed trajectories correspond to a simulated Møller scattering at $\theta_{\rm scat}^{CM} = 80°$ and $\phi_{\rm scat}^{CM} = 0°$ (see text for definitions) in the spectrometer.

The Møller polarimeter provides absolute measurement of the polarization, and has the benefit of a very good analysing power within its kinematic range. This allows to get 0.2 % statistical uncertainity within one hour data taking. However, the basic layout of the polarimeter (a target on the beam path) makes this measurement invasive. A rather large uncertainity comes from the target polarization. Moreover it is only able to run at very low current (0.5 μA typically). This forces to reduce the beam intensity at the injector, which might affect the beam polarization, thus increasing systematic uncertainities on the polarization measurement. Finally, the total accuracy provided by the Møller polarimeter on a polarization measurement is about 3 %.

Compton polarimeter

The Compton polarimeter exploits Compton scattering of the polarized electrons of the beam on a circularly polarized photon beam [62]. It is composed of a 0.85 m long optical Fabry-Perot cavity which contains the photon beam [63, 64]. A magnetic chicane of four dipoles is used to deflect the electron beam from the regular beam path to the cavity axis. The two beams cross over each other at the interaction point at the center of the cavity. An electron detector and a photon detector measure the scattered electron and the backscattered photon in coincidence. A schematic view of the Compton polarimeter is available in Fig. 2.4.

The photon beam is given by a Nd:YaG laser beam ($\lambda = 1064$ nm) delivering 230 mW of power. The polarization of this primary photon beam can be reversed by a rotable quarter-wave plate, and is better than 99 % for both positive and negative polarization. The Fabry-Perot cavity amplifies the power of this beam increasing the probability of an interaction. In optimal conditions, *i.e.* when the laser frequency is equal to the cavity

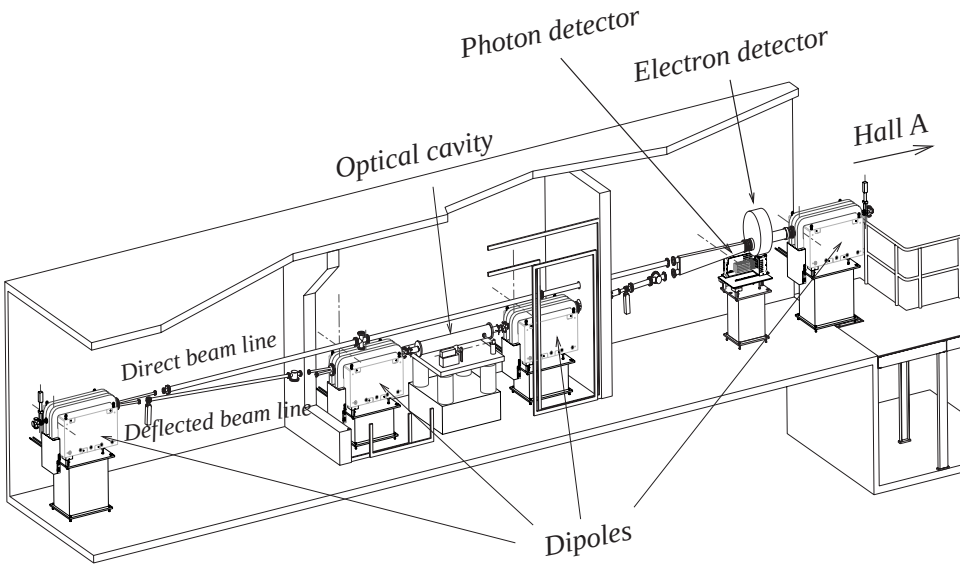

Figure 2.4: Schematic layout of the Compton polarimeter.

resonance frequency, the primary beam power is multiplied by up to 7300.

The magnetic chicane is composed of two dipoles upstream of the cavity to deflect the beam, and two dipoles downstream of the cavity to merge the beam back to the regular beam path. The third dipole plays the role of a spectrometer for the scattered electrons, which have transfered a part of their energy to the photon. They are more deviated by the dipole than the spectator electrons, and are measured by the electron detector, composed of four silicon micro-strips detectors, which reconstruct the electron trajectories, thus giving access to their momentum. The backscattered photons are measured by a lead glass calorimeter. The beam polarization is accessed by the Compton counting rate asymmetry between positive and negative photon polarizations.

The Compton polarimeter gives an absolute, non invasive measurement of the beam polarization. It is able to run at usual beam currents without perturbing the beam. Thus, despite a very low analysing power, the statistical uncertainity can be brought to a negligible level, since continuous measurements can be done while running the experiments. However, on the one hand, the Compton counting rate asymmetry is very sensitive to the beam position, and on the other hand, the detectors resolutions can easily be degraded by a huge background resulting, for example, from a bad beam tune. Finally, in usual conditions, the total achieved polarization measurement accuracy is 2 % [65].

2.3 Target system

Several targets are available in Hall A, for different physics purposes. For proton physics, there are liquid hydrogen targets. To study neutron physics, liquid deuterium targets and gaseous helium targets are available. The study of the ^{16}O nucleus is also possible thanks to a Waterfall target.

For the DVCS/π^0 experiment, only the liquid hydrogen and deuterium targets were used. We briefly describe the scattering chamber specific to DVCS/π^0 experiment, and

we give some details about the cryogenic target system.

2.3.1 Scattering chamber

The role of the scattering chamber is to provide a vacuum space around the target in order to minimize electromagnetic interactions of the outgoing particles, especially the electron, with the air. For the DVCS/π^0 experiment, we used a custom scattering chamber. The DVCS scattering chamber is a 1 cm thick aluminum 63.5 cm radius spherical shell. This thickness allows low energy protons down to 305 MeV/c to go through it. To minimize the interactions of the scattered electron with the chamber wall a 500 μm thick kapton window replaces the aluminum in front of the left HRS angular coverage used for DVCS. The angular coverage of this window is between 16.5° and 49.5° in the horizontal plane taking the downstream beam axis as 0°, and $\pm$4° in vertical relative to the horizontal plane. The spherical form of this chamber respects the spherical symmetry of the reaction, and makes the energy loss independent of the scattering angle, within the angular dependence of the particle momentum.

2.3.2 Cryogenic target system

The cryogenic target system is composed of three independent cryogenic loops. The first loop is filled with liquid hydrogen (LH_2), the second with liquid deuterium (LD_2), and the third with gaseous ^{3}He or ^{4}He. Each of the cryogenic loops provide its cryogenic fluid to a target ladder, containing several targets stacked vertically, and which can be remotely moved to put in beam the desired target. The target ladder is composed of the following targets:

- a 4 cm long and a 15 cm long target cells filled with LH_2, which circulates continuously;
- another 4 cm long and another 15 cm long target cells filled with LD_2;
- a multifoil target, with seven 1 mm thick carbon foils, to calibrate the spectrometer optics;
- a 4 cm long and a 15 cm long dummy targets, identical to the standard targets but with no fluid circulating, to study the target wall effects;
- a cross hair 1 mm thick aluminum target to measure the beam position with respect to the target;
- a BeO target to visualize the beam spot at the target thanks to a camera;
- a 1 mm thick carbon foil;
- and an "empty target", which actually corresponds to put nothing on the beam path, to reduce radiation on the detectors when the beam is tuned, or when the beam characteristics are measured by invasive measurements.

The standard and dummy cryotargets cells are 63.5 mm in diameter and are made out of aluminum. The side walls of the cells are 178 μm thick and the entrance and exit windows are respectively 71 μm and 102 μm thick. The operating temperatures and pressures of

the LH_2 and LD_2 are 19 K, 0.17 MPa and 22 K, 0.15 MPa, respectively. Under these conditions, the respective densities of the LH_2 and LD_2 are 0.0723 $g \cdot cm^{-3}$ and 0.167 $g \cdot cm^{-3}$.

These targets can operate up to a beam intensity of 130 μA without boiling. For such high currents however, the beam has to be rasterized to avoid local boiling. Given the following expression of the luminosity $\mathcal{L}$:

$$\mathcal{L} = \frac{I}{e} L_{\text{targ}} \frac{\mathcal{N}_A}{M_H} \rho_H, \tag{2.3}$$

with I the beam current, L_{targ} the target length, $\mathcal{N}_A$ the Avogadro number, M_H the atomic mass number of the hydrogen atom, and ρ_H the density of the hydrogen, the maximal luminosity with the hydrogen target is $5 \cdot 10^{38}$ $cm^{-2}s^{-1}$. With the 2.5 μA current used for DVCS/π^0 experiment, the raster is not needed, and the achieved luminosity is $1.0 \cdot 10^{37}$ $cm^{-2}s^{-1}$.

2.4 High Resolution Spectrometers (HRS) and detector package

The High Resolution Spectrometers (HRS) are part of the standard Hall A instrumentation. There are two identical HRS (see Fig. 2.2):

- the electron arm (or left HRS or HRS-L), on the left side of the Hall, is usually dedicated to the electron three-momentum measurement;
- the hadron arm (or right HRS or HRS-R), on the right side of the Hall, is usually dedicated to the proton three-momentum measurement.

In the DVCS/π^0 experiment, the left HRS has been used to provide a very accurate measurement of the scattered electron. The right HRS has been used to register single counting rates for a relative monitoring of the luminosity.

We give the broad lines of the design of the HRS, and we list their characteristics and performances. We also characterize the spectrometer optics. The detector package used to equip the electron arm in order to identify and measure the electron three-momentum is finally described.

2.4.1 Design, characteristics and performances

The spectrometers are composed of four superconducting magnets, three quadrupoles **Q** and one indexed dipole (with field gradient) $\mathbf{D_n}$, in the configuration $\mathbf{QQD_nQ}$ (see Fig. 2.5). These magnets are laid on a motorized support, which can be moved circularly relatively to the center of the Hall. This support also carries on top of the HRS the shield hut which hosts the detector package and shields it against radiations.

The first quadrupole, $\mathbf{Q_1}$, focusses the trajectories in the vertical plane. The second one, $\mathbf{Q_2}$, focusses the trajectories in the horizontal plane. The contribution of both expands the spectrometer acceptance. The dipole is here to provide the dispersion which is necessary to measure the particle momentum. This dispersion is improved by a 45° bending angle of the dipole. The magnetic field gradient of the indexed dipole focusses in

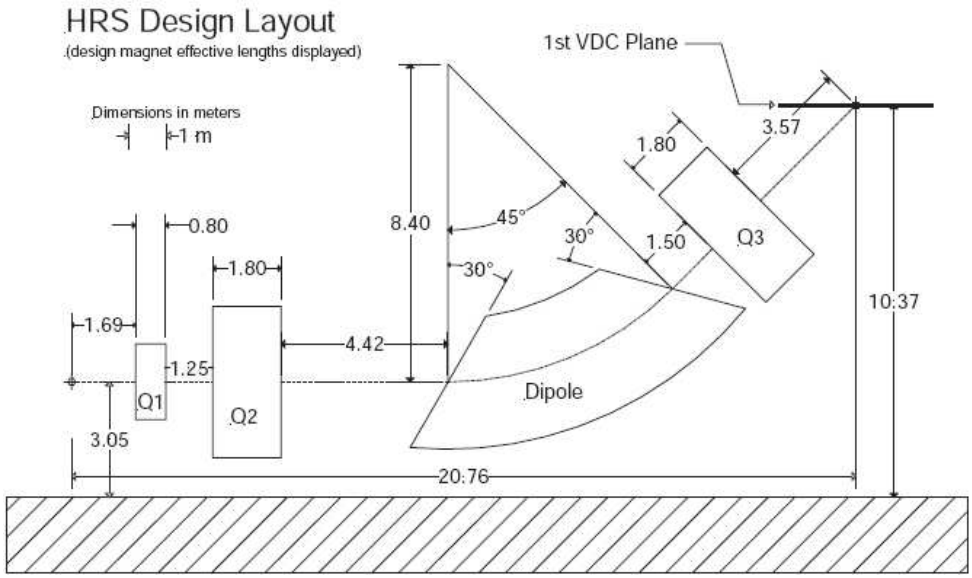

Figure 2.5: Schematic layout of the spectrometer magnets with their measurement.

the dispersive plane, thus giving the system a focal plane. The last quadrupole, $\mathbf{Q_3}$, defocalizes the trajectories in the dispersive plane to maximize magnification in the dispersive plane. These magnets are described within extensive details in [66].

The presence of this quadrupole after the dipole also allows to achieve simultaneously a good horizontal position and angular resolution. The optical length (*i.e.* the length of the central ray) is 23.4 m, and the achieved dispersion at the focal is (12.4 m)/($\delta p/p$). All these characteristics allow the spectrometers to achieve the performances listed in Table 2.1. This table reveals the excellent resolutions on the particle momentum ($\mathcal{O}(10^{-4})$) and direction ($\mathcal{O}(10^{-3})$ rad), that allows to reconstruct the electron three-vector very accurately.

2.4.2 Optics

The optics of the spectrometer defines the path of a particle through the magnets from the target (where the particle is "produced") to the focal plane (where the particle is detected). As in light optics, the central ray is defined by the minimal path which could be taken by a particle.

Optics description

The trajectory of a particle in the spectrometer is defined, in the TRANSPORT formalism [67], by the following vector:

$$\mathbf{x} = \begin{bmatrix} x \\ \theta \\ y \\ \phi \\ l \\ \delta \end{bmatrix}, \tag{2.4}$$

with x the displacement in the dispersive plane of the trajectory relative to the central ray, $\theta = p_x/p_z$ is the tangent of the angle the trajectory makes with the central ray in the

Momentum	
Range	0.3 GeV $< p_{\mathrm{HRS}} <$ 4.0 GeV
Acceptance	-4.5 % $< \delta p/p_{\mathrm{HRS}} <$ 4.5 %
Resolution	$1.0 \cdot 10^{-4}$
Direction	
Range	$12.5° < \theta_{\mathrm{HRS}} < 150°$
Acceptance	$\pm$30 mrad (Horizontal)
	$\pm$60 mrad (Vertical)
Resolution	0.5 mrad (Horizontal)
	1.0 mrad (Vertical)
Vertex	
Acceptance	($\pm$5.0 cm)/ $\sin\theta_{\mathrm{HRS}}$
Resolution	(1.0 mm)/ $\sin\theta_{\mathrm{HRS}}$

Table 2.1: HRS-L characteristics and performances. p_{HRS} is the "central" momentum, defined by the field generated by the dipole. $\delta p = p_{\mathrm{meas.}} - p_{\mathrm{HRS}}$, with $p_{\mathrm{meas.}}$ the measured momentum of the particle. θ_{HRS} is the angle of the HRS central trajectory relative to the beam line direction.

dispersive plane, y and ϕ are homologous to respectively x and θ in the non-dispersive plane, l is the difference between the trajectory length and the central ray length, and $\delta = \delta p/p_{\mathrm{HRS}}$, defined in the previous subsection. If one considers the coordinates of this trajectory at a precise point, the quantity l is the result of the integration over trajectory before, and thus is not available directly.

The trajectory vector of the particle at the target $\mathbf{x}_{tg}$ is transfered to the trajectory vector at the focal plane $\mathbf{x}_{fp}$ by a transfer matrix $\mathcal{T}_{tg,\,fp}$: $\mathbf{x}_{tg} = \mathcal{T}_{tg,fp}\mathbf{x}_{fp}$. The explicit first order representation of this equation is

$$\begin{bmatrix} x_{fp} \\ \theta_{fp} \\ y_{fp} \\ \phi_{fp} \\ \delta_{fp} \end{bmatrix} = \begin{bmatrix} -2.48 & 0 & 0 & 0 & 12.4 \\ -0.15 & -0.40 & 0 & 0 & 2.04 \\ 0 & 0 & -0.40 & -1.30 & 0 \\ 0 & 0 & 0.54 & -0.78 & 0 \\ 0 & 0 & 0 & 0 & 1.0 \end{bmatrix} \times \begin{bmatrix} x_{tg} \\ \theta_{tg} \\ y_{tg} \\ \phi_{tg} \\ \delta_{tg} \end{bmatrix}, \tag{2.5}$$

where all coefficients are in "natural units" (meters, radians, fractions of δ or dimensionless). Note that at first order the dispersive variables (x, θ, δ) are completely decorrelated from the non dispersive variables (y, ϕ). In the dispersion plane, the spectrometer optics is point-to-point, that means to a x_{tg} corresponds only one x_{fp} at δ constant, or, in other words, x_{fp} does not depend on θ_{tg}. In the non-dispersive plane, the optics is neither point-to-point nor parallel-to-point (y_{fp} independent of y_{tg}), in order to obtain simultaneously a good resolution on y and ϕ.

In practice, the spectrometer measures x_{fp}, θ_{fp}, y_{fp}, ϕ_{fp}, but δ_{fp} is not measured. The variables at the vertex are accessed by inversing $\mathcal{T}^{-1}_{tg,\,fp}$. However, we have five variables to determine, and we have four measured quantities. To resolve this, we fix x_{tg}, and we compute the other variables at the target, including y_{tg} which gives access to the vertex. With the vertex and the beam direction determined by the BPMs, we compute the "real" value of x_{tg}, which allows to perform some corrections on the other dispersive variables.

To minimize the systematic errors on such a procedure, one needs to consider the spectrometer optics beyond the first order. The complete spectrometer optics is written

under the following tensorial form [68]:

$$y_{tg} = \sum_{j,k,l} Y_{j,k,l} \theta_{fp}^j y_{fp}^k \phi_{fp}^l; \tag{2.6}$$

$$\theta_{tg} = \sum_{j,k,l} T_{j,k,l} \theta_{fp}^j y_{fp}^k \phi_{fp}^l; \tag{2.7}$$

$$\phi_{tg} = \sum_{j,k,l} P_{j,k,l} \theta_{fp}^j y_{fp}^k \phi_{fp}^l; \tag{2.8}$$

$$\delta_{tg} = \sum_{j,k,l} D_{j,k,l} \theta_{fp}^j y_{fp}^k \phi_{fp}^l; \tag{2.9}$$

where $Y_{j,k,l}$, $T_{j,k,l}$, $P_{j,k,l}$ and $D_{j,k,l}$ are polynomials in x_{fp}. If one considers, for example, $Y_{j,k,l}$:

$$Y_{j,k,l} = \sum_{i=1}^{M} C_i^{Y_{j,k,l}} x_{fp}^i \tag{2.10}$$

which gives for y_{tg}:

$$y_{tg} = \sum_{j,k,l} \sum_{i=1}^{M} C_i^{Y_{j,k,l}} x_{fp}^i \theta_{fp}^j y_{fp}^k \phi_{fp}^l; \quad i+j+k+l \leq 4. \tag{2.11}$$

The $C_i^{Y_{j,k,l}}$ are determined experimentally by various procedures of optics calibration and are accessibles through databases.

Optics calibration

Several calibrations procedures have to be done for the full optics determination. We will give only two of these procedures, although they are several others. The procedures for optics calibrations are decribed in detail in [68]. The calibration of the transport tensor is done by the sieve slit. The sieve slit is a tungsten plate with a 2-D lattice of holes (Fig. 2.6 on the left). During a sieve slit calibration, the slit is put in the so-called sieve plane, and stop all electrons except at the location of the holes. The distribution of holes in the sieve plane then may be seen in the focal plane (Fig. 2.6 on the right). Since we know their location in the sieve plane, these data bring some constraints on the transportation. Some holes have different sizes, for anambiguous identification in the focal plane.

Other constraints on the optics may be obtained *via* the multifoil target calibration. This target is composed of seven 1 mm-thick foils of carbon (see last section), which position relative to the center of the hall is known very precisely. One may than reconstruct the vertex distribution. This distribution shows very acute peaks (Fig. 2.7). The comparison of the reconstructed positions of these peaks and the actual positions of the foils gives other constraints on the optics tensor. Again, these are only two examples of procedures for the optics calibration.

2.4.3 Detector package for HRS-L

The detector package is located on top of the spectrometer, after the magnets. Its purpose is to measure and identify the particles. It is composed of many subdetectors which can

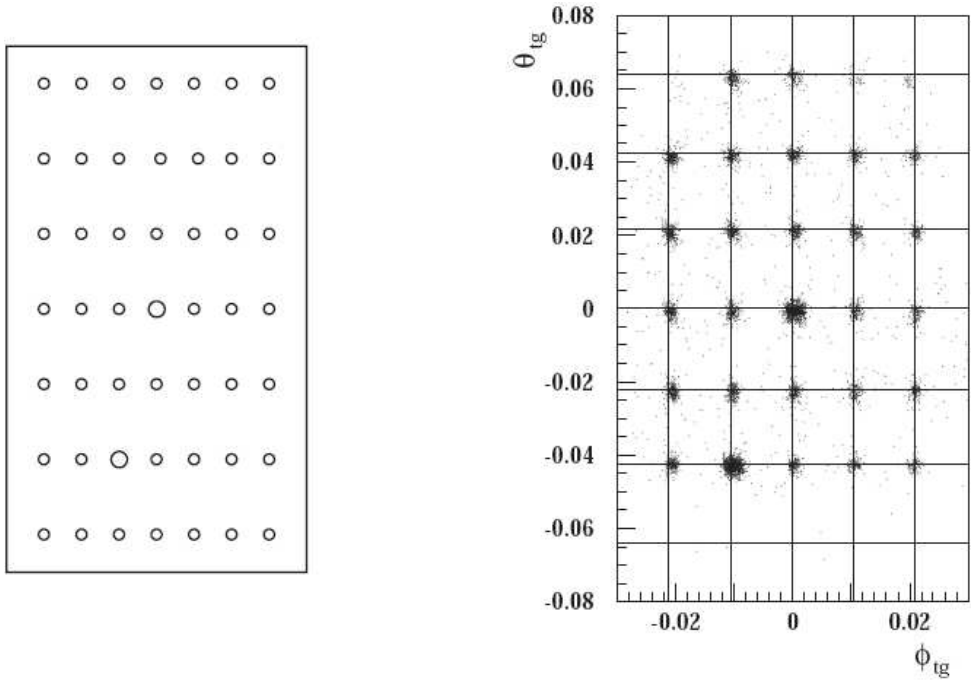

Figure 2.6: Left: Drawing of the sieve slit. Note the two large holes that allow an unambiguous identification of each hole. Right: reconstruction of the sieve slit holes in the focal plane.

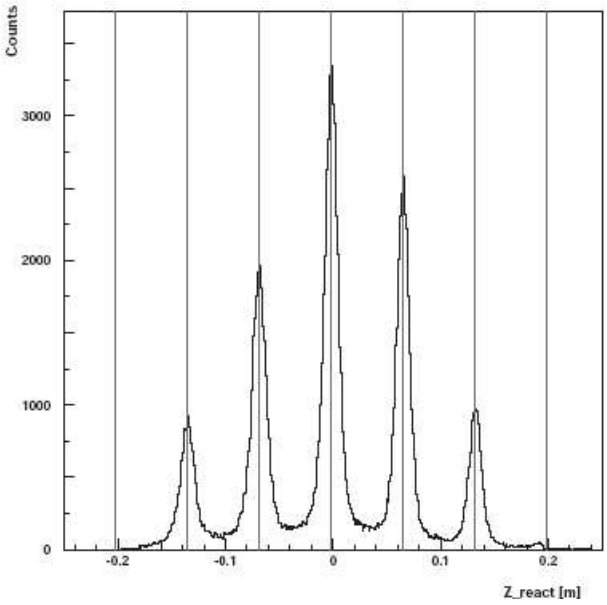

Figure 2.7: Vertex distribution obtained with the multifoil target, at a 16° angle from the beam line. The vertical lines are the expected reconstructed positions of the foils.

be different from one experiment to another, depending on the specific requirements of the experiment. An overall picture of the detector package is shown on Fig. 2.8.

We describe the detector package we used for the left HRS during the DVCS/π^0 experiment, in order to measure the electrons and to separate them from pions. This package includes Vertical Drift Chambers (VDCs), two planes of scintillators S1 and S2, a CO_2 gas Čerenkov counter, and the so-called pion rejector. The right HRS was just equiped with the VDCs and S1 and S2m.

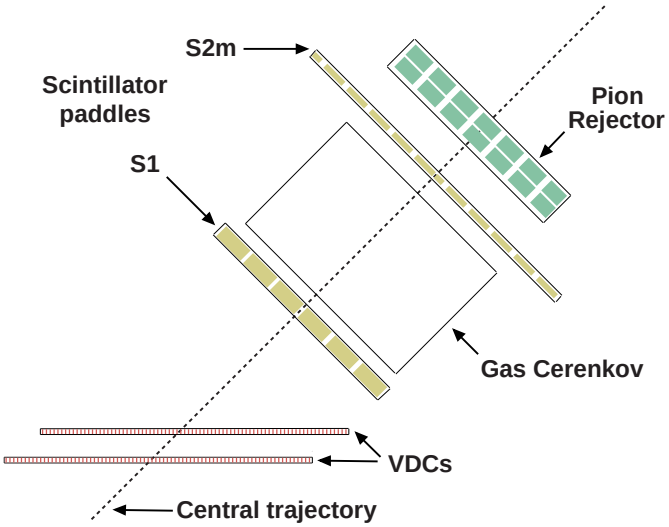

Figure 2.8: Schematic layout of the Left HRS detector package as we used it for the DVCS/π^0 experiment.

Vertical drift chambers

The Vertical Drift Chamber (VDCs) provide information on the particle trajectory. They are called "vertical" beacuse their purpose is to measure the dispersion in the vertical plane. Their are two VDCs in each spectrometer, and each VDC is composed of two wire planes in UV configuration. The wire planes are oriented 90° from each other, and their orientations are rotated 45° with respect to the dispersive and non-dispersive planes. They are set up in the horizontal plane, thus making a 45° angle with the spectrometer central ray. The layout of the VDCs is shwon Fig. 2.9.

Each plane is composed of 368 sense wires, spaced 4.24 mm apart. They are immersed in a gas mixture of argon (62 %) and ethane (38 %). The electric field applied between the anaode wires and the cathod planes are 4.0 kV. We owe to these specifications a position resolution $\sigma_{x,\,y}$ of about 100 μm and an angular resolution $\sigma_{\theta,\,\phi}$ of about 0.5 mrad. More details on the VDCs are available in [69, 70].

Scintillators S1 and S2m

The role of the scintillators is to deliver a trigger signal for the spectrometer. To this purpose, there are two scintillators, S1 and S2m planes separated 2 m from each other and laid perpendicularly to the spectrometer central ray. S1 is composed of 6 overlapping 5mm thick plastic scintillator paddles, and each paddle is read by two photomultipliers tubes (PMTs), *i.e.* one on each side of the paddle. S2m is composed of 16 plastic scintillator paddles. The combined fast responses of the plastic scintillator and of the photomultipliers give a time resolution of about 0.30 ns per plane. The trigger is given by the coincidence of S1 and S2m. Note that in order to measure the ineffiencies of the trigger given by the two scintillators, it is possible to do the coincidence between one of the scintillators and the Čerenkov counter.

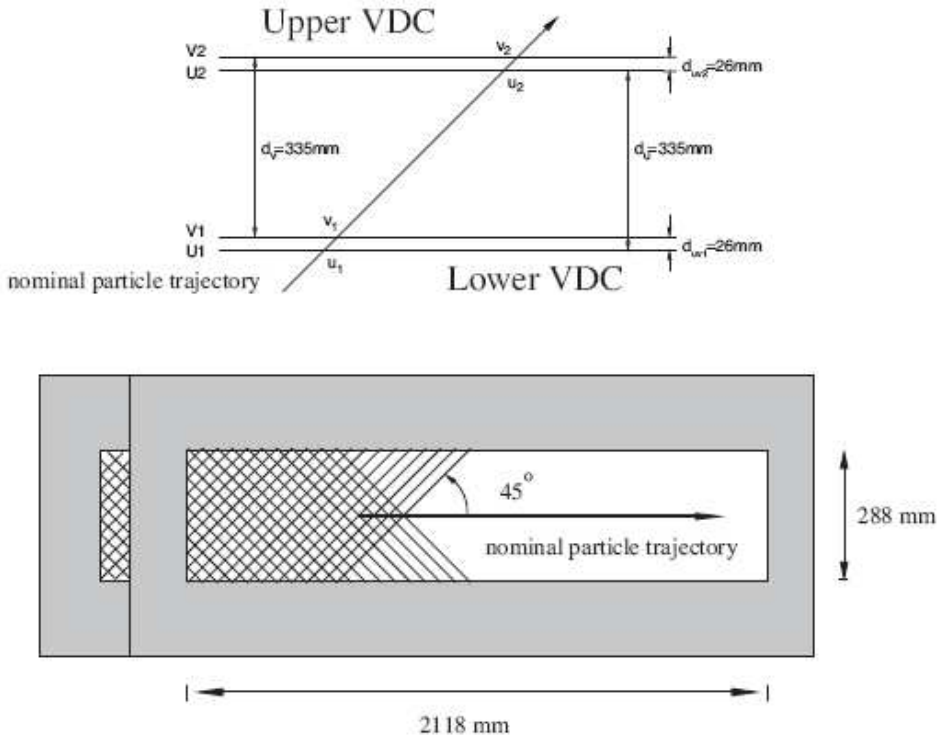

Figure 2.9: Schematic layout of the VDCs. Side view of the wire planes setup (top). Top view showing the orientation of the wire planes. On both views are available the projection of the central ray (bottom).

Gas Čerenkov counter

The purpose of the gas Čerenkov counter is the electron identification. It is located between S1 and S2. It is filled with CO_2 at atmospheric pressure, with a refraction index of $n = 1.000449$ at 589.2 nm (sodium D line). The threshold of this counter for electron detection is 0.017 GeV, whereas it is 4.8 GeV for pion detection, allowing a 99 % efficiency for electron identification. The light produced by an electron passing through the gas is collected by ten spherical mirrors, each read by a PMT. In the left HRS, the particle has to cross 80 cm of gas, leading to an average of seven photoelectrons by event. The signal of this counter is obtained by summing the signals of all PMTs. More details on the CO_2 Čerenkov counter can be found in [71].

Pion rejector

The pion rejector is made of two layers of 34 lead glass blocs, used as shower detectors. The lead glass blocks are $15 \times 15 \times 30(35)$ cm and laid perpendicularly to the spectrometer central ray (see Fig. 2.10). The rejection is based on the difference of energy deposited by an electron or a pion in the lead glass.

The combination of the pion rejector and of the Čerenkov counter provides a pion suppression at the order of 10^5.

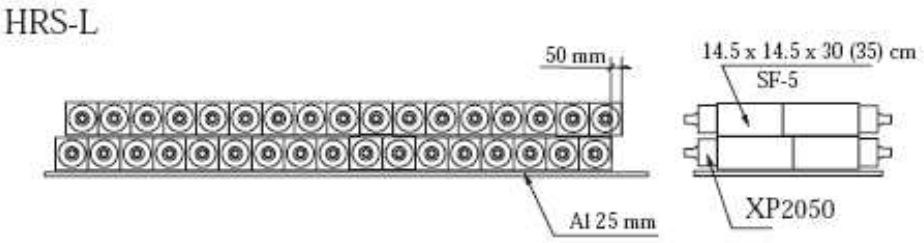

Figure 2.10: Schematic setup of the pion rejector of left HRS.

2.5 PbF_2 electromagnetic calorimeter, plastic scintillator proton array

The PbF_2 electromagnetic calorimeter and the proton array are specific to the DVCS/π^0 experiment. The purpose of the calorimeter is to reconstruct the two photons issued from the π^0 decay (or the DVCS photon). The proton array has been conceived to detect the recoil proton.

To obtain good constraints on the reaction kinematics, the calorimeter has to have a good resolution on both energy and position. To maximize the acceptance within reasonable costs and channel multiplicities, this calorimeter has to be located as close as possible to the target (actual distance was 1.1 m from the target). The kinematics constrained the calorimeter to be very close to the beam line (down to 14.8° for Kin3). To fit in the small space available close to the beam and near the target, the calorimeter needs to be very compact. At small angles relative to the beam line, the calorimeter is exposed to a high flux of Møller electrons. Because of this, the calorimeter needs to be resistent to radiation, and to be as much insensitive as possible to both electromagnetic and hadronic low energy background.

We give the respective geometries of the electromagnetic calorimeter and of the proton array. We briefly describe the setup which supports the calorimeter and the proton array. Then, we focus on the calorimeter. We highlight the properties of lead fluoride, and give a detailed description of a single calorimeter element. We also describe the custom electronic device which has been developed for an accurate readout of the signals issued from each calorimeter channel.

2.5.1 Electromagnetic calorimeter and proton array geometries

The calorimeter meets the requirements of compactness thanks to the use of lead fluoride (PbF_2). The electromagnetic calorimeter is a 11 (horizontal) $\times$ 12 (vertical) matrix (132 at total) of $3 \times 3 \times 18.5$ cm^3 lead fluoride (PbF_2) elements. The overall transverse dimensions are 33×36 cm^2. These dimensions allow a global acceptance in $t_{min} - t < 0.3$ GeV^2 for $H(e, e'\pi^0)p$.

The proton array is composed of one hundred 30 cm long organic scintillators blocks, arranged in five layers following a "3/4 crown" geometry (see Figs. 2.11 and 2.12). This geometry has been adopted to ensure compatibility with the beam line. The angular coverage is (relative to the virtual photon direction) from 18° to 38°. The minimal angle is imposed by the compatibility with the calorimeter, whereas the maximal angle ensures

the acceptance in t to be roughly the same as the calorimeter acceptance.

2.5.2 Calorimeter/proton array support and setup

The calorimeter support lays on the BigBite stand, which allows the circular motion of the calorimeter. It is composed of a steel support equiped with rails, in order to allow the retraction of the calorimeter (Fig. 2.11). This device is long enough to move back

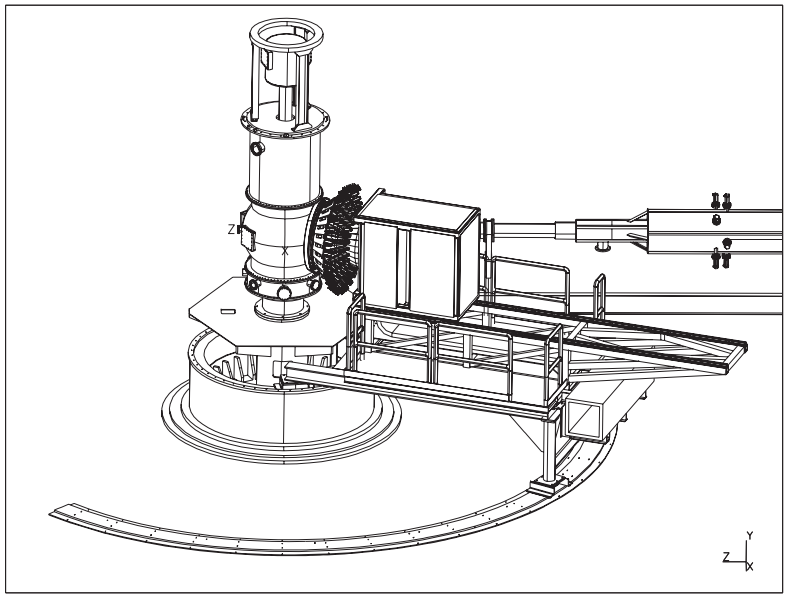

Figure 2.11: Schematic view of the calorimeter and the proton array support. We distinguish (from bottom to top) the Bigbite stand (which carries the patch rack), the rail support, and the black box.

the electromagnetic calorimeter front surface to a 5.5 m distance from the target. The possibility of retraction is essentially used for calibration purposes. The photomultipliers gain monitoring uses the so-called XY table, a plane equiped with Light Emitting Diodes (LED), to illuminate every single block of the calorimeter. For several reasons, this device may not be in front of the calorimeter during data taking. The XY table is moved in front of the calorimeter during beam-off periods, but the calorimeter has to be pulled 45 cm away from its usual position to perform this operation. The elastic calibration of the calorimeter (see Chapter 4) also requires it to be retracted as much as possible from the target to be performed in optimal conditions. Note that the calorimeter support also carries the patch panel, where are plugged all high-voltage and readout cables.

The calorimeter and the XY table are hermetically enclosed in a black box in order to isolate them from the ambient light (Fig. 2.12). This black box carries the proton array, and slides on the rails for the calorimeter motion. To maximize the hermeticity, the high-voltage and the readout cables are passed through a S-shaped cable tray

2.5.3 PbF_2 properties and block design

As we pointed out before, the calorimeter owes its compact dimensions to the use of lead fluoride (PbF_2). The physical properties of the PbF_2 are listed in table 2.2. Referring to this table, the blocks are 20 PbF_2 radiation lengths long. The Molière radius being

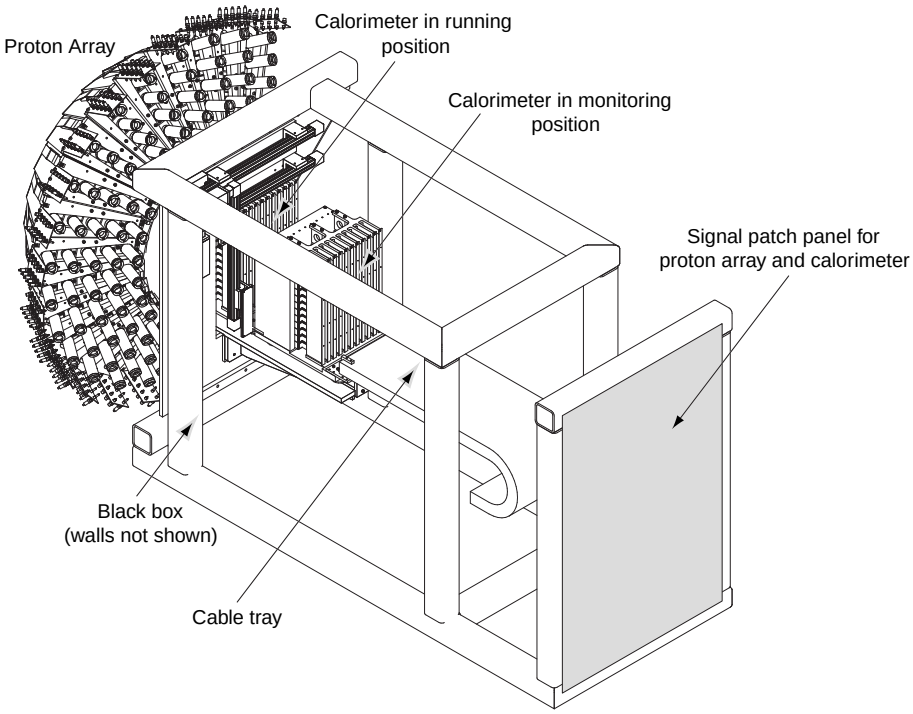

Figure 2.12: Schematic backside view of the calorimeter and the proton array setup in the black box, with the cable tray. The calorimeter is shown in running and monitoring position. Note the patch panel shown on this early version of the design has been removed to be put behind the Calorimeter support (Fig. 2.11)

density ρ	$7.77\ \mathrm{g \cdot cm^{-3}}$
refraction index n	1.818
radiation length X_0	0.93 cm
Molière radius $R_{\mathcal{M}}$	2.22 cm

Table 2.2: Physical properties of the lead fluoride. The refraction index is given at 400 nm wavelength.

slightly inferior to the block width, the electromagnetic shower is generally included in 9 blocks at most. Thus, for a photon which goes in an inner calorimeter block, 99 % of the shower energy is contained in the calorimeter.

The lead fluoride is also a pure Čerenkov radiator. Compared to scintillation which has a certain decay constant, Čerenkov radiation is immediate. This allows a fair improvement of the response width compared to a mixed scintillator/Čerenkov radiator such as the lead tungstate $PbWO_4$. The direct consequence of this feature is a better resolution and, coupled with the fast electronics (see next subsection) a better separation of the pile-up. Moreover, the refraction index of $n \sim 1.8$ "naturally" cuts particles with $\beta < c/n = 0.56$ such as, for instance, electrons of less than 345 keV, leading to a drastic reduction of the sensitivity to low energy background (Fig. 3.8).

The average radiation hardness of the PbF_2 blocks produced by SICCAS is acceptable [72], with a transparency level above 60 % after a dose of 10^5 Gy in the 400-600 nm wavelength range (Fig. 2.13). However, during the experiment, some blocks at random positions in the calorimeter showed to be more affected by the radiation, with a huge

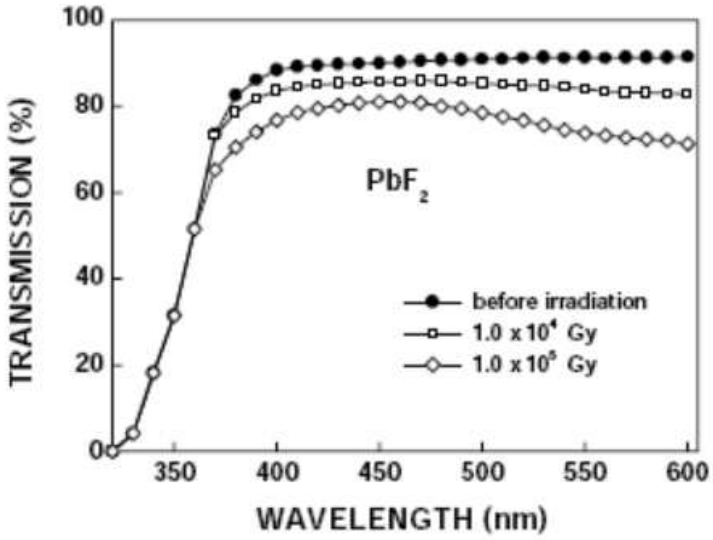

Figure 2.13: Transparency of a PbF_2 block as a function of the wavelength at different levels of radiation doses (10^4 Gy and 10^5 Gy with a ^{60}Co source); figure extracted from [72]).

decrease of the transparency (darkening). This is probably due to a poorer block quality for some particular batches of crystals.

The granularity of the calorimeter allows to reconstruct the photon position with an accuracy of 2 mm (see Chapter 4.1.2). To prevent the optical light generated by Čerenkov radiation to go from one block to another, the blocks are wrapped in Tyvek© (internal wrapping) and Tedlar© (external wrapping). The amount of light collected by the PMT is about 1000 photoelectrons per GeV deposited in a block (estimated by Monte Carlo simulations).

The Čerenkov light are read by Hamamatsu R7877 10 dynode stages PMTs, based on R5900U/R7600U [73]. These PMTs are very fast with a rise time of about 1 ns, and very compact, with overall dimensions of $25.7 \times 25.7 \times 22 mm^3$, with a sensitive surface of 18×18 mm^2. The quantum efficiency is about 15 %.

The PMTs and the blocks are held together with a system composed of a cubic carved copper piece which receives the PMT and a front hole plate linked together with two brass foils. The front plate is equiped with two screws to fit to the actual PbF_2 block length.

2.5.4 Analog ring samplers

It is important to achieve both a high timing resolution and a high background rejection power. A 1 GHz digitizing circuit was constructed at Clermont Ferrand for this experiment. The Analog Ring Samplers (ARS) [74] have been conceived in order to achieve an accurate readout of the calorimeter (and of the proton array) signals, which rise time is at the order of few nanoseconds. These devices allow to record the analog waveform of the PMT output signal as it would be available on a 1 GHz oscilloscope (see Fig. 2.14).

An ARS consists in an array of 128 capacitors cells, which continuously samples the signal. The signal is successively integrated over a short period δt by each of the cells. When 128 δt have been sampled, the new signal is overwritten on the "128-δt old" signal. The sampling frequency is fixed at 1 GHz, but the front-end electronics has a bandwidth of about 300 MHz.

To record the signal sampled by the capacitor cells, a STOP signal must be sent to

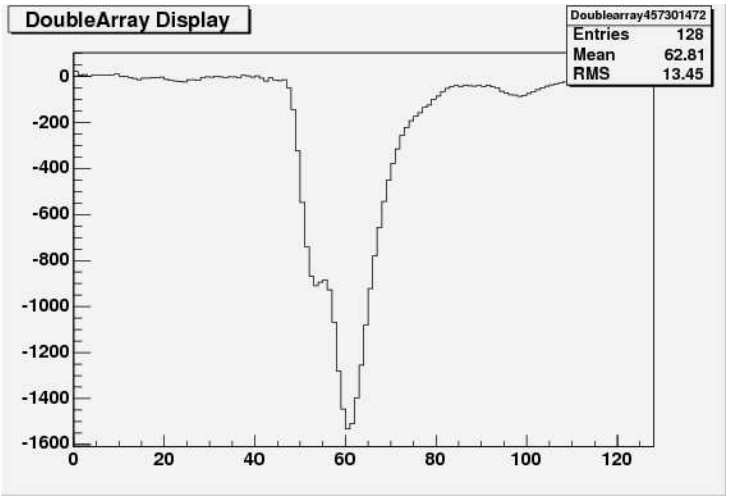

Figure 2.14: Example of ARS output with a two-pulse pile-up in the calorimeter.

the ARS, and the cells switch from the "track state" (continuous sampling) to the "hold state" (the sampling is stopped and the last recorded signal is held in the capacitor). Then, the following depends on the signal sent to the ARS by the trigger:

- if the ARS receives a VALID signal, the signals in the capacitors are read and digitized. For the ARS used for the DVCS experiment, this digitization times is 128 μs;
- if the ARS receives a CLEAR signal, the capacitors are fastly cleared. This operation lasts 500 ns.

The output signal of an ARS can be fitted offline. This is particularly useful for multipulse separation (see Fig. 2.14). The minimal Δt between two pulses to achieve separation depends on the separation algorithm accuracy (see Chapter 4). In practice, two pulses arriving with 6 ns delay can be separated.

2.6 Data Acquisition, DVCS Trigger

This section is devoted to data acquisition (DAQ) at CEBAF, and the specific trigger which has been developped for DVCS. Optimization of both is necessary to minimize the dead time and the data volume.

We describe the data acquisition at CEBAF within CEBAF Online Data Acquisition system (CODA) framework. We give the principle of the DVCS trigger, particularly at the calorimeter level.

2.6.1 Data acquisition with CEBAF online data acquisition system

The data acquisition has two main purposes. The first is to decide whether the event has to be recorded or not *i.e.* to manage the trigger. The second is to read out the detector signals and to record them. All these operations have to be performed as fast as possible to minimize the dead time.

At the software level, the DAQ is implemented, at Jefferson Lab, by CODA. CODA is able to handle most of commercially available electronic components, such as Fastbus, and VERSAModule Eurocard (VME) digitization devices (Analog Digital Converters (ADCs), Time-to-Digital Converters (TDCs), scalers), VME computer units (crates), Ethernet networks, and a Mass Storage tape Silo (MSS) for long-term data storage. The supported commercial software is the VxWorks operating system, which runs on Unix/Linux workstations.

The custom softwares needed to achieve DAQ goals are the Read Out Controllers (ROC), the Event Builders (EB), Event Recorders (ER) and Event Transfers (ET). The EBs, ERs and ETs are common to one experiment. The ROCs have to be implemented for each of the detectors we wish to use (one ROC per detector), and each ROC runs on its own VME crate. The ROC used for the left HRS has been fully implemented and tested years before the experiments, but we had to develop our own ROCs for the calorimeter and the proton array, including procedures that are able to read out ARS signals. Each VME unit running a ROC is connected, *via* a trigger interface, to the Trigger Supervisor (TS), which orders data read-out to the VME crate.

The trigger supervisor is a multifunction VME board that receives up to eight external trigger entries, T1 to T8. One can configure the trigger supervisor to order data read-out for a defined combination of triggers. While the ROCs process, the trigger supervisor tags the DAQ as BUSY. When the process is finally done, its new status is directly exchanged to the trigger supervisor, which inhibits all triggers to synchronize them with the ROCs. After this operation, the DAQ is ready to record a new event (DAQ ENABLE).

2.6.2 DVCS Trigger

The DVCS trigger is basically given by the coincidence of an electron (measured by the HRS) and at least one high energy photon (measured by the calorimeter). We describe the overall trigger scheme for DVCS, and we focus on the algorithm used to perform a good photon selection in the calorimeter.

DVCS trigger logic

The DVCS trigger scheme is represented in figure 2.15. The first step for DVCS event selection is the selection of the electron in the HRS. For this reason, we kept as much as possible from the standard trigger logic to build our own trigger logic.

As we already specified in subsection 2.4.3, the electron is detected by a AND coincidence between S1 and S2m ("T1" for the trigger supervisor), and a signal in the Čerenkov counter. The coincidence between one of the scintillators and the Čerenkov counter ("T2" for the trigger supervisor) is also considered. The timing of the event is given by the right PMT of S2m. In the DVCS experiment, the HRS trigger took about 150 to 160 ns to take a decision.

The AND of the spectrometer is submitted at the same time to the trigger supervisor and to a logic unit to which the calorimeter trigger module is enslaved. The calorimeter trigger module sends the STOP signal to the ARS, and the photon candidates are searched (see next subsubsection). If there is at least one good photon candidate, the DVCS trigger is sent to the trigger supervisor, which orders the read out. Else, the calorimeter trigger module sends the CLEAR signal to the ARS, forcing them to a fast clean up.

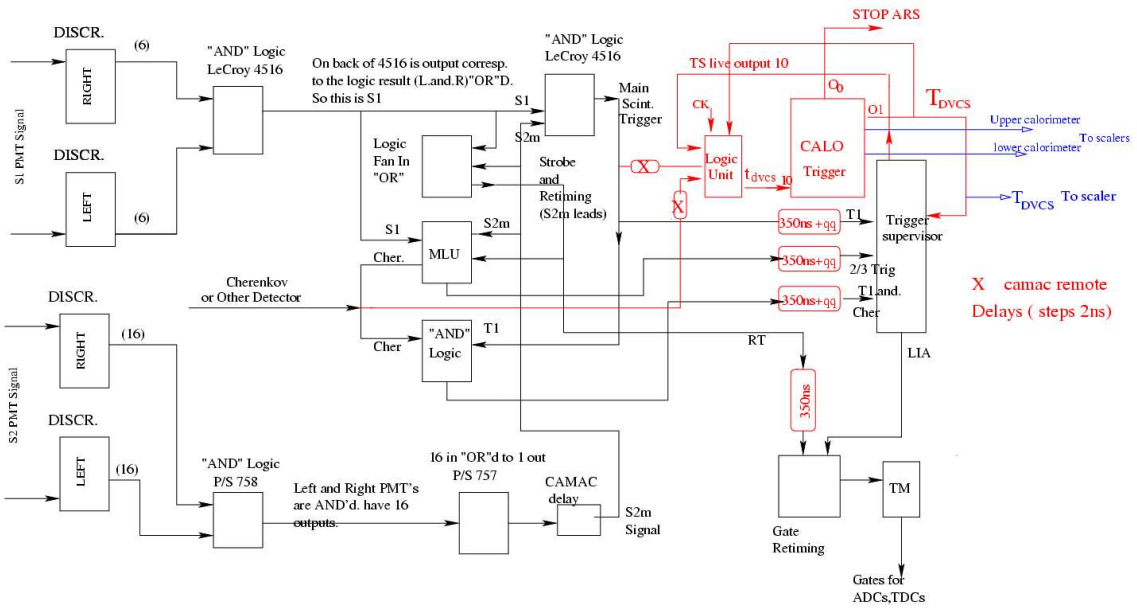

Figure 2.15: Overview of the DVCS trigger logic. The standard Hall A DAQ is represented in black. The modifications to the standard DAQ performed for this experiment are represented in red.

Since the selection of a good DVCS event depends uppermost on the electron selection, the signals issued from the calorimeter have to be delayed. This delay is implemented by 57 m long cables that go from the patch panel behind the calorimeter to the calorimeter trigger module, located in the shield hut at the top of the spectrometer.

DVCS/π^0 photon selection

We focus on the selection of pertinent physicis signal in the calorimeter. The position of the calorimeter, near the target and at a close angle from the beam line leads it to face a large electromagnetic background. Fortunately, this background is mostly composed of low energy particles, whereas the signal (high energy π^0 decay photons, DVCS photons) is at rather high energy. However, to fix an energy threshold on a single block does not suit. Indeed, the shower created by a photon of energy above 1 GeV is usually extended on 9 blocks. Even though 90 % of this energy will be located in the central block, the measurement of the amount of energy collected in the neighboring blocks is necessary to reduce the uncertainties on the photon on the one hand, and to improve the reconstruction of the photon position (see chapter 4) on the other hand. Thus, the threshold is not fixed on a single block, but on a 4-block cluster (see Fig. 2.16).

Practically, the photon trigger generation is made in two steps:

- the calorimeter channels are all digitized individually, using a 7 bit Fast ADC, which provides very fast digitized signals, with a time jitter which is smaller than 100ns;
- when all signals are digitized, the pedestals are subtracted on each channel, and neighbors channels are compared 4 by 4 (see Fig. 2.16).

If a group of four blocks collected an energy above 1.2 GeV (which is equivalent to 60 ADC channels), the AND signal is generated and sent to the trigger supervisor, in order to read out the corresponding ARS. Note that we used to read only the ARS corresponding to the hit cluster in order to save data volume and dead time due to the ARS read out.

11	23	35	47	59	71	83	95	107	119	131
10	22	34	46	58	70	82	94	106	118	130
9	21	33	45	57	69	81	93	105	117	129
8	20	32	44	56	68	80	92	104	116	128
7	19	31	43	55	67	79	91	103	115	127
6	18	30	42	54	66	78	90	102	114	126
5	17	29	41	53	65	77	89	101	113	125
4	16	28	40	52	64	76	88	100	112	124
3	15	27	39	51	63	75	87	99	111	123
2	14	26	38	50	62	74	86	98	110	122
1	13	25	37	49	61	73	85	97	109	121
0	12	24	36	48	60	72	84	96	108	120

9	9	8	10	9	10	8	9	8	8	10
11	10	11	11	9	12	11	9	9	8	9
9	8	9	9	9	8	8	8	9	6	9
9	9	10	9	8	9	7	8	9	10	9
9	8	8	10	9	10	8	8	7	17	8
9	8	8	9	9	9	8	9	5	4	12
9	8	8	9	9	10	11	8	8	7	10
9	10	9	15	9	9	12	9	41	15	5
9	9	9	9	10	9	9	7	14	12	10
9	9	8	8	9	10	8	10	10	8	12
9	10	10	9	9	9	9	8	7	9	9
9	8	9	9	9	9	10	7	8	8	8

Figure 2.16: Left: example of two overlapping 4-blocks clusters, in blue and red. Right: example of an event in the calorimeter. The energies of each channel are expressed in ADC channels. In this case, 4 clusters (highlighted by a yellow border) total more than 60 ADC channels, thus satisfying the trigger conditions.

Chapter 3

Calorimeter calibration

This chapter treats the calibrations of the PbF_2 electromagnetic calorimeter. There are two main types of calibrations: the hardware calibrations to ensure a good response of the PMTs of the calorimeter, and the software calibrations, which were necessary to correct some experimental effects such as, for instance, the background noise.

In the first section are described all calibrations methods which were applied during the experiment in order to optimize the calorimeter response. In the second section is presented the specific calorimeter calibration that I implemented for π^0 analysis. The third section is devoted to the calorimeter calibration issues for the next DVCS/π^0 experiment in Hall A.

3.1 Calorimeter calibration methods for the experiment

The main concern of this section is the "first order" calibration of the calorimeter block, mostly at the hardware level. To have a good and exploitable response for a calorimeter, one shall deal with:

- the tuning of the relative gains of the PMTs in order to have for all channels the same response for a signal of same magnitude;
- the determination of the relation between the PMT response and the actual energy of the signal.

For the DVCS/π^0 experiment, the first has been performed by a cosmic calibration and a LED calibration. The second used an elastic calibration.

All these methods are sequentially detailed in the following. More details on these methods can be found in the thesis manucripts of A. Camsonne [75], C. Muñoz-Camacho [76], and M. Mazouz [77].

3.1.1 Cosmic calibration

The cosmic calibration uses the flux of cosmic rays passing through the calorimeter. The cosmic rays have been chosen for the following reason. The energy deposit depends only on the quantity of matter traversed. Thus, a bunch of cosmic muons going in the same direction in a block will leave the same energy. It is therefore an excellent reference signal.

The cosmic calibration just requires the identification of the cosmic muon. The apparatus used for identification is composed of two pairs of plastic scintillator paddles, placed on the top and the bottom of the calorimeter. The setup is available on Fig. 3.1. For

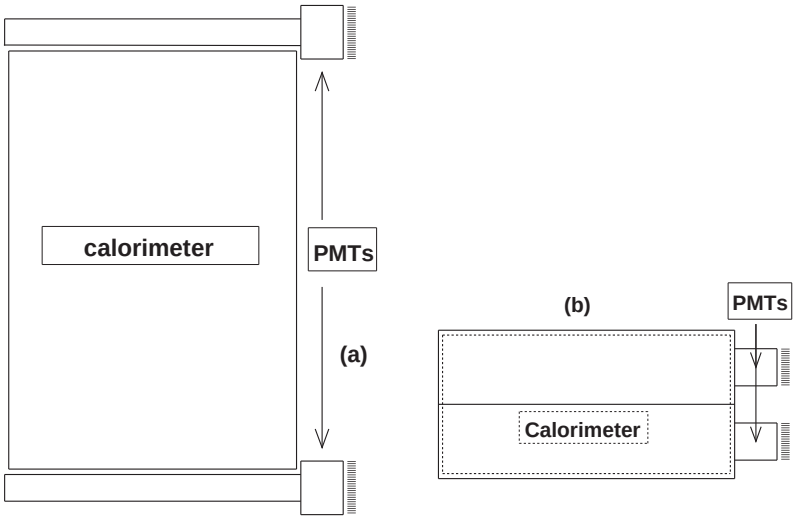

Figure 3.1: Schematic setup of the scintillators for the cosmic trigger. (a): seen from the calorimeter front face. (b): seen from the calorimeter top. Note the PMTs and the scintillator width are not on scale with the calorimeter dimensions.

the calibration, we consider only the events which arrived vertically on the block, *i.e.* the muons which deposited energy on all blocks of the same column. The crossed path in the lead fluoride corresponds to a 35 MeV deposit in each block, which is equivalent to 35 Čerenkov photons, according to Monte Carlo. To record a sufficient statistics (about 300 events per column), one calibration run has to last 10 hours. A relevent energy distribution is obtained with such statistics. These distributions are fitted individually by a gaussian, and the voltage applied to the block PMTs are adjusted in order to center all distributions at the same value. Several iterations are necessary to perform the calibration. At the end of the calibration (Fig. 3.2), the dispersion of the energy deposit known

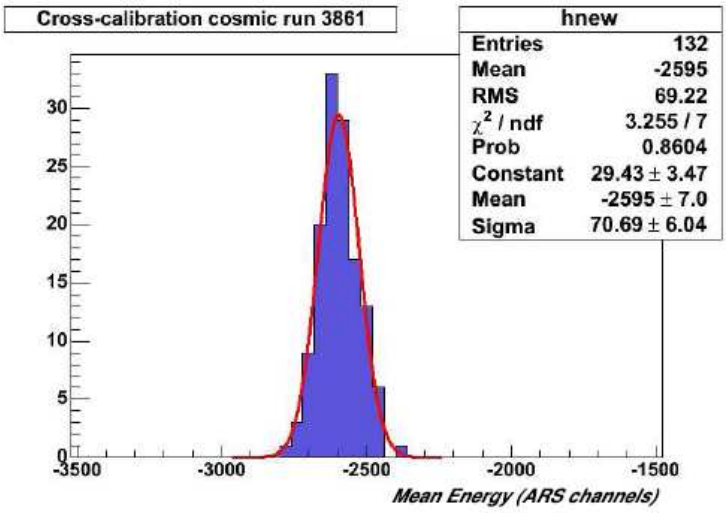

Figure 3.2: Distribution of mean energy deposit (in ARS channels) in all blocks at the end of the cosmic calibration.

with an accuracy of 2.7 %.

3.1.2 LED calibration

The LED calibration consists in illuminating the front of all PbF_2 blocks with a LED pulser, to measure the response of the block. In order to be sure to have the same signal for all blocks, we take exactly the same LED and move it in front of all blocks thanks to the XY table (see section 2.5). To be reproducible, this method requires the LED to be put exactly at the same place for each block. To this purpose, a survey of the calorimeter relatively to the XY table has been performed. It consists in scanning the blocks with the LED, by steps of 1 mm $\times$ 1 mm, and to measure the response of the block. The center is located where the maximal response is recorded. The four corner blocks positions are determined with this procedure, and the positions of all other blocks are deduced. Actually, three measures are enough, the fourth is performed to cross-check the method.

The LED calibration gives results which are in agreement within 9 % with the cosmic calibration alone. Fig. 3.3 shows the LED calibration performed with the high voltages determined with cosmic calibration.

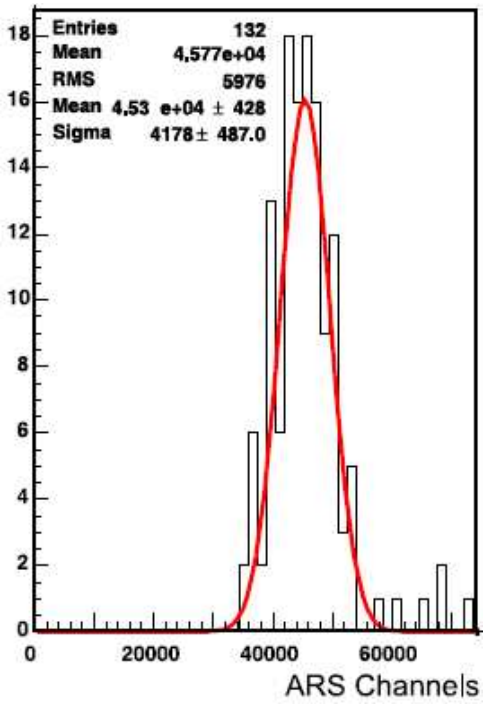

Figure 3.3: Calorimeter cross-calibration measured with LED, with the high voltages provided with the cosmic calibration.

This calibration method has the advantage to be greatly faster than the cosmic calibration. For instance, it allows to monitor the stability of the PMTs gains (Fig. 3.4) in time after switch on. This also offered the possibility to perform a frequent monitoring of the PMT gain.

However, during the experiment data taking, the LED monitoring became less and less reliable, at least for some blocks. Indeed, because of the low energy background, some crystals were darkening at the surface facing the target, absorbing a part of the LED light, and mimicking a loss of gain for the PMT. The shower of an high energy particle develop

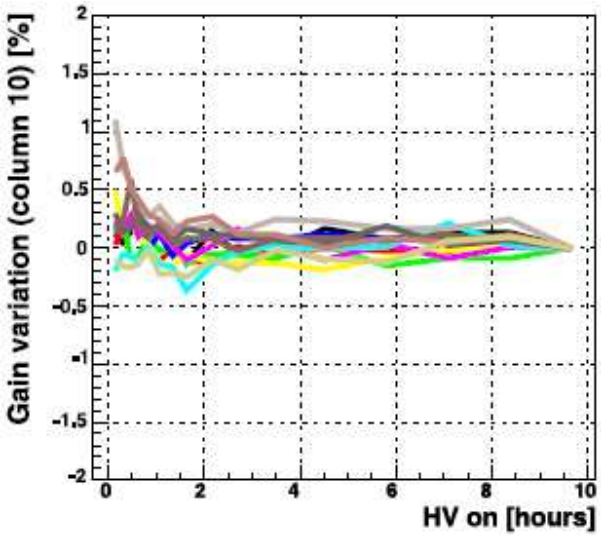

Figure 3.4: PMT relative gain variation as a function of the time after switch on.

at a certain depth in the crystal, behind such an effective screen due to the darkening. The risk is therefore to overestimate the energy deposit for these particular channels.

3.1.3 Elastic calibration

The purpose of the elastic calibration is to provide an absolute calibration of the calorimeter response. To achieve this, we use the elastic *ep* reaction, which is a two-body reaction, thus easier to constrain.

For the elastic calibration, the proton was measured with the HRS, which gives a very accurate measurement, implying a very good constraint on the scattered electron measured by the calorimeter. The elastic calibration runs require specific settings. In order to cover all the vertical acceptance of the calorimeter, it was moved back from 1.1 m to 5.5 m. Three HRS settings are necessary to cover the horizontal acceptance (Fig. 3.5). This choice resulted of an optimization of the data taking time for elastic calibration

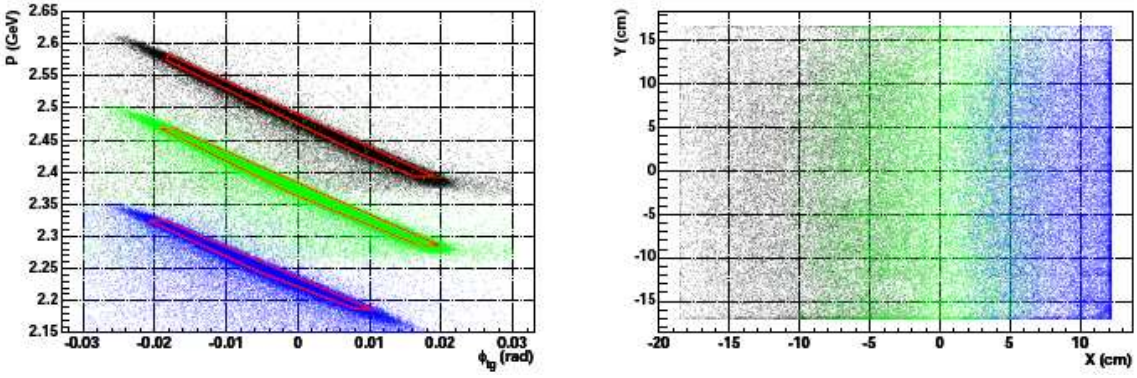

Figure 3.5: Distribution of elastic events in the $[\phi_{tg} : p_{HRS}]$ plane (left) and in the $[x_{calo}, y_{calo}]$ plane (right) for the three settings (materialized in three different colors). The red lines on the left figure materialize the HRS collimators.

(see section 3.3.1).

The calibration with elastic data is detailed below. Let us consider an elastic event j, with the energy of the electron E^j determined by the proton energy measurement:

$$E^j = E_b + M - E_p^j \tag{3.1}$$

and A_i^j the signal amplitude recorded by the block i. The relation between E^j and A_i^j is given by

$$E^j = C_i A_i^j \tag{3.2}$$

with C_i the calibration coefficient. To determine the C_i, the following χ^2 is built

$$\chi^2 = \sum_{j=1}^{N} \left(E_j - \sum_i C_i A_i^j \right)^2 \tag{3.3}$$

which is minimized by the following linear set of equations

$$\sum_i \left[\sum_{j=1}^{N} A_k^j A_i^j \right] C_i = \sum_{j=1}^{N} E^j A_k^j \qquad k \in 0, 131 \tag{3.4}$$

which yields

$$C_i = \left[\sum_{j=1}^{N} A_k^j A_i^j \right]^{-1} \sum_{j=1}^{N} E^j A_k^j. \tag{3.5}$$

A first elastic calibration was made at the beginning of the experiment, and another one was made at the end, in order to evaluate the evolution of the calibration coefficients. The result of these calibrations are shown on Fig. 3.6. A non-negligible variation of the

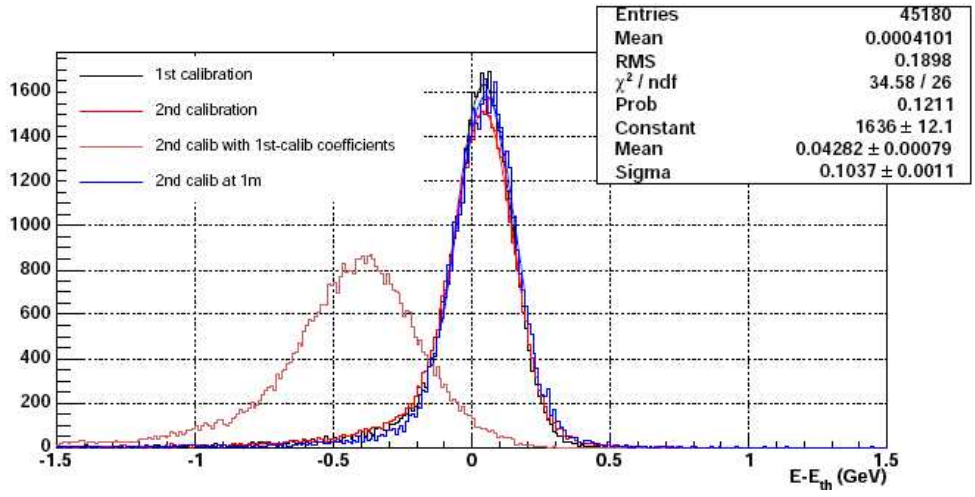

Figure 3.6: Energy resolution reconstructed over all the calorimeter with elastic calibrations. The dotted histogram shows the elastic data taken for the second calibration with the coefficients obtained for the first calibration. Note between the beginning and the end of the experiment, the calibration coeffecients experienced large variations (brick-red distribution, energy resolution at second calibration with first calibration coefficients).

calibration coefficients was observed.

In spite of its elegance, this calibration is not the most optimized calibration for the analysis. In the elastic setting, the calorimeter is at wider angles from the beam line and larger distances from the interaction point than during data taking. This implies different background conditions and an optimized calibration method to take this noise into account. This calibration method is developed in the next section.

3.2 Optimized calorimeter calibration for π^0 analysis

In constrast with the calibration methods described in the previous sections, this calibration is an analysis calibration, developped and optimized for π^0 analysis. The data sample used for this calibration is basically the one we wish to analyse (refer to Chapter 4.2 for the description of this data sample). It has been recorded with the calibration coefficients obtained from the combinations of all calibration procedures described above. In addition, these calibration coefficients have been corrected *a posteriori* from the radiation damage due to the physical background. This calibration is applied only in the inner calorimeter blocks (Fig. 3.7).

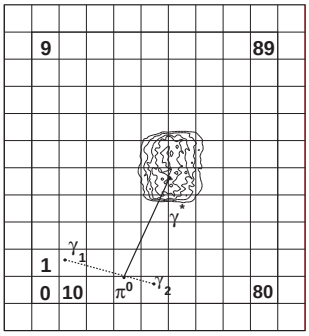

Figure 3.7: Projection on the calorimeter of the virtual photons γ^* within cuts for Kin3. Also shown is the block relabeling used for the calorimeter calibration described in the text. The calorimeter is viewed from the rear, with the downstream beam passing to the right.

The necessity of this supplementary calibration is explained further. Meanwhile, the physical background which motivated it is briefly described. The calibration method is then developed within details and the results are exposed.

3.2.1 Necessity of another calibration

The calibration coefficients obtained with the elastic calibration are valid only at first order during data taking. In experimental conditions indeed, the physical background distorts measurements of the photon energies. This background is composed of low energy particles issued from the electromagnetic interactions of the beam on the target. In addition to the distortion of the physical signal due to parasitic energy deposit, it is also responsible of the radiation damage on the crystals. This background highly depends on the scattering angle (Fig. 3.8), so the distortion of energy measurement depends on the position of the photon in the calorimeter. Fig. 3.9 shows the missing mass distribution for block 5 and 85. For block 85 which is very close to the beam, the proton peak is shifted to the right and smeared compared to block 5 which is very far from the beam.

These distortions may have consequences on the analysis. The shift in missing mass squared peak position and resolution observed close to the beam (Fig. 3.10) leads to an artificial depletion of events when an exclusivity cut (*i.e.* in missing mass squared) is applied, implying spurious contributions in the ϕ_π dependence of the cross section.

3.2.2 Calibration method

The method developed for this calibration is based on the fact that the reconstructed missing mass squared for each block must be equal to the proton mass squared, which is

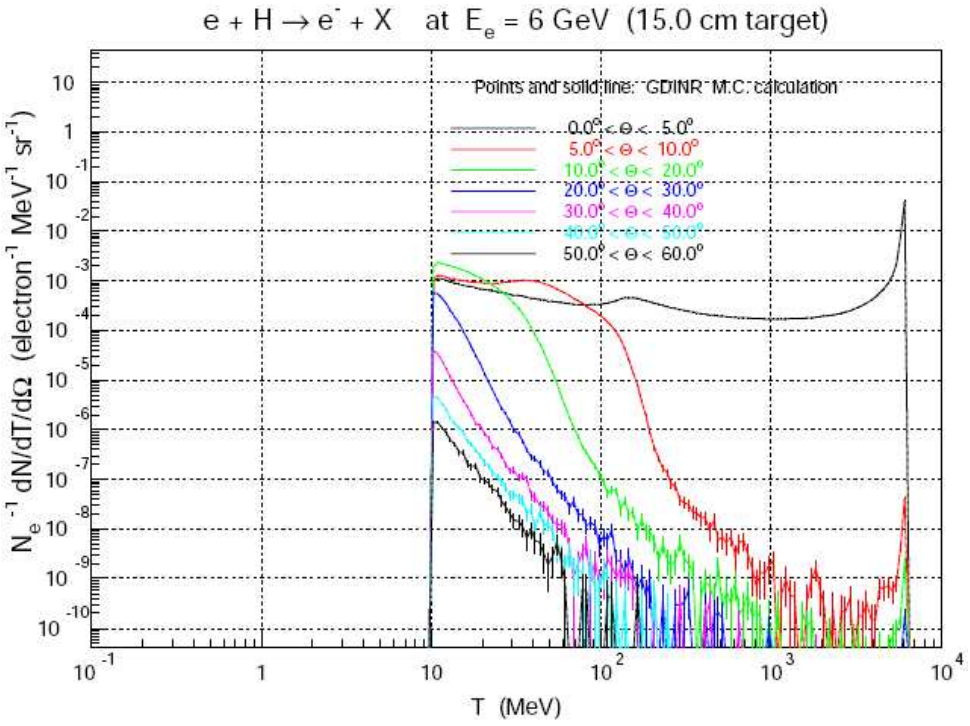

Figure 3.8: Total electron flux for different energies as a function of the scattering angle, computed by the DINREG code of P. Degtiarenko [78].

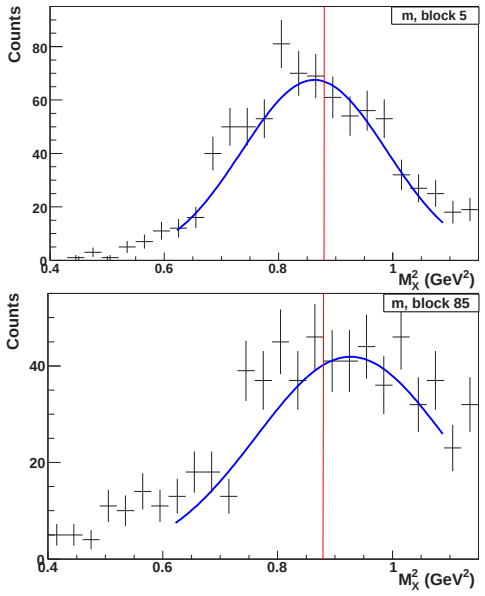

Figure 3.9: Missing mass squared distribution for block 5 (upper panel) and 85 (lower panel). The proton mass is materialized by the red line.

the only particle whose momentum is not measured.

The first step of this calibration is the reconstruction of the missing mass squared distribution of every inner block of the calorimeter. These distributions are built with the full data sample within the analysis selection cuts (see Chap. 4.2), and the correlations between the missing mass squared and the invariant mass distributions are corrected.

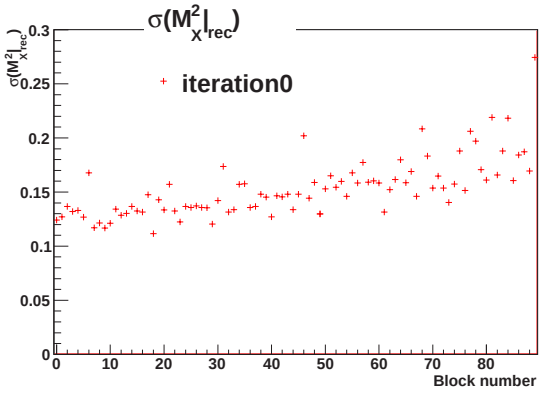

Figure 3.10: Resolution of missing mass squared in each block as a function of the block number. The resolution broadens as we get closer from the beam (large block numbers)

For each event, the missing mass squared can be written

$$M_X^2 = E_X^2 - \vec{P_X^2}, \tag{3.6}$$

with

$$E_X^2 = k + M - k' - q_\mu - q_\nu \quad \text{and} \quad \vec{P_X^2} = \vec{k} - \vec{k'} - \vec{q_\mu} - \vec{q_\nu} \tag{3.7}$$

where q_μ and q_ν are the two photons issued from the decay of electroproduced π^0, respectively measured in the block μ and ν. We assert this under the hypothesis that the energy of the photon is driven by the block where the electromagnetic shower makes the largest energy deposit.

For each event, the missing mass squared value is computed, and fills up both missing mass squared distributions of the two hit blocks with the larger energy deposit. This induces correlations between missing the mass squared distributions of all blocks. Then, we fit each missing mass block distribution by a gaussian, between $0.62 < M_X^2 < 1.09$. This fit gives the missing mass squared position and resolution for each block. The deviation of this missing mass to the proton mass gives the correction to apply to the considered block.

Considering the block μ, the correction of each photon Δq_μ hitting it is related with the missing mass squared deviation of the block $\Delta M_X^2|_\mu$. One could access the relation between the photon energy correction and the missing mass squared deviation by a M_X^2 derivation relative to q_μ:

$$\begin{aligned} \frac{\partial M_X^2}{\partial q_\mu} &= \frac{\partial E_X^2}{\partial q_\mu} - \frac{\partial \vec{P_X^2}}{\partial q_\mu} \\ &= 2E_X \frac{\partial E_X}{\partial q_\mu} - 2\vec{P_X} \frac{\partial \vec{P_X}}{\partial q_\mu} \\ &= -2E_X + 2\frac{\vec{P_X}.\vec{q_\mu}}{q_\mu} \end{aligned} \tag{3.8}$$

As E_X is more than 1 GeV and $\frac{\vec{P_X}.\vec{q_\mu}}{q_\mu}$ is less than half a GeV, we decide to neglect the term depending on $\vec{P_X}$ in (3.8), that gives, applied to the block μ:

$$\frac{\Delta M_X^2|_\mu}{\Delta q_\mu} = -2E_X. \tag{3.9}$$

As an expression of Δq_μ as a function of ΔM_X^2 we finally get

$$\Delta q_\mu = -\frac{\Delta M_X^2|_\mu}{2E_X}. \tag{3.10}$$

With such a correction applied to both photons q_μ and q_ν, the missing mass squared is reconstructed event by event. However, the resulting reconstructed missing mass $M_X^2|_\mu$ for the block μ has some contributions from all other blocks $\nu \neq \mu$ *via* the corrections of the photons Δq_ν, depending on the missing mass squared deviations $\Delta M_X^2|_\nu$. Because the block missing mass squared distributions -and calibration coefficients are correlated, and also because of the apprixmations lying in the method, several iterations have to be proceeded for calibration. We express the correction of the photon energy at iteration n, with the error ΔM_X^2 at iteration $n-1$:

$$\Delta q_\mu|^n = +\frac{\Delta M_X^2|_\mu^{n-1}}{2E_X} \tag{3.11}$$

here $\Delta M_X^2|_\mu^{n-1} = \langle M_X^2|_{n-1}\rangle - M_P^2$.

When the calibration has been performed for the data, we apply the same method on the simulation. In addition to the photon energy calibration however is performed a simultaneaous smearing of the simulation resolution. For this purpose the simulation resolution has been set sharper than data. The goal of this smearing is to equate for each block the missing mass squared resolutions for the simulation and the data. It is made according to a gaussian distribution with deviation for each block $\Delta\sigma_\mu$ obeying to the following relations

$$\Delta\sigma_\mu = \sqrt{(\sigma_\mu)_{data}^2 - (\sigma_\mu)_{simu}^2},\ (\sigma_\mu)_{data} > (\sigma_\mu)_{simu}; \tag{3.12}$$

$$\Delta\sigma_\mu = 0 \qquad ,\ (\sigma_\mu)_{data} < (\sigma_\mu)_{simu}. \tag{3.13}$$

This can be summarized by the following formula

$$(\vec{q_\mu})_n^i = \frac{(\vec{q_\mu})_{n-1}^i}{|q_\mu|_{n-1}^i}\ \text{Gauss}\left((q_\mu)_{n,\,mean}^i, \frac{\Delta\sigma_\mu}{\sqrt{2}}\right) \tag{3.14}$$

where

$$(q_\mu)_{n,\,mean}^i = |q_\mu|_{n-1}^i + \frac{\langle (M_X^2)_\mu\rangle_{simu} - \langle (M_X^2)_\mu\rangle_{data}}{4E_X^i}. \tag{3.15}$$

Note that in this case, the correcting term is ponderated by another factor 2, which gives $4E_X^i$ in the denominator instead of $2E_X^i$ in the case of the data calibration. This relative coefficient compensates the calibration coefficients correlations, which are not compensated by the weaker statistical fluctuations.

In order to verify the calibration convergence, we build, for instance for data calibration, the following estimators:

- the average over all blocks of the missing mass peak positions;
- the RMS of the distribution of missing mass peak positions compared to this average.

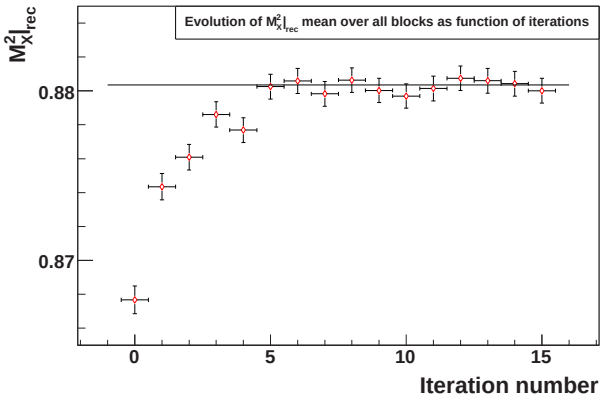

Figure 3.11: Evolution during the iterating process (from iteration 0 to 15) of the missing mass squared averaged over all blocks for Kin3. Notice that it oscillates around the reference value defined by M_p^2.

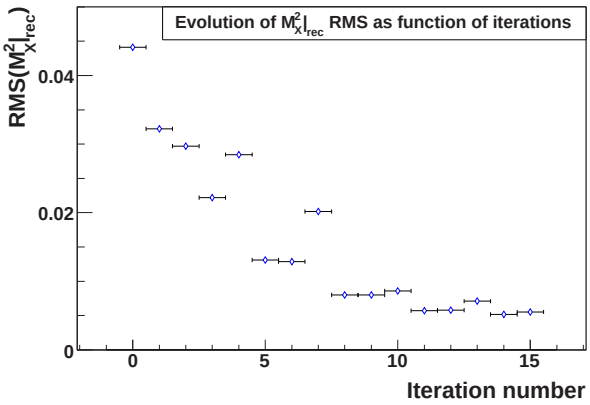

Figure 3.12: Evolution during the iterating process (from iteration 0 to 15) of the missing mass squared RMS regarding to the mean missing mass squared for Kin3.

For data calibration, the average and the RMS of the distribution of individual block missing mass squared peak position are plotted as a function of the iteration number on Figs. 3.11 and 3.12, respectively.

The selection of the "good" iteration (*i.e.* the iteration for which the calibration has converged) is based on a compromise between a good agreement between both computed estimators and their expected value, and a reasonable number of iterations. For the simulation similar estimators are built for the missing mass peak position and resolution. This makes four estimators, which computed values have to be close to expected values all together.

The results of this method for data and calibration in terms of individual blocks reconstructed missing mass squared and on global reconstructed missing mass squared and pion mass are given in the following subsection.

3.2.3 Calibration results

The result of the data calibration is shown on Fig. 3.13. This figure shows the reconstructed missing mass squared peak position as a function of the block number before and after iteration. After calibration, the average missing mass squared peak position agrees

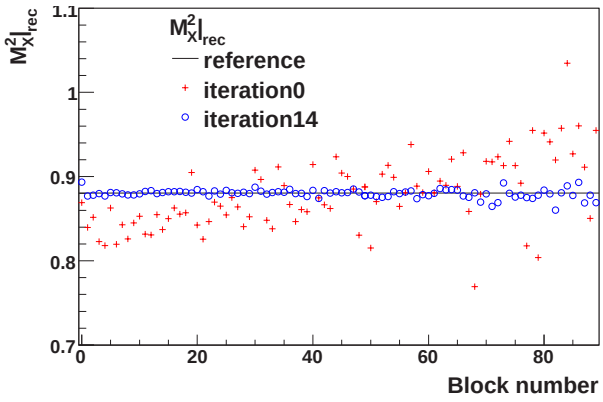

Figure 3.13: Reconstructed missing mass squared value for iteration 0 (red crosses) and iteration 14 (open blue circles) for data, Kin3.

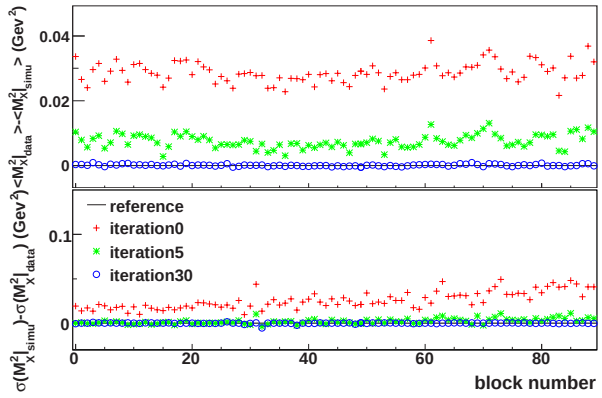

Figure 3.14: Difference (data − simulation) of missing mass peak position (upper panel) and resolution (lower panel) before calibration (crosses), after calibration (open circles), and at a random iteration during calibration (asterisks), for Kin2.

with the proton mass at a level better than 0.01 %. The dispersion of the missing mass squared peaks positions for all blocks around this average is better than 0.01 GeV^2, RMS.

The result of the simulation calibration is shown on Fig. 3.14. This figure shows the difference (data − simulation) for the missing mass squared peak position on upper panel and the resolution on lower panel. The calibration gives an average difference (data − simulation) for missing mass squared position below 0.02 %, and the dispersion around this average is better than $4{\cdot}10^{-4}$ GeV^2, RMS. The average (data − simulation) resolution is below 0.1 %, and the RMS is below 0.01 GeV^2, RMS.

The data and simulation missing mass squared spectra reconstructed with these calibrations are available on figure 3.15. On this figure is also available the effect of the calorimeter threshold, E_{Thr} on the missing mass spectrum. To help the visualization of this effect, the missing mass is plotted for three values of E_{Thr}, and the yields are corrected by a factor $1/(1-2(E_{Thr}/|\vec{p_\pi}|))$ which estimates the number of π^0 missed because of the cut. For a calibration cross check purpose, we recompute the $\gamma-\gamma$ invariant mass distribution using this calibration, compared to the physical pion mass. This comparison is available in Table 3.1.

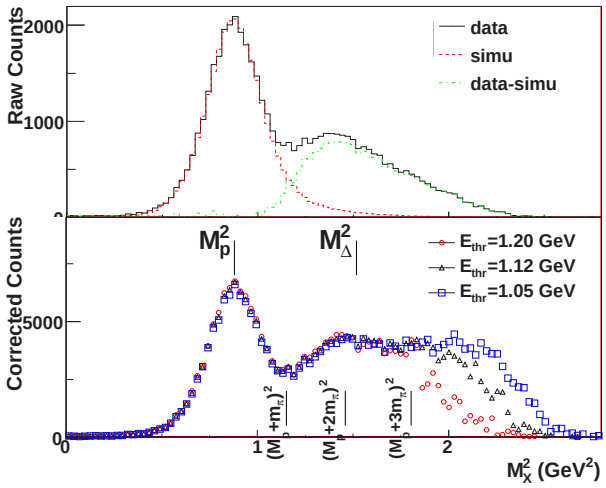

Figure 3.15: Upper panel: Raw $\mathrm{H}(e,e'\pi^0)X$ missing-mass distribution for Kin3 (solid histogram), compared to the simulation (dashed histogram), and the difference between the two (dotted histogram). Lower panel: $\mathrm{H}(e,e'\pi^0)X$ missing-mass distribution for different values at the calorimeter threshold. This correction adds to the distribution all π^0 events missed because of the threshold value.

	$\langle m - m_{\pi^0} \rangle$ (GeV)	$\sqrt{\langle (m - m_{\pi^0})^2 \rangle}$ (GeV)
KIN 3		
data	-0.00081	0.0088
simulation	+0.00072	0.0089
KIN 2		
data	-0.00017	0.0079
simulation	+0.00191	0.0085

Table 3.1: Mean deviation and resolution width of the $\pi^0 \to \gamma\gamma$ reconstruction of the data and simulation. Events are selected by $M_X^2 < 1.15$ GeV^2 and a calorimeter threshold $E_{Thr} = 1.0$ GeV.

Comparison with Malek Mazouz' results

Malek Mazouz performed similar calibrations during last DVCS experiments. The details on these calibrations are exposed in his thesis manuscript [77]. The main difference lies on the selection cuts we applied on the data sample to perform our calibration.. The samples used for these two different methods are selected with the same cuts, except for the calorimeter threshold, which has been ignored by Malek. However, a cut in missing mass squared to select the elastic peak naturally selects higher energy photons, so the influence might not be significant. On the other hand, in his method, Malek does not correct the $M_X^2/m_{\gamma\gamma}$ correlation.

To perform a pertinent comparison between missing mass squared and invariant mass spectra obtained with the two different calibrations, it is better to apply my calibration coefficients on the sample selected by Malek's cuts. The result of this comparison is available in Table 3.2. The accidentals were subtracted for both distributions, and none of the distributions were corrected with the $M_X^2/m_{\gamma\gamma}$ correlation. Note that on invariant mass spectra, the invariant mass cut was not applied.

There are small discrepencies between these results. They may lie in the fact that

	This method	Method described in [77]
Kin2		
M_X^2 (GeV^2)	0.880	0.885
σM_X^2 (GeV^2)	0.152	0.145
$m_{\gamma\gamma}$ (GeV)	0.1357	0.1350
$\sigma(m_{\gamma\gamma})$ (GeV)	9.02×10^{-3}	8.61×10^{-3}
Kin3		
M_X^2 (GeV^2)	0.908	0.872
σM_X^2 (GeV^2)	0.197	0.193
$m_{\gamma\gamma}$ (GeV)	0.1340	0.1349
$\sigma(m_{\gamma\gamma})$ (GeV)	1.024×10^{-2}	1.011×10^{-2}

Table 3.2: Characteristics of missing mass squared and invariant mass distributions, corrected with the two calibration methods.

the calibration method described in this document includes $M_X^2/m_{\gamma\gamma}$ correlation correction and is applied on a sample which is not corrected from this effect. However, these discrepencies are small enough so that these distributions remain compatible. This gives credit to both methods, although the method described in this chapter generally gives worse results.

3.3 Calorimeter calibration issues for the next DVCS/π^0 experiment

This section explores different issues for the calorimeter calibration of the next DVCS/π^0 experiment. The calorimeter will be similar to the one used in this experiment, except that the number of channels grows from 132 (12×11) blocks to 208 (16×13). Several methods have to be combined in order to calibrate the calorimeter and to monitor these calibrations.

Prior to data taking, the calibration methods we used for this experiment would be the same. Because of the larger calorimeter, the elastic settings for this experiment have to be determined again. The optimization of the elastic setting has been performed, and the possibility to use the π^0 calibration either as a substitution to elastic calibration or a monitoring of the calibration has been explored.

3.3.1 Elastic calibration

As specified above, the calorimeter will be extended from 11 blocks to 13 in width (+6 cm wide) and mostly from 12 blocks to 16 in height (+12 cm), so we have to determine other settings which would optimize the beam time spent to take elastic calibration data. This optimization is made by a Monte Carlo simulation.

The Monte Carlo simulation generates elastic events ponderated by the elastic cross section (refer to Chapter 1.2.1) in the acceptance of the detectors. Spectrometer acceptance cuts are available on Table 3.3.

$\lvert x_{\text{HRS plane}}\rvert < 2.8$ cm (Horizontal collimator)
$\lvert y_{\text{HRS plane}}\rvert < 6.0$ cm (Vertical collimator)
$\lvert p' - p_{\text{HRS}}\rvert / p_{\text{HRS}} < 4.5\%$

Table 3.3: Spectrometer cuts for elastic simulation.

For efficiency reasons, the kinematics are determined by the proton, which is measured in the spectrometer. We compute the tightest bounds of the proton solid angle corresponding to the spectrometer, to maximize the efficiency of Monte Carlo generation. The proton direction is generated in this solid angle, and the proton momentum is generated in the spectrometer acceptance. The electron direction and momentum are then computed thanks to two body kinematics relations, and the elastic cross section is computed for the cross section ponderation.

The cross section ponderation uses the Metropolis method. This method consists in the following. Prior to the simulation, a "reference" cross section value is fixed, as a starting point. For the first event, the cross section is computed. If the value of the event cross section is above the reference cross section, the event is kept and the cross section value replaces the reference for the next event. Else, a random variable is generated between 0 and the reference cross section. If this variable is below the cross section value of the event, this event is kept and the cross section value replaces the reference for the next event. If it is above, the event is rejected, and the reference is conserved for the next event.

During the event generation the cross section is summed in order to compute the integrated luminosity of the simulation, given by:

$$\left[\int \mathcal{L} dt\right] = M/\Delta\sigma. \tag{3.16}$$

with M the number of counts in the simulation, and $\Delta\sigma$ the integrated cross section:

$$\Delta\sigma = \int d\sigma(\Omega) \overset{\text{discrete}}{=} \left[\sum_{i=1}^{N} \sigma_i\right] \times \Delta\Omega \tag{3.17}$$

with N the number of generated events and $\Delta\Omega$ the simulation phase space fixed here by the proton solid angle. With the integrated luminosity, the required beam time Δt_{beam} to get M counts for the elastic run is:

$$\Delta t_{beam}(\text{s}) = \frac{\left[\int \mathcal{L}\text{dt}\right](\text{nb}^{-1})}{\mathcal{L}_{\text{beam}}(\text{cm}^{-2}\text{s}^{-1})} \times 10^{33}. \tag{3.18}$$

The coefficient 10^{33} converts nb^{-1} into $\text{cm}^{-2}\text{s}^{-1}$.

This simulation will be peformed for two beam energies, at 4 passes and 5 passes of the accelerator (as DVCS/π^0 data taking), assuming 1.11 GeV par pass. It will have for main advantage to obtain a energy dependence on the energy resolution of the calorimeter. In addition to that, the energy range covered by the scattered electron will be, at 4

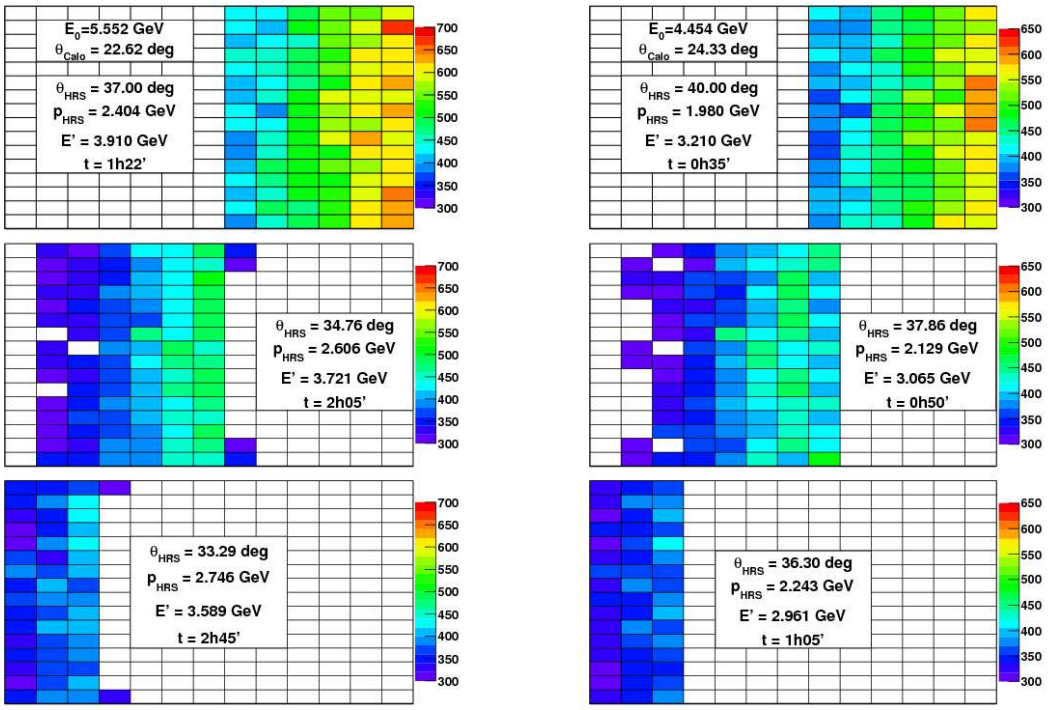

Figure 3.16: Elastic settings for next DVCS/π^0 experiment for 5 passes beam (left panels) and 4 passes beam (right panels). Each panel shows the individual block counting rates above 300 events for one setting. Beam time estimation has been made on the basis of a beam current of 2.5 μA.

pass, more representative of the typical energy of a signal photon. The choice of three settings for the illumination of all the calorimeter has been made. The results of these simulations are shown on Fig. 3.16. The settings have been fixed in order to get a minimal statistics of 300 electrons per block in at least one of the three settings for each block.

To monitor more frequently this calibration, we will use a method, described in the following, which is derived from the π^0 calibration method.

3.3.2 Calibration with π^0

The calibration method which is discussed here has for purpose to substitute elastic calibration for calibration monitoring. Elastic calibration indeed requires specific settings which are very time consuming to set up. For instance, the inversion the magnetic field in the HRS dipole (required to measure the proton in the HRS) takes about 4 hours. A substitution to elastic calibration would thus allow a more regular calibration monitoring.

This calibration method is inspired from the π^0 analysis calibration method exposed in the latter section. The main difference is that we use the invariant mass of the two photons $m_{\gamma\gamma}$ instead of the missing mass squared. The reason is the following: in the event that the blocks experience a huge gain variation (25 % for instance, which was typically the total average gain shift for the duration of the previous DVCS experiment), the missing mass squared distribution would be smeared enough that the exclusive peak would be merged with the inclusive distribution (see upper panels of Fig 3.17). The resulting peak

then includes a large fraction of inclusive events, and the calibration coefficients required to center this distribution to the proton mass would be highly biased. On the other

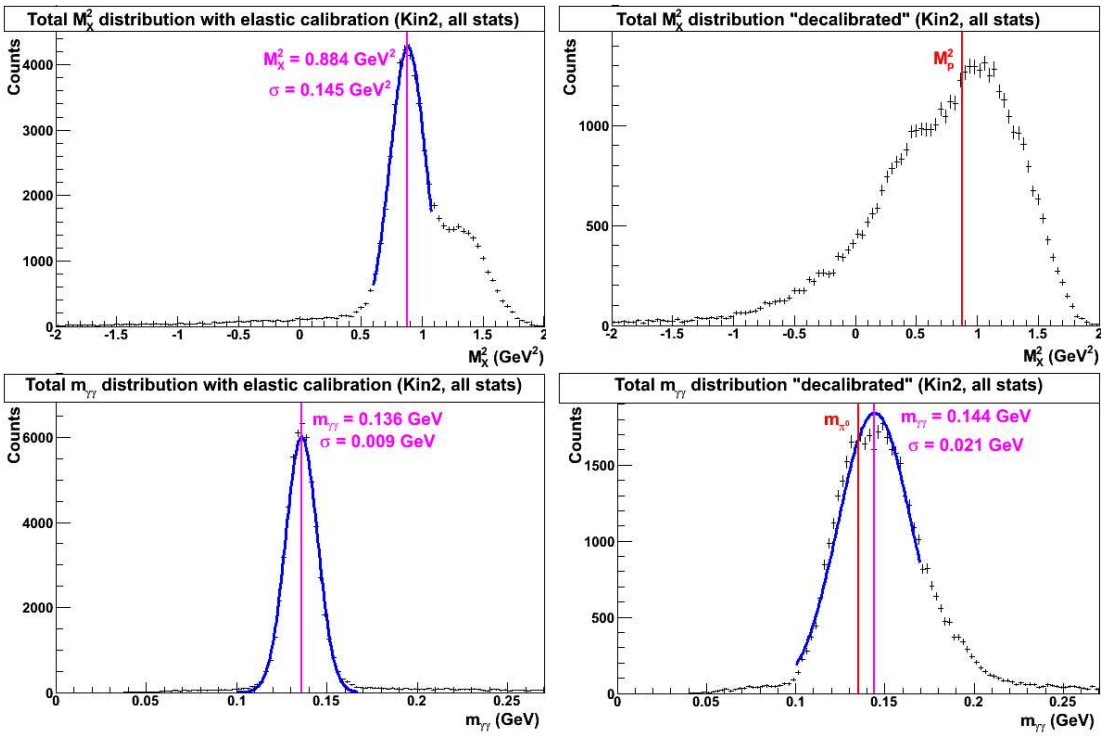

Figure 3.17: Upper panels: reconstructed missing mass squared distributions with elastic calibration (left) and smeared by 25 % (right). Lower panels: reconstructed invariant mass distributions with elastic calibration (left) and smeared by 25 % (right). The smearing method is explained in the text. The comparisons of left and right panels allows to remark that a huge smearing has much less incidence on the invariant mass than on the missing mass.

hand, the fraction of non-resonant events in the invariant mass distribution is really weak (lower panels of Fig. 3.17), so the reliability of the method is much less sensitive to the magnitude of the gain variation.

Other than that, the method is very similar to the method described in section 3.2. The expression of the photon energy variation becomes:

$$\Delta q_\mu = + \frac{\Delta m_{\gamma\gamma}|_\mu}{\frac{\sqrt{q_\nu}}{\sqrt{q_\mu}} \sin(\frac{\theta_{q_\mu q_\nu}}{2})} = +2 \frac{\Delta m_{\gamma\gamma}|_\mu}{m_{\gamma\gamma}} q_\mu \tag{3.19}$$

where $\theta_{q_\mu q_\nu}$ is the angle between the two photons q_μ and q_ν.

To perform a frequent monitoring, we would like to test the method on data samples which are as small as possible. The old DVCS/π^0 experiment ran 400 hours at a beam current of 2.5 μA, including 106 hours for Kin2, and 183 hours for Kin3. The average dead time was $\sim$ 15 %. Assuming a similar beam current, a similar dead time, and 12 h of effective data taking per day, one day could allow to record 11.3 % of the total statistics of the previous experiment for Kin2 6.6 % of the total statistics for Kin3. The method has been tested for one-day long (*i.e.* 12 h data taking), one-and-a-half-day long (*i.e.* 16 h data taking) and two-days long (*i.e.* 24 h data taking) data samples, for Kin3. To ensure a smoother convergence for such low statistics, the expression of the photon energy correction has to be multiplied by a factor $\lambda < 1$. For this study, λ is set to 1/8, which

turns Eq. (3.19) into

$$\Delta q_\mu = +\frac{1}{4}\frac{\Delta m_{\gamma\gamma}|_\mu}{m_{\gamma\gamma}} q_\mu. \tag{3.20}$$

Fig. 3.18 and Fig. 3.19 show respectively the calibration convergence for a 16-hours long and a 24-hours long data sample respectively. Both samples have been selected from Kin3 data sample. Fig. 3.18 shows that the convergence is not really smooth for the 16-

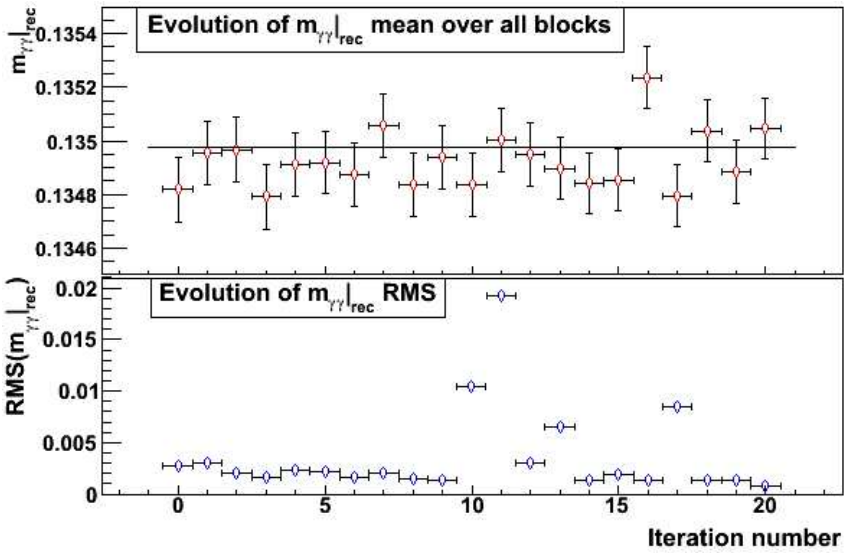

Figure 3.18: Upper panel: Evolution during the iterating process of the average invariant mass peak position over all blocks for a 16-hours long data sample selected from Kin3. Lower panel: evolution during the iterating process of the invariant mass position RMS relative to the average for the same sample.

hours long data sample. Indeed, if the average invariant mass peak position is generally around the pion mass, the RMS of the invariant mass peak position distribution over all block around this average sometimes "jumps" to very high values. This is due to the failing of the gaussian fit of a single block invariant mass distribution. The obvious cause of this gaussian fit fail is a lack of statistics in this single block. This figure demonstrates then that the calibration method is not reliable with only 16 hours of data taking. On the other hand, Fig. 3.19 shows a smooth convergence is realized with 24 hours data taking. Of course this figure only shows the convergence behavior for one sample, but we verified that this behavior was the same for all independent 24-hour long data samples we could select from Kin3. This means that the calibration method is pretty reliable with 24 hours of data taking. Calibration convergence for 12-hours samples shows the same behavior as 16-hours samples.

To complete this study, we wish to verify if this method is able to correct a gain variation. To simulate the gain variation, an event-by-event smearing of the photons energies is performed within the following procedure. If one considers an event for which the two photons hit the block μ and ν, respectively. The energy of the photon 1 (respectively 2) is smeared by:

$$q_{\mu(\nu)\text{ smeared}} = q_{\mu(\nu)}(1 + \frac{G_{\mu(\nu)}}{10}), \tag{3.21}$$

where $G_{\mu(\nu)}$ is the "decalibration" coefficient (*i.e.* the gain variation) of the block μ (respectively ν), generated in a reduced centered gaussian distribution.

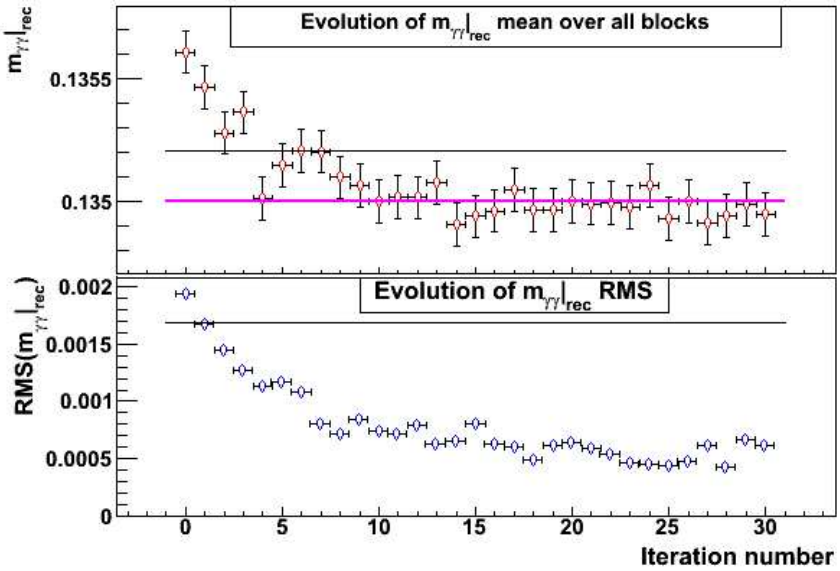

Figure 3.19: Upper panel: Evolution during the iterating process of the average invariant mass peak position over all blocks for a 24-hours long data sample selected from Kin3. Lower panel: evolution during the iterating process of the invariant mass position RMS relative to the average for the same sample.

The calibration convergence for a 24-hours long Kin3 data sample smeared by 10 % on average is displayed on Figure 3.20. The influence of such a calibration procedure on the reconstructed invariant mass and missing mass squared distributions are available on Table 3.4.

	$m_{\gamma\gamma}$ (GeV)	M_X^2 (GeV^2)
before calibration		
Mean	0.1364	0.947
σ	0.01335	0.292
after calibration		
Mean	0.1350	0.882
σ	0.0096	0.164

Table 3.4: Results of the gaussian fit of the $m_{\gamma\gamma}$ and M_X^2 distributions for a 24-hours long Kin3 data sample, smeared by 10 % on average, before and after calibration.

The two clusters calibration is able to monitor the gain variation for a 24-hours data sample, or, in other words, every two days in average. However, it could not replace completely the elastic calibration. Indeed, at the beginning of the experiment, the π^0 calibration takes more time. For the next DVCS/π^0 experiment, elastic calibration would take, with reasonable beam currents, 16 hours in the worst case. The two cluster calibration would take at least 24 h of data taking μA, implying that we could get a reasonable calibration within about two days. Moreover, the resolution on the missing mass squared is better for elastic calibration than for two cluster calibration.

The two clusters calibration should then be used complementary to elastic calibration though. A weekly based recalibration after the first elastic calibration at the beginning of the experiment performed with the data recorded during one week would be very helpful

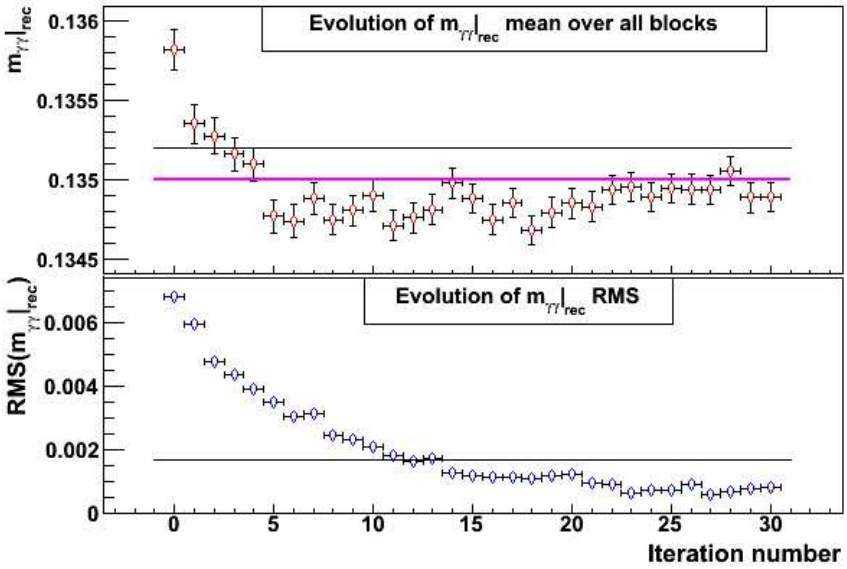

Figure 3.20: Upper panel: Evolution during the iterating process of the average invariant mass peak position over all blocks for a 24-hours long data sample selected from Kin3. Lower panel: evolution during the iterating process of the invariant mass position RMS relative to the average for the same sample.

for a frequent calibration monitoring. In addition to this, these recalibrations would include background noise effect.

Chapter 4

Data analysis methods

The main concern of this chapter is the description of the analysis methods which were developped to reconstruct an event from the raw detector signals, and to extract the cross sections from the reconstructed events.

We focus first on the raw calorimeter data analysis, including ARS pulse analysis and clustering. We briefly describe the final data sample we recorded. We give the actual extraction method of the cross sections. The radiative corrections are detailed, and the systematic errors are evaluated. Finally, a cross-check method for cross section is described.

4.1 Raw calorimeter data analysis

This section treats the analysis of the raw calorimeter signal. There are two main issues for the analysis methods described here. First, we need to extract information such as the energy from the signal recorded by the ARS. This is the purpose of the waveform analysis. The second and final step is to reconstruct the photon energy and position with the informations provided by each recorded block. This is the purpose of the clustering algorithm.

The waveform analysis is described for all possible scenarios including multipulse anlaysis. We describe the different steps of implementation of the clustering algorithm. These methods are also described within extensive details in the respective thesis manuscripts of A. Camsonne, C. Muñoz Camacho, and M. Mazouz [75, 76, 77].

4.1.1 Waveform analysis

The main goal of the waveform analysis is to extract from the ARS output the energy, the arrival time and other information relevant for a further reconstruction of the event. It consists of a fit of the energy distribution recorded by the ARS. Many scenarios can occur:

- no significant energy is recorded, a baseline which includes electronic noise and "continuous" background is fitted;
- a significant signal is recorded by the ARS, a baseline and the pulse amplitude are fitted;
- many significant signals arrive at close times, and are recorded by the ARS, then a multipulse fit is performed.

All these scenarios are considered sequentially for each of the ARS output from the most simple to most sophisticated, until the considered scenario describes the reality in a satisfying way. In the case of a one pulse or a multipulse fit, each of the pulses are compared to a reference pulse shape under the assumption that the pulse shape is independent of the pulse energy.

Defining the following notations, the ARS output as x_i the value of the energy registered in the capacitor i, with $i \in \{0, 127\}$. A single pulse may then be parameterized as $x_i = a \times h_i$ where h_i is the reference pulse shape.

Baseline fit (No pulse)

In the case there is no significant energy, the signal is fitted by a constant. The constructed χ^2 for this fit is:

$$\chi^2 = \sum_{i=i_{min}}^{i_{max}} (x_i - b)^2 \tag{4.1}$$

minimized by

$$\frac{1}{i_{max} - i_{min}} \sum_{i=i_{min}}^{i_{max}} x_i \tag{4.2}$$

where $[i_{min}; i_{max}]$ is the analysis window which can be configured differently for each ARS, as long as it meets the following condition $0 \leq i_{min} < i_{max} \leq 127$. This possibility of a different analysis window for each channel was required to compensate slight offsets in the time of flight due to the spatial location of the crystal. A test χ^2 $(= \chi^2_t)$ is defined as:

$$\chi^2_t = \sum_{i=\chi^2_{min}}^{\chi^2_{max}} (x_i - b)^2, \tag{4.3}$$

where χ^2_{min} and χ^2_{max} satisfy $i_{min} \leq \chi^2_{min} < \chi^2_{max} \leq i_{max}$. If $\chi^2_t < \chi^2_0$ with χ^2_0 fixed, the baseline fit is considered to be satisfied, and is recorded. Else, the one-pulse scenario is considered.

One-pulse fit

If $\chi^2_t > \chi^2_0$, the one-pulse fit is necessary. We construct the following time dependent χ^2

$$\chi^2(t) = \sum_{i=i_{min}}^{i_{max}} (x_i - a(t)h_{i-t} - b(t))^2 \tag{4.4}$$

with t the arrival time of the signal, included between t_{min} and t_{max}, corresponding to the analysis window limits i_{min} and i_{max}. For fixed t, This χ^2 is minimized by the following relation:

$$\begin{pmatrix} \sum_{i=i_{min}}^{i_{max}} x_i h_{i-t} \\ \sum_{i=i_{min}}^{i_{max}} x_i \end{pmatrix} = \begin{pmatrix} \sum_{i=i_{min}}^{i_{max}} h^2_{i-t} & \sum_{i=i_{min}}^{i_{max}} h_{i-t} \\ \sum_{i=i_{min}}^{i_{max}} h_{i-t} & \sum_{i=i_{min}}^{i_{max}} 1 \end{pmatrix} \begin{pmatrix} a(t) \\ b(t) \end{pmatrix}. \tag{4.5}$$

Inverting this 2×2 matrix, we obtain

$$\begin{pmatrix} \bar{a}(t) \\ \bar{b}(t) \end{pmatrix} = \begin{pmatrix} \sum_{i=i_{min}}^{i_{max}} h^2_{i-t} & \sum_{i=i_{min}}^{i_{max}} h_{i-t} \\ \sum_{i=i_{min}}^{i_{max}} h_{i-t} & \sum_{i=i_{min}}^{i_{max}} 1 \end{pmatrix}^{-1} \begin{pmatrix} \sum_{i=i_{min}}^{i_{max}} x_i h_{i-t} \\ \sum_{i=i_{min}}^{i_{max}} x_i \end{pmatrix}. \tag{4.6}$$

First, one finds the t that gives the minimum $\chi^2(t)$. Then, if the value of the test χ^2:

$$\chi^2_t(t) = \sum_{i=\chi^2_{min}}^{\chi^2_{max}} (x_i - \bar{a}(t)h_{i-t} - \bar{b}(t))^2 \tag{4.7}$$

is not larger than a certain fixed value χ^2_1, the one pulse fit is considered to be acceptable. Else, a more sophisticated fit is performed.

Multipulse fit

If $\chi^2_t(t) > \chi^2_1$, the ARS output has to be fitted with a two-pulse fit algorithm. The constructed χ^2 for this particular fit has the following structure:

$$\chi^2(t) = \sum_{i=i_{min}}^{i_{max}} (x_i - a(t,t')h_{i-t} - a'(t,t')h_{i-t'} - b(t))^2 \tag{4.8}$$

with a' the amplitude of the second signal, and t' the arrival time of the second signal included between t_{min} and t_{max}. To minimize this χ^2, the amplitudes a, a', and b have to obey the following relation

$$\begin{pmatrix} \sum_{i=i_{min}}^{i_{max}} x_i h_{t+i} \\ \sum_{i=i_{min}}^{i_{max}} x_i h_{i-t'} \\ \sum_{i=i_{min}}^{i_{max}} x_i \end{pmatrix} = \begin{pmatrix} \sum_{i=i_{min}}^{i_{max}} h_{i-t}h_{i-t} & \sum_{i=i_{min}}^{i_{max}} h_{i-t}h_{i-t'} & \sum_{i=i_{min}}^{i_{max}} h_{i-t} \\ \sum_{i=i_{min}}^{i_{max}} h_{t+i}h_{i-t'} & \sum_{i=i_{min}}^{i_{max}} h_{i-t'}h_{i-t'} & \sum_{i=i_{min}}^{i_{max}} h_{i-t'} \\ \sum_{i=i_{min}}^{i_{max}} h_{t+i} & \sum_{i=i_{min}}^{i_{max}} h_{i-t'} & \sum_{i=i_{min}}^{i_{max}} 1 \end{pmatrix} \begin{pmatrix} a(t,t') \\ a'(t,t') \\ b(t,t') \end{pmatrix}. \tag{4.9}$$

The test χ^2 for a two-pulse fit is defined by

$$\chi^2_t(t,t') = \sum_{i=\chi^2_{min}}^{\chi^2_{max}} (x_i - \bar{a}(t,t')h_{i-t} - \bar{a}'(t,t')h_{i-t'} - \bar{b}(t,t'))^2. \tag{4.10}$$

If $\chi^2_t(t,t') < \chi^2_2$ (χ^2_2 fixed), the two-pulse fit is considered good enough. Else, a specific decision has to be taken for these events. Fortunatelly, in almost all cases, the two-pulse fit was good enough to describe the signal recorded by the ARS. Note that if the time between t and t' is below the time separation of the algorithm $\Delta\tau \sim 6$ ns, the one-pulse fit is then kept as the good one, even though $\chi^2_t(t) > \chi^2_1$.

4.1.2 Clustering

The purpose of clustering is to reconstruct the photon characteristics (energy, position, *etc.*...), from the energy information extracted from all recorded channels. If the energy reconstruction is straightforward (it is the simple sum of each block of the cluster), the reconstruction of the photon position to a resolution level which is better than the block size requires a more sophisticated algorithm. Moreover, in the two-cluster event case, the configurations where the two clusters are neghbors is likely to happen, and a specific method has to be applied to disentangle them.

We present the method used to separate two distinct neighboring clusters, and particularly the photon reconstruction algorithm with the information of the blocks in a reconstructed cluster.

Cluster separation

The algorithm of cluster separation is based on the cellular automata algorithm developped extensively in [79]. The principle of this algorithm is a step-by-step "contamination" of the blocks by a "virus". At the end of the algorithm, all blocks infected by the same "virus" belong to the same cluster.

The full implementation of the algorithm starts by the identification of local maxima in the group of blocks selected by the trigger. The local maxima are the "sources of infection". The "contamination" spreads to each block from its most energetic neighbor, meaning that the value of the local maxima is affected to their neighboring blocks. In case a block is the first neighbor of two local maxima, the highest of the two values is affected. When a block has been affected a value of a local maxima, it cannot be changed anymore. Then, the contamination spreads step by step following the two rules set above until all selected blocks have been infected. This process is summarized in Fig. 4.1.

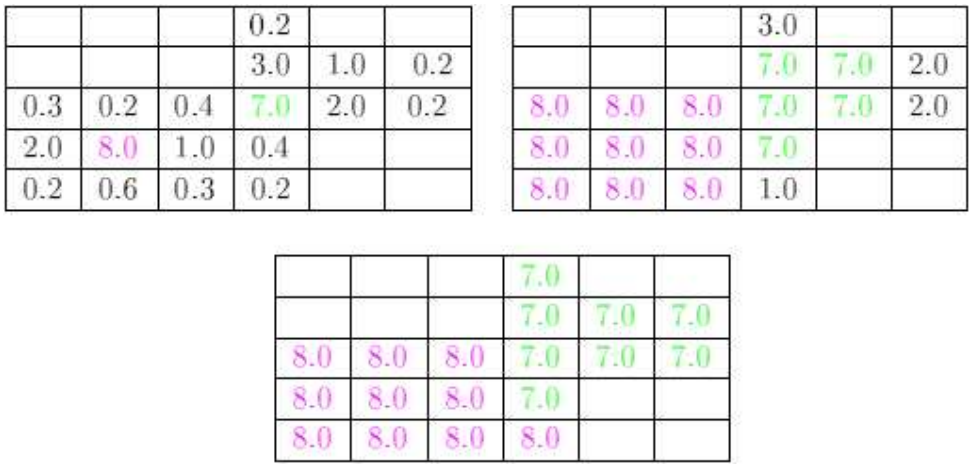

Figure 4.1: Illustration of the different steps of the cellular automata procedure. On the upper left panel, the local maxima are identified. On the upper right panel is shown the first step of the contamination, and the lower panel shows the two final clusters.

To discriminate two clusters, this algorithm requires the two maxima of each of the cluster to be separated by at least one calorimeter block, implying ~ 6 cm between the centroids of the two clusters. For a π^0 at Kin3, the typical angle between the two photons in the laboratory is 5°, implying a separation distance between the two photons at the front face of the calorimeter nearly 10 cm, safely above the minimal distance required for cluster separation.

Photon reconstruction

When all clusters are defined, it is possible to reconstruct the photon. The photon energy is the sum of the energies of all blocks. If we write the energy deposited in a block E_i as a function of the recorded signal A_i

$$E_i = A_i C_i, \tag{4.11}$$

where C_i is the calibration coefficient, then the photon energy is

$$E_\gamma = \sum_{i \in \text{Blocks}} A_i C_i. \tag{4.12}$$

The shower centroid is reconstructed by building the barycenter of all the blocks of the cluster logarithmically ponderated by the energy deposited on these blocks:

$$x = \frac{\sum_{i\in\text{Blocks}} w_i x_i}{\sum_{i\in\text{Blocks}} w_i} \tag{4.13}$$

where x_i is the geometric position of the block i and

$$w_i = \max\left\{0; \left[W_0 + \ln\frac{E_i}{E_\gamma}\right]\right\}, \tag{4.14}$$

with W_0 a parameter which allows the tuning of the relative respective block weights, as well as it defines, inside the cluster, the deposited energy threshold under which the block has to be neglected, thus defined by $E_i = E_\gamma e^{-W_0}$. Large values of W_0 allows blocks with small energy losses and increase their relative weights, whereas small values of W_0 favours the contributions of blocks with large energy deposits. The most pertinent value of W_0 has been determined thanks to Monte Carlo simulations and elastic calibrations.

The reconstructed position x given by Eq. (4.13) has to be corrected for the extended target effect, and for the shower centroid depth in the calorimeter d, which is supposed to be independent of the energy in our energy range:

$$x_{corr} = x\left(1 - \frac{d}{\sqrt{L_{vc}^2 + x^2}}\right) \tag{4.15}$$

where L_{vc}^2 is the actual distance between the vertex and the calorimeter front face at the photon position.

This algorithm is able to determine the photon position within a 2 mm resolution for a 4.2 GeV particle (determined with the elastic calibration), which is compatible with the 3 mm resolution for a 3 GeV particle determined by Monte Carlo. This resolution is at least 10 times better than an individual block size.

4.2 Data sample

As already pointed out in chapter 2, the present data were acquired as part of Jefferson Lab Hall A DVCS experiment E00-110 [55]. Three kinematic points were considered for DVCS, all defined at the same $x_{Bj} = 0.36$, and at three different Q^2: 1.5 GeV^2 (Kin1), 1.9 GeV^2 (Kin2) and 2.3 GeV^2 (Kin3). Instead of DVCS we consider the triple coincidence H$(e, e'\gamma\gamma)X$ events. The 5.75 GeV electron beam was incident on the 15 cm liquid hydrogen target, for a typical luminosity of 10^{37} cm$^{-2}\cdot$s^{-1}. Electrons were detected in the left High Resolution Spectrometer (HRS), and the photons in PbF_2 electromagnetic calorimeter.

The high resolution of the spectrometer allows to accurately define the virtual photon. The virtual photon footprint on the calorimeter can be seen on Fig. 3.7. The vertex resolution of the HRS together with the the position resolution of the electromagnetic calorimeter allow a good reconstruction of the real photon momentum direction. The validation threshold for the data acquisition trigger was set to about 1 GeV equivalent for each photon cluster for most of the data taking period. However, during few days of data taking, meanwhile in Kin2 settings, the threshold has been set fairly higher (about 1.6 GeV instead of 1 GeV) in order to solve temporary issues (Fig 4.2). Such a high threshold

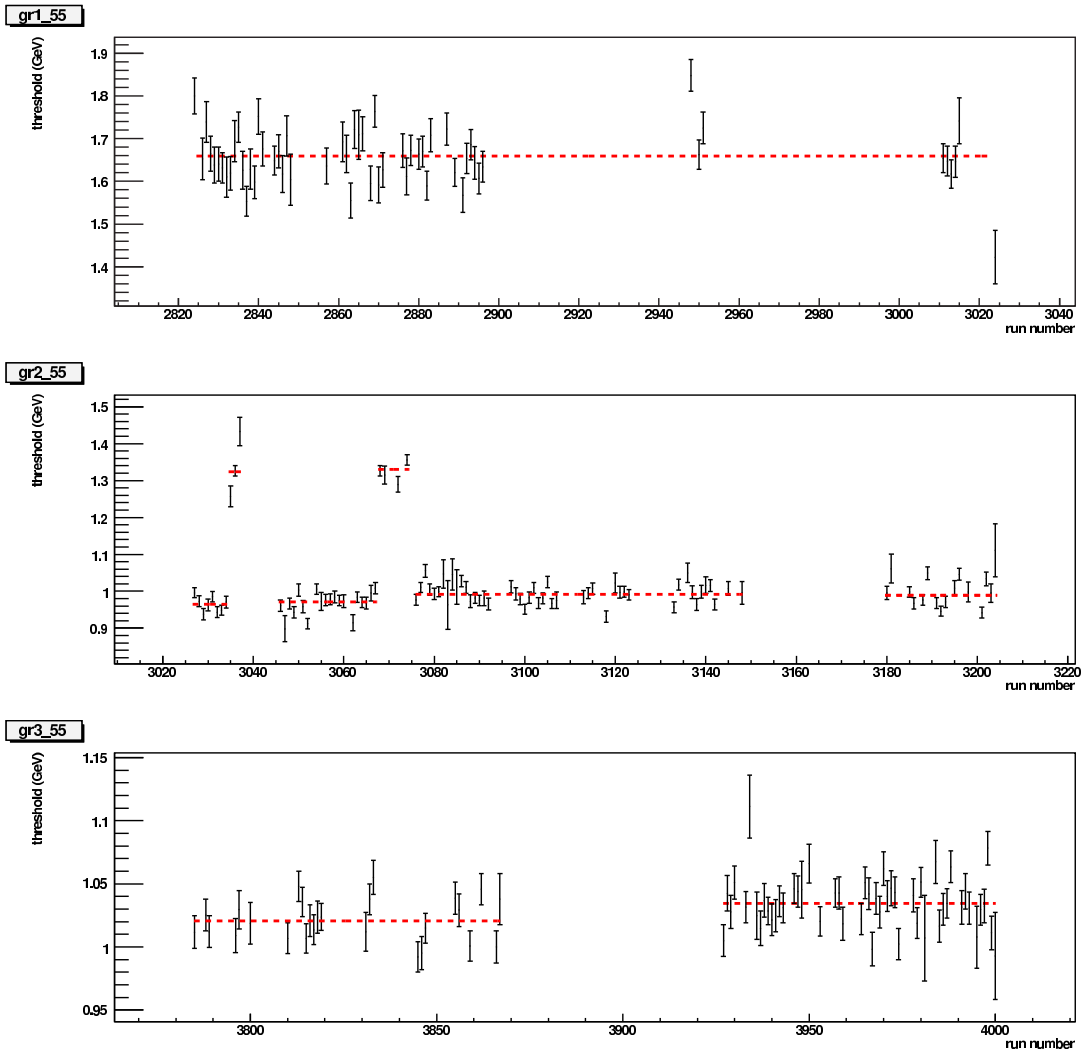

Figure 4.2: Threshold for the individual 4-block tower number 55, plotted as function of the run number. Whereas for most of the runs the threshold is around 1 GeV, it is more than 1.6 at the beginning of the period.

compared to the typical pion energy (a little bit less than 3 GeV) removes most of the π^0 statistics. For this reason, these runs were not considered in the π^0 analysis. For similar reasons, the π^0 analysis was not performed for Kin1. At the lowest Q^2, the energy of the produced particle is generally below 2.5 GeV. The fixed threshold of 1 GeV per photon also cuts a large part of the statistics.

The position and the central momentum of the HRS defines the kinematics of the event. In Table 4.1 are listed the setups corresponding to the two kinematics points Kin2 and Kin3. Fig. 4.3 shows the distribution of H$(e, e'\pi^0)X$ events in the $[x_{Bj}, Q^2]$ plane, for

Kinematic	θ_{HRS} (°)	p_{HRS} (GeV)	Q^2 (GeV^2)	x_Bj	θ_{Calo} (°)
Kin2	19.32	2.95	1.9	0.36	18.25
Kin3	23.91	2.35	2.3	0.36	14.8

Table 4.1: Experimental setup for the two kinematics Kin2 and Kin3.

missing mass squared $M_X^2 = (q + p - q')^2 \leq 1.15$ GeV^2. Note the "bean" shapes of these

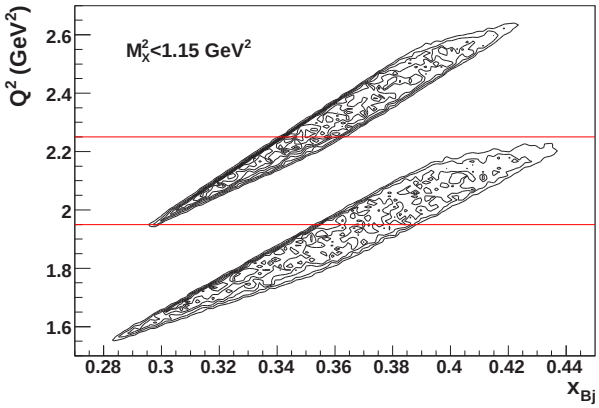

Figure 4.3: Distribution of $H(e, e'\pi^0)X$ events in the $[x_{Bj}, Q^2]$ plane, for Kin2 ($x_{Bj} = 0.36$, $Q^2 = 1.9$ GeV^2) and Kin3 ($x_{Bj} = 0.36$, $Q^2 = 2.3$ GeV^2). Events for KinX2 ($x_{Bj} = 0.40$, $Q^2 = 2.1$ GeV^2) and KinX3 ($x_{Bj} = 0.33$, $Q^2 = 2.1$ GeV^2) are bounded by the two horizontal lines.

kinematics are due to the spectrometer acceptance. The two kinematics fully overlap in x_{Bj}, which allows to study the Q^2-dependence of the cross section at fixed x_{Bj}. They also overlap partially in Q^2, between the two lines on Fig. 4.3, allowing the study of the W-dependence of the cross section.

On Fig. 4.4 is plotted the arrival time of each of the two clusters relative to the electron timing. On this distribution, we select the events which are between $\{-3; +3\}$ ns in x and

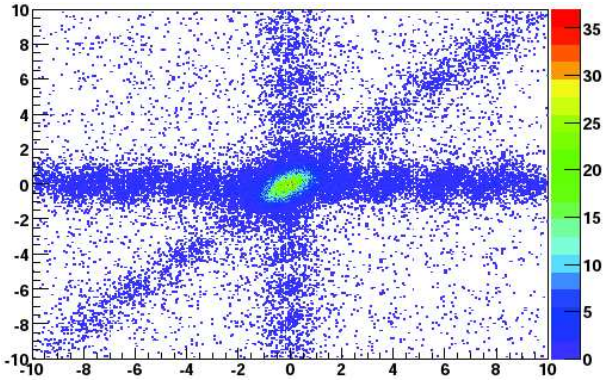

Figure 4.4: Distribution of the two clusters timing (the second (vertical) versus the first (horizontal)) relative to the electron arrival time.

$\{-3; +3\}$ ns in y. The achieved coincidence resolving time between the scattered electron and either photon cluster is 0.6 ns, rms. The analysis relies on two specific qualities of the experiment:

- thanks to the resolution of the spectrometer and the calorimeter, one can use the missing-mass squared to ensure exclusivity. The exclusive sample is selected by putting a cut on the missing-mass squared at the proton plus the pion mass squared;
- for exclusive events, the reconstruction of the invariant momentum transfer t and t_{min} relies on the positions of the reconstructed photons, leading to a resolution in t better than the one obtained with the energy. All data are presented as a function of $t_{min} - t$, which is directly linked to the angle of the pion production

relative to the virtual photon direction in the center of mass θ_π^{CM}: $t_{min} - t = 2q^{CM}q'^{CM}(1 - \cos\theta_\pi^{CM})$.

In the $ep \to e'\gamma_1\gamma_2 X$ reaction, there are six four-vectors, equivalent to 24 independent kinematic variables. The measured four-vectors k, p, and k', and four-momentum conservation, reduce the number of independent variables to 8. The measurement of the two directional vectors $\hat{k}(\gamma_1) = \vec{q_1}/q_1$ and $\hat{k}(\gamma_2) = \vec{q_2}/q_2$ from the target vertex (reconstructed by the HRS) to the two cluster positions in the calorimeter provides four more kinematic constraints. Finally, the hypothesis that the observed calorimeter showers are due to photons ($m_{q_1} = m_{q_2} = 0$) provides two more kinematic constraints. It remains 2 unknowns to constrain the reaction to an exclusive production of π^0:

- $m_{\gamma\gamma}^2 = (q_1 + q_2)^2$ is the invariant mass of the two photons, and should be equal to the neutral pion mass m_{π^0} for π^0 events;
- M_X^2 is the missing mass squared of the event, and should be equal to the proton mass M in case of an exclusive event.

Both of them are determined by the previous constraints plus the energies of the two photons. Fig. 4.5 displays the distribution of the $\mathrm{H}(e, e'\gamma\gamma)X$ events in the [M_X^2, $m_{\gamma\gamma}$] plane, for Kin3. The upper left panel of this figure shows a clear correlation between the

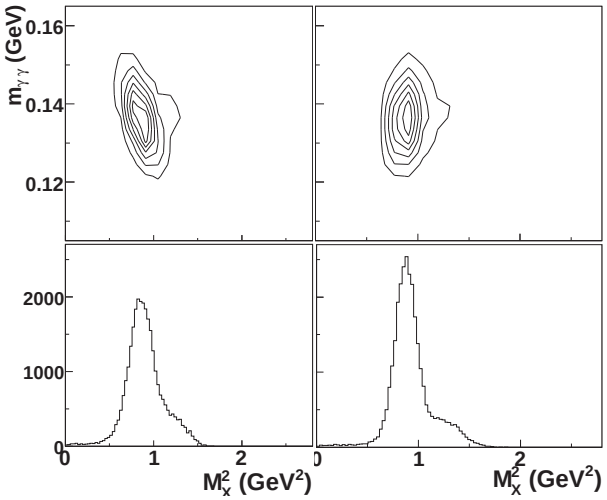

Figure 4.5: Upper panels: distribution of $\mathrm{H}(e, e'\gamma\gamma)X$ events within cuts in [M_X^2, $m_{\gamma\gamma}$] plane for Kin3. Raw distribution showing a clear correlation between these two variables (left). The same distribution after a rotation around (M_p^2, m_{π^0}) to improve the M_X^2 resolution (right). Lower panels: the projection on the M_X^2 axis of the [M_X^2, $m_{\gamma\gamma}$] distribution shown in the upper panels. The lower right panel shows that the resolution is indeed improved by the correction given by Eq. (4.16).

two variables in the exclusive region ($M_X^2 \simeq M_p^2$). This is a consequence of resolution fluctuations in the energies E_1 and E_2 of the two photons issued from a π^0, which correlate fluctuations in M_X^2 and $m_{\gamma\gamma}$. The missing mass in the right panels is obtained by an empirical adjustment:

$$M_X^2\big|_{Corr} = M_X^2\big|_{Raw} + C \times (m_{\gamma\gamma} - m_\pi), \tag{4.16}$$

with $C = 13$ GeV. This transformation produces a noticeable improvement in the M_X^2 distribution (lower right panel of Fig. 4.5). The coefficient C has been found by an

interpolation of the upper left plot on Fig. 4.5. However, a further improvement of this coefficient can be done analytically [80].

The accidentals are subtracted from the statistics in the following way:

- The events with one cluster in coincidence with the electron and one cluster in random coincidence are subtracted ($\{-11;-5\}$ ns in x and $\{-3;+3\}$ ns in y on Fig. 4.4).
- The events with the two cluster in true coincidence but random coincidence with the electron are also subtracted ($\{5;11\}$ ns in x and $\{5;11\}$ ns in y on Fig. 4.4).
- The completely accidentals ($\{-11;-5\}$ ns in x and $\{5;11\}$ ns in y on Fig. 4.4) are added once, since they have been already subtracted twice with the two other subtractions.

4.3 Cross-section extraction

The basic principle of this extraction method is the comparison between the number of counts recorded within defined experimental bins, and the number of counts in the same experimental bins of a simulation of our experiment. This simulation includes the resolution and acceptance of the HRS, the external and internal radiative effects on the incident and scattered electron. All the experimental setup, including the target, the scattering chamber, and the calorimeter were modeled using GEANT3. This specific modeling of the experiment has for goal to evaluate the acceptance and the response of the PbF_2 calorimeter.

Simulation events are generated uniformly in the target vertex v along the beam line, and uniformly in a phase space $\Delta^5\Phi$. The simulation is weighted by the cross section defined in Chapter 1.1.

In order to extract the differential cross section, it is advantageous to incorporate all model-independent kinematic dependences of the differential cross section into the experimental simulation. To this end, we express the virtual cross section in Eq. (1.1) in terms of structure functions as described in the paper of Drechsel and Tiator [5] directly related to bilinear combinations of the CGLN helicity amplitudes [81].

We write the expression of the virtual cross section, differential in t, in terms of the hadronic tensor

$$\begin{aligned}\frac{d^2\sigma_v(h)}{dtd\phi_\pi} &= \frac{d\cos\theta_\pi^{CM}}{dt}\frac{d^2\sigma_v(h)}{d\Omega_\pi} = \frac{1}{2q^{CM}q'^{CM}}\frac{d^2\sigma_v(h)}{d\Omega_\pi} \\ &= \frac{1}{2q^{CM}k_\gamma^{CM}}\left[\frac{W_{xx}+W_{yy}}{2} + \epsilon_L W_{zz} - \sqrt{2\epsilon_L(1+\epsilon)}\Re\mathrm{e}W_{xz} + \epsilon\frac{W_{xx}-W_{yy}}{2}\right. \\ &\left. + h\sqrt{2\epsilon_L(1-\epsilon)}\Im\mathrm{m}W_{yz}\right]\end{aligned} \tag{4.17}$$

The transverse-longitudinal interference terms W_{xz} and W_{yz}, corresponding to σ_{TL} and $\sigma_{TL'}$, have a leading $\sin\theta_\pi^{CM}$ dependence. The linear polarization interference term $W_{xx}-W_{yy}$, corresponding to σ_{TT} has a leading $\sin^2\theta_\pi^{CM}$ dependence.

For this reason, we define reduced structure functions r_Λ, which are directly related to bilinear combinations of the CGLN helicity amplitudes F_i [81], and which remove this

phase-space dependence:

$$r_T = \frac{W_{xx} + W_{yy}}{2} \tag{4.18}$$

$$r_L = W_{zz} \tag{4.19}$$

$$\begin{pmatrix} r_{TL} \\ r_{TL'} \end{pmatrix} = \frac{1}{\sin\theta_\pi^{CM}} \begin{pmatrix} -\frac{1}{\cos\phi_\pi} \Re e W_{xz} \\ \frac{1}{\sin\phi_\pi} \Im m W_{yz} \end{pmatrix} \tag{4.20}$$

$$r_{TT} = \frac{1}{\sin^2\theta_\pi^{CM}} \frac{1}{\cos 2\phi_\pi} \frac{W_{xx} - W_{yy}}{2} \tag{4.21}$$

In addition to that, the Q^2- and the W- dependences of the hadronic tensor $(W_{xx} + W_{yy})/2 + \epsilon_L W_{zz} = r_T + \epsilon_L r_L$ have to be included, because our kinematics cover a wide range in x_{Bj} as well as in Q^2.

We perform a preliminary extraction of the cross section on the kinematic points Kin2 and Kin3 (respectively KinX2 and KinX3) to get an estimate of the Q^2 (respectively W) dependence of the hadronic tensor. The extracted Q^2 and W dependences are then introduced explicitly in the formalism to perform a second "definitive" extraction. The dependence is modeled in the form $(Q^2)^n$ and W^δ. With the first iteration, the cross sections changed by 3%, but with a second iteration the cross sections changed only by 0.3%.

The simulation has been generated in Q^2, x_{Bj}, t, ϕ_e, and ϕ_π. The full expression of the five fold differential cross section in terms of the r_T, r_L, r_{TL}, r_{TT} and $r_{TL'}$ is then given by:

$$\begin{aligned} \frac{d^5\sigma}{dQ^2 dx_{Bj} d\phi_e dt d\phi_\pi} &= \frac{d\cos\theta_e dk'}{dQ^2 dx_{Bj}} \frac{d\cos\theta_\pi^{CM}}{dt} \frac{d^5\sigma}{d\Omega_e dk' d\Omega_\pi} \\ &= \frac{y}{2kx_{Bj}(1-y)} \times \frac{1}{2q^{CM}q'^{CM}} \times \frac{\alpha}{2\pi^2} \frac{k'}{k} \frac{k_\gamma}{Q^2} \frac{1}{1-\epsilon} \times \frac{q'^{CM}}{k_\gamma^{CM}} \\ &\times \Big[r_T + \epsilon_L r_L + \sqrt{2\epsilon_L(1+\epsilon)} \sin\theta_\pi^{CM} \cos\phi_\pi r_{TL} \\ &+ \epsilon \sin^2\theta_\pi^{CM} \cos 2\phi_\pi r_{TT} + h\sqrt{2\epsilon_L(1-\epsilon)} \sin\theta_\pi^{CM} \sin\phi_\pi r_{TL'} \Big] \end{aligned} \tag{4.22}$$

We define a compact notation that summarizes (4.22) in the form:

$$\frac{d^5\sigma}{d^5\Phi} = \sum_\Lambda \frac{d^3\Gamma_\Lambda}{d^3\Phi_e} r_\Lambda = \sum_\Lambda \mathcal{F}_\Lambda(x_v) r_\Lambda \tag{4.23}$$

with $\mathcal{F}_\Lambda(x_v)$ containing all the kinematic dependence, $\Lambda \in \{T + \epsilon_L L, TL, TT, TL'\}$ and x_v summarizing all variables k, Q^2, x_{Bj}, W, t, considered at the vertex. The notation $T + \epsilon_L L$ reflects the fact that we used only one incident energy and consequently, we were not able to disentangle $d\sigma_T$ from $d\sigma_L$ by a complete Rosenbluth separation.

The experimental data used for the analysis have the kinematical coverage shown in Fig. 4.3. The Δt bins are the same in the generation and experimental phase spaces, but resolution and radiative effects can cause migration of events from one bin to the others (Fig. 4.6). Rather than extracting average cross sections in the experimental bins, we use the simulation and the theoretical form of Eq. (4.23) to directly extract differential cross sections from the experimental yields.

We divide the acceptance into 24 equal bins in $\phi_\pi \in [0, 2\pi]$ and 8 bins in $t_{min} - t \in [0, 0.3]$ GeV^2 for both the helicity dependent and independent parts of the cross section.

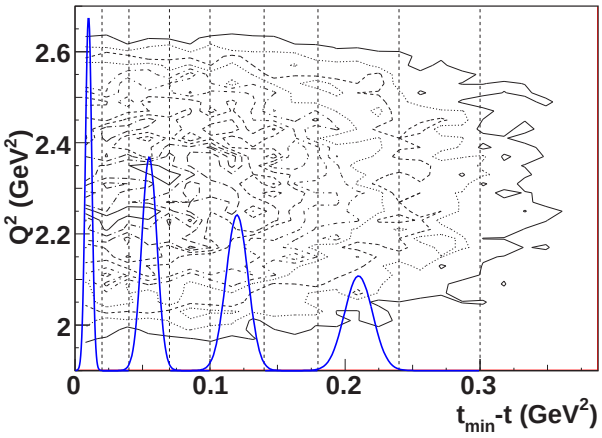

Figure 4.6: Raw $\mathrm{H}(e,e'\gamma\gamma)X$ distribution in the $[t_{min}-t,\ Q^2]$ plane with cuts for Kin3. The vertical lines delimit the bins we chose in $t_{min}-t$ for our analysis. Superimposed is the $(t_{min}-t)$ resolution for each alternate bin, showing that each bin is larger than the resolution.

A bin j_d in the kinematic variables reconstructed by the detector is defined by the limits $\phi \in [\phi(j_d), \phi(j_d)+\Delta\phi(j_d)]$, $(t_{\min}-t) \in [(t_{\min}-t)(j_d), (t_{\min}-t)(j_d)+\Delta(t_{\min}-t)(j_d)]$, etc ...

The statistics $\Delta N(j_d)$ in a bin j_d are determined by the physical cross section at the vertex convoluted with the detector response:

$$\Delta N(j_d) = \mathcal{L}u \times \int_{\Delta x_d} dx_d \int_{\Delta x_v} dx_v \mathcal{R}(x_d, x_v) \sum_{\Lambda} \mathcal{F}_\Lambda(x_v) r_\Lambda \tag{4.24}$$

where:

- x_v summarizes the reaction vertex variables,
- x_d summarizes the reaction vertex variables as reconstructed in the detector,
- Δx_d summarizes the range of integration for bin j_d,
- Δx_v summarizes the range of integration for all bins j_v,
- $\mathcal{L}u$ is the integrated luminosity,
- $\mathcal{R}(x_d, x_v)$ is the probability distribution for an event originating at the vertex with kinematics x_v to be reconstructed by the detector with vertex kinematics x_d. This expresses the effects of detector resolution, internal and external radiation, detector efficiency, that could migrate events from vertex kinematics x_v to the detector kinematics x_d.

For the analysis and simulation, the integral is split into a sum over the bins Δx_v in the kinematic variables at the reaction vertex:

$$\Delta N(j_d) = \mathcal{L}u \int_{\Delta x_d} dx_d \sum_{j_v} \int_{\Delta x_{v\in \text{bin } j_v}} dx_v \mathcal{R}(x_d, x_v) \sum_{\Lambda} \mathcal{F}_\Lambda(x_v) r_\Lambda \tag{4.25}$$

Because the functions $\mathcal{F}_\Lambda(x_v)$ contain the main part of the dependence on the variables at the vertex, the quantity r_Λ in a bin Δx_v will be assimilated to its average $\langle r_\Lambda \rangle_{x_v} \equiv r_{v,\Lambda}$

in this bin. Then, the last equation can be summarized in a vector notation:

$$\Delta N(j_d) = \sum_{j_v} K^{\Lambda}_{j_d,j_v} r_{j_v,\Lambda} \tag{4.26}$$

with

$$K^{\Lambda}_{j_d,j_v} = \mathcal{L}u \int_{\Delta x_d} \int_{\Delta x_{v\in \text{bin } j_v}} \mathcal{R}(x_d, x_v)\mathcal{F}_{\Lambda}(x_v) dx_d dx_v \,. \tag{4.27}$$

The integration is replaced by a summation over the simulated events i

$$K^{\Lambda}_{j_d,j_v} = \mathcal{L}u \sum_{i\in\{j_v,j_d\}} \frac{\mathcal{F}_{\Lambda}(x_v)}{N_{\text{gen}}} \Delta^5\Phi \tag{4.28}$$

where the sum is over events originating in vertex bin j_v and reconstructed in bin j_d. N_{gen} is the number of events generated in the simulation, $\Delta^5\Phi$ is the total phase space factor. The matrices $K^{\Lambda}_{j_d,j_v}$ are constructed from simulation events, summed over all events within cuts.

We define $N_d = N^+ + N^-$ with N^+ (N^-) the number of counts within cuts with positive (negative) electron helicity.

The cuts are the same for simulation and data. They are summarized in Table 4.2.

Spectrometer cuts
-6.0 cm $< v <$ +7.5 cm
$\lvert x_{\text{HRS plane}}\rvert < 3.5$ cm
(Horizontal collimator)
$\lvert y_{\text{HRS plane}}\rvert < 7.0$ cm
(Vertical collimator)
$\lvert k' - p_{\text{HRS}}\rvert / p_{\text{HRS}} < 4.5\%$
$r >$ +0.005 m
Calorimeter cuts
-15.0 cm $< x_{calo} <$ +12.0 cm
$\lvert y_{calo}\rvert < 15.0$ cm
Physics cuts
105 MeV $< m_{\gamma\gamma} <$ 165 MeV

Table 4.2: Cuts applied in the primary extraction. r is the value of the so-called r-function. The r-function defines the distance of the particle from the acceptance bound, and is positive (negative) if the particle is in (out of) the acceptance [82].

A χ^2 is built, assuming that the statistical error on the simulation is much smaller than the statistical error on the data

$$\chi^2 = \sum_{j_d} \frac{\left(N_d - \sum_{j_v} K^{\Lambda}_{j_d,j_v} r_{j_v,\Lambda}\right)^2}{N_d}. \tag{4.29}$$

We minimize this relation relative to $r_{j_v,\Lambda}$

$$\begin{aligned} 0 &= -\frac{1}{2}\frac{\partial\chi^2}{\partial r_{j_v,\Lambda}}\bigg|_{\bar{r}_{j_v,\Lambda}} \\ &= \sum_{j_d} K^{\Lambda}_{j_d,j_v} \frac{\left(\sum_{j'_v,\Lambda'} K^{\Lambda'}_{j_d,j'_v}\bar{r}_{j_v,\Lambda'} - N_d\right)^2}{N_d} = \sum_{j'_v,\Lambda'} M^{\Lambda,\Lambda'}_{j_v,j'_v}\bar{r}_{j_v,\Lambda'} - Y^{\Lambda'}_{j_v} \end{aligned} \tag{4.30}$$

with:

$$M^{\Lambda,\Lambda'}_{j_v,j'_v} = \sum_{j_d} \frac{K^{\Lambda}_{j_d,j_v} K^{\Lambda'}_{j_d,j'_v}}{N_d}, \tag{4.31}$$

and

$$Y^{\Lambda'}_{j_v} = \sum_{j_d} \frac{K^{\Lambda}_{j_d,j_v} N_d}{N_d}. \tag{4.32}$$

The r_Λ coefficients are finally given by:

$$\bar{r}_{j_v,\Lambda'} = \sum_{j'_v,\Lambda'} [M^{-1}]^{\Lambda,\Lambda'}_{j_v,j'_v} Y^{\Lambda'}_{j_v}, \tag{4.33}$$

and the covariant matrix of these quantities is given by $[M^{-1}]^{\Lambda,\Lambda'}_{j_v,j'_v}$. Note that all vertex bins populate experimental bins, but the detector bin at the largest experimental bin in $(t_{min} - t)$ can receive contributions from larger values of $(t_{min} - t)$, not generated in the simulation. Hence, although we extract an $\bar{r}_{j_v,\Lambda}$ value for the last bin, we do not include it in our results, its role is only to populate the lower $(t_{min} - t)$ bins. The average values of the kinematic variables Q^2, ϵ, x_{Bj}, W, t, t_{min}, *etc* ... in a bin at the vertex are

$$\overline{x}_{j_v} = \frac{\sum_{i\in\Delta x_v} x_v K^{\Lambda}_{j_d,j_v} r_{j_v,\Lambda}}{\sum_{i\in\Delta x_v} K^{\Lambda}_{j_d,j_v} r_{j_v,\Lambda}}. \tag{4.34}$$

Because the $r_{j_v,\Lambda}$ are by construction constant over the bin Δx_v and the integrals of $\mathcal{F}_{TL}$, $\mathcal{F}_{TT}$, and $\mathcal{F}_{TL'}$ cancel when integrating over ϕ_π, we can write:

$$\overline{x}_{j_v} = \frac{\sum_{i\in\Delta x_v} x_v K^{T+\epsilon_L L}_{j_d,j_v}}{\sum_{i\in\Delta x_v} K^{T+\epsilon_L L}_{j_d,j_v}}. \tag{4.35}$$

These values are summarized in Table 5.2 for quantities independent of the $(t_{min} - t)$ bin and in Table 5.3 for quantities depending of the $(t_{min} - t)$ bin. Both of these tables are available in Appendix 1. Finally, the cross sections at the point $\overline{x}_{j_v}$ in a bin j_v are obtained from:

$$\frac{d\sigma_\Lambda}{dt} = \mathcal{F}_\Lambda(\overline{x}_{j_v})\bar{r}_{j_v,\Lambda} \tag{4.36}$$

The results will be exposed in Chap. 5.

4.4 Corrections

In this section, the corrections that were applied in the analysis to minimize systematic errors are exposed extensively. The instrumental corrections are described. We give some details on the radiative corrections. We evaluate the contamination of our π^0 sample by the following channel: $ep \to ep\omega$ with $\omega \to \pi^0\gamma$.

4.4.1 Instrumental corrections

We give some comments on the instrumental corrections given in Table 4.3. In this experiment, the errors due to instrumentation come from two principal sources:

- the spectrometer can measure more than one track for the same event.
- one of the two photons in the calorimeter can create more than one cluster.

In both cases, since these kinds of events are supposed to be small, we prefer to remove the events from our statistics rather than to develop reconstruction algorithms. A summary of these corrections are available in Table 4.3.

Correction	Kin3	Kin2
Multi-tracks in HRS	1.079	1.096
Triple Cluster in Calo	1.035	1.020
Radiative correction	0.91 ± 0.02	0.91 ± 0.02

Table 4.3: Correction factors applied in the data analysis. The radiative correction factor is the combination of the virtual radiative correction factors (vertex renormalization and vacuum polarization) and the cut-off independent real radiation effects. These radiative effects are calculated according to [83]. Further details on corrections are given in next section.

HRS multitracks corrections

In the event that the HRS is measuring more than one track, the event is removed from the statistics. The probability for multitrack events to occur depends mostly on the DIS counting rate in the spectrometer acceptance. For Kin 2, the spectrometer is nearer to the beam than for Kin3, meaning a broader spatial acceptance. Moreover, the Q^2 is lower, meaning a larger counting rate due to the leptonic factor in the DIS cross section. Table 4.4 shows the proportion of multiple tracks events in the HRS. More technical details on the determinations of this corrections are available in [84].

Three-cluster corrections

Most of one cluster events are DVCS, but some may be π^0 events with an asymmetric decay, thus with one photon which does not pass the threshold. Most of two clusters events are π^0, but there may be a single DVCS event with another accidental photon. Three clusters events are mostly π^0 with another accidental photon. Thanks to Monte Carlo simulations, one can disentangle the proportion of n-cluster events owning to the relevent category, and thus obtain the corrections to apply.

Kinematics	Kin1	Kin2	Kin3
Proportion of multitracks (%)	9.38	8.72	7.32

Table 4.4: Percentage of multiple tracks in Number of tracks in the HRS for each kinematics normalized to the same number of events for each kinematic.

4.4.2 QED radiative corrections

The electromagnetic radiative effects on the electron affects the kinematics variables Q^2, W, x_{Bj}. When one considers a lepton-nucleon process, there are several different radiative effects (see Fig. 4.7):

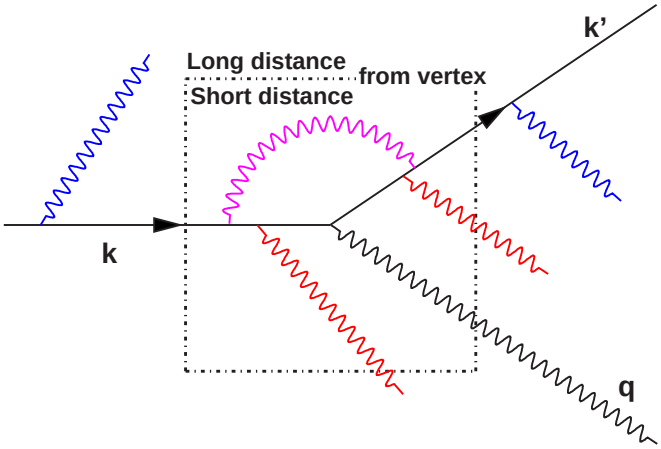

Figure 4.7: Diagram showing examples of the different radiative effects that could be observed in an lepton-nucleon reaction. The dashed-dotted box materializes the "limit" between short distances (where occur internal real and internal virtual radiative effects) and long distances (where occur external radiative effects) from the vertex. Examples of external radiative effects are represented in blue. Examples of internal real radiative effects are represented in red. An instance of a internal virtual radiative correction is shown in magenta.

- the external radiative effects occur at long distances from the vertex, meaning that the electromagnetic field neighboring the electron when it radiates is not the one of the nucleon interacting with the electron for the considered process. A typical example of external radiative process is the bremstrahlung;
- the internal real radiative effects occur at short distances from the vertex *i.e.* in the electromagnetic field of the nucleon with which its interacts. The particles created by such processes are real. In other words, they go from short distances to long distances. A typical example of an internal real radiative process is the Bethe-Heitler;
- the internal virtual radiative effects occur at short distances from the vertex. However, in constrast with internal real processes, the virtual processes create virtual particles, that are created and reabsorbed in the neighborhood of the vertex.

External radiation corrections

For practical reasons, the external pre-radiation was simulated by the equivalent radiator approximation [85, 86]. External pre-radiation is modeled by generating an event-by-event energy loss $\Delta k_{in\ ext}$ of the incident electron (E_0) following a distribution ($b \simeq 4/3$):

$$I_{in}(k_0, \Delta k_{in\ ext}, t_{in}) = \frac{bt_{in}}{\Delta k_{in\ ext}} \left[\frac{\Delta k_{in\ ext}}{k_0}\right]^{bt_{in}} \tag{4.37}$$

where t_{in} is the event-by-event target thickness (in radiation lengths) traversed by the electron before the scattering vertex. The inversion of this relation gives:

$$\frac{\Delta k_{in\ ext}}{k_0} = U_{ext}^{1/bt_{in}}, \tag{4.38}$$

where U_{ext} is uniform between 0 and 1. External radiation by the scattered electron in the target and the scattering chamber material is modeled by the GEANT3 simulation described in the previous section.

Internal real radiation corrections

The internal real radiative effects at the vertex are treated by the equivalent radiator approximation [85, 86]. Pre-radiation is modeled by generating an event-by-event energy loss $\Delta k_{in\ int}$ of the incident electron (k_0) following a distribution which is similar to Eq. (4.37):

$$I_{in}(k_0, \Delta k_{in\ int}, \delta_S/2) = \frac{\delta_S/2}{\Delta k_{in\ int}} \left[\frac{\Delta k_{in\ int}}{k_0}\right]^{\delta_S/2} \tag{4.39}$$

with the Schwinger term:

$$\delta_S = \frac{2\alpha}{\pi}\left[\ln\frac{Q^2}{m_e} - 1\right] \tag{4.40}$$

which models the internal pre-radiation. Again, the inversion of this relation gives :

$$\frac{\Delta k_{in\ int}}{k_0} = U_{int}^{1/bt_{in}}, \tag{4.41}$$

with U_{int} uniform between 0 and 1. Eqs. (4.37) and (4.39) can be combined into one:

$$I_{in}(k_0, \Delta k_{in}, t_{in}) = \frac{bt_{in} + \delta_S/2}{\Delta k_{in}} \left[\frac{\Delta k_{in}}{k_0}\right]^{bt_{in}+\delta_S/2} \tag{4.42}$$

The scattered energy at the vertex is $k'_v = k_0 - \Delta k_{in} - Q^2/(2M_p x_{Bj})$. Internal post-radiation is modeled by a similar distribution in the post-radiated energy Δk_{out}:

$$I_{out} = \frac{\delta_S/2}{\Delta k_{out}} \left[\frac{\Delta k_{out}}{k'_v}\right]^{\delta_S/2} \tag{4.43}$$

and its inversion

$$\frac{\Delta k_{out}}{k'_v} = U_{out}^{1/bt_{in}}, \tag{4.44}$$

with U_{out} uniform between 0 and 1.

Note that the internal real radiative corrections are simulated in the event generation, but not in the full GEANT simulation of the detector.

Virtual radiation correction

In contrast with other radiative corrections which have to be included directly in the simulation, the application of virtual radiative corrections consists in a simple corrective coefficient applied either to the experimental or to the simulated yields (see Table 4.3). The internal virtual radiation was calculated by Vanderhaeghen *et al.* for DVCS. Their work include an combined analytical-numerical method to compute radiative effects at first order in α_{QED}, including emission-reabsorption of a photon by the incident and scattered electron, and fermionic loops in photon exchange. Extensive details on this calculations are available in [83].

4.4.3 Data sample contamination from $ep \to ep\omega$ with $\omega \to \pi^0\gamma$

Two classes of inclusive hadronic electro-production channels compete with the exclusive $\mathrm{H}(e,e'\pi^0)p$ reaction: the $\mathrm{H}(e,e'\pi^0)N\pi, N\pi\pi, ...$ channels, with a threshold at $M_X^2 = (M_p + m_\pi)^2 = 1.15$ GeV^2 and the $\mathrm{H}(e,e'\pi^0)\gamma p$ channel. The first class includes N^* and non-resonant $N\pi$ production in the final state, and diffractive $\rho^+ \to \pi^+\pi^0$ production via the $ep \to e\rho^+ n$ reaction. All these channels can be observed in a missing-mass squared distribution (Fig. 3.15) and are ruled out by exclusivity cut within resolution effects. The $\mathrm{H}(e,e'\pi^0)\gamma p$ channel originates from the diffractive $ep \to ep\omega$ reaction, with a 8.5 % branching-ratio decay channel [87]. In our acceptance, the $(e,e'\pi^0)$ missing-mass squared threshold for exclusive ω electroproduction is 1.0 GeV^2, thus slightly lower than the $N\pi$ threshold of 1.15 GeV^2.

The purpose of this section is to evaluate the proportion of π^0 events coming from $\omega(782)$ electroproduction and decay into $\pi^0\gamma$. The evaluation of π^0 contamination by $\omega \to \pi^0\gamma$ has been made possible thanks to the publication of $ep \to ep\omega(782)$ cross sections in [88]. We study the influence of the M_X^2 cut on ω contamination. We also study the influence of the calorimeter threshold E_{Thr}, and the correlations between the two.

We consider, for each $t_{min} - t$ bin, the reaction $ep \to ep\omega$ with $\omega(q_\omega^0, \mathbf{q}_\omega)$ produced at the corresponding angle θ_π^{CM}. This ω decays in $\omega \to \pi^0\gamma$ with π^0 going very forward in ω rest frame (ω.R.F.). This leads to the following final state:

- the scattered electron and the two γ issued from the π^0 which are measured;
- the recoil proton and a low energy photon $p_\gamma = (p_\gamma^0, \mathbf{p}_\gamma)$, which are not measured.

If we compute the missing mass squared M_X^2 as a function of the unmeasured quantities, we get:

$$\begin{aligned} M_X^2 &= (p'^0 + p_\gamma^0)^2 - (\mathbf{p}' + \mathbf{p}_\gamma)^2 \\ &= M^2 + 2p_\gamma^0(p'^0 - |\mathbf{p}'|\cos\theta_{\mathbf{p}',\mathbf{p}_\gamma}). \end{aligned} \tag{4.45}$$

Estimating the value of $\cos\theta_{\mathbf{p}',\mathbf{p}_\gamma}$ is not easy, so we set it to 1 (maximizes estimation)

$$\Rightarrow M_X^2 = M_p^2 + 2p_\gamma^0(p'^0 - |\mathbf{p}'|). \tag{4.46}$$

The calculation of the photon energy gives:

$$p_\gamma^0 = \frac{q_\omega}{m_\omega} p_\gamma^{0\,\omega.R.F} + \frac{|\mathbf{q}_\omega|}{m_\omega} p_\gamma^{0\,\omega.R.F} \cos\theta_\gamma^{\omega.R.F}. \tag{4.47}$$

The proportion of $\omega \to \pi^0\gamma$, noted $X_{\omega\ in\ \pi^0}$, that pass missing mass cut and contaminate our π^0 statistics, is computed To do this, it is assumed that the $\omega \to \pi^0\gamma$ decay is isotropic.

$$\begin{aligned} X_{\omega\ in\ \pi^0} &= \frac{\int_{-1}^{\Theta=\theta_\gamma^{\omega.R.F}} \int_{\phi=0}^{2\pi} 1 \times \sin\Theta d\Theta d\phi}{\int_{\Theta=-1}^{1} \int_{\phi=0}^{2\pi} 1 \times \sin\Theta d\Theta d\phi} \\ &= \frac{1 - \cos\theta_\gamma^{\omega.R.F}}{2}. \end{aligned} \tag{4.48}$$

Now we need to know the absolute value of ω electroproduction cross section. We use ω electroproduction cross section measurements of CLAS [88]. In this reference is available a parametrization of ω electroproduction cross section under the form

$$\frac{d\sigma(ep \to ep\omega)}{dt} = \sigma_0 \times e^{bt}, \tag{4.49}$$

with b fitted between -1.5 GeV^2 $< t < t_{min}$, and $\int_{-2.7\text{GeV}^2}^{t_{min}} \frac{d\sigma(ep\to ep\omega)}{dt} dt = \sigma$. σ_0 is determined by integrating Eq. (4.49) over the experimental acceptance.

For the kinematics of CLAS which are equivalent to our kinematics we have results given in table 4.5. The obtained cross section must be multiplied by the branching ratio

variable	Kin2	Kin3
$Q^2(\text{GeV}^2)$	2.05	2.35
x_{Bj}	0.37	0.37
$t_{min}(\text{GeV}^2)$	-0.34	-0.37
$b(\text{GeV}^{-2})$	1.35	0.97
$\sigma(nb)$	1002	581
$\sigma_0(nb)$	2090	1569

Table 4.5: Recapitulative table of results given in [88] and their corresponding kinematic points.

of $\omega \to \pi^0\gamma$, noted $BR_{\omega\to\pi^0\gamma}$ available in [87], which equals 8.92%.

Finally, The neutral pion contamination is given by the following quantity:

$$\frac{\frac{d\sigma(ep\to ep\pi^0)}{dt}}{\frac{d\sigma(ep\to ep\omega^0)}{dt} \times BR_{\omega\to\pi^0\gamma} \times X_{\omega\ in\ \pi^0}}, \tag{4.50}$$

which has been plotted as a function of $t_{min} - t$, for Kin2 and for Kin3, considering their respective optimal values of M_X^2 cut on Fig. 4.8. This contamination remains below 0.3 %

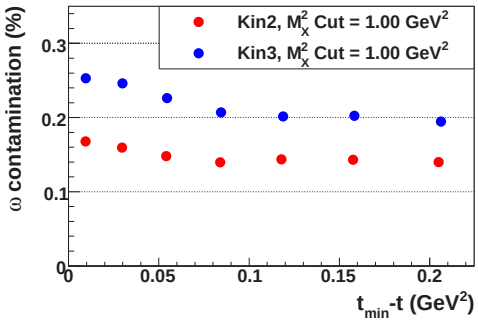

Figure 4.8: contamination of π^0 data by $\omega \to \pi^0\gamma$ as a function of $t_{min} - t$, for Kin2 and Kin3 at their respective optimal exclusivity cut.

for Kin3 and below 0.2 % for Kin2 for the considered cuts. For the cuts values which have been considered for the present analysis (see next section) the ω contamination remains below 0.3 %.

Let us evaluate now the influence of the calorimeter threshold. We assume that the photon issued from ω decay is emitted at such an angle in the ω rest frame that it has enough energy to pass the threshold. The only thing we have to compute is the minimal emission angle of the gamma in the ω.R.F to allow it to pass the threshold. It implies the emission angle of the π^0 and, straightforwardly, the maximal energy q'^0 with the photon issued from the ω in the threshold. With this values, two configurations appear:

- $E_{\pi^0} < 2E_{Th}$. In this case, the contamination is ruled out by the two photons mass cut: $X_{\omega\ in\ \pi^0} = 0$

- $E_{\pi^0} > 2E_{Thr}$. In that case, there may be up to 3 clusters. Events are either removed from data sample (in case of 3 clusters), or cut by missing mass cut or two photons mass cut. The contamination is $X_{\omega\ in\ \pi^0} = 0$ but we have correlations between missing mass squared cut and calorimeter threshold.

The ratio $E_{\pi^0} < 2E_{Thr} \Leftrightarrow \frac{E_{\pi^0}}{2E_{Thr}}$ has been plotted for Kin2 and Kin3, considering their optimal calorimeter threshold in 4.9. This figure shows that this ratio is below 1 for each

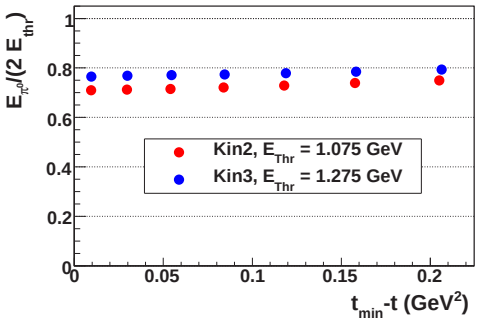

Figure 4.9: contamination of π^0 data by $\omega \to \pi^0\gamma$ as a function of $t_{min} - t$, for Kin2 and Kin3 at their respective optimal calorimeter threshold.

t_{min-t} bin, showing that M_X^2 cut and E_{Thr} are not correlated by ω contamination. Finally, the contamination of π^0 electroproduction by ω is determined by the missing mass squared cut only.

4.5 Systematic Errors

The systematic errors originate from several sources. There are instrumental sources of systematic errors, and the systematics which come from the extraction method, and particularly on the values of certain cuts liable for physics such as the missing mass cut. We emphasize the systematics due to the missing mass squared cut on the one hand, and due to the calorimeter threshold on the other hand. The estimations for the instrumental systematic errors are listed, and summarized.

4.5.1 Systematic effect due to M_X^2 cut

The systematic effect due to the exclusivity cut is due to inclusive channels which can be observed in the missing mass squared distribution shown on Fig. 3.15. The variation of this cut may vary the cross section because of these inclusive channels, which are not simulated, but may be included in the data yields, depending on the M_X^2 cut value.

The method to estimate the systematic effect of the cut on the cross section is to observe the cross section dependence on the cut. The estimator used is:

$$R = \frac{\sum_{Bin=0}^{6}(r_T + \epsilon_L r_L)(\text{Cut})}{\sum_{Bin=0}^{6}(r_T + \epsilon_L r_L)_{\text{optimal cut}}}. \tag{4.51}$$

This quantity is plotted as a function of the M_X^2 cut on Fig. 4.10. On this figure we observe, as expected, the increase of the cross section along with the missing mass cut increase above the interval of stability. However, we do not observe the expected stability

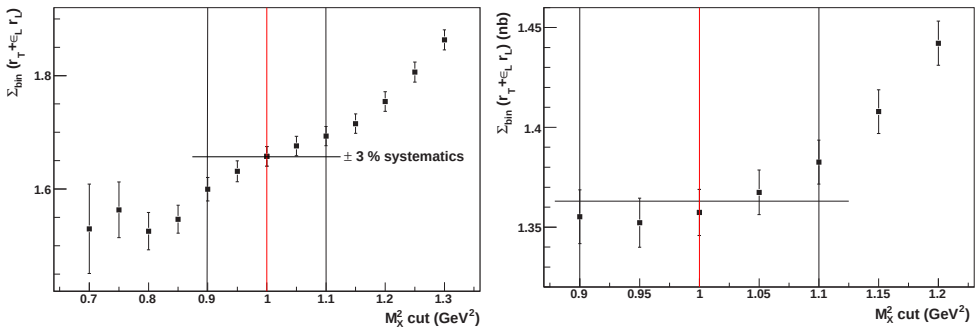

Figure 4.10: Total cross section integrated over $t_{min} - t$ and ϕ_π, for Kin2 (left) and Kin3 (right), as a function of the M_X^2 cut. The vertical lines indicate, from left to right, the minimal, optimal and maximal M_X^2 cut values of the stability domain.

either for Kin2 and Kin3, although the systematic errors are larger for Kin2 (3 % systematic error for Kin2, meanwhile only 1.5 % for Kin3). The lower boundary of the interval has been set for statistics reasons. The interval of stability and the optimal exclusivity cut has been given for both kinematics in Table 4.6.

4.5.2 Systematic effect due to E_{Thr}.

The influence of the calorimeter threshold to the cross section comes, again, from a difference between the data yields and the simulation yields. There are two types of threshold:

- The hardware threshold, which is fixed by the trigger.
- The software threshold, which is the analysis cut, set stronger than than the hardware threshold.

We plot the quantity given in Eq. (4.51) as a function of the software threshold on Fig. 4.11. The stability of the cross section is observed when the software threshold is above

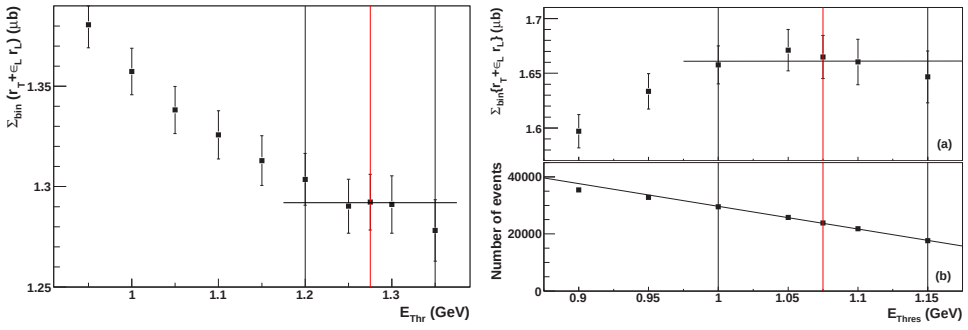

Figure 4.11: (a): Total cross section integrated over $t_{min} - t$ and ϕ_π, for Kin2 (left) and Kin3 (right), as a function of E_{Thr}. The vertical lines indicate, from left to right, the minimal, optimal and maximal E_{Thr} values of the stability domain (see Table 4.6 for Kin3 values). (b): The number of events as a function of E_{Thr}. The stability domain for E_{Thr} shows the statistics linearly decreasing with E_{Thr}.

the hardware threshold and dominates. The upper boundary of the stability interval has been fixed for statistics reasons.

Variable	Minimum	Optimum	Maximum
Kin3 / KinX3			
M_X^2 cut (GeV^2)	0.90	1.00	1.10
E_{Thr} (GeV)	1.20	1.275	1.35
Kin2 / KinX2			
M_X^2 cut (GeV^2)	0.90	1.00	1.10
E_{Thr} (GeV)	1.00	1.075	1.15

Table 4.6: Values of the M_X^2 cut and E_{Thr} defining the global cross-section stability domain. Minimum and Maximum are the bounds of this domain, and Optimum is the cut value set in the middle of the stability interval.

4.5.3 Summary of systematic errors

The interval of stability and the optimal software calorimeter threshold are given for both kinematics in Table 4.6. The reduced structure functions r_Λ are extracted at the optimal value of the cuts. The systematic errors are taken as the maximum difference between the r_Λ computed at the optimum cuts and the r_Λ computed at each of the four extremities of the stability domain.

In Table 4.7 are listed all instrumental sources of systematics effects, and their magnitude. All these errors are independent and are added quadratically. The first "Total Quadratic" row is the total instrumental systematic error on all helicity-independent cross section contributions. The second one is the total instrumental systematic error on the helicity-dependent term.

	Kin3 KinX3	Kin2 KinX2
Exclusivity cut	1.5 %	3.0 %
Calorimeter threshold	1.0 %	
HRS acceptance	2.2 %	
Radiative corrections	1.5 %	
Target length	0.5 %	
Hadronic tensor integration	0.3 %	
Multi tracks corrections	0.1 %	
3 clusters corrections	0.1 %	
Luminosity	0.1 %	
Dead time	0.1 %	
Particle identification	0.1 %	
Total Quadratic	3.3 %	4.2 %
Beam polarization	2.0 %	
Total Quadratic	3.9 %	4.6 %

Table 4.7: Experimental systematic errors. The first "Total Quadratic" row shows the quadratic sum of all experimental helicity-independent systematic errors. The second "Total Quadratic" row shows the quadratic sum of all experimental systematic errors including helicity-dependent effects.

4.6 π^0 cross section results cross check

A cross check of the π^0 cross section results is performed evaluating, by two different methods, the proportion of one-cluster π^0 events contaminating DVCS statistics. If the π^0 decay is very asymmetric, one of the two photons shall not pass the trigger, meanwhile the other might have enough energy to mimic a DVCS photon. Therefore, this type of events contaminate DVCS statistics. To evaluate the contamination of DVCS statistics by one-cluster π^0 events, one needs to know the number of π^0, and the fraction of π^0 giving one cluster in the calorimeter. One may either start with the raw two-cluster event statistics and determine the probability of each pion to give only one cluster (first method, used for DVCS analysis), or start with the pion cross section, and determine thanks to the simulation the total number of one-cluster events (second method). Each of the two methods shall give the same result. Thanks to this, we may test the reliability of the cross section.

4.6.1 Evaluation of DVCS/π^0 contamination: DVCS analysis method

This method has been exposed within extensive details in [76]. In the first method we select inclusive π^0 events, that means we select the 2-cluster sample with cuts listed in Table 4.2 except the exclusivity cut. We reconstruct the pion, and we simulate its decay in two photons a large number of times $N = 5000$. Note the pion is selected with the calibration applied, but it is reconstructed without applying the calibration. Practically, we simulate the isotropic decay of the resonance at the actual mass $m_{\gamma\gamma}$ for each event. Finally, the allowance of both photons in the rest frame within cuts are checked.

If both photons are in the acceptance, we count them. If only one photon is in the acceptance, we compute its supposed quadrimomentum transfer, t, its $\phi_{\gamma\gamma}$, and its missing mass squared, $M^2_{X\ DVCS}$, as if it was a real DVCS photon. This photon has finally to pass the DVCS exclusivity cut, requiring $M^2_{X\ DVCS} < 1.15$ GeV^2. When all decays are simulated for a real 2-cluster event, we have:

- n_0 decays leading to no cluster;
- n_1 decays leading to a 1-cluster event;
- n_2 decays leading to a 2-cluster event.

Each 1-cluster event with a value t, $\phi_{\gamma\gamma}$ populates the corresponding DVCS t and $\phi_{\gamma\gamma}$ bin, and are ponderated by

$$W_i = \frac{1}{n_2}. \tag{4.52}$$

The DVCS/π^0 contamination yields obtained by this method are available on the upper panels of Fig. 4.12 (black histograms).

4.6.2 Evaluation of DVCS/π^0 contamination: Direct method

For this method we consider the 1-cluster π^0 simulation. We select the π^0 sample with the spectrometer cuts given in Table 4.2. We also apply the calorimeter threshold and acceptance cuts for the measured cluster. However, we do not apply any cut on the

missing mass squared, and it is not possible as well to apply a 2-gamma invariant mass, since one photon is not measured. These events were not calibrated with π^0 calibration as well.

For each event we compute, with the vertex variables, the $t_{min} - t$ generated for this event. We ponderate this event with the cross section weight given by the following expression:

$$W_{Xsec,i} = \frac{\left[\int \mathcal{L}dt\right] psf_i}{N_{gen}} \sum_{\Lambda} \mathcal{F}_{\Lambda}(x_v) r_{\Lambda} \times \frac{1}{[RadCor] \times [MulTrk] \times [TrClus]} \tag{4.53}$$

where:

- $[RadCor]$ is the intern virtual radiative correction
- $[MulTrk]$ is the HRS multi-track correction
- $[TrClus]$ is the triple-cluster event correction

Then, we compute the t and the $\phi_{\gamma\gamma}$ that the photon would have if it was a DVCS event.

The DVCS/π^0 contamination yields obtained by this method are available on the upper panels of Fig. 4.12 (red histograms).

4.6.3 Comparison between the two methods

The comparison between the method exposed in subsections 4.6.1 and 4.6.2 is summarized in Fig. 4.12. The ratio of the two DVCS/π^0 contamination yields obtained by the

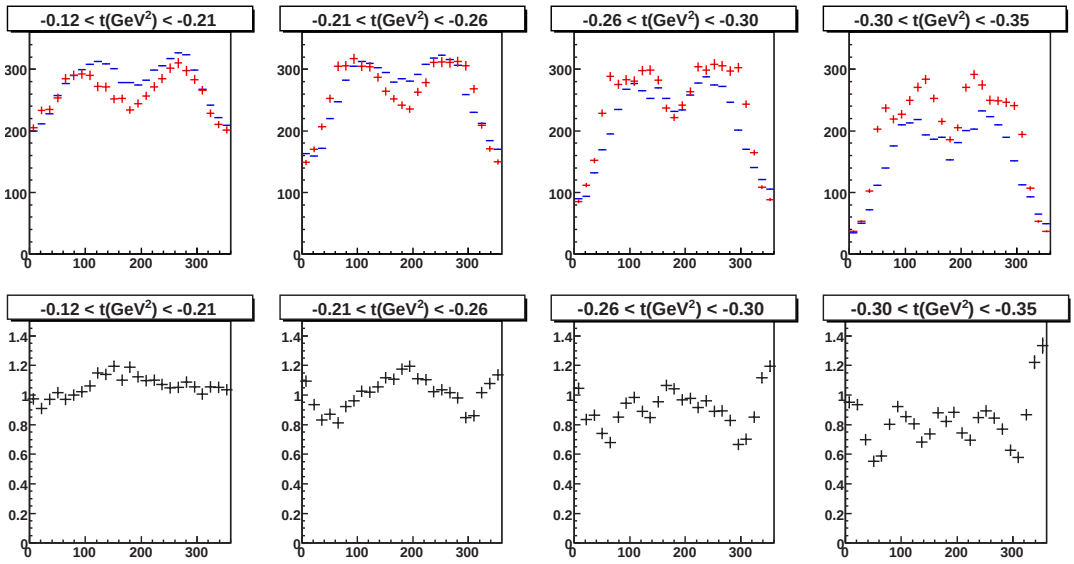

Figure 4.12: Comparison, for Kin2, between DVCS/π^0 contamination evaluated for the two different methods exposed in the text. On upper panel are plotted the contamination yields as a function of $\phi_{\gamma\gamma}$ for each DVCS t bin. Blue histograms are the estimations given by the method exposed in subsection 4.6.1, red histograms are the estimations given by the method exposed in subsection 4.6.2. On lower panels are plotted the ratio red histogram/blue histogram, each of the lower panel for its corresponding upper panel.

two different methods is equal to 1 on average, and fluctuates by $\sim 10\%$ on the lower t

bin, by 20 % for the intermediate t bins, and by 40 % for the higher t bin. Several tests of stability of both methods relatively to the calorimeter threshold have been performed, demonstrating the reliability of these methods, implying the reliability of the cross check and of the π^0 cross section results.

Chapter 5

Results and Discussion

This chapter is dedicated to the results of neutral pion analysis in Hall A. Our kinematical coverage allowed to separate all ϕ_π contributions to the $ep \to ep\pi^0$ cross sections, and to extract Q^2- and W-dependences. We show the π^0 electroproduction cross section components for Kin2 and Kin3, and for KinX2 and KinX3. These results are cross checked by a comparison between the method performed to subtract one-cluster π^0 from DVCS [36, 76] and a direct one-cluster π^0 subtraction method using the π^0 cross section. We confront these results with several models among those described in Chapter 1, including Regge-inspired calculations, GPD predictions and SIDIS approach.

In this chapter, the results are presented as the four cross section components following the usual decomposition found in the literature:

$$\begin{aligned}\frac{d^2\sigma_v}{dtd\phi_\pi} = \frac{1}{2\pi}\Big\{ & \frac{d\sigma_T}{dt} + \epsilon_L \frac{d\sigma_L}{dt} \\ & + \sqrt{2\epsilon_L(1+\epsilon)}\frac{d\sigma_{TL}}{dt}\cos\phi_\pi \\ & + \epsilon\frac{d\sigma_{TT}}{dt}\cos 2\phi_\pi \\ & + h\sqrt{2\epsilon_L(1-\epsilon)}\frac{d\sigma_{TL'}}{dt}\sin\phi_\pi \Big\}.\end{aligned} \tag{5.1}$$

5.1 Results for π^0 electroproduction.

The exclusive π^0 electroproduction cross section ϕ_π dependences were extracted for Kin2, Kin3, KinX2 and KinX3. The Q^2- and W-dependences of these cross sections have also been estimated. The tables of results, with statistics and systematic errors, are available in Appendix 1.

5.1.1 Cross sections results

We expose here the different ϕ_π contributions to $\mathrm{H}(e,e'\pi^0)p$ cross section for Kin2, Kin3, KinX2 and KinX3. For each of the following plots, the cross section has been computed from the extracted r_Λ value at the kinematics given in Tables 5.2 and 5.3. The latter table also gives the $t_{min} - t$ values where the data points are indicated for each bin.

Fig. 5.1 represents $\sigma_T + \epsilon_L\sigma_L$ for Kin2 and Kin3. These cross sections are rather flat in $t_{min} - t$, and they are about 0.4 (resp. 0.7) $\mu\mathrm{b}\cdot\mathrm{GeV}^{-2}$ for Kin3 (resp. Kin2). The

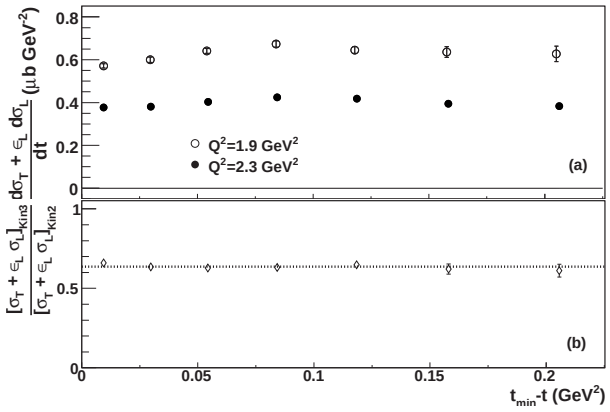

Figure 5.1: (a) separated $\mathrm{H}(e,e'\pi^0)p$ cross section $\sigma_T+\epsilon_L\sigma_L$ as a function of $t_{min}-t$ for $x_{Bj}=0.36$. Error bars represent statistical errors only. (b): ratio of $\sigma_T+\epsilon_L\sigma_L$ for the two kinematics as a function of $t_{min}-t$. The fit of this ratio (dashed line) indicates the Q^2-dependence of the cross section.

available statistics allowed us to achieve, for the ϕ_π-independent cross section, a statistical precision of 2.5%. For reasons of visibility, this calculation has been multiplied by a factor 10.

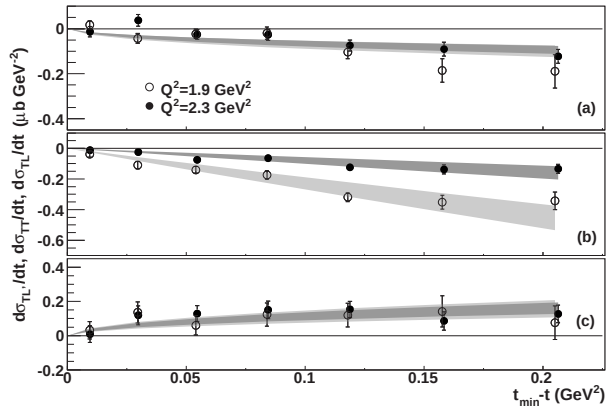

Figure 5.2: σ_{TL} (a), σ_{TT} (b) and $\sigma_{TL'}$ (c) $\mathrm{H}(e,e'\pi^0)p$ cross-section components as a function of $t_{min}-t$ for the two Q^2-values. Kin2 is represented by the open circles, and Kin3 by the solid circles. Error bars represent statistical errors only. The bands (light for Kin2 and dark for Kin3) are explained in the text. Refer to Table 5.4 for more detailed cross-section values, statistical and systematic errors.

σ_{TL}, σ_{TT}, and $\sigma_{TL'}$ are plotted as a function of $t_{min}-t$ for Kin2 and Kin3 on Fig. 5.2. We performed on these components fits proportional to $\sin\theta_\pi^{CM}$ (for σ_{TL} and $\sigma_{TL'}$), and proportional to $\sin^2\theta_\pi^{CM}$ (for σ_{TT}). These fits, including their statistical and systematic errors, are the bands represented on Fig. 5.2. Their reduced χ^2 are around 1.25, pointing a fair agreement with the data. This indicates that the main t-dependence of $\sigma_{TL,TL'}$, and σ_{TT} may be given by $\sin\theta_\pi^{CM}$ and $\sin^2\theta_\pi^{CM}$ respectively.

Fig. 5.3 shows $\sigma_T+\epsilon_L\sigma_L$ for KinX2 and KinX3. These data are within a statistical precision of about 5% for the total cross section.

Fig. 5.4 represents σ_{TL}, σ_{TT} and $\sigma_{TL'}$ for KinX2 and KinX3. The fits proportional to $\sin\theta_\pi^{CM}$ for σ_{TL} and $\sigma_{TL'}$, and proportional to $\sin^2\theta_\pi^{CM}$ for σ_{TT} are also represented. These fits, including statistical and systematic errors, are shown as bands in Figs. 5.2 and

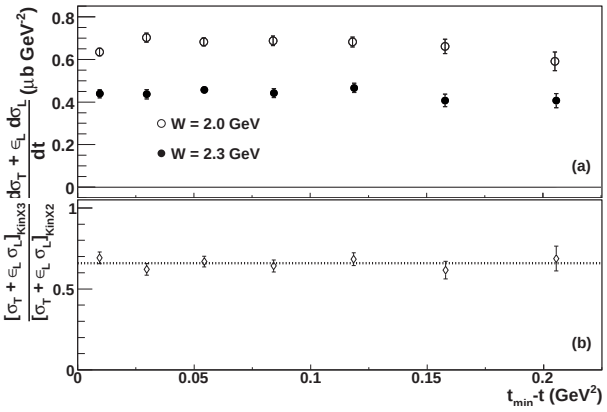

Figure 5.3: (a): Separated H$(e, e'\pi^0)p$ cross section $\sigma_T + \epsilon_L\sigma_L$ as a function of $t_{min} - t$ for $Q^2 = 2.1$ GeV^2. Error bars represent statistical errors only. (b) Ratio of $\sigma_T + \epsilon_L\sigma_L$ for the two kinematics as a function of $t_{min} - t$. The fit of this ratio (dashed line) indicates the W-dependence of the cross section.

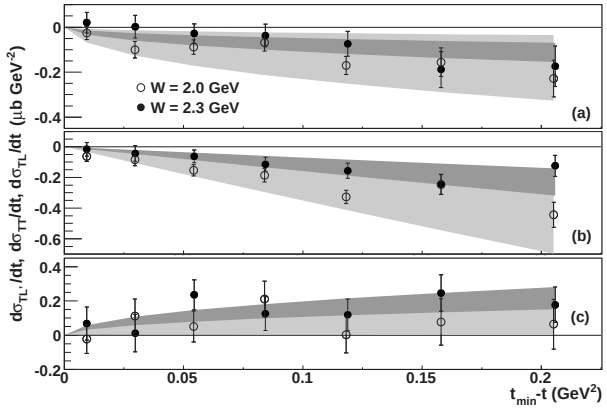

Figure 5.4: σ_{TL} (a), σ_{TT} (b) and $\sigma_{TL'}$ (c) H$(e, e'\pi^0)p$ cross-section components as a function of $t_{min} - t$ for the two x_{Bj}-values. KinX2 is represented by the open circles, and KinX3 by the solid circles. Error bars represent statistical errors only. The bands (light for KinX2 and dark for KinX3) are explained in the text. Refer to Table 5.5 for more detailed cross-section values, statistical and systematic errors.

5.4, and in Tables 5.6 and 5.7. Their reduced χ^2 are below 1, indicating a good agreement for our data. This confirms that there is no t-dependence beyond the angular dependence of the hadronic tensor for the ϕ_π-dependent components of the cross section.

The cross sections values plotted in all these figures are available in Tables 5.4 and 5.5 (Appendix 1), together with . All these results are cross-checked in section 4.6.

5.1.2 Q^2- and W- dependences of the cross section

We investigate the dependences of the cross sections on Q^2 and W, in order to compare them to QCD predictions at leading twist in GPD framework. To estimate the $Q^2(W)$-dependence, the ratio of $\sigma_T + \epsilon_L\sigma_L$ for Kin2 and Kin3 (KinX2 and KinX3) is plotted as a function of $t_{min} - t$ (see bottom panels of Figs. 5.1 and 5.3). This ratio is fitted by a constant. If the fit is reasonable (*i.e.* reduced χ^2 below or around 1), then it means that the ratio is independent of t. If so, the average value obtained from the fit which is then compared to the ratio of $Q^2(W)$ for Kin2 and Kin3 (KinX2 and KinX3) raised to

the power n

$$\frac{\sigma_T + \epsilon_L \sigma_L|_{Kin(X)3}}{\sigma_T + \epsilon_L \sigma_L|_{Kin(X)2}} = \left(\frac{Q^2(W)|_{Kin(X)3}}{Q^2(W)|_{Kin(X)2}} \right)^n . \tag{5.2}$$

at the W- and Q^2- values for the two kinematics.

The dependences of $\sigma_T + \epsilon_L \sigma_L$ in bottom panels of Figs. 5.1 and 5.3 yields the following conclusions:

- $[\sigma_T + \epsilon_L \sigma_L]_{Kin3} / [\sigma_T + \epsilon_L \sigma_L]_{Kin2}$ is flat in $t_{min} - t$ with a reduced $\chi^2 < 1$. The ratio is found to be 0.633 ± 0.009, indicating a Q^2-dependence of the total cross section of about $1/Q^{4.5}$;
- $[\sigma_T + \epsilon_L \sigma_L]_{KinX3} / [\sigma_T + \epsilon_L \sigma_L]_{KinX2}$ is also flat in $t_{min} - t$ with a reduced $\chi^2 < 1$. This ratio is found to be 0.660 ± 0.015, indicating a W-dependence of the total cross section of about $1/W^{3.5}$.

The Q^2- and W-dependences of the relevant quantities (σ_T, $\{W_{xx} + W_{yy}\}/2 + \epsilon_L W_{zz}$, σ_T, and σ_L, with VGG conventions) have been summarized in Table 5.1. The Q^2- and W-

Quantity	Q^2-dependence	W-dependence
$\sigma_T + \epsilon_L \sigma_L$	$(Q^2)^{-2.39 \pm 0.08}$	$(W)^{-3.48 \pm 0.11}$
$\frac{W_{xx}+W_{yy}}{2} + \epsilon_L W_{zz}$	$(Q^2)^{-1.26 \pm 0.08}$	$(W)^{-1.58 \pm 0.20}$
σ_L (VGG)	$(Q^2)^{-1.50 \pm 0.08}$	$(W)^{1.28 \pm 2.52}$

Table 5.1: Q^2- and W-dependences for the total cross section, the total hadronic tensor, and the longitudional cross section with VGG conventions. For σ_L, the dependences have been evaluated neglecting σ_T. The Q^2- and W-dependences of σ_T alone (*i.e.* assuming $\sigma_L = 0$) are the same as the Q^2- and W-dependences of $\sigma_T + \epsilon_L \sigma_L$.

dependences for the cross sections are rather low. The Q^2-dependence of the total cross section is similar to the Hall C π^+ transverse electroproduction cross section [15]. The dependences of σ_L are obtained within s-channel helicity conservation (implying $\sigma_T \ll \sigma_L$) which is most likely improbable. This, and other issues about the data will be discussed in the following section.

5.2 Discussion

In this section, I discuss the physics underlying our data. Particularly, I attempt to give a satisfying description of our data within one of the models presented in Chapter 1.

Over the studied $t_{min} - t$ range, the r_Λ values from Equations (4.20) and (4.21) are constant within errors, as evidenced by the fits in Figs. 5.2 and 5.4. This means that there is no supplementary contribution to the cross sections amplitudes beyond the leading angular dependences given by the phase space. Also, the total cross section $\sigma_T + \epsilon_L \sigma_L$ shows an almost flat behavior.

The Q^2-dependence of $\sigma_T + \epsilon_L \sigma_L$ is similar to the Hall C π^+ transverse electroproduction cross section [15]. In addition to that, neutral pion has no charge and no spin, so the virtual photon cannot couple directly to a π^0 from the pion cloud. Thus, in contrast with

charged pion electroproduction, where the pion pole contribution to σ_L is a significant channel, the total cross section for $ep \to ep\pi^0$ might be dominated by σ_T.

In addition to these remarks, we are interested in confronting our data and several models of neutral pion production. The cross section will be compared to Regge-based calculations from J. M. Laget [89] (section 1.3). The Q^2-dependence will be compared with QCD predictions in the GPD framework (section 1.4) Finally, we attempt on an interpretation of our data within semi-inclusive formalism (section 1.5).

5.2.1 Confrontation with Regge calculations

The latest development of Regge-inspired model is essentially due to J. M. Laget, M. Vanderhaeghen, and M. Guidal. This model is known as VGL. The description of this model is available in [19, 20].

The new feature of this model, compared to previous ones is the implementation of gauge invariance for the t-channel exchange. The t-channel pion diagram is indeed not gauge invariant by itself. Gauge invariance is obtained by reggeizing the s-channel (or u-channel) nucleon exchange (Fig. 1.5) the same way the t-channel has been reggeized. We multiply the $s(u)$-channel amplitude by $\mathcal{P}^{\pi}_{Regge} \times (t - m_{\pi}^2)$. The reggeized $s(u)$-channel diagram and t-channel diagrams together satisfy gauge invariance.

This model takes advantage of previous Regge analysis of photoproduction data to fix propagator trajectories and coupling constants at vertices. This gives to the model a predictive property.

On another side, a further development of this model has been done to express charged pion electroproduction cross sections as a function of form factors with Regge trajectories instead of Born term [18]. That model allows then to optimize the charged pion form factor extraction (see sub-section 1.2.2).

J. M. Laget proposes a modelization for π^0 electroproduction, derived from VGL. This modelization includes the ω, the ρ^0 and the b_1 pole trajectories (Fig. 5.5 a). As well as Goldstein and Owens [30] it includes π^0 rescattering amplitudes (Fig. 5.5 b). It even includes several inelastic rescattering terms, such as charged pion rescattering with charge exchange (Fig. 5.5 c).

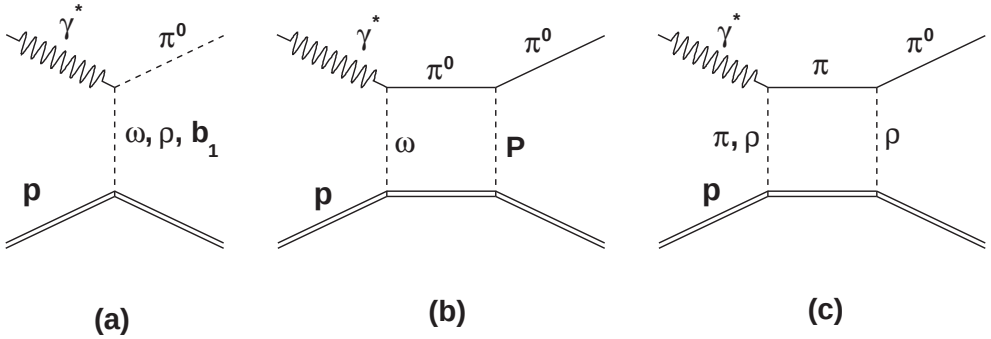

Figure 5.5: Diagrams of neutral pion production in J. M. Laget model: (a) is the pole trajectories term, (b) is the elastic rescattering term, and (c) is the inelastic rescattering term.

The results of these calculations are available on Fig. 5.6. Only considering charged

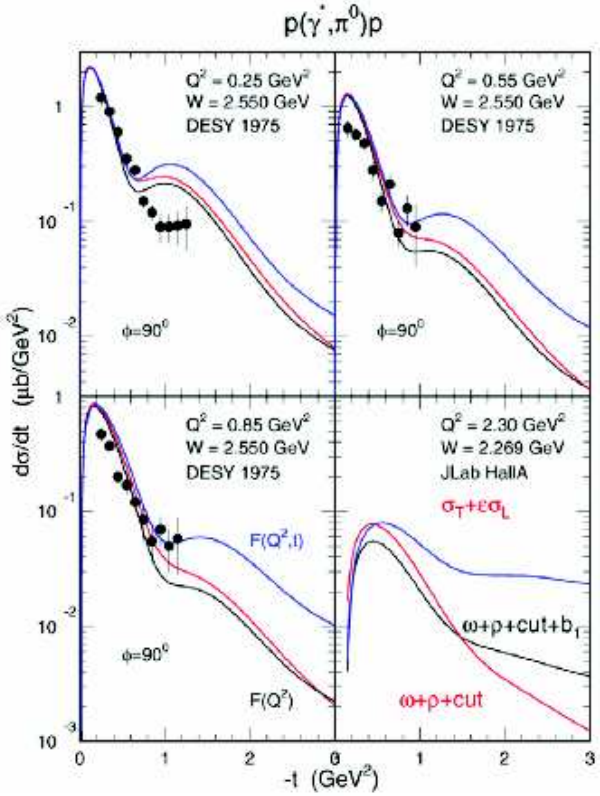

Figure 5.6: Computations of Jean Marc Laget [89] for π^0 electroproduction. The data are from [31]. In the lower right panel is the prediction for our data within [89] framework.

pion rescattering in inelastic rescattering term, the model by J. M. Laget is able to describe low Q^2 electroproduction cross section data from DESY [31] (see Fig. 5.6), and π^0 beam spin asymmetries at $1.5 < Q^2(\text{GeV})^2 < 3$ and $2 < W(\text{GeV}) < 3$ from JLab Hall B [90]. Similar computations have been done with this model for π^+ data from Hall C [14, 15], including the pion pole. These data are π^+ electroproduction cross sections at $Q^2 = 1.60$ and 2.45 GeV^2 for [14] (resp. $Q^2 = 2.15$ and 3.90 GeV^2 for [15]) with a transverse-longitudinal separation. The model successfully describe the longitudinal cross section. The transverse cross section however cannot be described by the model including only pion rescattering.

The t-channel Meson Exchange (TME) model calculations by J. M. Laget for Kin3 are shown alone on Fig. 5.6. On the one hand, the TME calculation for the total cross section (Figs. 5.6 and 5.1) shows a dip at $t = t_{min}$, and at $t_{min} - t = 0.2$ GeV^2, the total cross section is about 0.05 $\mu\text{b} \cdot \text{GeV}^{-2}$. On the other hand, the total cross section is about 0.4 $\mu\text{b} \cdot \text{GeV}^{-2}$ over all the $t_{min} - t$ range. This makes a disagreement by at least a factor 10 between our data and the TME model calculation, as well as a disagreement in shape. One should note however that this model fairly describes π^0 beam spin asymmetries published by R. De Masi for Hall B [90], which is in agreement with the beam spin asymmetry we can compute thanks to $\sigma_{TL'}$.

A further improvement of this model [89] is the consideration of ρ^+ rescattering. It used to be considered as negligible for photoproduction and low Q^2 data. At larger Q^2, the ρ electroproduction cross section is high enough to give a non negligible contribution

at $Q^2 > 1$ GeV^2, without influencing data at low Q^2.

This t-channel meson exchange model only includes ω and ρ^0 channels, plus charged pion rescattering with charge exchange. Another more recent calculation by J. M. Laget includes charged ρ production, including nucleon and Δ resonances ($\rho^+\Delta^0$ and $\rho^-\Delta^{++}$) in the intermediate state [89]. The addition of these channels greatly improves the agreement of the model to our data (see Fig. 5.7). This improvement of the t-channel meson exchange

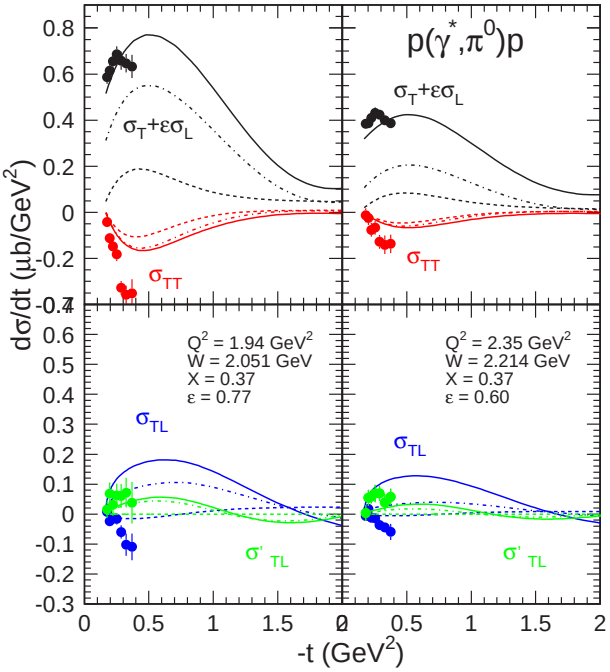

Figure 5.7: New calculations, at Kin2 (left panels) and Kin3 (right panels) of the t-channel meson exchange model. Dashed lines: pole contributions and Pomeron cut alone. Dash-dotted lines: without $\rho\Delta$ cuts. Full lines: $\rho\Delta$ cuts included.

model has been made possible thanks to measurements of ρ^+ electroproduction by Fradi *et al.* [91]. This new model of π^0 electroproduction reproduces fairly well $\sigma_T + \epsilon_L\sigma_L$ and $\sigma_{TL'}$. Note however that if the agreement with $\sigma_T + \epsilon_L\sigma_L$ is greatly improved, there remains a point of disagreement concerning the sign of σ_{TL}, and the magnitude of $\sigma_T T$.

5.2.2 Confrontation with GPD predictions

To test whether our data are compatible with GPDs predictions, we compare the Q^2-dependences of the measured cross sections to the GPD predictions at the asymptotic limit, which are $1/Q^6$ for σ_L (within [34, 35] conventions) and $1/Q^8$ for σ_T. Table 5.1 lists the Q^2 dependences for the $\sigma_T + \epsilon_L\sigma_L$ and σ_L within the conventions of [34, 35]. Within these conventions, the longitudinal cross section we extracted (assuming we could neglect σ_T, which is very unlikely) would depend on $(Q^2)^{-1.50}$, which disagrees by more than one power with the asymptotic $(Q^2)^{-3}$ dependence. The transverse cross section is also in disagreement by more than one power ($(Q^2)^{-2.39}$ instead of $(Q^2)^{-4}$) with the Q^2-dependence in the Bjorken regime ($Q^2 \to \infty$ and $t/s \to 0$). This is a strong proof that we are far from the QCD leading twist prediction.

5.2.3 Interpretation within semi-inclusive framework

The description of the transverse cross sections σ_T of exclusive processes with inclusive formalism is possible, within high intrinsic transverse momenta of partons, or, which is equivalent, a high transfer of transverse momentum during the quark hadronization. The work of Kaskulov, Gallmeister and Mosel [92] could be a beginning for a SIDIS-based formalism dedicated to the description of exclusive data.

The starting point of the Kaskulov Gallmeister Mosel model is the work of Horn *et al.* [14, 15]. They published $ep \rightarrow en\pi^+$ cross sections with transverse-longitudinal separation, at $Q^2 = 1.60$ and 2.45 GeV^2 [14] and $Q^2 = 2.15$ and 3.90 GeV^2 [15], in the valence region ($x_{Bj} \simeq 0.3$), and above the resonance region ($W > 2$ GeV). As we evoked in sub-section 5.2.1, Regge based models such as VGL [19, 20, 18] describe really well the longitudinal cross section. In contrast with this, the Regge predictions given by the previously cited models disagree by more than one order of magnitude with the measured transverse cross section, and this disagreement increases with Q^2.

The exclusive π^+ total cross section calculations by Kaskulov, Gallmeister and Mosel (KGM) (shown on Fig. 5.8) combines independent recalculation with a Regge model (red curves on Fig. 5.8) using similar theoretical VGL ingredients (refer to sub-section 5.2.1) for σ_L on the one hand; and estimation of inclusively produced pions in the forward direction for σ_T on the other hand. This is on the latter item we wish to insist on in this sub-section.

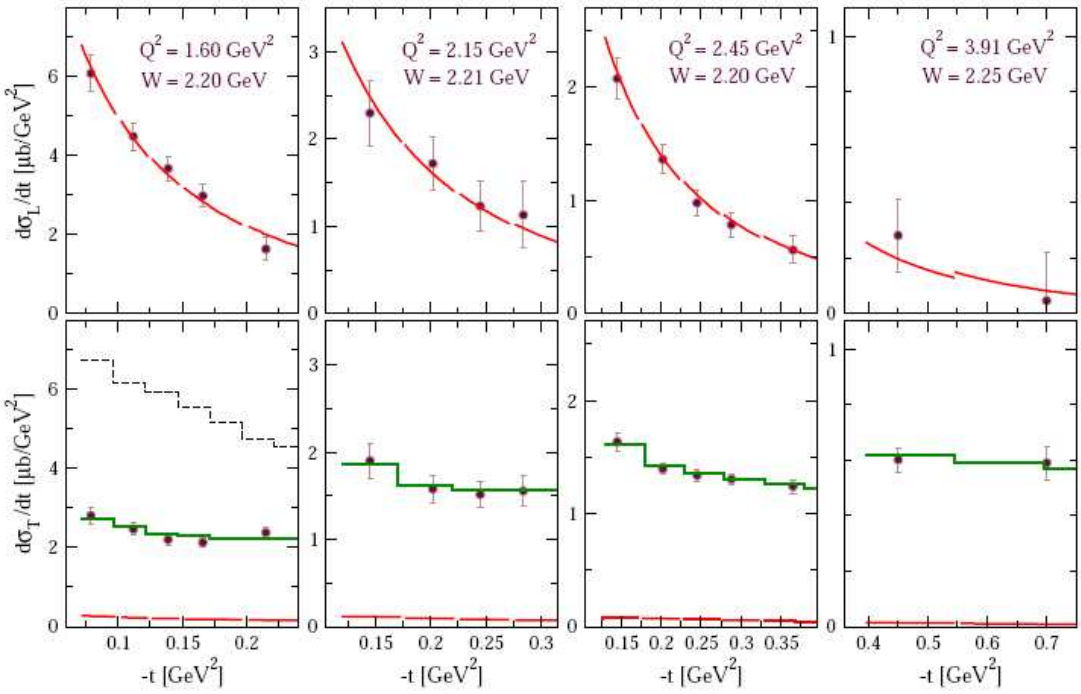

Figure 5.8: longitudinal (upper panels) and transverse (lower panels) cross sections by Horn *et al.*. The red curves are the Regge calculations by Kaskulov, Gallmeister, Mosel. The discontinuities are due to the slight differences of kinematics from one t bin to the other. The green histograms on lower panels are the calculations of the inclusive model by Kaskulov, Gallmeister, Mosel, using the optimized value parameter $\sqrt{\langle k_{q\perp}^2 \rangle} = 1.2$ GeV. The dashed histogram in lower left panel is the same calculation at $\sqrt{\langle k_{q\perp}^2 \rangle} = 0.4$ GeV.

The model of transverse pion production is directly inspired by the model of the SIDIS

process (see 1.5):

- the virtual photon strikes a quark with an intrinsic transverse momentum $k_{q\perp}$;
- this excited quark tries to escape the nucleon, but is retained by the color interaction;
- this interaction increases with the distance of the quark from the relic nucleon (or di-quark), but the gluons carrying this interaction remain confined in a tube, the so-called "color string";
- at "medium" distance this string breaks, the quark hadronizes in the required hadron;
- in contrast with a classic DIS process, where the string breaks in several other hadrons and/or destroys the di-quark, the breaking of the string only hadronizes the single quark into the measured hadron, and the di-quark into the recoil nucleon.

The process described is schematized on Fig. 5.9. This model corresponds to the so-

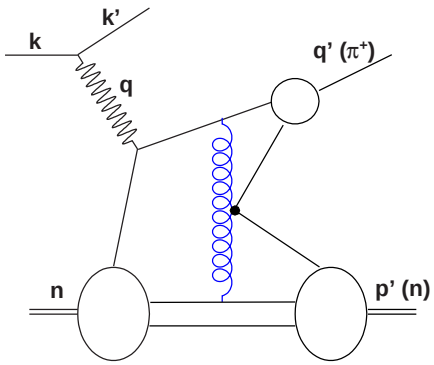

Figure 5.9: Diagram of exclusive electroproduction of π^+ according to the Lund model. Note the blue curly line does not represent a gluon, but the color string. The black blob represents the breaking of this string.

called Lund model, which describes quark hadronization in terms of color strings breaking (fragmentation). The Lund model is explained in extensive detail in [48].

To implement these calculations, KGM uses the framework of PYTHIA/JETSET. These two tools are usually employed to generate high energy proton-proton collisions in hadron colliders, such as the TeVatron or the LHC. In that case, PYTHIA simulates the parton-parton interaction. It includes common parton distributions, and a parton intrinsic transverse momentum gaussian distribution, which deviation $\sqrt{\langle k_{q\perp}^2 \rangle}$ can be tuned. JETSET simulates the quark fragmentations in jets. It includes common fragmentation distributions. Thus, PYTHIA has been used for electron-proton interaction, and JETSET for the hadronization of the quark and the di-quark in a π^+ and a neutron respectively. They started from the default configuration of PYTHIA/JETSET, and tuned only the intrinsic transverse momentum gaussian distribution deviation $\sqrt{\langle k_{q\perp}^2 \rangle}$. The best description of the data is obtained for $\sqrt{\langle k_{q\perp}^2 \rangle} = 1.2$ GeV (green histograms on Fig. 5.8). This

value is fairly higher than the default value, which is about 0.25 GeV. A lower value for $\sqrt{\langle k_{q\perp}^2 \rangle}$ (e.g. by the authors 0.4 GeV) increases the cross section at forward angles and the cross section slope (dashed histogram on Fig. 5.8). The necessity of such a high transverse momentum for partons may actually come from the hadronization, since the fragmentation functions do not scale at high z values.

This model allows to formulate some hope for an interpretation of exclusive data within a semi inclusive framework. The Q^2-dependence of the measured $ep \to ep\pi^0$ cross section is similar to the Q^2-dependence of the Hall C $ep \to en\pi^+$ transverse cross section which has been successfully described by the model presented above. Moreover, as we pointed out at the beginning of this section, the transverse current is likely to dominate the cross section. For these reasons, we consider our data within the context of Semi-Inclusive Deep Inelastic Scattering (SIDIS).

In the exclusive regime ($z \to 1$), we do not have a reliable parameterization of $D_q^h(z)$. This is the reason why we cannot compare directly the cross sections. The idea to perform our analogy then is to compare the relative value of the Cahn effect ($\cos\phi$ term in Equation (1.56)) to the total cross section. The relative ratio of these two quantities is given by [51]:

$$\frac{4(2-y)\sqrt{1-y}z\langle k_{q\perp}^2\rangle \mathbf{q}'_T}{\langle \mathbf{q}_T'^2\rangle \sqrt{Q^2}} \times \frac{1}{(1+(1-y)^2)}. \tag{5.3}$$

This quantity is compared to the experimental ratio $(\sqrt{2\epsilon_L(1+\epsilon)}\sigma_{TL})/(\sigma_T+\epsilon_L\sigma_L)$ at the two kinematic points Kin2 and Kin3, and at each $t_{min}-t$ value. In Equation (5.3), the only quantities that are not kinematically constraints are $\langle k_{q\perp}^2\rangle$ and $\langle \mathbf{q}_T'^2\rangle$, or equivalently $\langle k_{q\perp}^2\rangle$ and $\langle q_\perp'^2\rangle$, since $\langle \mathbf{q}_T'^2\rangle = \langle q_\perp'^2\rangle + z^2\langle k_{q\perp}^2\rangle$. With this last relation, we rewrite Equation (5.3) as:

$$\frac{4(2-y)\sqrt{1-y}z_\pi \mathbf{q}'_T}{\left(\frac{\langle q_\perp'^2\rangle}{\langle k_{q\perp}^2\rangle}+z^2\right)\sqrt{Q^2}(1+(1-y)^2)} \tag{5.4}$$

The adjustment of this relation to our data only requires the variation of $\langle q_\perp'^2\rangle/\langle k_{q\perp}^2\rangle$. This adjustment is shown on Fig. 5.10. The reduced χ^2 of these fits are 2.12 for Kin3 and 2.65 for Kin2. Two conclusions arise from this figure:

- the minus sign affecting the $\cos\phi_\pi$ term in the SIDIS model is in agreement with the σ_{TL};
- $\langle q_\perp'^2\rangle$ must be equal to $\sim 5.0 \times \langle k_{q\perp}^2\rangle$ to reproduce the data.

In other words, the data is compatible with the Cahn effect if $\sim 5.0 \times \langle k_{q\perp}^2\rangle$.

The authors of [51] adjusted their model to semi-inclusive data from the EMC collaboration [93]. They give $\langle k_{q\perp}^2\rangle = 0.25$ GeV^2 and $\langle q_\perp^2\rangle = 0.20$ GeV^2, which gives a ratio $\langle q_\perp'^2\rangle/\langle k_{q\perp}^2\rangle \sim 0.8$. Their fits are shown in Fig. 5.11. Note on this figure that the lower the z, the better the agreement between model and data. This may explain the difference between their adjustment and ours. They extracted these values on data with high multiplicity of particles, whereas the multiplicity of particles is unity for our data.

Our data are consistent with an exclusive limit of SIDIS if $\langle q_\perp'^2\rangle/\langle k_{q\perp}^2\rangle$ is around 5.0 at $z_h > 0.9$. The exclusive limit of SIDIS could be defined by a SIDIS-inspired model applicable to data at $z \to 1.0$ or, more practically, when the measured hadron carries such

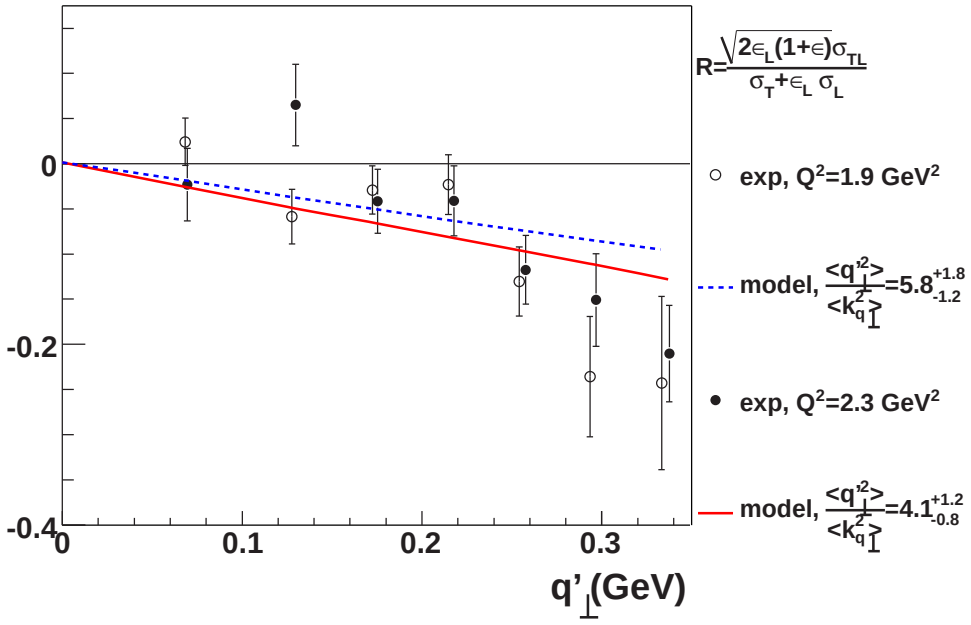

Figure 5.10: Ratio $\frac{\sqrt{2\epsilon_L(1+\epsilon)}\sigma_{TL}}{\sigma_T+\epsilon_L\sigma_L}$ for Kin2 (open circles) and Kin3 (solid circles) plotted as a function of $\mathbf{q}'_T$. The error are statistical only. Each kinematics is fitted by the model by Anselmino *et al.* in [51].

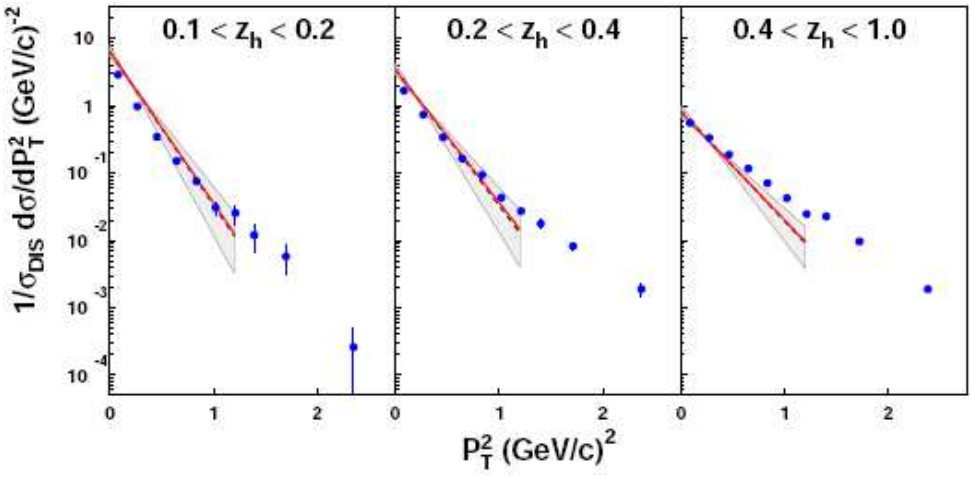

Figure 5.11: Fit of the data from [93] by the model of Anselmino *et al.* [51]. Data are plotted as a function of $\mathbf{q}'^2_T$ (noted P_T^2 here) and integrated over three ranges in z (noted z_h here): $0.1 < z < 0.2$, $0.2 < z < 0.4$, and $0.4 < z < 1.0$. The bands represents variations of $\pm$ 20 % for $\langle k^2_{q\perp}\rangle$ and $\langle q^2_\perp\rangle$.

a large fraction z of the total energy of the reaction that it does not allow the production of another particle.

We can compare this data within SIDIS interpretation to the π^+ cross section data published by T. Horn for Hall C collaboration and the work of Kaskulov, Gallmeister and Mosel. It is reasonable to think our longitudinal cross section could be described by Regge calculations, or be compatible with leading twist QCD scaling.

Kaskulov *et al.* reproduced transverse π^+ cross section from Hall C using jet fragmentation model, and adjusting the slope parameter of the quark transverse momentum distribution $\langle k^2_{q\perp}\rangle$ (Chapter 1.5 for definitions), neglecting the transverse momentum transfer

occuring during the $\langle q_\perp'^2 \rangle$ (that means $\langle k_{q\perp}^2 \rangle$ is actually the slope parameter for the transverse momentum of the measured hadron). We recall that they found this parameter to be $\langle k_{q\perp}^2 \rangle = 1.44$ GeV^2. If we consider our model, where $\langle q_\perp'^2 \rangle / \langle k_{q\perp}^2 \rangle \sim 3.0$, and we choose the slope parameter of the quark transverse momentum distribution to be the one given in [51], we get a slope parameter for the measured transverse momentum of the hadron $\langle \mathbf{q}_T'^2 \rangle \sim 1.0$ GeV^2, which is roughly consistent with the work of Kaskulov *et al.*.

Let us summarize on the interpretation of our data:

- the GPD model is very wrong to describe $\sigma_T + \epsilon_L \sigma_L$;
- the data are consistent with the Cahn effect proper to SIDIS, but we do not have a description of the cross section by a semi-inclusive formalism;
- the Regge model can predict $\sigma_T + \epsilon_L \sigma_L$ but struggles with σ_{TL} and σ_{TT}.

Another experiment with complete Rosenbluth separation needs to be performed for a better description of the data. This would improve our knowledge on of σ_L, and help to determine the reliability of a description in the GPD framework. Moreover, a transverse longitudinal separation would make PYTHIA/JETSET calculations by Kaskulov/Gallmeister/Mosel easier to apply to π^0 [94].

Conclusions

The DVCS/π^0 experiment at Jefferson Lab, Hall A successfully provided accurate cross section results for π^0 production [95] and for DVCS [36], in spite of a high-radiation environment, due to high luminosities ($\sim 10^{37}$ cm^{-2}s^{-1}), and small detection angles. This is a combined tribute to the HRS and the calorimeter. The left HRS allows to reconstruct an electron with a precision of 10^{-3} in position/direction, and to the 10^{-4} in momentum. It also reconstructs the vertex within $\sim$ 2 mm for our settings. The calorimeter allows the reconstruction of the photon energy with a resolution of $5\%/\sqrt{E}$ at 4.2 GeV, and the photon position in the calorimeter at the 2 mm level. This allows to achieve, for π^0 total cross section $\sigma_T + \epsilon_L\sigma_L$ statistical accuracies of 2.5 % for Kin2 and Kin3 and of 5 % level for KinX2 and KinX3. The accurate instruments on the beam line and in the detector package of the HRS combined with our cut optimization give systematic errors up to 10 % for the total cross sections for all considered kinematics.

The π^0 cross sections were rather difficult to interpret clearly. Let us review, among the models confronted to the data, which ones are able to describe these data:

- we are far from the Bjorken regime and the data do not obey to QCD leading twist behavior.
- on the one hand, the t-channel meson exchange model of J. M. Laget only including ω and π^+ completely failed to reproduce the data. On the other hand, the description of the data by the t-channel meson exchange model including all channels involving $\rho^\pm$ is in fair agreement with the data at Kin3;
- the attempt of interpretation of the π^0 data with a semi-inclusive formalism is compatible with the Cahn effect.

Actually, the latter interpretation is not even completely satisfying from a theoretical point of view. The problem with the SIDIS interpretation model comes from the scaling violation of the fragmentation functions at low multiplicity/high z. Thus, it is hard to give a reliable and accurate estimation of the unpolarized TMD with huge systematic errors on the fragmentation function.

A better understanding of our data would require a measurement of σ_L independent of σ_T. For this, a complete Rosenbluth separation is required. This is why a new DVCS/π^0 experiment has been planned in Hall A. This experiment has many features in common with the last one:

- the studied kinematic range will be the same, and we keep the same settings. There will be several beam energies: the maximal energy at 5 passes (hopefully the same energy or above compared to last DVCS experiment) and the beam at 4 passes. A 3 pass beam is also planned for a $Q^2 = 1.5$ GeV^2 kinematic point;

- the detector package of the HRS and the beam line will be the same. However, independently of this experiment, an upgrade of the Compton polarimeter has been performed;

- the layout for the calorimeter will remain the same. To protect the most exposed blocks of the calorimeter from the noise, a shielding has been developed. This shielding includes a thickness of polyethylene in front of the calorimeter, plus a beveled edge made out of tungsten to protect the first block row of the calorimeter from the hot radiation spots in the scattering chamber and the beam line;

- the calorimeter has been upgraded from 132 (12×11) blocks to 208 (16×13) blocks, in order to improve its acceptence, mostly for π^0. Otherwise, the specifications as well as the block design are the same. The ARS have been kept for the readout;

- several changes are applied to the trigger. First, the calorimeter event selection has been changed. The "four-block cluster" threshold is too tight for π^0, particularly for Kin 1. The next calorimeter trigger would rather consider the global energy deposit in the calorimeter, which would improve the statistics for Kin1, and allow to extract π^0 cross sections at this kinematic point. Secondly, the trigger has been upgraded with a FIFO (First In First Out) device, in order to stock events which have to be read-out meanwhile the DAQ can be reset to ENABLE. This would greatly reduce the effect of the dead time (hopefully by up to a factor of 10). Finally, and to improve the consideration of the background noise, a random trigger has been developed. This trigger will register background at random positions and random times. It will be possible then to use these "background" data for studies. The price to pay for these improvements will be a huge volume of data;

- the proton array, which was not fully useful for π^0 or for DVCS analysis, has simply been given up. In both analysis, the resolution on missing mass squared is good enough for exclusive events selection.

During the time this document is been written, the upgrade is implemented by my collaborators and myself. The main requirements are the increase of the number of channels of the calorimeter. One hundred new PbF_2 blocks have been ordered from SICCAS. These blocks have been tested for radiations damages. New Hamamatsu R7877 PMTs have been purchased for the supplementary channels, and to replace the ones which died because of the two high anode current due to noise at the end of the previous experiment. The new blocks are being wrapped and assembled. This required the manufacturing of new brass assemblies. The wrapping/assembling of the old blocks has to be renewed. The number of channels actually did not increase, and was even reduced (132+125 before vs 208 now), so the ordering of cables were necessary only to replace the broken ones. The calorimeter stand is being renovated and the shielding is being manufactured.

At the same time, the analysis codes are being actualized. Several calibrations methods have been developed for the calorimeter.

The measurements provided by this new experiment would hopefully be at the same precision level. These new data, put in parallel with the old ones, and, hopefully, with Hall B π^0 cross section which are still under analysis, may lead to a better understanding of the data presented in this document.

Appendix 1: Tables of kinematics and results for $\mathrm{H}(e, e'\pi^0)p$ cross sections

These are the tables for π^0 electroproduction cross sections shown in Figures 5.1, 5.2, 5.3, 5.4 and 5.10 in Chapter 5. The actual kinematics are summarized in Table 5.2 for quantities independent of the $(t_{min} - t)$ bin and in Table 5.3 for quantities depending of the $(t_{min} - t)$ bin. The cross section are displayed in Tables 5.4 (Kin2 and Kin3) and 5.5 (KinX2 and KinX3). The parameterizations of the ϕ_π-dependent components of the hadronic tensor are displayed in Tables 5.6 (Kin2 and Kin3) and 5.7 (KinX2 and KinX3).

	$Q2$ dependence		x_{Bj} dependence	
	Kin3	Kin2	KinX3	KinX2
N_{π^0}	15516	23429	5952	9860
N_{Gen}	2.14×10^9	2.14×10^9		
$\int \mathcal{L}dt$	5.10×10^9 nb^{-1}	2.99×10^9 nb^{-1}		
Q^2 (GeV^2)	2.350 ± 0.002	1.941 ± 0.010	2.155 ± 0.268	2.073 ± 0.001
x_{Bj}	0.368 ± 0.001	0.368 ± 0.005	0.335 ± 0.045	0.394 ± 0.003
W (GeV)	2.217 ± 0.004	2.055 ± 0.012	2.272 ± 0.072	2.016 ± 0.008
t_{min} (GeV^2)	-0.173 ± 0.001	-0.170 ± 0.005	-0.137 ± 0.048	-0.199 ± 0.003
ϵ	0.649 ± 0.002	0.769 ± 0.003	0.648 ± 0.001	0.768 ± 0.003
E_0 (GeV)	5.752 ± 0.001	5.753 ± 0.001	5.752 ± 0.001	5.753 ± 0.001
E' (GeV)	2.348 ± 0.007	2.937 ± 0.020	2.322 ± 0.029	2.951 ± 0.016
q^{lab} (GeV)	3.734 ± 0.007	3.142 ± 0.017	3.732 ± 0.009	3.151 ± 0.014
p_π^{CM} (GeV)	0.904 ± 0.002	0.806 ± 0.007	0.937 ± 0.043	0.783 ± 0.005
k_γ^{CM} (GeV)	0.910 ± 0.002	0.813 ± 0.007	0.942 ± 0.042	0.790 ± 0.005

Table 5.2: Average measured kinematics for the four kinematics of the experiment. Errors are the maximal deviation of the values in the seven $t_{min} - t$ bins, compared to the averages listed.

$Q2$ dependence			x_{Bj} dependence		
$t_{min} - t$ (GeV^2)	$\sin\theta_\pi^{CM}$	$\sin^2\theta_\pi^{CM}$	$t_{min} - t$ (GeV^2)	$\sin\theta_\pi^{CM}$	$\sin^2\theta_\pi^{CM}$
Kin3			KinX3		
0.0095	0.077	0.007	0.0095	0.076	0.007
0.0298	0.144	0.021	0.0297	0.143	0.020
0.0546	0.194	0.038	0.0545	0.193	0.037
0.0843	0.241	0.058	0.0843	0.240	0.058
0.1188	0.285	0.081	0.1188	0.284	0.081
0.1583	0.328	0.108	0.1579	0.326	0.106
0.2063	0.372	0.139	0.2057	0.370	0.137
Kin2			KinX2		
0.0094	0.085	0.008	0.0094	0.085	0.008
0.0296	0.159	0.026	0.0296	0.160	0.026
0.0540	0.215	0.046	0.0542	0.216	0.047
0.0839	0.267	0.071	0.0840	0.268	0.072
0.1179	0.315	0.099	0.1181	0.316	0.100
0.1577	0.362	0.131	0.1579	0.364	0.133
0.2050	0.410	0.168	0.2051	0.412	0.170

Table 5.3: Average for $t_{min} - t$, $\sin\theta_\pi^{CM}$ and $\sin^2\theta_\pi^{CM}$

Q^2 dependence		
	Kin3 $x_{Bj} = 0.369$, $Q^2 = 2.353\text{GeV}^2$	Kin2 $x_{Bj} = 0.368$, $Q^2 = 1.940\text{GeV}^2$
$t_{min} - t$ GeV^2	$d\sigma_T/dt + \epsilon_L d\sigma_L/dt$ nb/GeV^2	
0.010	377 ± 10 ± 12	571 ± 10 ± 24
0.030	381 ± 12 ± 12	600 ± 12 ± 25
0.054	403 ± 10 ± 13	641 ± 12 ± 27
0.084	425 ± 11 ± 14	673 ± 15 ± 28
0.118	418 ± 11 ± 14	645 ± 16 ± 27
0.158	395 ± 13 ± 13	636 ± 25 ± 27
0.206	384 ± 13 ± 13	628 ± 36 ± 26
	$d\sigma_{TL}/dt$	
0.010	-13 ± 23 ± 10	17 ± 19 ± 13
0.030	38 ± 26 ± 24	-43 ± 22 ± 12
0.054	-25 ± 22 ± 11	-23 ± 21 ± 12
0.084	-26 ± 25 ± 13	-19 ± 27 ± 14
0.118	-75 ± 24 ± 9	-103 ± 30 ± 21
0.158	-91 ± 30 ± 8	-185 ± 52 ± 43
0.206	-123 ± 31 ± 10	-189 ± 74 ± 34
	$d\sigma_{TT}/dt$	
0.010	-12 ± 23 ± 14	-39 ± 19 ± 7
0.030	-25 ± 27 ± 15	-110 ± 24 ± 13
0.054	-74 ± 22 ± 4	-141 ± 22 ± 17
0.084	-64 ± 25 ± 14	-174 ± 28 ± 17
0.118	-124 ± 24 ± 16	-319 ± 29 ± 23
0.158	-137 ± 29 ± 15	-352 ± 45 ± 53
0.206	-134 ± 30 ± 15	-343 ± 57 ± 68
	$d\sigma_{TL'}/dt$	
0.010	9 ± 49 ± 20	31 ± 51 ± 15
0.030	119 ± 55 ± 21	136 ± 61 ± 24
0.054	129 ± 46 ± 12	61 ± 56 ± 41
0.084	151 ± 51 ± 30	123 ± 68 ± 20
0.118	153 ± 47 ± 17	120 ± 69 ± 24
0.158	87 ± 54 ± 23	142 ± 91 ± 36
0.206	127 ± 51 ± 15	76 ± 99 ± 80

Table 5.4: Separated cross section values from Equation (5.1) (first value) together with statistic errors (second value) and systematic errors (third value) for each of the seven considered bins.

x_{Bj} dependence		
	Kin3 $x_{Bj} = 0.335$, $Q^2 = 2.155\text{GeV}^2$	Kin2 $x_{Bj} = 0.394$, $Q^2 = 2.072\text{GeV}^2$
$t_{min} - t$ GeV^2	$d\sigma_T/dt + \epsilon_L d\sigma_L/dt$ nb/GeV^2	
0.010	439 ± 19 ± 14	635 ± 17 ± 26
0.030	437 ± 22 ± 14	703 ± 21 ± 29
0.054	457 ± 18 ± 15	683 ± 19 ± 28
0.084	442 ± 21 ± 14	688 ± 23 ± 29
0.118	466 ± 22 ± 15	682 ± 23 ± 28
0.158	407 ± 29 ± 13	662 ± 34 ± 28
0.205	406 ± 34 ± 13	591 ± 44 ± 25
	$d\sigma_{TL}/dt$	
0.010	20 ± 46 ± 38	-26 ± 30 ± 22
0.030	2 ± 50 ± 17	-100 ± 37 ± 61
0.054	-28 ± 43 ± 15	-88 ± 32 ± 54
0.084	-37 ± 50 ± 19	-68 ± 38 ± 487
0.118	-74 ± 55 ± 27	-170 ± 40 ± 562
0.158	-188 ± 80 ± 27	-155 ± 63 ± 657
0.205	-174 ± 90 ± 32	-228 ± 82 ± 738
	$d\sigma_{TT}/dt$	
0.010	-16 ± 44 ± 16	-63 ± 33 ± 18
0.030	-44 ± 50 ± 32	-83 ± 41 ± 22
0.054	-63 ± 42 ± 15	-153 ± 36 ± 24
0.084	-114 ± 47 ± 8	-186 ± 43 ± 78
0.118	-156 ± 50 ± 18	-327 ± 44 ± 109
0.158	-244 ± 66 ± 35	-247 ± 65 ± 141
0.205	-124 ± 69 ± 42	-444 ± 82 ± 183
	$d\sigma_{TL'}/dt$	
0.010	68 ± 97 ± 35	-23 ± 84 ± 138
0.030	12 ± 109 ± 39	112 ± 100 ± 104
0.054	236 ± 88 ± 19	50 ± 90 ± 63
0.084	126 ± 99 ± 26	211 ± 104 ± 95
0.118	119 ± 93 ± 22	3 ± 106 ± 111
0.158	246 ± 106 ± 89	78 ± 136 ± 126
0.205	177 ± 104 ± 30	62 ± 146 ± 146

Table 5.5: Separated cross section values from Equation (5.1) (first value) together with statistic errors (second value) and systematic errors (third value) for each of the first seven bins in $t_{min} - t$ for $1.95\ \text{GeV}^2 < Q^2 < 2.25\ \text{GeV}^2$.

Q^2 dependence
Kin3 $x_{Bj} = 0.368$, $Q^2 = 2.350$ (GeV^2)
$\frac{W_{xx}-W_{yy}}{2} = [-562 \pm 62 \pm 32] \times \sin^2\theta_h^{CM} \cos 2\Phi_h$ nb
$\Re e(W_{xz}) = [97 \pm 18 \pm 8] \times \sin\theta_h^{CM} \cos\Phi_h$ nb
$\Im m(W_{xz}) = [-206 \pm 35 \pm 13] \times \sin\theta_h^{CM} \sin\Phi_h$ nb
Kin2 $x_{Bj} = 0.368$, $Q^2 = 1.941$ (GeV^2)
$\frac{W_{xx}-W_{yy}}{2} = [-1024 \pm 58 \pm 51] \times \sin^2\theta_h^{CM} \cos 2\Phi_h$ nb
$\Re e(W_{xz}) = [82 \pm 17 \pm 11] \times \sin\theta_h^{CM} \cos\Phi_h$ nb
$\Im m(W_{xz}) = [-142 \pm 38 \pm 19] \times \sin\theta_h^{CM} \sin\Phi_h$ nb

Table 5.6: Φ_h-dependent hadronic tensor parameterization for constant x_{Bj}. The first error is statistics, the second is systematics.

x_{Bj} dependence
KinX3 $x_{Bj} = 0.335$, $Q^2 = 2.155$ (GeV^2)
$\frac{W_{xx}-W_{yy}}{2} = [-770 \pm 135 \pm 63] \times \sin^2\theta_h^{CM} \cos 2\Phi_h$ nb
$\Re e(W_{xz}) = [121 \pm 43 \pm 17] \times \sin\theta_h^{CM} \cos\Phi_h$ nb
$\Im m(W_{xz}) = [-278 \pm 69 \pm 28] \times \sin\theta_h^{CM} \sin\Phi_h$ nb
KinX2 $x_{Bj} = 0.394$, $Q^2 = 2.073$ (GeV^2)
$\frac{W_{xx}-W_{yy}}{2} = [-1003 \pm 86 \pm 153] \times \sin^2\theta_h^{CM} \cos 2\Phi_h$ nb
$\Re e(W_{xz}) = [163 \pm 24 \pm 72] \times \sin\theta_h^{CM} \cos\Phi_h$ nb
$\Im m(W_{xz}) = [-101 \pm 58 \pm 55] \times \sin\theta_h^{CM} \sin\Phi_h$ nb

Table 5.7: Φ_h-dependent hadronic tensor parameterization for constant Q^2. The first error is statistics, the second is systematics.

Appendix 2: DVMP beyond 6 GeV: Deep $\phi(1020)$ electroproduction at JLab 12 GeV.

On the side of π^0 electroproduction analysis, I worked on a proposal for a $ep \to ep\phi(1020)$ experiment for Hall A for the JLab upgrade at 12 GeV. This experiment is expected to give very interesting information on the proton structure, and particularly on the gluon content in the valence region ($x_{Bj} > 0.1$). For several experimental reasons, the $ep \to ep\phi$ reaction will only be observed through the ϕ decay channel $\phi \to K^+K^-$. The K^+K^- pair will be detected in the Super BigBite Spectrometer, a large acceptance spectrometer which is under development for Hall A.

This supplementary chapter deals about the letter of intent for $\phi(1020)$ electroproduction at JLab 12 GeV which has been submitted to the Program Advisory Committee this year [96]. First, I expose the physics motivations for such an experiment. The experimental setup is described. The simulation of the $ep \to ep\phi$ in the apparatus is detailed, and the counting rate is provided. The analysis method to obtain the projected results is described, and the results and error bars are provided. Finally, I conclude on the faisibility of the Deep $\phi(1020)$ electroproduction experiment, and I give further prospects to improve it.

Physics motivations

Understanding the gluonic structure of matter is a vital challenge in hadronic physics. In particular, the spatial distribution is almost completely unknown. Measurements of the GPDs of quarks and gluons will allow us to construct the matter distribution of the proton. Exclusive electroproduction of the ϕ-meson is an essential probe of the gluon GPDs of the proton. The high luminosity capability of Hall A allows to obtain high precision differential cross sections measurements at the highest possible Q^2 for x_{Bj} fixed. The absolute cross sections will test models of the hard scattering amplitude. the t-dependence of the cross sections (more specifically the $\Delta_\perp^2$) measures the spatial distribution of gluons in the target, with calculable corrections from the finite size effects in the hard scattering kernel.

The forward parton distribution are illustrated in Figure 5.12. The momentum sum rule of quarks demonstrated that roughly half the proton momentum is carried by the gluons. For instance, in the MRST2002 NNLO analysis [97], the gluon sum rule is:

$$\int_0^1 dx[xg(x)] = 0.35 \quad \text{at } Q_0^2 = 1 \text{ GeV}^2. \tag{5.5}$$

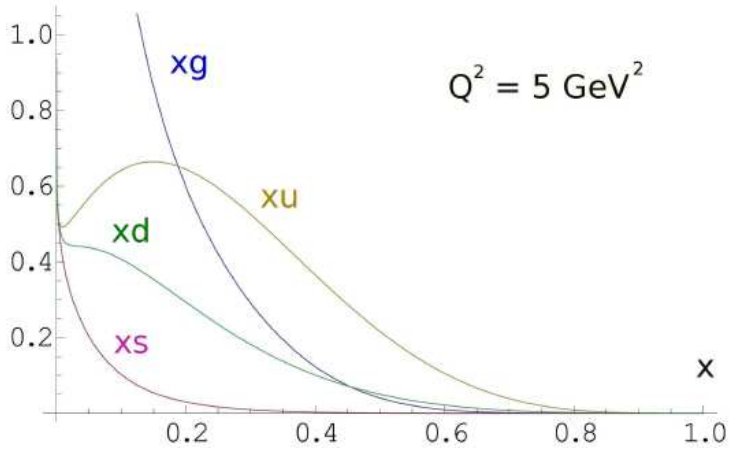

Figure 5.12: CTEQ parameterization of PDFs at $Q^2 = 5\ \mathrm{GeV}^2$. Note the gluon PDF at large x_{Bj} is comparable to the down quark PDF, thus much larger than strange quark PDF.

Even more interesting is that 60 % of this integral is obtained is obtained for $x > 0.15$. Thus gluons at large x are a very important and little studied part of the proton structure.

We recall the role of gluons in vector meson electroproduction. The factorization theorem and its consequences are explicited. The existing data are reviewed and their consequences on the factorization theorem applicability are discussed.

Gluons and vector mesons

Gluon GPDs contribute only to the diffractive channels that have vacuum quantum number in the t-channel, *i.e.* $eN \to eN\gamma$ and $eN \to eNV^0$, $V^0 \in \rho^0,\ \omega,\ \phi,\ J/\Psi, \ldots$ In general, deep virtual ϕ production will have contributions from both s-quark and gluon GPDs. However, at all values of momentum fraction x, the forward gluon PDF dominates over the strange quark PDF (Figure 5.12). Thus deep virtual ϕ production may offer a unique window into the gluon GPDs with JLab at 12 GeV. However, this interpretation will be quantitative only if theoretical models can extend the effective range of factorization down to $Q^2 \sim 4\ \mathrm{GeV}^2$.

The cross section for $ep \to ep\phi$ with $\phi \to K\bar{K}$ is 8-fold differential. For example, we choose the laboratory variables for the scattered electron (k', $\cos\theta_e$, ϕ_e), t and ϕ_ϕ for the ϕ production, and the Schilling and Wolf convention [98] for the $\phi \to K\bar{K}$ production variables:

- m^2_{KK} the invariant mass squared of the kaon pair
- $\cos\theta_K$, ϕ_K the polar and azimuthal angles of kaon production in the ϕ rest frame, with the polar axis along the ϕ direction.

If we assume the two kaon distribution unchanged across the resonance, then the general cross section can be written as:

$$\frac{d^8\sigma^{ep\to ep\phi}}{dQ^2 dx_B d\phi_e dt d\phi_\phi dm^2_{KK} d^2\Omega_K} = \Gamma\rho(m^2_{KK})\left[\frac{d\sigma_T}{dt} + \epsilon\frac{d\sigma_L}{dt}\right]\mathcal{W}(\cos\theta_K^{\phi\mathrm{RF}}, \phi_\phi, \phi_K) \qquad (5.6)$$

In this equation, Γ and ϵ are the same quantities as in the π^0 cross section equation, $\rho(m^2_{KK})$ is the K^+K^- mass density, and $\mathcal{W}$ is the angular decay distribution. The two

latter quantities are normalized to unity:

$$\int d\cos\theta_K^{\phi\mathrm{RF}} d\phi_\phi d\phi_K \mathcal{W}(\cos\theta_K^{\phi\mathrm{RF}}, \phi_\phi, \phi_K) = 1 \tag{5.7}$$

$$\int dm_{KK}^2 \rho(m_{KK}^2) = 1 \tag{5.8}$$

The general angular decay distribution depends on 24 independent density matrix elements. Its expression is given within full details in Appendix 3. Under s-channel helicity conservation (SCHC), the angular decay distribution $\mathcal{W}$ simplifies enormously to depend only on two free parameters:

$$\mathcal{W}(\cos\theta_K^{\phi\mathrm{RF}}, \phi_\phi, \phi_K) \overset{\mathrm{SCHC}}{\longrightarrow} \mathcal{W}(\cos\theta_K^{\phi\mathrm{RF}}, \Psi) \tag{5.9}$$

with $\Psi = \phi_K - \phi_\phi$ (Appendix 3):

$$\begin{aligned}\mathcal{W}(\cos\theta, \Psi, h) = \frac{1}{1+\epsilon R}\frac{3}{8\pi}\Big\{&\sin^2\theta(1+\epsilon\cos 2\Psi) + 2\epsilon\cos^2\theta \\ &+ \sqrt{2\epsilon(1+\epsilon)}\sqrt{R}\cos\delta_R \sin 2\theta\cos\Psi \\ &+ h\sqrt{2\epsilon(1-\epsilon)}\sqrt{R}\sin\delta_R\sin 2\theta\sin\Psi\Big\},\end{aligned} \tag{5.10}$$

$$R = \frac{d\sigma_L}{d\sigma_T} \tag{5.11}$$

$$r_{00}^{04} = \frac{\epsilon R}{1+\epsilon R} = \frac{\epsilon d\sigma_L}{d\sigma_T + \epsilon d\sigma_L} \tag{5.12}$$

Note that the usual electroproduction interference terms have been subsummed into $\cos 2\Psi$, $\cos\Psi$ and $\sin\Psi$ terms respectively, each with explicit θ_K dependence. In the latter two terms, δ is the relative phase of the longitudinal and transverse photo-absorption amplitude.

A measurement of the $\cos^2\theta_K$ dependence of the differential cross section allows us to extract the density matrix element r_{00}^{04}, and hence separate the longitudinal and transverse cross sections. The validity of SCHC is tested by measuring the size of all terms dependent on $\phi_K + \phi_\phi$ which are nominally zero in SCHC.

Factorization

As we already evoked in Chapter 1.4.4, exclusive meson production processes factorize, at sufficiently high Q^2, into a hard scattering kernel convoluted with quark and gluon generalized parton distributions [38]. This is illustrated by Figure 5.13.

The QCD factorisation theorem asserts that the *longitudinal* virtual photo-absorption cross section scales as a function of Q^2 at fixed x_{Bj} as

$$\sigma_L \to |\mathrm{GPD}|^2 \frac{Q_0^6}{Q^6} \quad \text{as } Q^2 \to \infty. \tag{5.13}$$

The cross section for photo-production of vector mesons with transversely polarized virtual photons is predicted to be higher twist and therefore to fall more rapidly with Q^2:

$$\frac{\sigma_T}{\sigma_L} \sim \frac{1}{Q^2} \quad \text{as } Q^2 \to \infty. \tag{5.14}$$

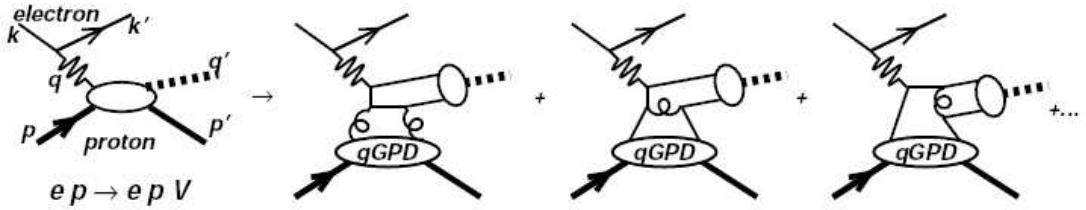

Figure 5.13: Factorization of the $ep \to ep\phi$. We took the same conventions as for π^0 production (Chapter 1.1.1).

In addition, the hard scattering kernel of σ_L satisfies s-channel helicity conservation. This means that for exclusive vector meson production by a longitudinally polarized virtual photon the final state vector-meson is also longitudinally polarized. Thus, within SCHC, σ_L can be separated from σ_T measuring the $\phi \to K^+K^-$ decay angular distribution.

The longitudinal cross section has the form (see also in Chapter 1.4.4):

$$\frac{d\sigma_L}{dt} = \frac{1}{16\pi Q^4(1-x_{Bj})\sqrt{1+4M^2x_{Bj}^2/Q^2}}|\mathcal{M}_V|^2 \tag{5.15}$$

The matrix element $\mathcal{M}_V$ is in general a sum over the helicity states of the ϕ-meson and the final state proton. However, in the limit of SCHC, the ϕ meson has only the longitudinal polarization state. In the colinear approximation, the leading twist longitudinal amplitude has the form

$$\mathcal{M}_\phi = \mathcal{M}_\phi^g + \mathcal{M}_\phi^s \tag{5.16}$$

with

$$\mathcal{M}_\phi^g = e\int_0^1 \mathcal{C}_\phi^g(x,\xi,Q^2)H_g(x,\xi,\Delta_\perp^2) + \dots \tag{5.17}$$

$$\mathcal{C}_\phi^g(x,\xi) = \frac{8\pi}{N_c\sqrt{Q^2}}\left[f_\phi\int_0^1 \frac{dz}{z}\Phi_\phi(z)\right]\left[\frac{1}{\xi+x}\frac{1}{\xi-x-i0^+}\right]\frac{1}{2\xi} \tag{5.18}$$

where $f_\phi = 221$ MeV is the ϕ decay constant determined from the $\phi \to e^+e^-$ width, Φ_ϕ is the ϕ Distribution Amplitude (DA), and H_g is the gluon GPD. The matrix element $\mathcal{M}_\phi^g$ also has a contribution from the spin flip GPD E_g. The $\sqrt{Q^2}$ factor in $\mathcal{C}$ together with the $1/Q^4$ kinematic factor in Equation (5.15) yields to the leading twist $1/Q^6$ dependence of σ_L. Before examining modifications to Equation 5.18, we review the existing deep virtual vector meson prodiuction data.

Existing data and subasymptotic factorization

The high W^2 data on exclusive photo-production of vector mesons and DVCS is summarized in Figures 5.14, 5.15 and 5.16 (see also the recent review [99]). Within statistics, the experimental results satisfy SCHC. The slope parameter b of Figure 5.16 was obtained by fitting the data to the form

$$\frac{d\sigma_L}{dt} = \frac{\sigma_0}{b}\left(\frac{W_0}{W}\right)e^{bt}. \tag{5.19}$$

We draw the following conclusions to these data:

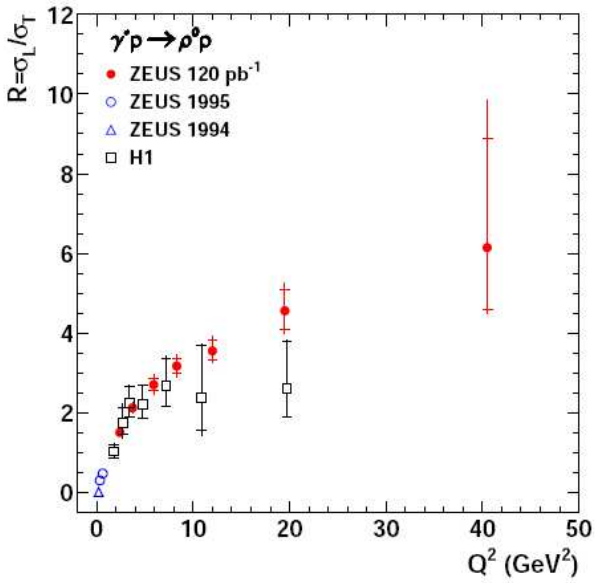

Figure 5.14: Ratio R for coherent ρ^0 production, as a function of Q^2. Compilation from G. Wolf [99]. The high statistics ZEUS data for $Q^2 > 10$ GeV^2 are consistent with a linear Q^2 dependence as predicted by the factorization theorem. In constrast to that, lower statistics H1 data suggested that R saturates at large Q^2.

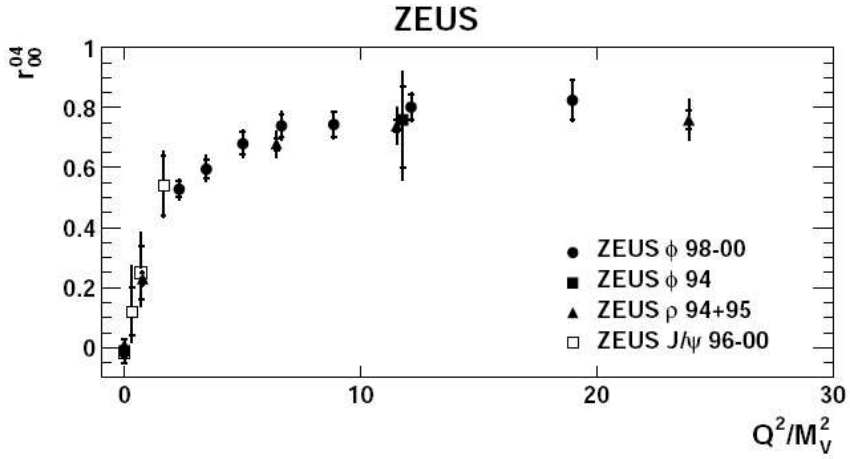

Figure 5.15: Longitudinal density parameter r_{00}^{04} for coherent vector meson production as a function of Q^2, extracted from [99]. The data exhibit a universal behavior for ρ, ϕ and J/Ψ production, suggesting a common reaction mechanism coupling to the gluon structure of the proton.

- The scaling behavior in Figures 5.15 and 5.16 suggest a universal hard mechanism. A hadronic component of the photon, of transverse size proportional to $1/(Q^2+M_V^2)$, couples to the gluonic structure of the proton. As a consequence, the size parameter b in Figure 5.16 can be conjectured as the sum of the transverse size of the hadronic photon plus the rms size (approximately constant at high W^2) of the gluon density in the proton.

- the longitudinal to transverse R, plotted in Figure 5.14 for ρ production exhibits a linear Q^2 dependence after 10 GeV^2, consistent with leading twist dominance. The longitudinal density parameter r_{00}^{04}, displayed in Figure 5.15 suggests that this behavior is universal to all vector meson channels.

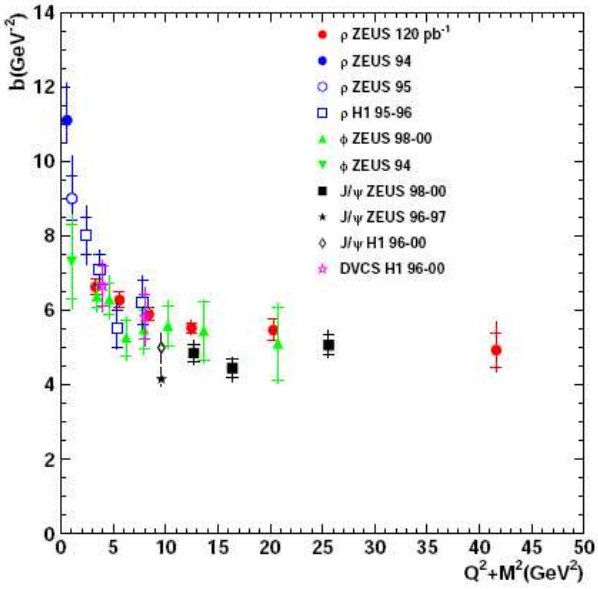

Figure 5.16: Universal scaling of the deeply virtual vector meson production as a function of $Q^2 + M_V^2$, with M_V the mass of the produced meson, extracted from [99]. The plot shows the t-slope parameter b from the fit of Equation (5.19)

In the valence region, the universality of vector meson production will be broken by the valence quark contributions to ρ and ω production. However, a conjecture states that the universal gluon mechanism observed in the HERA data will continue into the valence region for the ϕ and J/Ψ production. This experiment may be able to test this conjecture.

The world data for exclusive ϕ electroproduction at $Q^2 \simeq 3.8$ GeV^2 is displayed in Figure 5.17. The CLAS data point [100] is at $\langle Q^2 \rangle = 3.4$ GeV^2, $\langle W \rangle = 2.4$ GeV, or

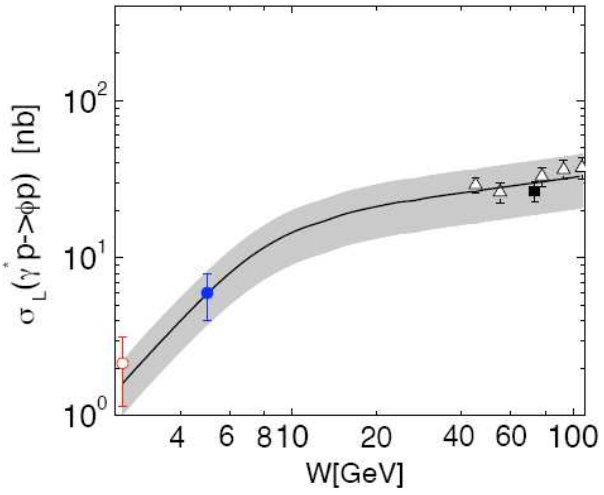

Figure 5.17: Deep virtual ϕ electroproduction at $Q^2 \simeq 3.8$ GeV^2. The data points in increasing W are from CLAS, HERMES and HERA. The curve and error band is the calculation of Goloskokov and Kroll [39, 40]. The error band reflects only the uncertainty of the forward gluon PDF.

equivalently $x_{Bj} = 0.41$. The success of the model of Goloskokov and Kroll [39, 40] suggests that even at modest values of Q^2, deep ϕ production can be described in terms of the gluon GPD of the proton, convoluted with a sub-asymptotic hard scattering kernel.

The conclusion from the HERA data on deep virtual production of vector mesons is that factorization is clearly observed for $Q^2 > 10$ GeV^2 within the precision of the data. For $Q^2 \sim 5$ GeV^2, the cross section is strongly modified from colinear factorization, but the cross section still exhibits a universal scaling behavior. This strongly suggests that the reaction mechanism is dominated by the perturbative exchange of two gluons, but the $\gamma^* g \to Vg$ hard scattering amplitude must be modified by finite size effects in impact parameter (or equivalently finite $k_\perp$ effects). Modifications to the colinear factorization of deep virtual production have been discussed by numerous authors [34, 39].

As an example, Goloskokov and Kroll adopt the Modified Perturbative Approach (MPA). They consider the intrinsic $k_\perp$ dependence of the hard scattering $\gamma g \to Vg$ kernel and of the leading Foch space $q\bar{q}$ wave-function of the meson. In the hard scattering kernel, they include the $k_\perp$ dependence of the quarks propagators in Figure 5.13 and Sudakov form factors which modify the $q\bar{q} \to \phi$ vertex. The Sudakov form factors accounts for the fact that a finite separation $\mathbf{b}$ of the $s\bar{s}$ pair in the transveerse plane produces a finite color dipole, which will radiate gluons. At high W^2, this gluon radiation will preferentially populate multi-particle final states. The experimental selection of the exclusive channel thereby post-selects configurations with small values of $|\mathbf{b}|$. This is expressed in the scattering amplitude *via* the Sudakov form factor which suppresses large separations. The net effect of these modifications is to strongly suppress the exclusive scattering amplitude at modest Q^2, but to eventually recover the colinear result for $Q^2 > 10$ GeV^2.

Experimental setup

This section describes the experimental setup which is required for the measurement of the H$(e, e'K^+K^-)p$. Basically, the electron will be detected in the left High Resolution Spectrometer described in Chapter 2.4 of this thesis. The kaon pair issued from the $\phi(1020)$ decay will be measured by the Super BigBite Spectrometer (SBS), and identified as kaons by the Ring Imaging CHerenkov (RICH) we got from the HERMES experiment [101]. The SBS is described and some details are given on the particle identification. I also discuss the experimental constraints and propose relevant kinematics within these constraints.

Kaon detection in the Super BigBite Spectrometer (SBS)

The Super BigBite Spectrometer is a large acceptance spectrometer which will be designed for Hall A [102]. It is composed of a vertical dipole magnet (generated magnetic field horizontal) laid on an iron yoke which defines the acceptance. Behind the yoke is located the detector package of the SBS. As for the HRS, the detector package may have a different composition. For our experiment, the detector package is likely to be the following:

- One or two GEM trackers; the first will be composed of 6 plans of 40×100 cm^2 active area, the second will be composed of 4 plans of 80×150 cm^2 active area.
- Interlaced between these two trackers is located the RICH, which will likely be upgraded to improve its spatial reconstruction.
- Behind all of that will finally be located the hadronic calorimeter.

Note that for our experiment, the SBS yoke has to be reduced of 18.5 cm on the beam side to ensure the compatibility with the HRS. This results in the dipole operated at half

maximum field. A projected view of the SBS and the first HRS quadrupole is available on Figure 5.18.

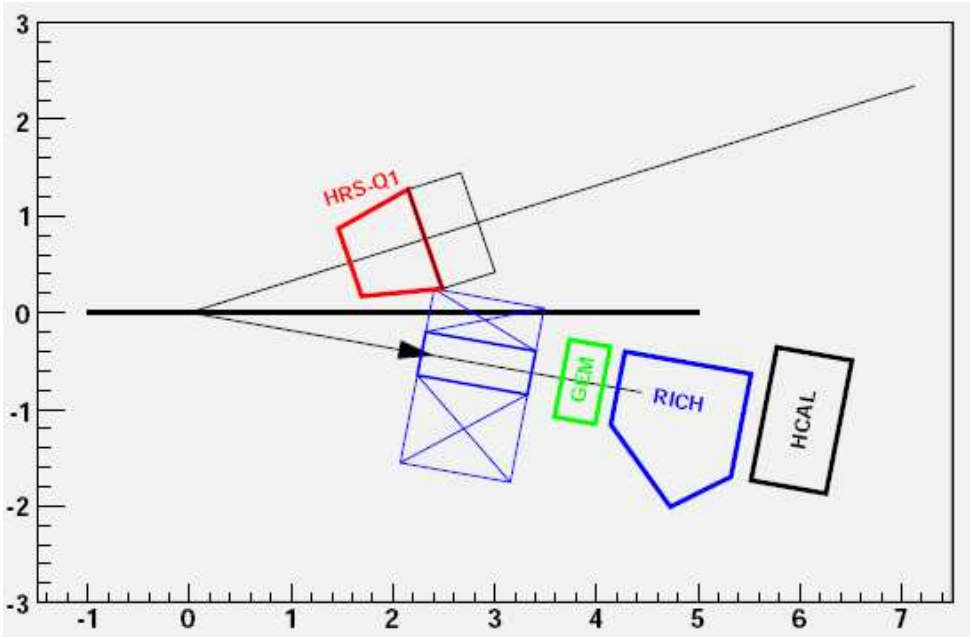

Figure 5.18: SBS and $\mathbf{Q}_1$ of left HRS at $\theta_e = \theta_{\rm HRS} = 18.18°$ and $\theta_q = \theta_{\rm SBS} = 10.55°$. The scales are in meters. The yoke of the SBS magnet (in blue) is symeetric on the "regular" SBS, and the yoke asymmetry relative to the SBS window translates the yoke reduction. The small corrector coils along the beam line to compensate for the non-zero field in the SBS yoke are not represented.

The SBS magnet is a square dipole of 48" (∼120 cm) by 48", with a gap of 18" (∼46 cm). The minimum distance from the target to the entrance of the SBS is dictated by the minimum iron yoke necessary to produce zero field on the beam line. The estimated minimum distance, perpendicular to the entrance face of the magnet, from the center of the gap to the beam line is 43 cm. Thus the SBS angle and distance from the target are correlated by:

$$D = 0.43/\tan\theta_{\rm SBS}. \tag{5.20}$$

The angular acceptance of the SBS can be estimated by the geometrical aperture of the back edge of the gap, relative to the target. Therefore, the horizontal and vertical acceptances are, in radians:

$$\theta_H = \pm\frac{\rm Gap/2}{1.2+D} = \pm\frac{0.23}{1.2+0.43/\tan\theta_{\rm SBS}} \tag{5.21}$$

$$\theta_V = \pm\frac{1.2/2}{1.2+D} = \pm\frac{0.60}{1.2+0.43/\tan\theta_{\rm SBS}} \tag{5.22}$$

with all numerical values in the two latter equations in meters. The other SBS specifications are given in table 5.8. This tables provides the momentum and angular resolutions for the "plain" SBS, and for the SBS modified for deep ϕ electroproduction experiment.

Particle identification

Kaon identification is achieved by the RICH detector pictured and described in Figure 5.19. This is one of the two identical HERMES RICH detectors. The particle ID perfor-

Momentum	
Range	$2.0\ \text{GeV} < p_{\text{SBS}} < 10.0\ \text{GeV}$
Resolution	$\sigma_p/p = 2.9 \cdot 10^{-3} + 3 \cdot 10^{-4} p$
	$\tilde{\sigma}_p/p = 5.8 \cdot 10^{-3} + 6 \cdot 10^{-4} p$
Direction	
Range	$3.5^\circ < \theta_{\text{SBS}} < 30^\circ$
Acceptance	Equation (5.21) (Horizontal)
	Equation (5.22) (Vertical)
Resolution	$\sigma_\theta = 0.14 + 1.3[\text{GeV}]/p$ mrad
	$\tilde{\sigma}_\theta = 0.28 + 2.6[\text{GeV}]/p$ mrad

Table 5.8: Planned performances for Super BigBite Spectrometer. σ_p/p and σ_θ are the resolutions for the original SBS project. $\tilde{\sigma}_p/p$ and $\tilde{\sigma}_\theta$ are the resolutions for the SBS modified for HRS compatibility.

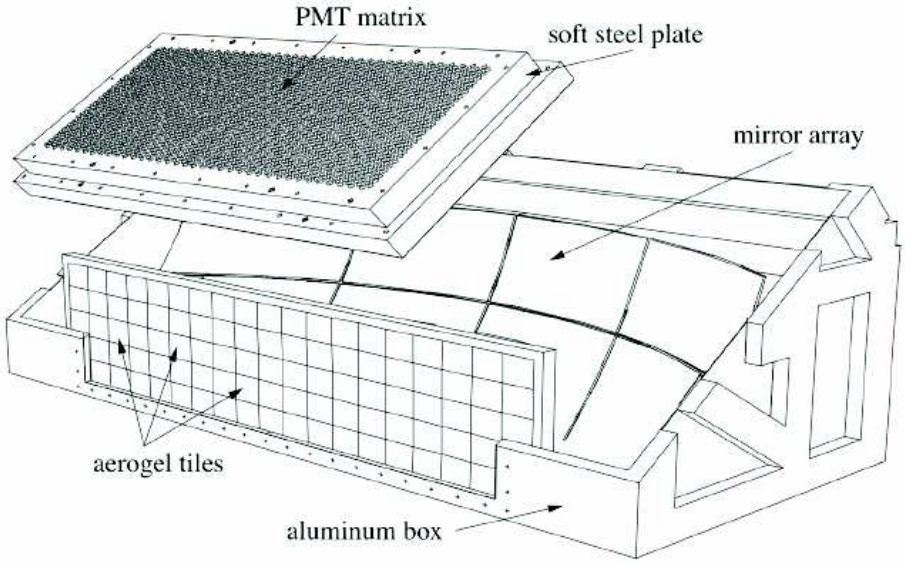

Figure 5.19: The HERMES RICH detector [101]. The Aerogel tiles have an index of refraction $n = 1.0304$. The space between the tiles and the mirror array is filled with C_4F_{10}, an ozone-safe gas with index $n = 1.0014$ at $\lambda = 633$ nm. The acceptance area is $60 \times 120\ \text{cm}^2$.

mance in the HERMES experiment is displayed in Figure 5.20. Excellent π/K separation is achieved for the full momentum range of interest to this experiment. In HERMES, a discriminator on each PMT channel was latched in a 100 ns trigger window. To handle the higher luminosity, we will implement a multihit TDC readout of each PMT, with 1 ns resolution.

Experimental constraints and proposed kinematics

In the Hall A at 12 GeV, several experimental features constrains the fixing of the kinematics. Let me list all of them, and set the kinematics which resulted from these constraints. First, we would like to study the reaction in the inclusive regime, *i.e.* $W^2 = Q^2(x_{Bj} - 1)/x_{Bj} + M^2 > 4\ \text{GeV}^2$. The specifications of the left spectrometer

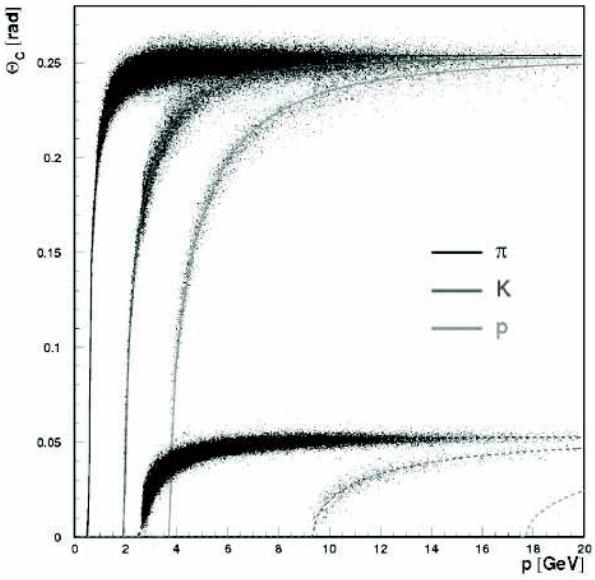

Figure 5.20: The HERMES RICH performance for pions, kaons and protons, as a function of their momentum. The upper scatter plots are the Čerenkov rings from the Aerogel radiator. The bottom scatter plots are the Čerenkov signals from the C_4F_{10} gas. π/K separation is obtained up to a 4.5 GeV/c momentum by discriminating on the radius of the Aerogel ring. From 4.5 to 9 GeV, the π/K separation is obtained by vetoing on the presence of the gas Čerenkov signal for pions.

limits the momentum of the scattered electron to be below 4.3 GeV. In order to maximize the two kaon pair acceptance in the SBS, it is our interest to get the higher boost possible for the ϕ. To achieve this, we have the minimize the angle and the energy of the virtual photon, and then to maximize the angle on the scattered electron. For the same reason, we choose to run at the highest beam energy possible, *i.e.* $k = 11$ GeV. However, we do not want the angle of the virtual photon to be to low, to avoid the SBS to be to far from the target. All these constraints have been summarized on Figure 5.21. Taking all these

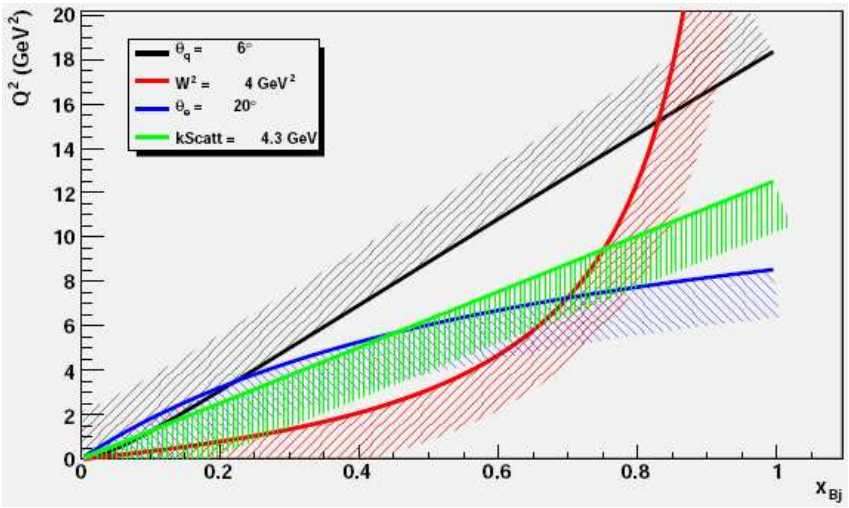

Figure 5.21: Experimental constraints materialized in the $[x_{Bj}; Q^2]$ plane, at beam energy $k = 11$ GeV.

constraints into account, the kinematics have been preliminary fixed as written down in table 5.9. The expected counting rate one may expect for each of these kinematics is

KIN #	k (GeV)	$p_{\rm HRS}$ (GeV)	$\theta_{\rm SBS}$ (deg)	Q^2 (GeV^2)	x_{Bj}	W^2 (GeV^2)	$\theta_{\rm SBS}$ (deg)	$z_{\rm SBS}$ (m)	$E_\phi^{\rm max}$ (GeV)	t_{min} (GeV^2)
1	11.0	4.19	18.18	4.6	0.36	9.06	10.55	2.31	6.65	-0.29
2	11.0	3.54	24.49	7.0	0.50	7.88	10.67	2.28	7.12	-0.64
3	11.0	3.38	30.04	10.0	0.70	5.17	11.86	2.05	6.50	-2.09

Table 5.9: Deeply virtual ϕ production kinematics with SBS and L-HRS. The first six columns are the electron kinematics. $\theta_{\rm SBS}$ is the central angle of the SBS, centered on the central direction of the virtual photon. $z_{\rm SBS}$ is the distance to the target. The maximal energy of the ϕ, $E_\phi^{\rm max}$ is obtained at the minimum momentum transfer value $t = t_{min}$.

provided and explained in the following section.

Simulation of $ep \to ep\phi$ in HRS$\otimes$SBS pair

This section is devoted to the Monte Carlo simulation of the reaction $ep \to ep\phi$, with the scattered electron measured by the HRS, and with $\phi \to K^+K^-$ and the kaon pair measured by the SBS. This simulation has several purposes:

- model the acceptance and the resolution smearing of these two instruments, as well as radiative effects;
- model the counting rate of $ep \to ep\phi_L$, and also the "background", $ep \to ep\phi_T$ and non resonant $ep \to epK^+K^-$.

I give some details on the simulation, and particularly on simulation of all experimental effects. The model of the cross section $\sigma_L^{ep\to ep\phi}$ used to estimate the counting rates is then described, as well as the cross sections $\sigma_T^{ep\to ep\phi}$ and $\sigma(ep \to epK^+K^-)$ and the relative poderation between $ep \to ep\phi$ and $ep \to epK^+K^-$ yields. The $ep \to ep\phi_L$ counting rate for each kinematic is also provided.

Simulation of experimental effects

I describe the simulation of the reaction H$(e, e'K^+K^-)p$ with e' in the HRS acceptance and K^+, K^- in the SBS acceptance. The kaon pair may either be resonant or non resonant, but in both case, and for practical reasons, an intermediate resonance is generated. Only the distribution of the two kaon mass m_{KK} differs from one case to the other.

Basically, the generation of H$(e, e'K^+K^-)p$ events starts by the generation of the electron uniformly in x_{Bj}, Q^2, ϕ_e. As in the H$(e, e'\pi^0)p$ simulation (Chapter 4.4.2), the real radiative effects on the incident electron are treated in the radiator equivalence approximation. In contrast with π^0 simulation however, both external and internal real energy losses of the scattered electron are also treated in the radiator equivalence approximation. The probability of an energy loss Δk_{out} for the scattered electron is:

$$I_{out}(k'_v, \Delta k_{out}, t_{out}) = \frac{bt_{out} + \delta_S/2}{\Delta k_{out}} \left[\frac{\Delta k_{out}}{k'_v}\right]^{bt_{out}+\delta_S/2} \tag{5.23}$$

with t_{out} is the quantity of material crossed by the scattered electron in the target.

The two kaon mass is then generated accordingly to the event type. For resonant K^+K^- events, the resonance mass is generated according to a relativistic Breit-Wigner distribution:

$$P(m^2_{KK})dm^2_{KK} = \frac{m_\phi \Gamma_\phi/\pi}{(m^2_{KK} - m^2_\phi)^2 + m^2_\phi \Gamma^2_\phi} dm^2_{KK}. \tag{5.24}$$

The inversion of this relation gives:

$$m^2_{KK} = m_\phi \Gamma_\phi \tan\left[\pi(U - 1/2)\right] + m^2_\phi, \tag{5.25}$$

with U uniform between 0 and 1. For the non resonant continuum, the mass is distribution is given by a s-wave in the Lorentz invariant phase space:

$$P(m^2_{KK})dm^2_{KK} = \frac{3}{2} \frac{\sqrt{m^2_{KK} - 4m^2_K}}{[m^2_{KK\max} - 4m^2_K]^{3/2}} dm^2_{KK}, \tag{5.26}$$

with $m_{KK\max}$ the maximal mass of the continuum, set to 1.5 GeV. The inversion of this relation gives:

$$m^2_{KK} = [m^2_{KK\max} - 4m^2_K]U^{2/3} + 4m^2_K, \tag{5.27}$$

with U uniform between 0 and 1. In both cases, the generated mass has to respect the condition $2m_K < m_{KK} < (W - M)$.

After the two kaon mass generation, t is generated uniformely between t_{min} and $\min(t_{min} - 1.5(\mathrm{GeV}^2), t_{max})$, with $t_{min}(t_{max}) = \frac{(Q^2 - m^2_\phi)^2}{4s} \pm (|q^{CM}| - |q'^{CM}|)^2$. ϕ_ϕ is generated uniformly in $[0, 2\pi]$. The decay $\phi \to KK$ is generated uniformly in $\cos\theta_K$ in the ϕ rest frame $\cos\theta^{\phi\mathrm{RF}}_K \in [-1, 1]$, and $\phi_K \in [0, 2\pi]$, and boosted in the lab frame, for both resonant and non resonant events. The $\phi \to KK$ angular distribution (Appendix 3) comes as a ponderation.

Then, the scattered electron and the two kaons are smeared by the HRS (Table 2.1) and the SBS (Table 5.8) resolutions, respectively. Practically the smearing of a particle is implemented the following way:

- The particle momentum is smeared by a gaussian distribution which deviation is the momentum resolution of the respective instrument.

- The projections of the particle direction in the horizontal and vertical planes of the instrument are computed. Then, these projections are smeared by a gaussian distribution which deviation is the adequate direction resolution of the respective instrument. Finally, the three component of the particle trivector are recomputed with these smeared projections.

Finally, the experimental (*i.e.* smeared) particle trivectors are matched with the acceptances of their respective instrument (given Table 2.1 for the HRS and in Table 5.8 for the SBS).

The choice of the HRS⊗SBS pair for the measurement of the reaction $\mathrm{H}(e, e'K^+, K^-)p$ has been initially made for several reasons:

- the relatives acceptances between the HRS (measures the electron in a very small acceptance) and the SBS (measures the kaon pair, which has several degrees of freedom relative to the electron) were expected to give good constraints on the phase space;

- the very accurate resolution of the HRS, coupled to the rather good resolution of the SBS was expected to give good constraints on the kinematics, and particularly on the exclusivity.

With the described simulation, one may verify that these requirements are met. Let us review the simulation achievements in terms of acceptance and resolutions.

The acceptance achievements are shown on Figure 5.22 for KIN1. On this figure are

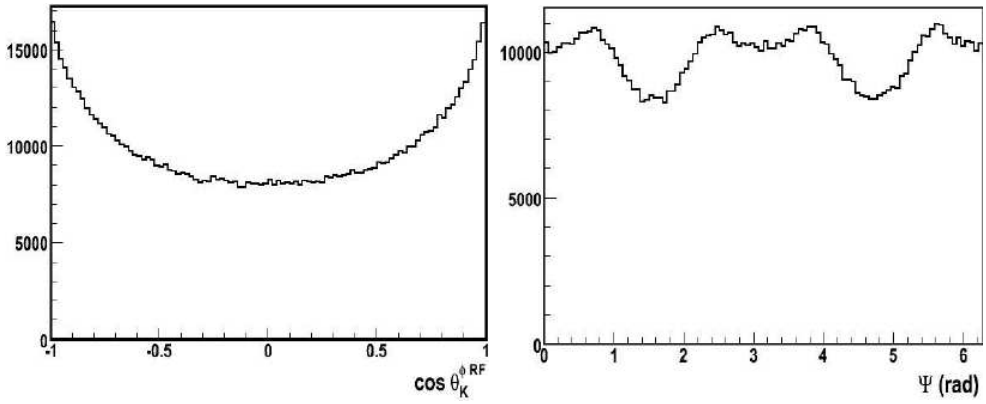

Figure 5.22: Left: Distribution of $\mathrm{H}(e,e'K^+K^-)X$ in the $\cos\theta_K^{\phi\mathrm{RF}}$ variable. The visible peak comes from the highest kaon pair masses. Right: Distribution of $\mathrm{H}(e,e'K^+K^-)X$ the Ψ variable, emphasizing the bounds of the SBS acceptence.

shown the distributions of the data sample $\mathrm{H}(e,e'K^+K^-)X$ (resonant plus non resonant) in the $\phi \to K^+K^-$ decay anglur variables, *i.e.* $\cos\theta_K^{\phi\mathrm{RF}}$, Ψ. These variables are indeed very useful for the separation of the different contributions to the $\phi \to KK$ decay (see Appendix 3). The acceptence is complete in both $\cos\theta_K^{\phi\mathrm{RF}}$ and Ψ. On the $\cos\theta_K^{\phi\mathrm{RF}}$ distribution, a peak, due part of the resonant events and part to the highest mass non resonant events, shows at $\cos\theta_K^{\phi\mathrm{RF}} \to \pm 1$. The height of this peak is just about the double of the baseline, which is not dramatic. On the Ψ distribution the SBS bounds are well visible, but the ratio "highest peak"/"lowest dip" is not more than 40 %.

The resolutions achievements are available on Figure 5.23. On this figure, the missing

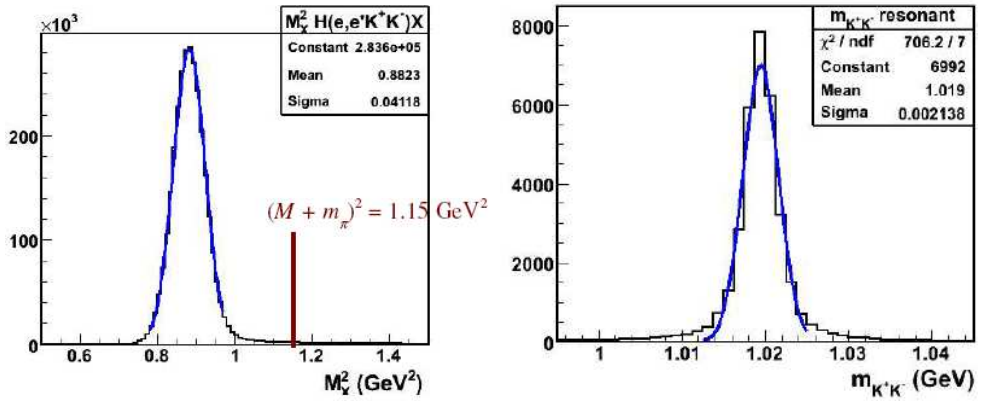

Figure 5.23: Left: Distribution of the missing mass squared for $\mathrm{H}(e,e'K^+K^-)X$ events. Right: Distribution of the two kaon resonant mass for $\mathrm{H}(e,e'\phi \to K^+K^-)X$ events. Both distributions have been fitted with a gaussian.

mass squared distribution for $\mathrm{H}(e,e'K^+K^-)X$ events is shown on the left. This distribution has been fitted by a gaussian, which deviation is at the 0.04 GeV^2 level. The

exclusivity cut set at $M_X^2 < (M+m_\pi) = 1.15\text{GeV}^2$ is materialized by the red line. The separation between exclusive $\text{H}(e,e'K^+K^-)p$ events and $\text{H}(e,e'K^+K^-)X,\ X \in p+n\pi,\Delta,...$ could then be performed in the best conditions. The two kaon mass distribution for $\text{H}(e,e'\phi \to K^+K^-)X$ (resonant events) is shown on the right panel of Figure 5.23. This distribution has been fitted with a gaussian. The most remarquable feature of this fit is paradoxally its awful reduced χ^2, which demonstrates that the generated relativistic Breit Wigner shape competes with the gaussian resolution of the reconstructed missing mass squared. In other words, the SBS resolution (even worsened by the SBS modifications) do not smear enough the kaon trajectories to drown the resonance mass shape under experimental effects.

$ep \to epK^+K^-$ cross section, counting rate

We give here the cross section ponderation for the resonant and non resonant $ep \to epK^+K^-$ processes. The resonant $ep \to epK^+K^-$ cross section is based on the model and calculations by Goloskokov and Kroll [39, 40]. They provided calculations of their model for our kinematics. Their calculations are shown on Figure 5.24. We parameterized this

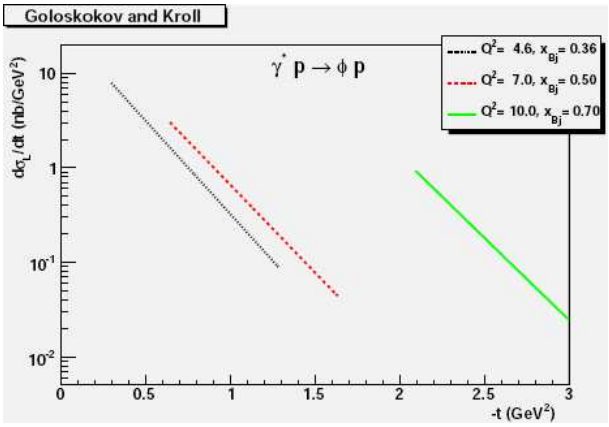

Figure 5.24: Longitudinal cross section $d\sigma_L/dt$ for $ep \to ep\phi$ process, as calculated by Goloskokov and Kroll.

cross section by the following expression:

$$\frac{d\sigma_L^{GK}}{dt}(Q^2, x_{Bj}, t_{min}-t) = ce^{-aQ^2}e^{b(x_{Bj})\times(t-t_{min})}, \tag{5.28}$$

with $c = 5.01 \cdot 10^1$, $a = 3.97 \cdot 10^{-1}$, and where:

$$b(x_{Bj}) = d + e \times \ln\frac{1}{x_{Bj}}, \tag{5.29}$$

with $d = 3.73$ and $e = 7.97 \cdot 10^{-1}$. The tranverse cross section σ_T is modeled directly σ_L:

$$\begin{aligned}\frac{d\sigma_T}{dt}(Q^2, x_{Bj}, t_{min}-t) &= \frac{1}{\left(\frac{\Lambda^2+Q_0^2}{\Lambda^2+Q^2}\right)^3} \times \frac{d\sigma_L^{GK}}{dt}(Q^2, x_{Bj}, t_{min}-t) \times \left(\frac{\Lambda^2+Q_0^2}{\Lambda^2+Q^2}\right)^4 \\ &= \frac{\Lambda^2+Q_0^2}{\Lambda^2+Q^2}\frac{d\sigma_L^{GK}}{dt}(Q^2, x_{Bj}, t_{min}-t)\end{aligned} \tag{5.30}$$

with $Q_0^2 = 3.8\ \mathrm{GeV}^2$. This gives the ratio longitudinal/transverse cross section:

$$R = \frac{\Lambda^2 + Q^2}{\Lambda^2 + Q_0^2} \tag{5.31}$$

Under the assumption of s-channel helicity conservation, which implies:

$$\mathcal{W}(\cos\theta_K^{\phi\mathrm{RF}}, \Psi) = \frac{3}{8\pi}\frac{1}{r_{00}^{04}}\left(1 - r_{00}^{04} + (3r_{00}^{04} - 1)\cos\theta\right) \tag{5.32}$$

and given this cross section model, the eightfold differential cross section we used to ponderate resonant events is:

$$\begin{aligned}\frac{d^8\sigma^{ep\to ep\phi}}{dQ^2 dx_B d\phi_e dt d\phi_\phi dm_{KK}^2 d^2\Omega_K} &= \frac{d^3\Gamma}{dQ^2 dx_B d\phi_e}\rho(m_{KK}^2)\epsilon\frac{d\sigma_L^{GK}}{dt}\mathcal{W}(\cos\theta_K^{\phi\mathrm{RF}}, \Psi) \\ &= \frac{d^3\Gamma}{dQ^2 dx_B d\phi_e}\rho(m_{KK}^2)\left[\frac{d\sigma_T}{dt}\sin^2\theta_K + 2\epsilon\frac{d\sigma_L}{dt}\cos^2\theta_K\right]\end{aligned} \tag{5.33}$$

where

$$\rho(m_{KK}^2) = \frac{m_\phi}{m_{KK}}\frac{\sqrt{m_{KK}^2 - 4m_K^2}}{\sqrt{m_\phi^2 - 4m_K^2}} \tag{5.34}$$

is the additionnal resonant mass density which is not included in the mass generation.

The cross section expression for non resonant events is similar to the expression in Equation 5.33. In constrast with the resonant case, the production of the two kaons is isotropic:

$$\Rightarrow \mathcal{W}(\cos\theta_K^{\phi\mathrm{RF}}, \Psi) = 1. \tag{5.35}$$

We use the same longitudinal and transverse cross sections model, so the eightfold differential cross section for non resonant events is:

$$\frac{d^8\sigma^{ep\to epK^+K^-\mathrm{NR}}}{dQ^2 dx_B d\phi_e dt d\phi_\phi dm_{KK}^2 d^2\Omega_K} = \Gamma\rho^{NR}(m_{KK}^2)\left[\frac{d\sigma_T}{dt} + \epsilon\frac{d\sigma_L^{GK}}{dt}\right]. \tag{5.36}$$

where $\rho^{NR}(m_{KK}^2)m_\phi/m_{KK}$.

The relative ponderation we used between resonant events and non resonant events to build a realistic data sample is paramterezed by the respective statistics in the resonant peak bounds, which are present in the ratio of $\sim 1:1$ in CLAS [100].

With this model, we have access to a rough estimation of the counting rate for longitudinal ϕ electroproduction. The estimation method is similar to the counting rate estimation method for elastic events (Chapter 3.3.1). The *approximate* counting rate N is given by:

$$N = \left[\int \mathcal{L}dt\right]\frac{PSF_{\mathrm{HRS}}}{N_{\mathrm{Gen}}}\sum_{i=1}^{N_{\mathrm{Gen}}}\Gamma_i\epsilon_i\left[\int dt\frac{d\sigma_L}{dt}\right]_i \times BR_{\phi\to KK} \times \mathrm{SBS}_{\mathrm{acc}}, \tag{5.37}$$

where $PSF_{\mathrm{HRS}} = \Delta p_{\mathrm{HRS}}\Delta\Omega_e$, N_{Gen} is the number of generated events, $BR_{\phi\to KK} = 0.492$ the branching ratio of the $\phi(1020)$ in two charged kaons, and $\mathrm{SBS}_{\mathrm{acc}} = 0.15$ takes into account the proportion of rejected events due to the SBS acceptance. The approximate counting rate is about $4\cdot 10^4$ events for KIN1, $5\cdot 10^3$ events for KIN2, and $5\cdot 10^2$ events for KIN3.

Analysis and Results for $\phi(1020)$ electroproduction

We are interested about the projected results as well as the projected error bars. We would wish to verify whether the cross section which is extracted is consistent with the model, and if the statistics allows accurate enough error bars. The analysis method is quickly described and the results are exposed.

Analysis method

Similarly to π^0 cross section extraction method, the analysis method for ϕ is based on comparison between simulation and "data" yields. In constrast with π^0 analysis however, the ϕ resonance peak is flooded in the continuum (Figure 5.26). For this reason we have

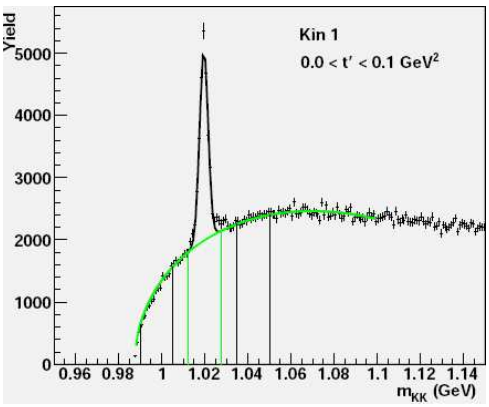

Figure 5.25: Distribution of m_{KK} for the simulation ponderated by the cross section model, for $0 < t_{min} - t\text{GeV}^2 < 0.1$. The black curve is the fit of the total yields, and the green curve is the continuum contribution. The cut lines delimit the yield ranges we use for the analysis. More details are available in the text.

to subtract the continuum yields from the peak. The method to subtract the continuum is the following:

- For each $t_{min} - t$ bin, the two kaon mass distribution is fitted on the range $2m_K < m_{KK} < 1.1$ GeV by a function $f(m_{KK}) = f_{NR}(m_{KK}) + f_\phi(m_{KK})$, with $f_\phi(m_{KK}) = A_\phi \exp\left[-(m_{KK} - m_\phi)/2\sigma_\phi^2\right]$ and $f_{NR}(m_{KK}) = A_{NR}[(m_{KK}^2 - 4m_K^2)/(m_\phi^2 - 4m_K^2)]^{1/2} \times [(m_{\max} - m_{KK})/(m_{\max} - m_\phi)]^p$.

- Three 0.015 GeV wide bins in m_{KK} are defined: one centered on the peak (at 1.02 GeV), and two shifted from the peak center value by 0.0225 GeV (at 0.9975 and 1.0425 GeV). The two side bins are selected to remove the continuum from the peak. The integral of the continuum function fit is computed in the two side bands and in the peak window.

- The yields in the two side bands are subtracted from the yields of the peak. These yields are weighted by the ratio of the continuum function integral of the peak window over the the continuum function integral for the side band.

The result of this subtraction is given for the first bin in $t_{min} - t$ and as a function of $\cos\theta_K^{\phi\text{RF}}$ in the left panel of Figure 5.26. These resonant yields are then fitted by a combination of $3/(8\pi) \times \Gamma \sin^2\theta_K^{\phi\text{RF}}$ and $3/(4\pi) \times \Gamma\epsilon \cos^2\theta_K^{\phi\text{RF}}$ contributions (right panel of Figure 5.26), to evaluate σ_T and σ_L. The results are available in the next subsection.

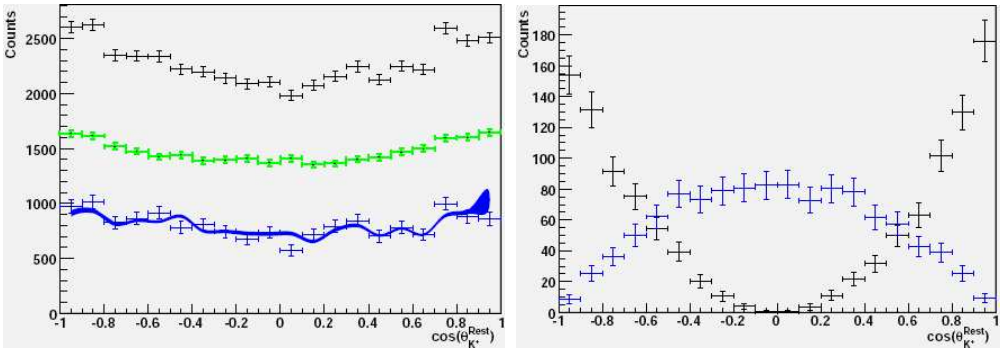

Figure 5.26: Left: Counts in $\cos\theta_K^{\phi\mathrm{RF}}$ for total yields (black), subtracted non resonant yields (green), resonant yields (blue). Details on the fit are given in the text. Right: $\cos^2\theta_K^{\phi\mathrm{RF}}$ (σ_L, black) and $\sin^2\theta_K^{\phi\mathrm{RF}}$ (σ_T, blue) contributions to resonant yields.

Projected results

The longitudinal ϕ cross section and error bars has been extracted for KIN1 with the method described in the previous subsection. From this extraction and with the help of the model and estimated counting rates, the longitudinal cross sections and errors bars have been extrapolated for KIN2 and KIN3. All of these are available as a function of $t_{min} - t$ on Figure 5.27.

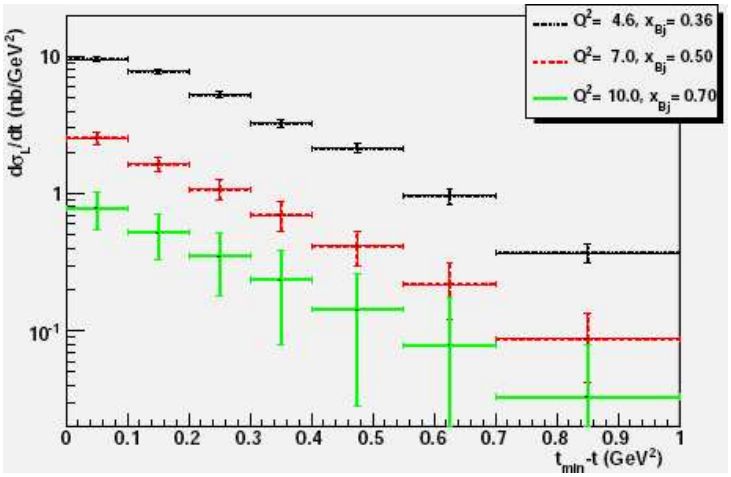

Figure 5.27: Projected $d\sigma_L/dt$ results and the error bars for KIN1 (black), KIN2 (red), and KIN3 (green).

For KIN1, the analysis method gives back the model cross section shape, but the abosulte value of the cross section is overestimated. The statistical error bars are obtained assuming a luminosity of 10^{37} cm^{-2}s^{-1} during one month for each kinematic. If one assumes a total systematic error of 10 % with the present statistical errors:

- For KIN1, the statistical effects are dominant for $t_{min} - t > 0.7$ GeV^2 (last bin). The acumulatic statistics are fairly sufficiant.
- For KIN2, the statistical errors are dominant for $t_{min} - t > 0.3$ GeV^2. About 6 times more statistics would then be required for a non dominance of statistical effects for $t_{min} - t > 0.55$ GeV^2.

- For KIN3, the statistical errors are dominant for all the $t_{min} - t$ range. No amount of statistics are recordable in a reasonable duration to balance this. This kinematic may have to be given up then, despite its huge interest.

With σ_L (Figure 5.27) and σ_T (not showed), we are able to compute r_{00}^{04}. The r_{00}^{04} we extracted is available as a fucntion of $t_{min} - t$ for KIN1 and with error bars, on Figure 5.28. On this figure, along with r_{00}^{04}, an estimation of the errors on a s-channel helicity

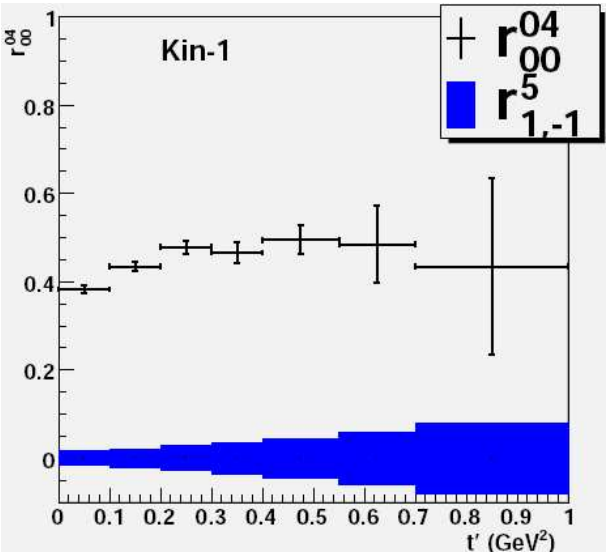

Figure 5.28: Projected r_{00}^{04} results and the error bars for KIN1. The blue error bands are the errors estimations for a SCHC violating term such as $r_{1,-1}^{5}$.

conservation violating term, $r_{1,-1}^{5}$ here, is also materialized by the blue error bands. The r_{00}^{04} is compatible within the error bars with the model we injected in the simulation. The errors estimation of the density matrix element $r_{1,-1}^{5}$ are better than 0.1 in every bin, that means the sensitivoty of SCHC violating terms is better than 10 %.

Conclusion and prospects for deep $\phi(1020)$ electroproduction experiment

The deeply virtual ϕ production experiment in Hall A at JLab 12 GeV seems to be faisible with the help of the HRS⊗SBS pair. The acceptance is complete (Figure 5.22) and, due to the apparatus, the resolutions in missing mass and in two kaon invariant mass are excellent (Figure 5.23). These resolutions allow, at least at Q^2, x_{Bj} not too high, an accurate extraction of the $ep \rightarrow ep\phi$ longitudinal cross section.

These cross section measurements will allow to test some models of the two-gluon exchange mechanism at relatively high Q^2. High precision measurements of the $t_{min} - t$-distributions (independent of the magnitude of the cross sections) provides a unique probe of the spatial distribution of gluons in the valence region. The s-channel helicity conservation could be tested at a level which is better than 10 %.

On the other hand, several issues could be explored to improve this work, either on theoretical/phenomenological and experimental points of view. To refine the simulation,

the K/π misidentification, which would be accessible through a complete GEANT4 simulation of the apparatus, and particularly of the RICH. The kinematic range would have to be restrained to $0.3 < x_{Bj} < 0.6$, in order to get reasonable statistics.

From the phenomenological point of view, the Q^2 dependence at fixed x_{Bj} also be very useful for testing models. To do this, careful studies have to be done on lower Q^2, since acceptance leaks could appear because of the lower ϕ boost, implying a larger aperture of the two kaons decay in the lab frame. It would also be interesting to test the validity of SCHC, by expanding the study of sensitivity to other SCHC violating terms. The ultimate goal for the experiment is to test the sensitivity of the cross sections to GPDs.

Appendix 3: $\phi(1020) \to K^+K^-$ decay distributions

We develop the full expression of the angular decay distribution for $\phi(1020) \to K^+K^-$, in the case of deeply virtual $\phi(1020)$ production. We use the coordinate system of Schilling and Wolf [98]:

$$\hat{z}_q = \frac{k - k'}{|k - k'|}, \quad \hat{y}_q = \frac{k \wedge k'}{|k \wedge k'|}, \quad \hat{x}_q = \hat{y}_q \wedge \hat{z}_q; \tag{5.38}$$

$$\hat{Y} = \frac{q \wedge q'}{|q \wedge q'|}, \quad \hat{Z} = \hat{z}_q, \quad \hat{X}_q = \hat{Y}_q \wedge \hat{Z}_q; \tag{5.39}$$

$$\hat{z}_K = \frac{q'^{CM}}{|q'^{CM}|}, \quad \hat{y}_K = \hat{Y}, \quad \hat{x}_K = \hat{y}_K \wedge \hat{z}_K; \tag{5.40}$$

The azimuthal production angle of the $\phi(1020)$ meson, $\phi_\phi = \Phi$ (compact notation) is defined by:

$$\cos\Phi = \hat{y}_q \cdot \hat{Y}, \quad \sin\Phi = \frac{\left(\hat{y}_q \wedge \hat{Y}\right) \cdot \hat{Z}}{\left|\hat{y}_q \wedge \hat{Y}\right|}. \tag{5.41}$$

The polar and azimuthal angle of the K^+ in the ϕ_{1020} rest frame, $\theta_K = \theta$ and $\phi_K = \phi$ (compact notations) are defined by:

$$\cos\theta = \frac{q^+ \cdot \hat{z}_K}{|q^+|}, \quad \sin\theta\cos\phi = \frac{q^+ \cdot \hat{x}_K}{|q^+|}, \quad \sin\theta\sin\phi = \frac{q^+ \cdot \hat{x}_K}{|q^+|}. \tag{5.42}$$

Within these conventions, the angular decay distribution for $\phi(1020) \to K^+K^-$ is expressed, in the most general case:

$$\mathcal{W}(\cos\theta, \phi, \Phi, h) = \mathcal{W}(\cos\theta, \phi, \Phi) + \mathcal{W}(h). \tag{5.43}$$

which is normalized by:

$$\int d\cos\theta d\phi d\Phi dh \mathcal{W}(\cos\theta, \phi, \Phi, h) = 1. \tag{5.44}$$

and with the helicity independent decay distribution:

$$\begin{aligned}\mathcal{W}(\cos\theta,\phi,\Phi) = \frac{3}{4\pi}\Big\{&\frac{1}{2}(1-r^{04}_{00}) + \frac{1}{2}(3r^{04}_{00}-1)\cos^2\theta - \sqrt{2}\Re e\, r^{04}_{10}\sin 2\theta\cos\phi - r^{04}_{1,-1}\sin^2\theta\cos 2\phi \\ &+ \sqrt{2\epsilon(1+\epsilon)}\cos\Phi\left[r^{5}_{11}\sin^2\theta + r^{5}_{00}\cos^2\theta - \sqrt{2}\Re e\, r^{5}_{10}\sin 2\theta\cos\phi - r^{5}_{1,-1}\sin^2\theta\cos 2\phi\right] \\ &- \epsilon\cos 2\Phi\left[r^{1}_{11}\sin^2\theta + r^{1}_{00}\cos^2\theta - \sqrt{2}\Re e\, r^{1}_{10}\sin 2\theta\cos\phi - r^{1}_{1,-1}\sin^2\theta\cos 2\phi\right] \\ &+ \sqrt{2\epsilon(1+\epsilon)}\sin\Phi\left[\sqrt{2}\Im m\, r^{6}_{10}\sin 2\theta\sin\phi - \Im m\, r^{6}_{1,-1}\sin^2\theta\sin 2\phi\right] \\ &- \epsilon\sin 2\Phi\left[\sqrt{2}\Im m\, r^{2}_{10}\sin 2\theta\sin\phi - \Im m\, r^{2}_{1,-1}\sin^2\theta\sin 2\phi\right]\Big\},\end{aligned} \tag{5.45}$$

and the helicity dependent decay distribution:

$$\begin{aligned}\mathcal{W}(h) = \frac{3h}{4\pi}\Big\{&\sqrt{1-\epsilon^2}\left[\sqrt{2}\Im m\, r^{2}_{10}\sin 2\theta\sin\phi - \Im m\, r^{2}_{1,-1}\sin^2\theta\sin 2\phi\right] \\ &+ \sqrt{2\epsilon(1-\epsilon)}\cos\Phi\left[\sqrt{2}\Im m\, r^{7}_{10}\sin 2\theta\sin\phi - \Im m\, r^{7}_{1,-1}\sin^2\theta\sin 2\phi\right] \\ &+ \sqrt{2\epsilon(1-\epsilon)}\sin\Phi\left[r^{8}_{11}\sin^2\theta + r^{8}_{00}\cos^2\theta - \sqrt{2}\Re e\, r^{8}_{10}\sin 2\theta\cos\phi - r^{8}_{1,-1}\sin^2\theta\cos 2\phi\right]\Big\}.\end{aligned} \tag{5.46}$$

In the case where s-channel helicity conservation (SCHC) applies, the expression of theangular decay distribution is greatly simplified. Indeed, SCHC implies all the above constraints:

$$\sqrt{2}\Re e\, r^{5}_{10} = \Im m\, r^{6}_{10} = \sqrt{R}\cos\delta_R; \tag{5.47}$$

$$\sqrt{2}\Re e\, r^{8}_{10} = \Im m\, r^{7}_{10} = \sqrt{R}\sin\delta_R; \tag{5.48}$$

$$r^{5}_{11} = r^{5}_{00} = r^{5}_{1,-1} = \Im m\, r^{7}_{1,-1} = \Re e\, r^{04}_{10} = 0; \tag{5.49}$$

$$r^{8}_{11} = r^{8}_{00} = r^{8}_{1,-1} = \Im m\, r^{6}_{1,-1} = \Re e\, r^{3}_{10} = 0; \tag{5.50}$$

$$r^{1}_{11} = r^{1}_{00} == \Re e\, r^{1}_{10} = r^{04}_{1,-1} = 0; \tag{5.51}$$

$$r^{2}_{10} = r^{3}_{1,-1} = 0; \tag{5.52}$$

$$r^{1}_{1,-1} = \Im m\, r^{2}_{1,-1} = \frac{\epsilon}{2(1+\epsilon R)} = \epsilon(1-r^{04}_{00}); \tag{5.53}$$

so:

$$\mathcal{W}(\cos\theta,\phi,\Phi,h) \overset{\text{SCHC}}{\rightarrow} \mathcal{W}(\cos\theta,\Psi,h), \tag{5.54}$$

with:

$$\begin{aligned}\mathcal{W}(\cos\theta,\Psi,h) = \frac{1}{1+\epsilon R}\frac{3}{8\pi}\Big\{&\sin^2\theta(1+\epsilon\cos 2\Psi) + 2\epsilon\cos^2\theta \\ &+ \sqrt{2\epsilon(1+\epsilon)}\sqrt{R}\cos\delta_R\sin 2\theta\cos\Psi \\ &+ h\sqrt{2\epsilon(1-\epsilon)}\sqrt{R}\sin\delta_R\sin 2\theta\sin\Psi\Big\}\end{aligned} \tag{5.55}$$

and $\Psi = \phi - \Phi$.

Bibliography

[Wilczek(1974)] F. Wilczek (1974), talk delivered at APS Div. of Particles and Fields Meeting, Williamsburg, Va., Sep 5-7, 1974.

[1] D. Mueller, D. Robaschik, B. Geyer, F. M. Dittes, and J. Horejsi, Fortschr. Phys. **42**, 101 (1994), hep-ph/9812448.

[2] X.-D. Ji, Phys. Rev. Lett. **78**, 610 (1997), hep-ph/9603249.

[3] R. Hofstadter and R. W. McAllister, Phys. Rev. **98**, 217 (1955).

[4] E. Amaldi, S. Fubini, and G. Furlan, Springer Tracts Mod. Phys. **83**, 1 (1979).

[5] D. Drechsel and L. Tiator, J. Phys. **G18**, 449 (1992).

[6] J. D. Bjorken and S. D. Drell (1964), bibliograph.Inst./mannheim 1967, 409 P.(B.i.-hochschultaschenbuecher, Band 101).

[7] G. M. Huber et al. (Jefferson Lab), Phys. Rev. **C78**, 045203 (2008), 0809.3052.

[8] M. Burkardt, Phys. Rev. **D66**, 114005 (2002), hep-ph/0209179.

[9] F. Halzen and A. D. Martin (1984), new York, Usa: Wiley (1984) 396p.

[10] S. R. Amendolia et al., Phys. Lett. **B146**, 116 (1984).

[11] S. R. Amendolia et al. (NA7), Nucl. Phys. **B277**, 168 (1986).

[12] P. Brauel et al., Phys. Lett. **B69**, 253 (1977).

[13] H. Ackermann et al., Nucl. Phys. **B137**, 294 (1978).

[14] T. Horn et al. (Jefferson Lab F(pi)-2), Phys. Rev. Lett. **97**, 192001 (2006), nucl-ex/0607005.

[15] T. Horn et al., Phys. Rev. **C78**, 058201 (2008), 0707.1794.

[16] F. Gutbrod and G. Kramer, Nucl. Phys. **B49**, 461 (1972).

[17] C. J. Bebek et al., Phys. Rev. **D13**, 25 (1976).

[18] J. M. Laget, Phys. Rev. **C76**, 052201 (2007), 0708.1250.

[19] M. Guidal, J. M. Laget, and M. Vanderhaeghen, Nucl. Phys. **A627**, 645 (1997a).

[20] M. Guidal, J. M. Laget, and M. Vanderhaeghen, Phys. Lett. **B400**, 6 (1997b).

[21] P. G. O. Freund and Y. Nambu, Phys. Rev. Lett. **34**, 1645 (1975).

[22] D. Robson, Nucl. Phys. **B130**, 328 (1977).

[23] M. Braunschweig, W. Braunschweig, D. Husmann, K. Luebelsmeyer, and D. Schmitz, Phys. Lett. **B26**, 405 (1968).

[24] M. Braunschweig, W. Braunschweig, D. Husmann, K. Luebelsmeyer, and D. Schmitz, Nucl. Phys. **B20**, 191 (1970).

[25] W. Brefeld et al., Nucl. Phys. **B100**, 93 (1975).

[26] R. L. Anderson et al. (1970), sLAC-PUB-0770.

[27] R. L. Anderson et al., Phys. Rev. Lett. **26**, 30 (1971a).

[28] R. L. Anderson et al., Phys. Rev. **D4**, 1937 (1971b).

[29] J. Froyland, Nucl. Phys. **B11**, 204 (1969).

[30] G. R. Goldstein and J. F. Owens, Phys. Rev. **D7**, 865 (1973).

[31] F. W. Brasse et al., Phys. Lett. **B58**, 467 (1975).

[32] C. Berger et al., Nucl. Phys. **B137**, 1 (1978).

[33] A. V. Radyushkin, Phys. Rev. **D56**, 5524 (1997), `hep-ph/9704207`.

[34] M. Vanderhaeghen, P. A. M. Guichon, and M. Guidal, Phys. Rev. **D60**, 094017 (1999), `hep-ph/9905372`.

[35] K. Goeke, M. V. Polyakov, and M. Vanderhaeghen, Prog. Part. Nucl. Phys. **47**, 401 (2001), `hep-ph/0106012`.

[36] C. Munoz Camacho et al. (Jefferson Lab Hall A), Phys. Rev. Lett. **97**, 262002 (2006), `nucl-ex/0607029`.

[37] A. V. Belitsky, D. Mueller, and A. Kirchner, Nucl. Phys. **B629**, 323 (2002), `hep-ph/0112108`.

[38] J. C. Collins, L. Frankfurt, and M. Strikman, Phys. Rev. **D56**, 2982 (1997), `hep-ph/9611433`.

[39] S. V. Goloskokov and P. Kroll, Eur. Phys. J. **C50**, 829 (2007), `hep-ph/0611290`.

[40] S. V. Goloskokov and P. Kroll, Eur. Phys. J. **C42**, 281 (2005), `hep-ph/0501242`.

[41] X.-d. Ji, J.-p. Ma, and F. Yuan, Phys. Rev. **D71**, 034005 (2005), `hep-ph/0404183`.

[42] X.-d. Ji, J.-P. Ma, and F. Yuan, Phys. Lett. **B597**, 299 (2004), `hep-ph/0405085`.

[43] J. Binnewies, B. A. Kniehl, and G. Kramer, Z. Phys. **C65**, 471 (1995a), `hep-ph/9407347`.

[44] J. Binnewies, B. A. Kniehl, and G. Kramer, Phys. Rev. **D52**, 4947 (1995b), `hep-ph/9503464`.

[45] T. P. McPharlin et al., Phys. Lett. **B90**, 479 (1980).

[46] J. J. Aubert et al. (European Muon), Phys. Lett. **B114**, 373 (1982).

[47] J. J. Aubert et al. (European Muon), Z. Phys. **C18**, 189 (1983).

[48] B. Andersson, G. Gustafson, G. Ingelman, and T. Sjostrand, Phys. Rept. **97**, 31 (1983).

[49] A. Airapetian et al. (HERMES), Eur. Phys. J. **C21**, 599 (2001), `hep-ex/0104004`.

[50] E. L. Berger, Z. Phys. **C4**, 289 (1980).

[51] M. Anselmino et al., Phys. Rev. **D71**, 074006 (2005), `hep-ph/0501196`.

[52] A. Bacchetta, AIP Conf. Proc. **1149**, 447 (2009), `0902.2712`.

[53] R. N. Cahn, Phys. Lett. **B78**, 269 (1978).

[54] D. W. Sivers, Phys. Rev. **D41**, 83 (1990).

[55] P. Y. Bertin, C. E. Hyde, R. Ransome, and F. Sabatié (2000), jefferson Lab Proposal, E00-110.

[56] C. W. Leemann, D. R. Douglas, and G. A. Krafft, Ann. Rev. Nucl. Part. Sci. **51**, 413 (2001).

[57] J. Alcorn et al., Nucl. Instrum. Meth. **A522**, 294 (2004).

[58] G. Laveissière, Ph.D. thesis, Université Blaise Pascal, Clermont-Ferrand II (2001).

[59] D. Marchand, Ph.D. thesis, Université Blaise Pascal, Clermont-Ferrand II (1998).

[60] F. Gougnaud et al. (1999), prepared for 7th International Conference on Accelerator and Large Experimental Physics Control Systems (ICALEPCS 99), Trieste, Italy, 4-8 Oct 1999.

[61] B. Wagner et al., Nucl. Instrum. Meth. **A294**, 541 (1990).

[62] N. Falletto, Ph.D. thesis, Université Joseph Fourier (1999).

[63] J. P. Jorda et al., Nucl. Instrum. Meth. **A412**, 1 (1998).

[64] N. Falletto et al. (HAPPEX), Nucl. Instrum. Meth. **A459**, 412 (2001).

[65] M. Baylac et al., Phys. Lett. **B539**, 8 (2002), `hep-ex/0203012`.

[66] G. Quemener, Ph.D. thesis, Université Blaise Pascal, Clermont-Ferrand II (1997).

[67] K. L. Brown and S. Howry (1970), sLAC-0091.

[68] N. Liyanage, Hall A Technical Note JLAB-TN-02-012, Jefferson Lab (2002), URL `http://hallaweb.jlab.org/publications/Technotes/technote.html`.

[69] K. G. Fissum et al., Nucl. Instrum. Meth. **A474**, 108 (2001).

[70] K. G. Fissum et al., Hall A Technical Note JLAB-TN-00-016, Jefferson Lab (2000), URL http://hallaweb.jlab.org/publications/Technotes/technote.html.

[71] M. Iodice et al., Nucl. Instrum. Meth. **A411**, 223 (1998).

[72] P. Kozma, P. Kozma, and R. Bajgar, Nucl. Instrum. Meth. **A484**, 149 (2002).

[73] H. Photonics, Tech. Rep., Hamamatsu Photonics (2010), URL http://jp.hamamatsu.com/resources/products/etd/pdf/R7600U_TPMH1317E01.pdf.

[74] F. Feinstein and D. Lechartre, DAPNIA CE Internal report, CEA Saclay (1996).

[75] A. Camsonne, Ph.D. thesis, Université Blaise Pascal, Clermont-Ferrand II (2005).

[76] C. Muñoz Camacho, Ph.D. thesis, Université Paris VI, France (2005).

[77] M. Mazouz, Ph.D. thesis, Université Joseph Fourier, Grenoble I (2006).

[78] P. V. Degtiarenko, M. V. Kossov, and H.-P. Wellisch, to be published in E.P.J.A.M.

[79] V. Breton et al., Nucl. Instrum. Meth. **A362**, 478 (1995).

[80] M. Mazouz, Tech. Rep. (2005), URL https://hallaweb.jlab.org/dvcslog/Pion/131.

[81] G. F. Chew, M. L. Goldberger, F. E. Low, and Y. Nambu, Phys. Rev. **106**, 1345 (1957).

[82] M. Rvachev, Hall A Technical Note Jlab-TN-01-055, Jefferson Lab (2001), URL http://hallaweb.jlab.org/publications/Technotes/technote.html.

[83] M. Vanderhaeghen et al., Phys. Rev. **C62**, 025501 (2000), hep-ph/0001100.

[84] M. Mazouz, P. Y. Bertin, A. Camsonne, and E. Voutier, Tech. Rep. (2005).

[85] L. W. Mo and Y.-S. Tsai, Rev. Mod. Phys. **41**, 205 (1969).

[86] Y.-S. Tsai, Rev. Mod. Phys. **46**, 815 (1974).

[87] W. M. Yao et al. (Particle Data Group), J. Phys. **G33**, 1 (2006).

[88] L. Morand et al. (CLAS), Eur. Phys. J. **A24**, 445 (2005), hep-ex/0504057.

[89] J.-M. Laget (2010), 1004.1949.

[90] R. De Masi et al. (CLAS), Phys. Rev. **C77**, 042201 (2008), 0711.4736.

[91] A. Fradi, Ph.D. thesis, Université Paris XI (2009).

[92] M. M. Kaskulov, K. Gallmeister, and U. Mosel, Phys. Rev. **D78**, 114022 (2008), 0804.1834.

[93] J. Ashman et al. (European Muon), Z. Phys. **C52**, 361 (1991).

[94] M. M. Kaskulov, K. Gallmeister, and U. Mosel, private communication.

[95] E. Fuchey et al. (DVCS HALL A) (2010a), 1003.2938.

[96] E. Fuchey et al. (DVCS HALL A) (2010b), letter of Intent for PAC 35.

[97] R. S. Thorne, A. D. Martin, W. J. Stirling, and R. G. Roberts, Acta Phys. Polon. **B33**, 2927 (2002), hep-ph/0207067.

[98] K. Schilling and G. Wolf, Nucl. Phys. **B61**, 381 (1973).

[99] G. Wolf (2009), 0907.1217.

[100] J. P. Santoro et al. (CLAS), Phys. Rev. **C78**, 025210 (2008), 0803.3537.

[101] N. Akopov et al., Nucl. Instrum. Meth. **A479**, 511 (2002), physics/0104033.

[102] B. Wojtsekhowski et al., Conceptual Design Report, Jefferson Lab (2009).

RESUMÉ

La décennie passée a vu une forte évolution de l'étude de la structure des hadrons par les processus exclusifs, permettant d'acceder a une description plus complète de cette structure. Les processus exclusifs incluent la diffusion Compton profondément virtuelle, ainsi que la production exclusive de mesons à haute énergie. Ce document s'attache particulierement a ce dernier, et plus particulièrement à la production exclusive de pions neutres. Cette thèse décrit l'analyse des événements en triple coïncidence $\mathrm{H}(e, e'\gamma\gamma)X$, qui fut un sous produit abondant de l'expérience DVCS qui a eu lieu duant l'automne 2004 dans le Hall A au Jefferson Laboratory, afin d'extraire la section efficace de $ep \to ep\pi^0$. Cette section efficace a été mesurée à deux valeurs de quadrimoment de tranfert $Q^2 = 1.9$ GeV^2 et $Q^2 = 2.3$ GeV^2. La précision statistique accomplie pour ces mesures est meilleure que 5 %. Le domaine cinématique permet d'étudier l'évolution en Q^2 et en W de la section efficace. Ces resultats ont été comparés avec des calculs inspirés de la phénoménologie de Regge, ainsi qu'avec les prédictions du formalisme des distributions de partons généralisées. Une interpretation dans le cadre de la diffusion profondément inelastique semi-inclusive est également discutée.

MOTS-CLEFS

Structure des hadrons; Production de meson profondément virtuelle; Expérience de haute precision; Formalisme de Regge, Distributions de partons généralisées; Diffusion profondément inelastique semi-inclusive.

ABSTRACT

The past decade has seen a strong evolution of the study of the hadron structure through exclusive processes, allowing to access to a more complete description of this structure. Exclusive processes include DVCS (Deeply Virtual Compton Scattering) as well as hard exclusive meson production. This document is particularly focussed on the latter, and more particularly on exclusive neutral pion production. In this thesis is described the analysis of triple coincidence events $\mathrm{H}(e, e'\gamma\gamma)X$, which were a consequent by-product of the DVCS experiment which occured during Fall 2004 at Jefferson Lab Hall A, to extract the $ep \to ep\pi^0$ cross section. This cross section has been measured at two values of four-momentum transfer $Q^2 = 1.9$ GeV^2 and $Q^2 = 2.3$ GeV^2. The statistical precision for these measurements is achieved at better than 5 %. The kinematic range allows to study the evolution of the extracted cross section as a function of Q^2 and W. Results are be confronted with Regge inspired calculations and Generalized (GPD) predictions. An intepretation of our data within the framework of semi-inclusive deep inelastic scattering is also discussed.

KEYWORDS

Hadron structure, Deeply virtual pion production; High precision experiment; Regge formalism; Generalized parton distributions; Semi-Inclusive Deep Inelastic Scattering (SIDIS).